Jeong Young Park *Editor*

Current Trends of Surface Science and Catalysis

Springer

Current Trends of Surface Science and Catalysis

Jeong Young Park
Editor

Current Trends of Surface Science and Catalysis

Springer

Editor
Jeong Young Park
Korea Advanced Institute of Science and Technology (KAIST)
Daejeon, Republic of Korea

ISBN 978-1-4614-8741-8 ISBN 978-1-4614-8742-5 (eBook)
DOI 10.1007/978-1-4614-8742-5
Springer New York Heidelberg Dordrecht London

Library of Congress Control Number: 2013949285

© Springer Science+Business Media New York 2014
This work is subject to copyright. All rights are reserved by the Publisher, whether the whole or part of the material is concerned, specifically the rights of translation, reprinting, reuse of illustrations, recitation, broadcasting, reproduction on microfilms or in any other physical way, and transmission or information storage and retrieval, electronic adaptation, computer software, or by similar or dissimilar methodology now known or hereafter developed. Exempted from this legal reservation are brief excerpts in connection with reviews or scholarly analysis or material supplied specifically for the purpose of being entered and executed on a computer system, for exclusive use by the purchaser of the work. Duplication of this publication or parts thereof is permitted only under the provisions of the Copyright Law of the Publisher's location, in its current version, and permission for use must always be obtained from Springer. Permissions for use may be obtained through RightsLink at the Copyright Clearance Center. Violations are liable to prosecution under the respective Copyright Law.
The use of general descriptive names, registered names, trademarks, service marks, etc. in this publication does not imply, even in the absence of a specific statement, that such names are exempt from the relevant protective laws and regulations and therefore free for general use.
While the advice and information in this book are believed to be true and accurate at the date of publication, neither the authors nor the editors nor the publisher can accept any legal responsibility for any errors or omissions that may be made. The publisher makes no warranty, express or implied, with respect to the material contained herein.

Printed on acid-free paper

Springer is part of Springer Science+Business Media (www.springer.com)

Preface

The global energy and environmental crises have become essential issues for mankind, driving rapid developments in interface chemistry for nanocatalysts. Production of only one desired molecule that may be used as a fuel or chemical out of several thermodynamically possible molecules is called catalytic selectivity and is the foundation of "green chemistry." For this goal, bridging materials and pressure gaps to meet the needs of industry is a major challenge.

Surface science has been combined with nanoscience, leading to the development of novel functional materials, and new catalysts and energy conversion devices. Surface science has evolved such that new instruments for surface analysis on the molecular scale could be used in a vacuum or at realistic conditions (e.g., at high pressures and at solid–liquid interfaces where chemical processes typically occur), which has led to new physical and chemical concepts at working conditions. Overall, the materials and techniques of modern surface science may bring the breakthroughs for solving the global energy and environmental problems that the world is facing.

This book, entitled "Current Trends of Surface Science and Catalysis," presents new strategies and paradigms in the development of new materials and techniques. We will discuss various architectures of model catalytic systems, including colloid nanoparticles with controlled size, shape, and composition. Noncolloidal nanocatalysts and their application will be outlined. New in situ surface techniques to bridge pressure gaps will be discussed as well. The influence of surface oxides and metal–oxide interfaces in heterogeneous catalysis and surface chemistry will be shown. The broad range of topics included in this volume share perspectives from surface science for research of nanocatalysts, renewable energy conversion, biointerface, electrochemistry, and environmental science.

I would like to express my sincere appreciation to all of the authors who contributed to this exciting project, revealing the depth and breadth of this field.

Daejeon, Republic of Korea — Jeong Young Park

Contents

Part I Introduction

1 **Bridging Materials and Pressure Gaps in Surface Science and Heterogeneous Catalysis** 3
Jeong Young Park and Gabor A. Somorjai
- 1.1 Introduction 3
- 1.2 Materials and Pressure Gaps 4
- 1.3 Size, Shape, and Compositional Control of Colloid Nanoparticles 6
- 1.4 Control of Catalytic Reactions via Tuning the Size and Composition of Bimetallic Nanoparticles 8
- 1.5 In Situ Surface Characterization to Bridge Pressure Gaps 10
- 1.6 The Role of Metal–Oxide Interfaces in Heterogeneous Catalysis 14
- 1.7 Conclusion 16

References 16

Part II Model Systems for Nanocatalysts to Bridge Materials Gap

2 **Shape-Controlled Nanoparticles: Effect of Shape on Catalytic Activity, Selectivity, and Long-Term Stability** 21
Hyunjoo Lee
- 2.1 Why Does Shape Matter for Catalytic Reactions? 21
- 2.2 The Synthesis of Shaped Nanocrystals 23
  - 2.2.1 Colloidal Method 23
    - 2.2.1.1 Surface-Capping Agent 24
    - 2.2.1.2 Inorganic Shaping Agent 25
    - 2.2.1.3 Reducing Agent 26
    - 2.2.1.4 Top-Down Etching 26
  - 2.2.2 Electrochemical Method 27

2.3 The Effect of Shape on Catalytic Activity, Selectivity, and Long-Term Stability 27
  2.3.1 Pt_3Ni Nanooctahedra 28
  2.3.2 Pt Nanodendrites 29
  2.3.3 Pt-Based Nanocubes 30
  2.3.4 Pt Overgrowth on Shaped Nanocrystals 31
  2.3.5 Selectivity Enhanced by Shape 33
  2.3.6 Long-Term Stability Enhanced by Shape 34
2.4 The Effect of the Surface-Capping Agent 35
  2.4.1 How the Catalytic Activity Can Be Varied by the Surface-Capping Agents 35
  2.4.2 Removal of the Surface-Capping Agents 36
  2.4.3 In Situ Shaping Without Surface-Capping Agents 36
  2.4.4 Participating in Catalytic Reactions 37
2.5 Issues to Be Resolved 38
  2.5.1 Size: Facet vs. Edge/Step/Vertex 38
  2.5.2 Stability 39
  2.5.3 Mass Production 40
References 40

3 Non-colloidal Nanocatalysts Fabricated with Nanolithography and Arc Plasma Deposition 45
Sang Hoon Kim and Jeong Young Park
3.1 Introduction 45
3.2 Nanocatalysts Fabricated with Lithography 46
  3.2.1 Nanolithography for Fabrication of Nanodots and Nanowires 46
  3.2.2 Catalytic Properties of Nanowires Fabricated with Lithography 48
3.3 Nanocatalysts Fabricated Via Arc Plasma Deposition 50
  3.3.1 Introduction to Arc Plasma Deposition 50
  3.3.2 Nanocatalysts on Two-Dimensional Supports Using APD 53
  3.3.3 Nanocatalysts on Three-Dimensional Supports Using APD 55
  3.3.4 Some New Applications for Nanoparticles Prepared Via APD 60
3.4 Summary and Outlook 61
References 61

4 Dendrimer-Encapsulated Metal Nanoparticles: Synthesis and Application in Catalysis 65
Wenyu Huang
4.1 Introduction 65
4.2 Synthesis of Dendrimer-Encapsulated Metal Nanoparticles 67

4.2.1 Synthesis of Monometallic DENs by Chemical Reduction ... 67
4.2.2 Synthesis of DENs in Organic Solutions ... 69
4.2.3 Synthesis of DENs by Galvanic Redox Displacement ... 69
4.2.4 Synthesis of Bimetallic DENs ... 69
4.3 Recent Advancement in Understanding the Structure of DENs ... 71
4.3.1 Metal Binding Sites for Pt^{2+} Ions ... 71
4.3.2 Oxidation State of Pt DENs ... 72
4.3.3 Glass Nature of the Cluster ... 76
4.4 Newly Developed Applications of DENs in Catalysis ... 77
4.4.1 Removal of Dendrimers for Heterogeneous Catalysis ... 77
4.4.2 Understanding the Nanoparticle Size Effect in Catalysis ... 79
4.4.3 Heterogenizing Homogeneous Catalysts and Their Use in a Continuous Flow Reactor ... 81
4.4.4 Increasing Diastereoselectivity and Chemoselectivity ... 85
4.5 Summary and Outlook ... 86
References ... 87

5 Core–Shell Nanoarchitectures as Stable Nanocatalysts ... 93
Sang Hoon Joo, Jae Yeong Cheon, and Joon Yong Oh
5.1 Introduction ... 93
5.2 Metal/Metal Oxide Core–Shell Nanocatalysts ... 95
5.2.1 Core–Shell Nanocatalysts with a Silica Shell ... 95
5.2.2 Non-Siliceous Oxide Shells ... 99
5.3 Metal/Metal Oxide Yolk–Shell Nanocatalysts ... 103
5.4 Supported Catalysts Coated with Shell Layers ... 110
5.5 Summary and Future Perspectives ... 113
References ... 115

6 Shape-Controlled Bimetallic Nanocatalysts in Fuel Cells: Synthesis and Electrocatalytic Studies ... 121
Yawen Zhang and Jun Gu
6.1 Introduction ... 121
6.2 Classification of Bimetallic Nanocatalysts in Fuel Cells ... 122
6.3 Synthetic Routes to Bimetallic Nanocatalysts ... 125
6.4 Key Factors to Control the Morphology of Bimetallic Nanocrystals ... 127
6.4.1 Reduction Rate of Metal Precursors ... 127
6.4.2 Facet-Specific Capping Agents ... 129
6.4.3 Combination of Underpotential Deposition and the Galvanic Replacement Reaction ... 133

6.5 Impact of Composition and Structure on Electrocatalytic Performance 134
6.5.1 Relationship Between Adsorption Strength and Electrocatalytic Activity 134
6.5.2 Mechanisms of Tuning Adsorption Energy 135
6.6 Summary 138
References 139

Part III In Situ Surface Characterization to Bridge Pressure Gaps

7 Role of Surface Oxides on Model Nanocatalysts in Catalytic Activity of CO Oxidation 145
Jeong Young Park, Kamran Qadir, and Sun Mi Kim
7.1 Introduction 145
7.2 Pt Oxide 146
7.3 Rh Oxide 149
7.4 Ru Oxide 153
7.4.1 CO Oxidation on Ru: From Single Crystals Towards Nanoparticles 153
7.4.2 Ru Oxide Powder and Supported Ru Catalysts 155
7.4.3 Size Effect Under Catalytic Carbon Monoxide Oxidation for Ru Nanoparticles 156
7.4.4 Engineering Ru Oxide on Nanoparticles through UV-Ozone Surface Treatment 157
7.4.5 Catalytic Activity of CO Oxidation on Ru Nanoparticles and Ru Oxides Probed with Ambient Pressure XPS 159
7.5 Pd Oxide 161
7.5.1 Pd Oxide on Single Crystal Surfaces 161
7.5.2 CO Oxidation on Polycrystalline Palladium 162
7.5.3 Oxidation Process of Pd(111) Probed by AP-XPS 162
7.5.4 Pd Oxide on Nanoparticles 163
7.6 Concluding Remarks on the Role of Surface Oxide 166
References 166

8 Influence of Atomic Structure, Steps, and Kinks on the Catalytic Activity: In Situ Surface Studies 171
Bas Hendriksen
8.1 Single-Crystal Studies of Heterogeneous Catalysis 171
8.2 Concepts and Theory: The Importance of Atomic-Scale Structure 172
8.2.1 Active Sites: Electronic and Geometric Effects 172
8.2.2 The Importance of the Gas Phase 175
8.3 Atomic Structure and the Active Phase 177
8.3.1 Structure-Sensitive Reactions 177
8.3.2 Oxides as the Active Phase 177

8.3.2.1 The Pressure-Gap Effect for Ruthenium 177
8.3.2.2 The Role of Oxides in CO Oxidation 180
8.4 Steps and Kinks 183
8.4.1 Step Decoration Experiments 184
8.4.2 CO-Induced Step Formation from UHV to Atmospheric Pressure 185
8.4.3 Steps and the Catalytically Active Oxide Phase 188
8.5 Summary 191
References 191

9 The Development of Ambient Pressure X-Ray Photoelectron Spectroscopy and Its Application to Surface Science 197
Bongjin Simon Mun, Hiroshi Kondoh, Zhi Liu, Phil N. Ross Jr., and Zahid Hussain
9.1 The Brief History of Ambient Pressure X-Ray Photoelectron Spectroscopy 197
9.2 The First Development of Synchrotron-Based AP-XPS at ALS 200
9.3 AP-XPS at ALS 202
9.4 AP-XPS at Photon Factory 205
9.5 Oxidation Study of Transition Metal Single Crystals 209
9.5.1 CO Oxidation on Pt(110) 209
9.5.2 NO Dissociation on Pt(111) 212
9.5.3 CO Oxidation on Pd(111) 217
9.6 Application to Real System: Solid Oxide Fuel Cell 221
9.7 Concluding Remarks: Futures on AP-XPS 223
References 225

10 Electronic Excitation on Surfaces During Chemical and Photon Processes 231
Jeong Young Park
10.1 Introduction 231
10.2 Theoretical Background of Energy Dissipation on Surfaces 232
10.3 Detection of Hot Electrons 234
10.3.1 Hot Electron Generation by Photons 234
10.3.2 Hot Electron Generation by Transfer of Energetic Molecules 234
10.3.3 Hot Electron Generation by Electron Beams 235
10.4 Detection of Hot Electrons from Exothermic Catalytic Reactions 237
10.4.1 Concept of Catalytic Nanodiodes 238
10.4.2 Fabrication and Characterization of Metal–Semiconductor Nanodiodes 239

10.5 Hot Electron Flows Detected on Catalytic Nanodiodes Under Exothermic Catalytic Reaction ... 241
10.6 Hot Electron Flows Detected Upon Photon Absorption ... 244
10.7 Influence of Hot Electrons on Surface Chemistry ... 246
10.7.1 Influence of Hot Electrons on Atomic and Molecular Processes ... 247
10.7.2 Hot Electron Effect on Metal–Oxide Hybrid Nanocatalysts ... 248
10.8 Concluding Remarks and Future Perspective ... 251
References ... 253

Index ... 259

Part I
Introduction

Chapter 1
Bridging Materials and Pressure Gaps in Surface Science and Heterogeneous Catalysis

Jeong Young Park and Gabor A. Somorjai

1.1 Introduction

Over the last several decades, surface science has undergone revolutionary advances that reveal the atomic- and molecular-level structural, dynamic, compositional, and thermodynamic properties of surfaces that are utilized in chemical process development. Adsorption and reaction rates and catalytic selectivity are also better understood, making the design of surfaces that deliver desired chemical properties possible. In this book, we highlight recent works in surface science and catalysis with an emphasis on the development of new catalytic model systems and in situ spectroscopic and microscopic techniques for applications in energy and environmental engineering. Colloid nanoparticle synthesis provides new opportunities to tune catalytic activity and selectivity via synthetic control of the size, composition, and shape of nanoparticles. Metal–oxide interfaces are catalytically active, suggesting the tunability of catalytic activity via engineering of metal–oxide interfaces. Energy conversion from photon or chemical energy to electrical energy has been studied via utilization of hot electron flows with metal–semiconductor nanodiodes. New in situ microscopic and spectroscopic techniques have been developed to uncover the atomic structure, mobility, reaction intermediates, and oxidation states that determine catalytic activity and selectivity. Breakthroughs in these research topics can help in the smart design of catalytic and energy materials with better performance and lower cost and may lead to new methods for renewable energy conversion.

J.Y. Park (✉)
Graduate School of EEWS (WCU) and NanoCentury KI, Korea Advanced Institute of Science and Technology (KAIST), Daejeon, Republic of Korea

Center for Nanomaterials and Chemical Reactions, Institute for Basic Science, Daejeon 305-701, South Korea
e-mail: jeongypark@kaist.ac.kr

G.A. Somorjai
Department of Chemistry, University of California, Berkeley, CA 94720, USA

J.Y. Park (ed.), *Current Trends of Surface Science and Catalysis*,
DOI 10.1007/978-1-4614-8742-5_1,

1.2 Materials and Pressure Gaps

The materials and pressure gaps have been a long-standing challenge in the field of heterogeneous catalysis and have transformed surface science and biointerfacial research. In heterogeneous catalysis, the materials gap refers to the discontinuity between well-characterized model systems and industrially relevant catalysts [1–6]. While the majority of surface science studies have been carried out on well-defined single crystal surfaces under ultrahigh vacuum (UHV) conditions, most catalytically active systems are employed at high pressure or at solid–liquid interfaces; this gap between UHV and industrial conditions is known as the pressure gap. The materials and pressure gaps are illustrated in Fig. 1.1. Single crystal metal surfaces have been useful model systems to elucidate the role of surface defects and the mobility of reaction intermediates in catalytic reactivity and selectivity [7, 8]. Surface scientists have been able to uncover many of the key aspects of heterogeneous catalysis by using metal single crystals as model catalyst systems. Despite the presence of defects, such as steps and kinks, single crystals are the simplest model catalysts due to the repetition of the same surface structure on terraces across the sample, as shown in Fig. 1.1. Their large size and high electrical conductivity allow their use in both photon- and electron-based surface science techniques and permit the study of low turnover (number of product molecules per site per second) catalytic reactions. These well-defined crystals allow for correlation of the surface structure with molecular adsorption and catalytic turnover by use of surface sensitive techniques, such as low energy electron diffraction (LEED), X-ray photoelectron spectroscopy (XPS), scanning tunneling microscopy (STM), and sum frequency generation (SFG) vibration spectroscopy.

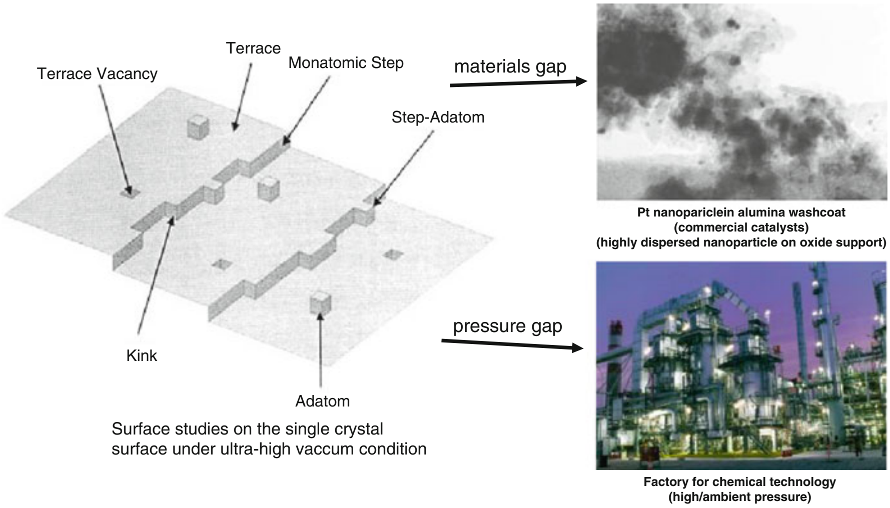

Fig. 1.1 Illustration depicting materials and pressure gaps

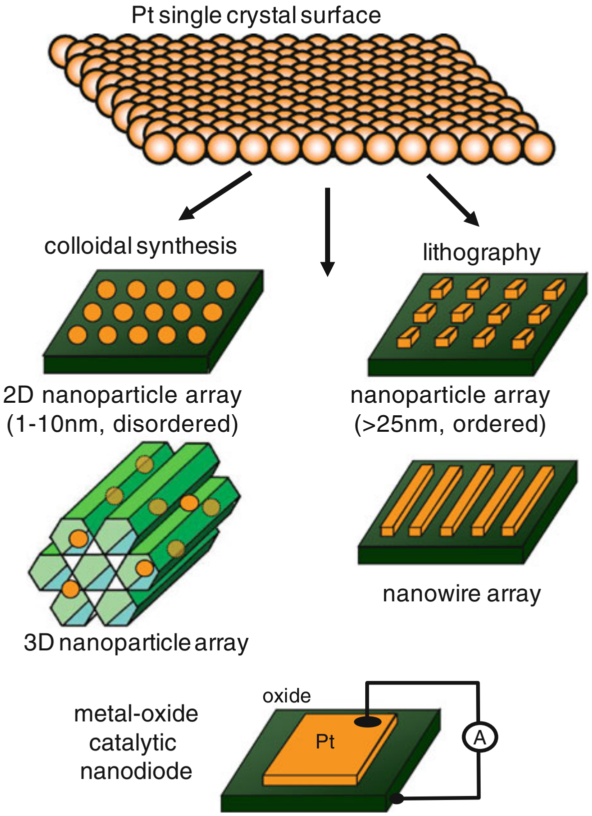

Fig. 1.2 Schematic showing the evolution of the catalyst model system from a single crystal metal surface to 2D and 3D nanoparticle arrays that are colloid synthesized and to nanowire arrays and nanodiodes that are fabricated using lithography. (Adapted from ref [5], reprinted with permission)

The use of single crystals as model catalytic systems has shed light on many surface phenomena, which, in turn, has helped to choose metallic clusters for use in industrial catalysis. Industrial catalysts, however, do not just consist of metal, but are made up of metal particles in the 1–100 nm size regime dispersed in a high surface area support. They are produced by synthesizing the metal particles and support separately and then dispersing the metal clusters onto the support using various techniques (e.g., wet-impregnation, co-precipitation, or ion-exchange). Thus, the single-crystalline metals used for modeling industrial catalysis inherently lack the complexity needed to uncover many of the factors important to catalytic turnover and selectivity. Considerations, such as metal support interactions and the importance of metallic cluster size, are of extreme importance to catalytic applications. This demand has driven development of new catalytic model systems. Figure 1.2 shows the evolution of catalytic model systems from the single crystal surface to more complex Pt nanostructure arrays and catalytic nanodiode schemes that aid in determining the role of size, shape, composition, oxidation states, and metal–oxide interfaces in catalytic activity and selectivity. This book will outline recent work on surface science studies of single crystals and nanoparticles in Parts I and II.

In order to transition from single crystal studies to more industrially relevant catalysts, two-dimensional (2D) or three-dimensional (3D) cluster arrays are useful because the instrumentation developed for single crystal studies can also apply [9]. Recently, many different methods have been used to prepare different types of 2D model catalysts, such as spin-casting of metal salt solutions onto planar oxide supports followed by calcination, evaporation of metal films onto oxide supports, plasma deposition, laser interference nanolithography, colloidal lithography, and photolithography. All of these methods have problems that limit their applicability to industrial catalysis. Non-lithographic methods are able to access the sub-100 nm size regime interesting for catalytic applications, but are unable to exert the control necessary to uncover any dependence on metallic cluster size and shape. The goal in 2D model catalyst development is to synthesize well-characterized and reproducible catalysts in the 1–30 nm range, where the high surface area properties of the catalysts are most pronounced, as described below.

1.3 Size, Shape, and Compositional Control of Colloid Nanoparticles

In colloidal synthesis, nanoparticles are the product of the reduction of metallic salts in solution. Chemical reduction methods, including alcohol reduction, hydrogen reduction, and sodium borohydride reduction, were reported. Capping agents, such as polymers, dendrimers, block copolymer micelles, and surfactants, are used for stabilizing the nanoparticles and preventing aggregation. By using hexachloroplatinic acid or rhodium acetyl acetonate as precursor monomers, it is possible to produce monodispersed metal nanoparticles where each is coated with a polymer layer that prevents aggregation in solution (Fig. 1.3). Under optimized reduction conditions, it is possible to control the size and shape of the platinum or rhodium nanoparticles. Figure 1.4 shows platinum nanoparticles with controlled size and shape [9–13]. High-resolution transmission electron microscopy (HRTEM) reveals the shape of the nanoparticles. In the case of Pt/Rh bimetallic nanoparticles under well-defined conditions, the particle size is proportional to the monomer concentration and can be controlled by changing the monomer concentration [14].

A 2D assembly of colloid nanoparticles was developed as a new model catalyst. The Pt nanoparticles were immobilized onto the native oxide layer of a Si wafer via Langmuir-Blodgett (LB) deposition, forming a monolayer of monodispersed Pt nanoparticles, as shown in Fig. 1.5. The average interparticle spacing can be tuned by varying the surface pressure in the LB film. This approach has the advantage of controlling the size and shape of the nanoparticles; an oxide–metal interface also

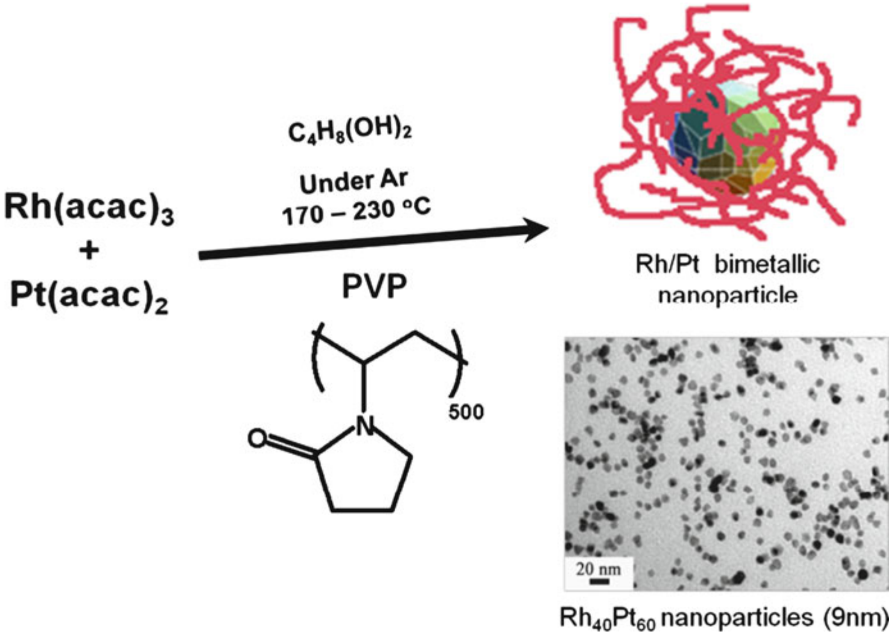

Fig. 1.3 Scheme showing the one-step synthesis of monodispersed Rh/Pt bimetallic nanoparticles [(acac) acetyl acetonate]. (Adapted from ref [28], reprinted with permission)

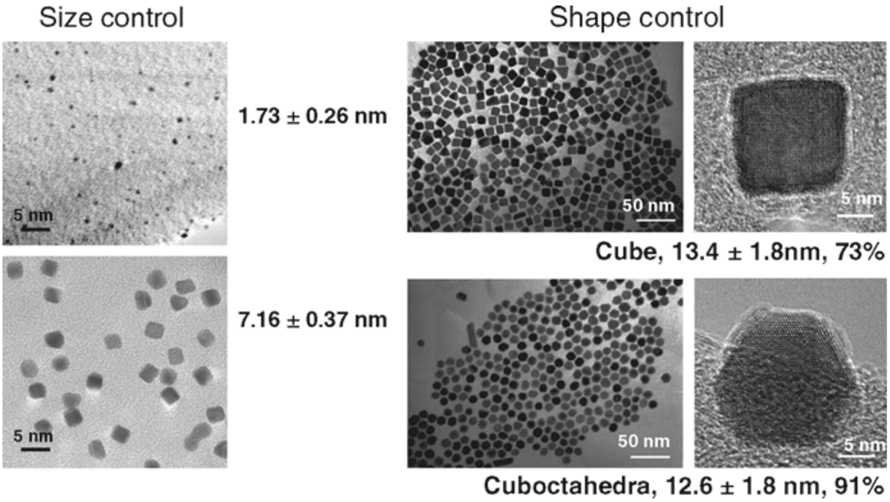

Fig. 1.4 Size and shape control of Pt colloid nanoparticles. Monodispersed platinum nanoparticles 1.7 and 7.2 nm in size (*left*) with well-controlled cubic or cuboctahedral shapes (*right*). Scale bar: (*left*) 5 nm, (*center*) 50 nm, and (*right*) 5 nm. The % values (*right*) refer to the % of nanoparticles with the corresponding shape. (Adapted from ref [28], reprinted with permission)

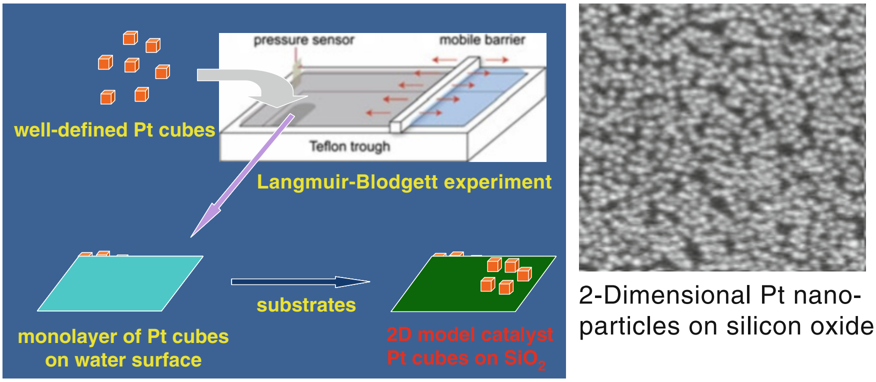

Fig. 1.5 Schematic of the Langmuir-Blodgett method and TEM image of 2D Pt nanoparticle arrays on a silicon oxide surface fabricated using the Langmuir-Blodgett method

forms between the nanoparticles and substrate when using colloidal synthesis. The bond configuration, structural, compositional, and electronic structures of 2D assemblies of colloid nanoparticles can be characterized using surface-sensitive techniques, including scanning probe microscopy, X-ray photoelectron spectroscopy, and SFG vibration spectroscopy.

1.4 Control of Catalytic Reactions via Tuning the Size and Composition of Bimetallic Nanoparticles

Composition is another important factor that influences catalytic activity and selectivity. Pt/Rh bimetallic nanoparticles with variable composition and constant size (9 nm) were synthesized using a one-pot polyol synthetic method [14]. The activity of CO oxidation on these bimetallic nanoparticles was studied. Colloid techniques use chloroplatinic acid or a rhodium precursor (like rhodium acetylacetonate) in the presence of a polymer (PVP) to make metal ions. These metal ions are then reduced in alcohol. Figure 1.6a shows XPS spectra measured on 2D Rh_xPt_{1-x} ($x=0$–1) nanoparticle arrays on a silicon surface. The intensity of the Rh3d peak increases, while the Pt4f and Pt4d peaks decrease as the composition of Rh increases. Figure 1.6b shows TEM images of monodispersed $Rh_{0.4}Pt_{0.6}$ nanoparticles. The particles were 9.3 ± 1.2 nm in size, which was determined by measuring 150 nanocrystals from a TEM image. Once monodispersed particles with the desired size and composition are obtained, we put them in a Langmuir trough and apply a certain surface pressure to deposit different densities of nanoparticle monolayer films. The turnover rate of a pure Rh nanoparticle is 20 times that of a Pt nanoparticle under the reaction conditions used (100 Torr O_2, 40 Torr CO at 180 °C). Rh_xPt_{1-x} ($x=0.2$–0.8) particles exhibit an intermediate activity, as shown in Fig. 1.6c, while the activation energy increases from 25 to 27 kcal mol^{-1} with increasing rhodium content.

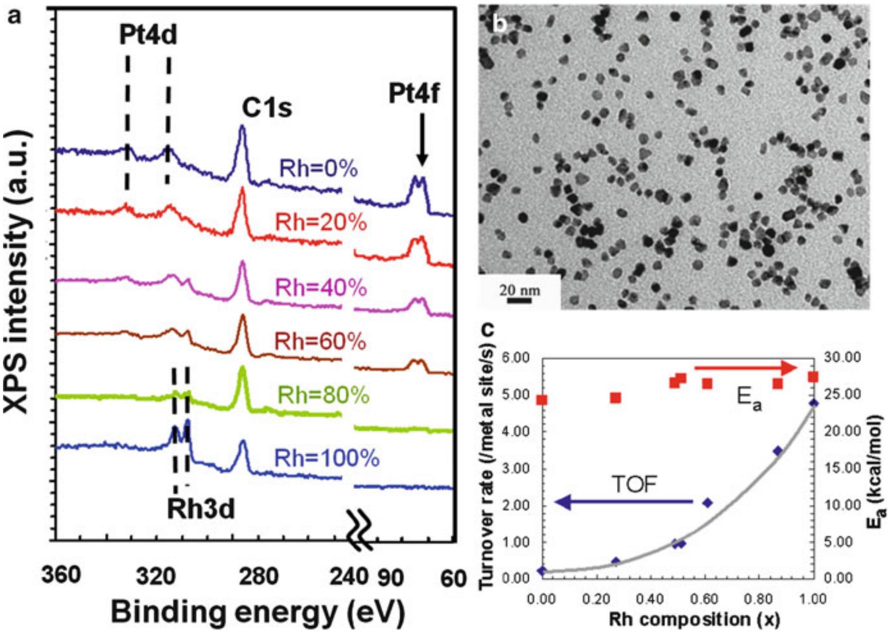

Fig. 1.6 (**a**) The XPS plots measured on two-dimensional Rh_xPt_{1-x} ($x = 0$–1) nanoparticle arrays on a silicon surface. (**b**) TEM images of the $Rh_{0.4}Pt_{0.6}$ nanoparticles. (**c**) Plot of the turnover frequency (TOF) of Rh_xPt_{1-x} measured at 180 and 200 °C, and the activation energies of nanoparticle arrays as a function of Rh composition ($x = 0$–1). (Adapted from ref [14], reprinted with permission)

The observation that pure Rh nanoparticles are more reactive than Pt nanoparticles is consistent with earlier CO oxidation studies on thin films and single crystals. This is associated with differences in the initial dissociative sticking probability of oxygen (Pt is 0.2 and Rh is 1.0). As shown in Fig. 1.6c, the reactivity of CO oxidation increases nonlinearly as a function of Rh composition. This tendency could be due to preferential migration of Pt to the surface, resulting in a higher surface concentration of Pt compared to the bulk concentration. The size of the $Rh_{0.5}Pt_{0.5}$ bimetallic nanoparticle arrays can be used to tune the activity of CO oxidation. The size was varied during synthesis using colloidal chemistry. The catalytic activity of CO oxidation increases as the size of the bimetallic nanoparticles decreases. Thermodynamic analysis and XPS measurements suggest that the higher catalytic activity of smaller bimetallic nanoparticles is associated with the preferential surface segregation of Rh, compared to Pt, on the smaller nanoparticles [15]. Figure 1.7 shows the turnover rate of CO oxidation measured on Rh/Pt nanoparticles as a function of size and composition. The general trend of the size and compositional dependence on catalytic activity is that the smaller and Rh-richer nanoparticles exhibit higher catalytic activities. This result suggests the intriguing capability of changing the catalytic activity in a bimetallic nanoparticle by varying the composition and size, with possible applications in tunable nanocatalysts [16, 17].

Fig. 1.7 Turnover rate of CO oxidation measured on Rh/Pt nanoparticles as a function of size and composition

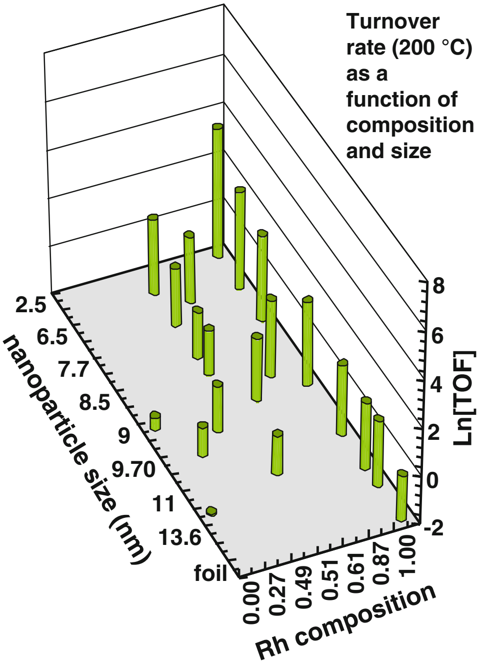

1.5 In Situ Surface Characterization to Bridge Pressure Gaps

Vacuum studies on single crystal surfaces revealed a number of important surface phenomena, leading to new concepts in surface science. The instrumentation techniques developed for surface studies include photon-in/electron-out (XPS), electron-in/electron-out (LEED surface crystallography and Auger electron spectroscopy (AES)), atomic, molecular beams, and ion beam in/ions out (secondary ion mass spectrometry (SIMS), and inelastic ion surface scattering (ISS)) techniques. All of these techniques have high scattering cross sections that would not survive the presence of high-pressure gas or liquid at the interfaces.

Since the 1980s, the surface science community has developed techniques that probe the structure, composition, mechanical properties, and dynamics of surfaces at high pressure. The research activity on in situ surface characterization will be covered in Part III. Several examples of high-pressure surface apparatuses are shown in Fig. 1.8. These include (a) high-pressure SFG vibration spectroscopy, (b) high-pressure STM, (c) high-pressure XPS, and (d) atomic force microscopy (AFM).

Of these, SFG vibrational spectroscopy is a surface-specific technique; it is quite useful for high-pressure studies based on the principle of second harmonic generation (see Fig. 1.8a). One or both laser frequencies are tuned, then spatially and temporally overlapped. By scanning one of the lasers in the infrared frequency

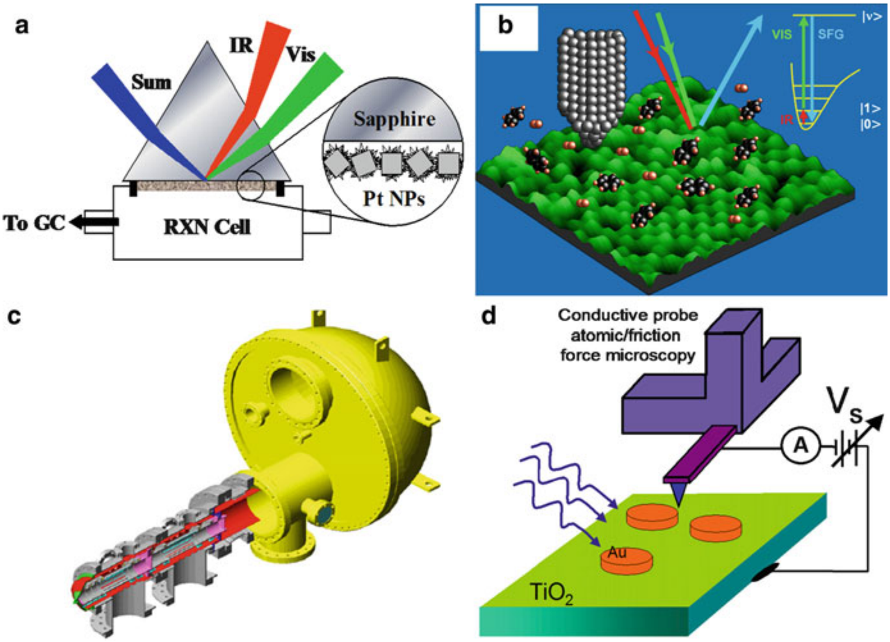

Fig. 1.8 Schemes of high-pressure surface apparatuses: (**a**) high-pressure sum frequency generation (SFG) vibration spectroscopy, (**b**) high-pressure STM, (**c**) ambient pressure XPS, and (**d**) in situ AFM. (Adapted from ref. [28], reprinted with permission)

regime, a sum frequency signal and, thus, a visible vibrational spectrum is obtained [7]. Such a signal is forbidden from a centrosymmetric medium, such as in the bulk of face-centered cubic crystals or in an isotropic high-pressure gas or a liquid. However, at a surface, which is not centrosymmetric, the second-order susceptibility is non-zero, and the surface yields a vibrational spectrum with monolayer sensitivity. It is also able to give vibrational frequencies of adsorbed molecules at pressures ranging through 10–12 orders of magnitude. High-pressure STM images (shown in Fig. 1.8b) reveal that at high pressure, surfaces form new structures that are not seen under ultrahigh vacuum. As more molecules adsorb onto the surface, the repulsive interaction among them becomes more important and causes the surface to reconstruct in new ways.

Using high-pressure STM, we always find that the adsorbed layer is mobile on the catalytically active surface, while ordered structures form if the reaction is inhibited by another adsorbate that poisons the catalytic reaction [18]. Catalytic hydrogen/deuterium exchange on a platinum (111) single crystal and its poisoning with carbon monoxide was also studied using STM and mass spectrometry at pressures ranging from mTorr to atmospheric. STM images acquired at room temperature under reaction conditions (200 mTorr H_2, 20 mTorr D_2) show a surface with no discernible order (Fig. 1.9a), as the adsorbate species diffuse much faster than the scanning rate of the instrument (10 nm per millisecond) [19]. However, after

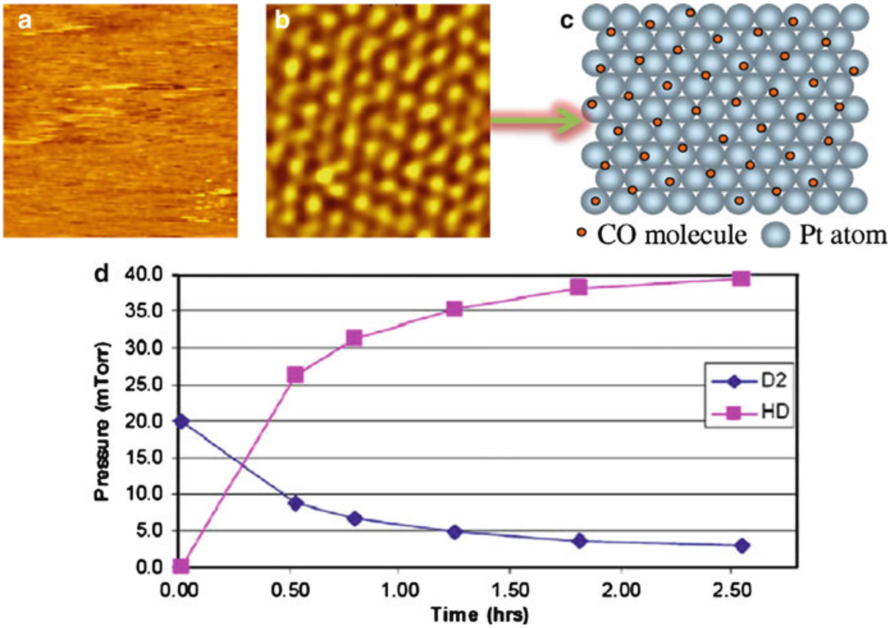

Fig. 1.9 High-pressure STM results. 90 Å × 90 Å STM images of catalytically active Pt(111) at 298 K in the presence of (**a**) 200 mTorr H_2 and 20 mTorr D_2 and (**b**) 200 mTorr H_2, 20 mTorr D_2, and 5 mTorr CO. (**c**) CO molecules are represented by the small *circles* and color coded according to their proximity to a top site (*dark*) or to a bridge site (*light*). (**d**) D_2 and HD at 296 K, 200 mTorr H_2, and 20 mTorr D_2 were monitored using mass spectroscopy. The evolution of the D_2 and HD partial pressures indicates that the Pt catalyst surface is actively producing HD, consistent with the STM image (**a**). (Adapted from ref. [18], reprinted with permission)

introducing 5 mTorr of CO to poison the reaction, STM images reveal an ordered surface with hexagonal symmetry (Fig. 1.9b), which is similar to that formed by pure CO on Pt(111) in this pressure range. The structure is incommensurate with that of the Pt(111) lattice and has a coverage of about 0.6 monolayer. A schematic of the proposed structure is shown in Fig. 1.9c. At room temperature and in the presence of 200 mTorr H_2 and 20 mTorr D_2, the surface is catalytically active, producing HD at a rate of 4.3 molecules/site/s, as shown in Fig. 1.5d. Upon introduction of 5 mTorr of CO, however, the production of HD dropped below the detection limit of our mass spectrometer. At 345 K, the turnover frequency in the absence of CO increased to 39 molecules/site/s, which is about ten times higher than at room temperature. The addition of 5 mTorr of CO at this temperature dramatically decreased the reactivity, but unlike in the room temperature case, the catalytic activity was still observed at 0.03 molecules/site/s. This implies that the immobile, ordered monolayer of CO molecules forms an incommensurate structure relative to the Pt(111) substrate. Removing a small fraction of the CO layer by heating the sample allowed the surface to become mobile and catalytically active.

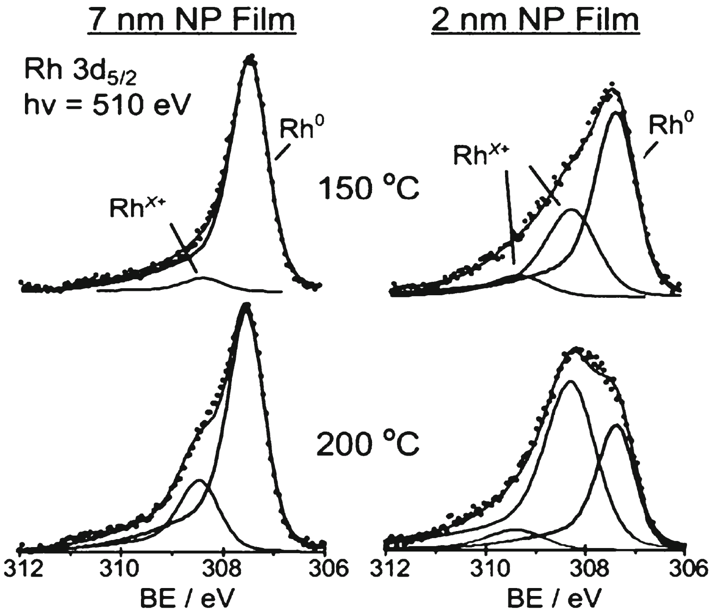

Fig. 1.10 XPS Rh3d peaks for 2 and 7 nm Rh nanoparticle arrays during CO oxidation taken with ambient pressure XPS. (Adapted from ref [10], reprinted with permission)

The surface composition and oxidation of single crystals or nanoparticles under gas or catalytic conditions can be studied by using ambient pressure X-ray photoelectron spectroscopy (AP-XPS) [20, 21]. A schematic representation of AP-XPS is shown in Fig. 1.8c, which illustrates a differentially pumped electrostatic lens system that refocuses the scattered electrons into the object plane of a standard electron energy analyzer in the high-vacuum region. The kinetic energy of the detected electrons can be varied by tuning the photon energy of the X-ray source. Figure 1.10 shows XPS Rh3d peaks for 2 and 7 nm Rh nanoparticle arrays during CO oxidation taken with ambient pressure XPS. The high catalytic activity of the smaller Rh nanoparticles is associated with the presence of Rh oxide, suggesting the intrinsic role of Rh oxide as a catalytically active species [10].

AFM is a technique whereby a small tip (tens of nm) is raster scanned across a surface. A laser light is reflected off of the back of the tip, and the reflected light is collected in a position-sensitive photodiode. This allows for gathering such information as surface topography and for measuring mechanical properties of the surface, such as friction, adhesion, stiffness, and plastic deformation. The friction and adhesion properties of colloid nanoparticles were investigated using AFM [22]. Figure 1.11 shows AFM images of Pt colloid nanoparticles with four types of capping layers: TTAB (tetradecyltrimethylammonium bromide), HDA (hexadecylamine), HDT (hexadecylthiol), and PVP (poly(vinylpyrrolidone)). The variation of friction when changing the capping layers is approximately 30 %; it appears that the friction depends on the packing and ordering of the capping layers.

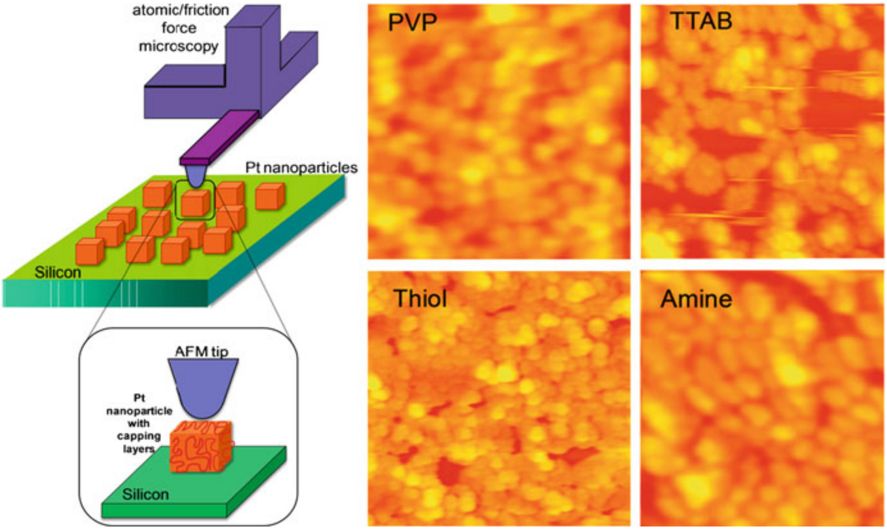

Fig. 1.11 (*Left*) Scheme of AFM on Pt nanoparticles. (*Right*) AFM images (500 × 500 nm) of Pt nanoparticles capped with various capping layers. (Adapted from ref. [22], reprinted with permission)

1.6 The Role of Metal–Oxide Interfaces in Heterogeneous Catalysis

One of the key issues in heterogeneous catalysis is the role of metal–oxide interfaces in altering catalytic activity. The smart design of nanocatalysts can improve the catalytic activity of transition metals on reducible oxide supports, such as Pt nanoparticles or nanowires on a titania substrate, as shown in Fig. 1.12, via strong metal–support interactions (SMSI). The SMSI effect refers to changes in the catalytic activity when group VIII metals (i.e., Fe, Ni, Rh, Pt, Pd, and Ir) are supported on certain oxides (e.g., TiO_2, TaO_5, CeO_2, NbO). For example, methane formation from CO or CO_2 and H_2 is enhanced by three orders of magnitude.

The role of the metal–oxide interface in enhancing catalytic activity was first suggested by Schwab and others, who performed oxidation of carbon monoxide on Ag/NiO. As reported by Hayek and others, the reaction rate in the oxide–metal model system depends on the oxidation state of the supporting oxide, the free metal surface area, and the number of sites at the interface between the metal and the support. The origin of such metal–oxide interactions is attributed to either geometric or electronic effects. The geometric effect assumes that the active surface area of the noble metal changes during the reduction process.

The electronic effect involves charge transfer between the metal and the oxide support. Elucidation of the origin of the metal–support interaction requires measurement of the charge transfer through the oxide–metal interface. To detect this

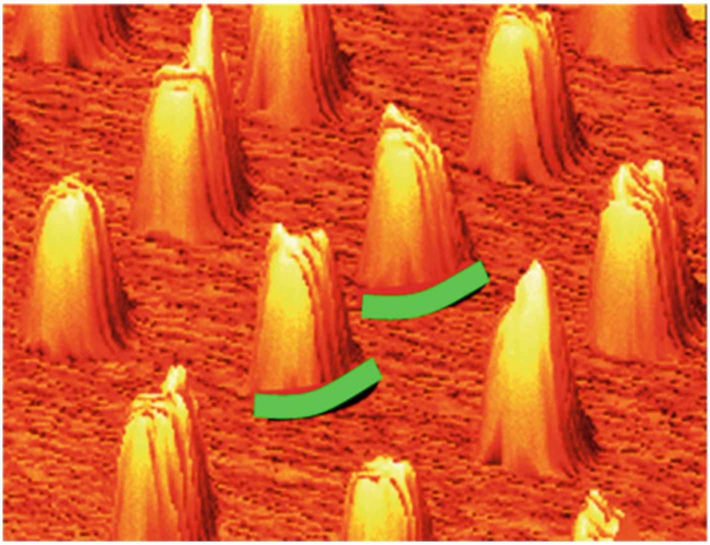

Fig. 1.12 AFM image of Pt nanoparticles on silicon oxide

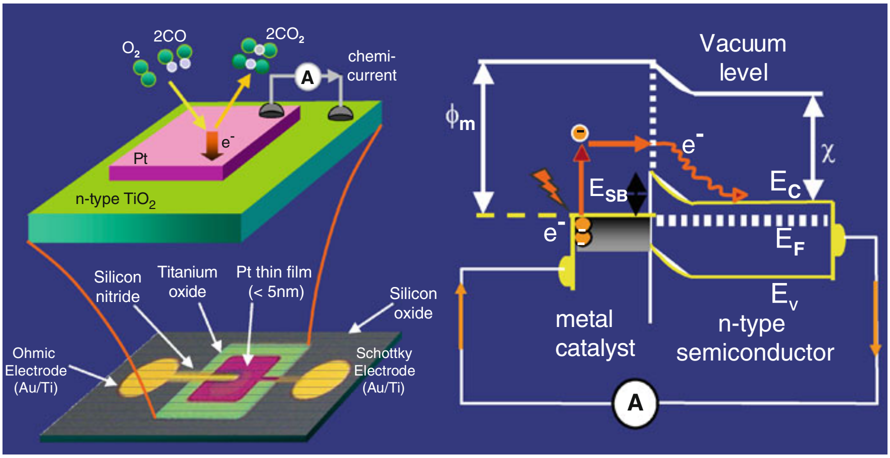

Fig. 1.13 (*left*) Scheme of catalytic nanodiodes and (*right*) energy diagram of catalytic nanodiodes

charge transfer or flow of hot electrons under catalytic reaction conditions, metal–semiconductor Schottky diodes have been developed [23, 24]. If the metal particle or film is the diameter or thickness of the electron mean-free path (~10 nm), hot electrons can be collected as they are transported across the metal without collision, as shown in Fig. 1.13. For an n-type Schottky diode, hot electrons are detected as a chemicurrent if their excess energy $E_{ex} = |E - E_F|$ is larger than the effective Schottky barrier, which is the difference between the conduction band minimum and the

Fermi energy, E_F, at the interface. Once hot electrons arrive at the oxide, they dissipate energy and thus cannot go back to the metal. Therefore, the Schottky energy barrier leads to irreversible, one-way charge transfer of hot electrons from the metal to the semiconductor, as shown in Fig. 1.13. After hot electrons move from the metal to the semiconductor, they are replaced by low-energy electrons supplied by the external leads connected to the Pt and the semiconductor, resulting in the continuous flow of hot electrons generated by the catalytic reaction.

The hot electron flows also correlate with the turnover rate of CO oxidation, as measured separately by gas chromatography [25]. Photon energy has been observed being converted into hot electron flows with metal–semiconductor diodes [26, 27]. The detection of hot electrons may lead to a fundamental understanding of energy dissipation and conversion processes, which would introduce new opportunities for energy conversion. The detection of hot electrons under various catalytic reactions and the influence of hot electrons in catalytic reactivity will be discussed in Chap. 10.

1.7 Conclusion

This chapter outlines new research directions in surface science and their relationship to nanocatalysts and renewable energy conversion. We envision three subjects which are important research directions: (1) development of new model systems and functional materials for applications in energy and the environment, (2) in situ surface characterization to reveal surface phenomena under conditions where catalytic processes or energy conversion commonly take place, and (3) new device schemes for energy conversion. Due to advancements in these research areas, surface science is entering a new era and will become an area of research essential to truly achieving renewable energy sources, which is an important goal for mankind.

References

1. Somorjai GA, Li Y (2010) Introduction to surface chemistry and catalysis. Wiley, New York
2. Ertl G, Knözinger H, Schüth F, Weitkamp J (2008) Handbook of heterogeneous catalysis, vol 8. Wiley, New York
3. Ertl G, Freund HJ (1999) Catalysis and surface science. Phys Today 52:32–38
4. Freund HJ et al (2001) Bridging the pressure and materials gaps between catalysis and surface science: clean and modified oxide surfaces. Top Catal 15:201–209
5. Somorjai GA, York RL, Butcher D, Park JY (2007) The evolution of model catalytic systems; studies of structure, bonding and dynamics from single crystal metal surfaces to nanoparticles, and from low pressure (<10(−3) torr) to high pressure (>10(−3) torr) to liquid interfaces. Phys Chem Chem Phys 9:3500–3513. doi:10.1039/b618805b
6. Somorjai GA, Park JY (2008) Molecular surface chemistry by metal single crystals and nanoparticles from vacuum to high pressure. Chem Soc Rev 37:2155–2162. doi:10.1039/b719148k
7. Somorjai GA, Park JY (2007) Frontiers of surface science. Phys Today 60:48–53

8. Campbell CT (1997) Ultrathin metal films and particles on oxide surfaces: structural, electronic and chemisorptive properties. Surf Sci Rep 27:1–111
9. Song H, Kim F, Connor S, Somorjai GA, Yang PD (2005) Pt nanocrystals: shape control and langmuir-blodgett monolayer formation. J Phys Chem B 109:188–193
10. Grass ME et al (2008) A reactive oxide overlayer on rhodium nanoparticles during CO oxidation and its size dependence studied by in situ ambient-pressure X-ray photoelectron spectroscopy. Angew Chem Int Ed 47:8893–8896. doi:10.1002/anie.200803574
11. Zhang Y et al (2007) One-step polyol synthesis and langmuir-blodgett monolayer formation of size-tunable monodisperse rhodium nanocrystals with catalytically active (111) surface structures. J Phys Chem C 111:12243–12253
12. Lee H et al (2006) Morphological control of catalytically active platinum nanocrystals. Angew Chem Int Ed 45:7824–7828
13. Joo SH et al (2010) Size effect of ruthenium nanoparticles in catalytic carbon monoxide oxidation. Nano Lett 10:2709–2713. doi:10.1021/nl101700j
14. Park JY, Zhang Y, Grass M, Zhang T, Somorjai GA (2008) Tuning of catalytic CO oxidation by changing composition of Rh-Pt bimetallic nanoparticles. Nano Lett 8:673–677. doi:10.1021/nl073195i
15. Park JY, Zhang Y, Joo SH, Jung Y, Somorjai GA (2012) Size effect of RhPt bimetallic nanoparticles in catalytic activity of CO oxidation: role of surface segregation. Catal Today 181:133–137. doi:10.1016/j.cattod.2011.05.031
16. Somorjai GA, Park JY (2008) Colloid science of metal nanoparticle catalysts in 2D and 3D structures. Challenges of nucleation, growth, composition, particle shape, size control and their influence on activity and selectivity. Top Catal 49:126–135. doi:10.1007/s11244-008-9077-0
17. Norskov JK, Bligaard T, Rossmeisl J, Christensen CH (2009) Towards the computational design of solid catalysts. Nat Chem 1:37–46. doi:10.1038/nchem.121
18. Somorjai GA, Park JY (2009) Concepts, instruments, and model systems that enabled the rapid evolution of surface science. Surf Sci 603:1293–1300. doi:10.1016/j.susc.2008.08.030
19. Montano M, Bratlie K, Salmeron M, Somorjai GA (2006) Hydrogen and deuterium exchange on Pt(111) and its poisoning by carbon monoxide studied by surface sensitive high-pressure techniques. J Am Chem Soc 128:13229–13234. doi:10.1021/ja063703a
20. Salmeron M, Schlogl R (2008) Ambient pressure photoelectron spectroscopy: a new tool for surface science and nanotechnology. Surf Sci Rep 63:169–199
21. Tao F et al (2008) Reaction-driven restructuring of Rh-Pd and Pt-Pd core-shell nanoparticles. Science 322:932–934. doi:10.1126/science.1164170
22. Park JY (2011) Tuning nanoscale friction on Pt nanoparticles with engineering of organic capping layer. Langmuir 27:2509–2513. doi:10.1021/la104353f
23. Hervier A, Renzas JR, Park JY, Somorjai GA (2009) Hydrogen oxidation-driven hot electron flow detected by catalytic nanodiodes. Nano Lett 9:3930–3933. doi:10.1021/nl9023275
24. Nienhaus H (2002) Electronic excitations by chemical reactions on metal surfaces. Surf Sci Rep 45:3–78
25. Park JY, Somorjai GA (2006) The catalytic nanodiode: detecting continuous electron flow at oxide-metal interfaces generated by a gas-phase exothermic reaction. Chemphyschem 7: 1409–1413
26. Somorjai GA, Frei H, Park JY (2009) Advancing the frontiers in nanocatalysis, biointerfaces, and renewable energy conversion by innovations of surface techniques. J Am Chem Soc 131:16589–16605. doi:10.1021/ja9061954
27. Lee YK et al (2011) Surface plasmon-driven hot electron flow probed with metal–semiconductor nanodiodes. Nano Lett 11:4251–4255. doi:10.1021/nl2022459
28. Somorjai GA, Park JY (2008) Molecular factors of catalytic selectivity. Angew Chem Int Ed 47:9212–9228. doi:10.1002/anie.200803181

Part II
Model Systems for Nanocatalysts to Bridge Materials Gap

Chapter 2
Shape-Controlled Nanoparticles: Effect of Shape on Catalytic Activity, Selectivity, and Long-Term Stability

Hyunjoo Lee

2.1 Why Does Shape Matter for Catalytic Reactions?

The effect of surface structure on catalytic reactions has been investigated for decades. Often, single-crystalline surfaces with defined atomic arrangements have been prepared and the adsorption and reaction of chemical compounds on their surfaces have been investigated. Figure 2.1 shows an STM image of NO adsorbed onto the Pd(111) surface on which a hexagonal arrangement is clearly seen. Low-index surfaces of (100), (110), and (111) have been prepared for various metals, including Pt, Rh, and Ni. Catalytic reactions on these surfaces have been studied under very low pressure conditions.

Various reactions have been studied on different crystalline surfaces. For example, aromatization from hexane to benzene or from heptane to toluene was compared for Pt(111) and Pt(100) surfaces [2]. The reaction rate of aromatization was much faster on the Pt(111) surface, which has a hexagonal atomic arrangement. The effect of the surface crystalline structure on selectivity in the hydrogenolysis of methylcyclopentane was also investigated [3]. The Pt(100) surface led to more fragmentations with carbon numbers less than 6, while the Pt(111) surface produced a significant amount of benzene. No benzene was produced using the Pt(100) surface.

Electrocatalytic reactions have also been very good model systems for investigating the effects of surface crystalline structure. For example, in electrocatalytic formic acid oxidation, the amount of current produced and the extent of surface poisoning were shown to be dependent on the surface structure of the catalyst [4]. The Pt(100) surface produced approximately six times more current than the Pt(111) surface. The Pt(100) surface suffers from severe poisoning in the forward scan, producing no current (the large current appears only in the backward scan), whereas the Pt(111) surface displayed little poisoning, as proven by similar oxidation peaks

---

H. Lee (✉)
Department of Chemical and Biomolecular Engineering,
Yonsei University, Seoul 120-749, Republic of Korea
e-mail: azhyun@yonsei.ac.kr

J.Y. Park (ed.), *Current Trends of Surface Science and Catalysis*,
DOI 10.1007/978-1-4614-8742-5_2,

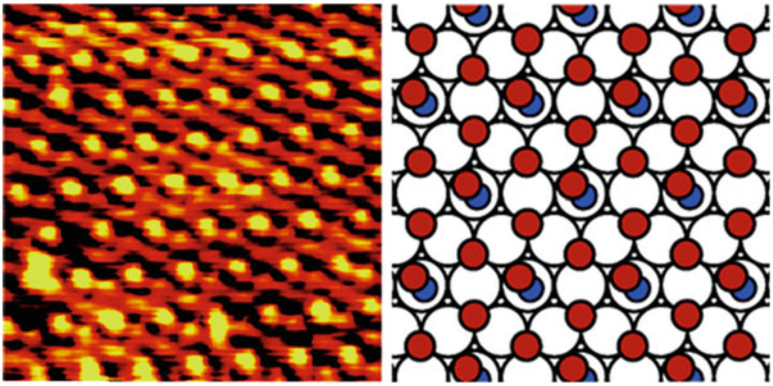

Fig. 2.1 STM image of NO adsorbed onto the Pd(111) surface (adapted from ref. [1])

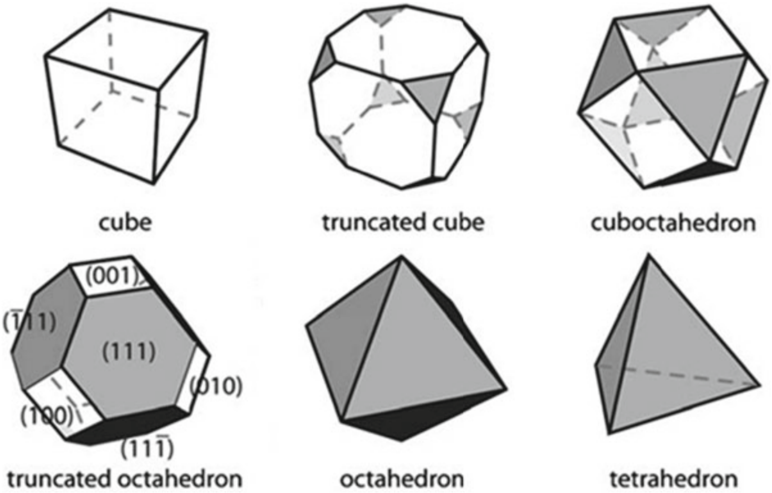

Fig. 2.2 Shaped nanocrystals with well-defined surface structures (adapted from ref. [6])

seen in both the forward and backward scans. This dependence on the surface structure can result from the formation of distinct intermediates adsorbed on the surface. Recently, Bratlie et al. reported that the same dienyl benzene intermediates are observed by sum frequency generation on both the Pt(100) and Pt(111) surfaces, whereas π-allyl c-C_6H_9 forms only on the Pt(100) surface [5]. As a result, the Pt(100) surface produced only the fully hydrogenated product (cyclohexane), but the Pt(111) surface produced the partially hydrogenated product (cyclohexene) as well as the fully hydrogenated product. Many other works have also demonstrated a dependence on surface structure for catalytic activity and selectivity.

When nanoparticles have a particular shape, the facets of the nanoparticles can have a predetermined atomic arrangement. Figure 2.2 shows various shapes of single-crystalline polyhedral nanocrystals. In the case of face-centered cubic (FCC) metals, such as Pt, Au, Ag, Pd, and Rh, cubic nanoparticles only have (100) facets, while octahedral or tetrahedral nanoparticles only have (111) facets. The truncated forms of these nanoparticles, such as cuboctahedra, have both (100) and (111) facets. Anisotropic nanoparticles have also been reported in the shapes of rods or plates with (110) facets.

By controlling the shape to have particular facets, the atomic arrangement can be modulated, which can potentially allow for enhancements in activity and selectivity. Knowledge of the effect of the surface crystalline structure on catalytic properties has been increasing for decades, which can be used to design the catalysts at nanometer scale with higher activity and selectivity. Recent review papers about shape-controlled nanoparticles and their catalysis can be also found elsewhere [7–12].

2.2 The Synthesis of Shaped Nanocrystals

Controlling the shape of nanoparticles has been mainly achieved using colloidal or electrochemical methods. In the colloidal method, a metal precursor is dissolved in a solvent with an organic surface-capping agent, which enables the nanoparticles to be stably dispersed in the solution. Then, the metal is reduced by adding a reducing agent or by raising the temperature. This method can produce a relatively large quantity of nanoparticles and no special equipment is necessary. The electrochemical method generates shaped nanocrystals on the electrode surface. The metal or metal oxide nanoparticles undergo nucleation and overgrowth on the surface. While many exotic shapes have been observed using the electrochemical method, it usually produces very large particles and mass production is not possible. Rarely, lithographic or vaporization methods have been reported to make shapes. Arrayed square nanoparticles and crescent moon shapes were also developed [13, 14], but these nanoparticles are fairly large and require the use of complicated, expensive equipment. Here, I will mainly discuss the colloidal method and briefly introduce the electrochemical method.

2.2.1 Colloidal Method

Many studies have been performed to produce shaped nanoparticles in a colloidal solution. In general, a shape can be formed by modulating the overgrowth step. When the nuclei overgrow, a precursor can be added to a particular overgrowth direction. Overgrowth in a particular direction can be enhanced or suppressed by using (1) a surface-capping agent, (2) an inorganic shaping agent, or (3) a reducing agent. Furthermore, unique shapes can be synthesized by combining this bottom-up synthesis with top-down etching. The shapes are usually obtained by a combination of these methods, rather than using only one.

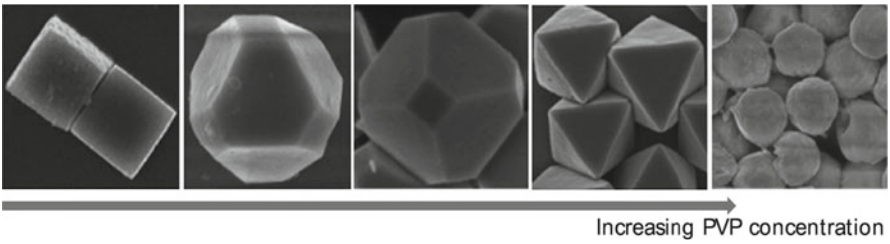

Fig. 2.3 Shaped Cu_2O nanocrystals produced by controlling the amount of surface-capping agents (adapted from ref. [16])

2.2.1.1 Surface-Capping Agent

In 1996, the first shape-controlled Pt nanoparticles were synthesized by using different amounts of the surface-capping agent sodium polyacrylate [15]. El-Sayed et al. reported Pt cubes and Pt tetrahedra ~10 nm in size. When the ratio of capping materials to the metal precursor (K_2PtCl_4) was 1:1, cubes were produced; when the ratio was 5:1, tetrahedra were produced, as shown in Fig. 2.3. The polyacrylate might be bound to the (111) facet more strongly, resulting in only the (111) facets remaining when excess polyacrylate was used. Although this argument cannot fully explain the formation of cubic nanoparticles, it provides some explanation for the observed shape evolution from cube to tetrahedra. The change in shape from cube to octahedra was also observed in copper oxide nanocrystals when polyvinylpyrrolidone (PVP) was used as the capping material [16].

Additionally, icosahedral, decahedral, octahedral, tetrahedral, and triangular plate-like Pd nanocrystals were synthesized by varying the quantity of oleylamine [17]. However, the correlation between the change in shape and the amount of surface-capping agent was not always observed. Although organic capping materials, such as amphiphilic polymers, alkylammonium halide, and oleylamine, should always be used for dispersion in the colloidal solution, changes in the shape induced by controlling the amount of surface-capping agent have rarely been reported. Different shapes can be realized more easily by using different types of surface-capping agents, but these methods are not desirable for use in catalytic applications. Different surface-capping agents can affect the catalytic properties by blurring the effect of the surface crystalline structure.

Some organic compounds can act as shape-controlling agents. When cubic Pt nanoparticles were synthesized with oleylamine and oleic acid, it was found that the use of oleic acid was necessary for the formation of the cubic shape [18]. In this case, oleic acid did not act as the surface-capping agent because poorly dispersed nanoparticles were obtained if oleylamine was not also added. Similarly, Pt_3Ni cubes were synthesized in the presence of oleic acid, whereas Pt_3Ni octahedra were obtained when oleic acid was replaced with diphenyl ether [19]. Benzoic acid or aniline has also been used to synthesize octahedral and truncated octahedral Pt_xNi_{1-x} nanoparticles. These organic substances acted as crystal growth inhibiting agents producing more Pt(111) facets [20].

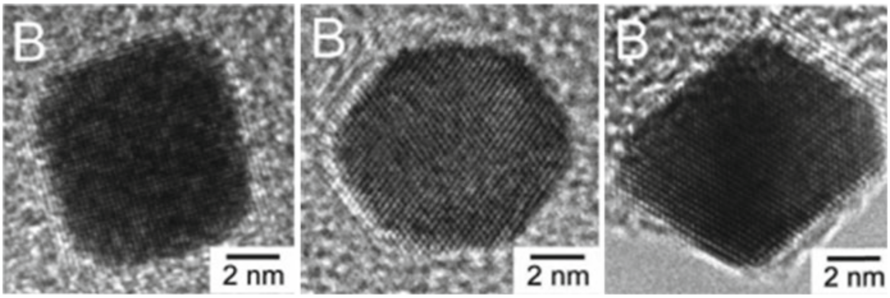

Fig. 2.4 Shaped Pt nanocrystals synthesized by controlling the amount of Ag ions (adapted from ref. [21])

2.2.1.2 Inorganic Shaping Agent

A more popular method to control the shape is by using an inorganic shaping agent. Adding a small amount of inorganic ions during synthesis can change the shape of the nanocrystals formed. Figure 2.4 shows the synthesis of cubic, cuboctahedral, and octahedral Pt nanoparticles by adding different amounts of Ag ions [21]. When more Ag ions were added, the (111) facets persisted more than other facets, which produced octahedral nanoparticles. The same size (~7 nm) of nanoparticles was successfully made using PVP as the capping agent.

However, it was observed that the surface of these nanoparticles was contaminated by residual Ag ions. When these different shapes of nanoparticles catalyzed ethylene hydrogenation, which is a surface-insensitive reaction, no difference in the activity was expected for the various shaped nanoparticles. However, the cubes had a turnover frequency of 8.6 s^{-1}, whereas the turnover frequency of the octahedra was 0.02 s^{-1} [22]. The Ag residing on the Pt nanoparticles hindered the catalytic reaction. The catalytic reaction on Pt octahedra with the greatest residual Ag ion concentration showed the poorest activity. Although beautifully shaped nanocrystals were obtained, the effect of the surface crystalline structure on catalytic activity could not be observed because of surface contamination.

$Fe(CO)_6$ was also used to prepare cubic Pt nanoparticles [18], but whether a trace amount of Fe was actually incorporated into the Pt nanoparticles was not clear because FePt composite nanoparticles can be easily formed using similar synthetic conditions [23, 24]. $W(CO)_6$ was also used to synthesize Pt-based nanocubes, including Pt_3Co, Pt_3Fe, Pt_3Ni [25], and Pt_3Ni nanooctahedra [26]. However, the different shapes (Pt_3Ni cubes and Pt_3Ni octahedra) did not result from $W(CO)_6$, but were the result of the type of Ni precursor used. The authors suggested that $W(CO)_6$ participates in the nucleation step; therefore, the W species might not be a shape-controlling factor, though it is essential to synthesize high-quality shaped nanoparticles. CO organic ligands might play a role in producing the cubic shape. Similarly, gaseous CO was also reported to produce cubic Pt alloy nanoparticles [19, 27]. NO_2 caused a change in shape from cubic to octahedral in the synthesis of Pd nanocrystals [28].

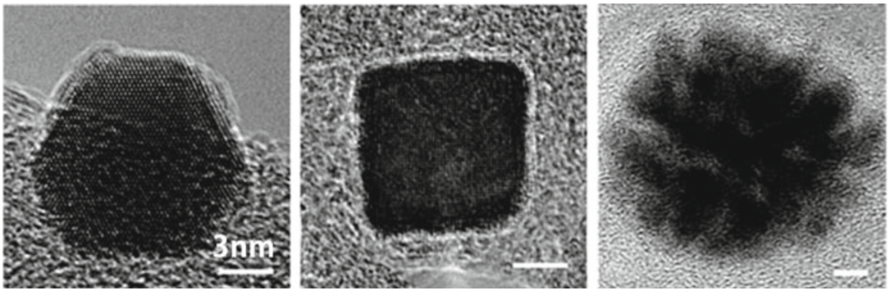

Fig. 2.5 Shaped Pt nanocrystals synthesized by using different reducing agents (adapted from ref. [31])

Most recently, various halide ions were utilized for shape control. Bromide ions were used to synthesize Rh nanocubes [29]. NaI was added to synthesize Pt_xPd_{1-x} nanocubes, whereas substituting NaI with NaCl produced PtPd nanooctahedra [30].

2.2.1.3 Reducing Agent

Different shapes can also be synthesized by using various reducing agents. Figure 2.5 shows cuboctahedral, cubic, and dendritic-shaped Pt nanoparticles synthesized using hydrogen gas, $NaBH_4$, and ascorbic acid, respectively, as reducing agents under otherwise identical conditions [31]. Compared with hydrogen gas, $NaBH_4$ increased the pH of the reacting aqueous solution, slowing the reduction rate of the platinum precursor. In this case, the surface of the shaped nanoparticles can be the same without potential contamination by organic or inorganic shape-controlling agents. The effect on shape caused by different surface crystalline structures could be evaluated using these nanoparticles.

2.2.1.4 Top-Down Etching

The methods discussed above generate shaped nanoparticles by using a bottom-up approach. The metal precursor is reduced forming nuclei in a colloidal solution that are subsequently overgrown into particular shapes. Other unique shapes can be produced by selective etching of shaped nanoparticles. Xia et al. reported the synthesis of nanoboxes composed of either Pd–Ag or Pt–Ag [32]. Starting from Ag nanocubes, the addition of Na_2PdCl_4 caused galvanic replacement, dissolving out Ag and forming a Pd–Ag composite shell. Recently, we synthesized shaped Au–Pt composite nanoparticles with Pt nanoparticles selectively deposited on the Au(100) facets [33]. Then, the Au was selectively etched by CN^- ions, while the part covered by the Pt was preserved [34]. Figure 2.6 shows the change in the shape of the nanoparticles before and after etching. The combination of bottom-up synthesis and top-down etching can enrich the collection of shape-controlled nanoparticles.

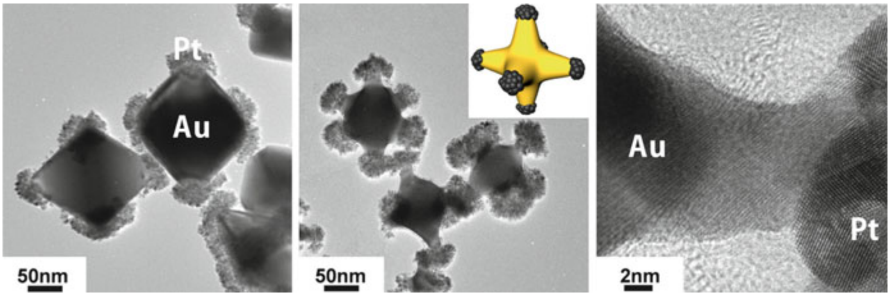

Fig. 2.6 (*Left*) Au@Pt nanoparticles where Pt is selectively deposited at Au(100) facets. (*Center*) The Au surface is etched while the Pt is preserved. (*Right*) HR-TEM image of the tip of the etched Au@Pt nanoparticle (adapted from [33, 34])

2.2.2 Electrochemical Method

Shaped nanoparticles can be synthesized directly on an electrode surface. The first nanocrystals composed of high-index facets (tetrahexahedral Pt nanocrystals with (730) facets) were made using an electrochemical method [35]. Here, the spherical Pt nanoparticles were first deposited on a glassy carbon electrode, and then a square-wave potential treatment was applied, resulting in tetrahexahedral Pt nanocrystals. The same group further developed this procedure to synthesize tetrahexahedral Pd nanocrystals directly, without forming nanospheres [36]. Figure 2.7 shows a schematic of the synthesis and SEM images of the shaped nanocrystals. Various shapes of Fe nanocrystals, including rhombic dodecahedra, tetragonal bipyramids, and cubes, were also synthesized [37]. Choi et al. reported a series of works producing shaped Cu_2O nanocrystals using electrochemical methods. A variety of snow-like crystals could be synthesized by controlling the concentration of the copper precursor, temperature, voltage, etc. [38, 39]. Nanocrystals that are electrochemically deposited on the electrode have many advantages: shape modulation is easier, the surface of the nanocrystals is cleaner because of the lack of organic surface-capping agents, and contact between the nanocrystals and electrode is much better than in the case where colloidal nanoparticles are deposited on the electrode. However, the particle size is much larger for the electrochemical method (even up to >1 μm), and significant mass production is not possible. Additionally, this method is not appropriate for catalytic applications using precious metal catalysts.

2.3 The Effect of Shape on Catalytic Activity, Selectivity, and Long-Term Stability

Shaped nanoparticles have been utilized as catalysts for various electrocatalytic, gas-phase, and liquid-phase reactions. The shape often results in enhanced activity, selectivity, and long-term stability. Many examples have been reported for single

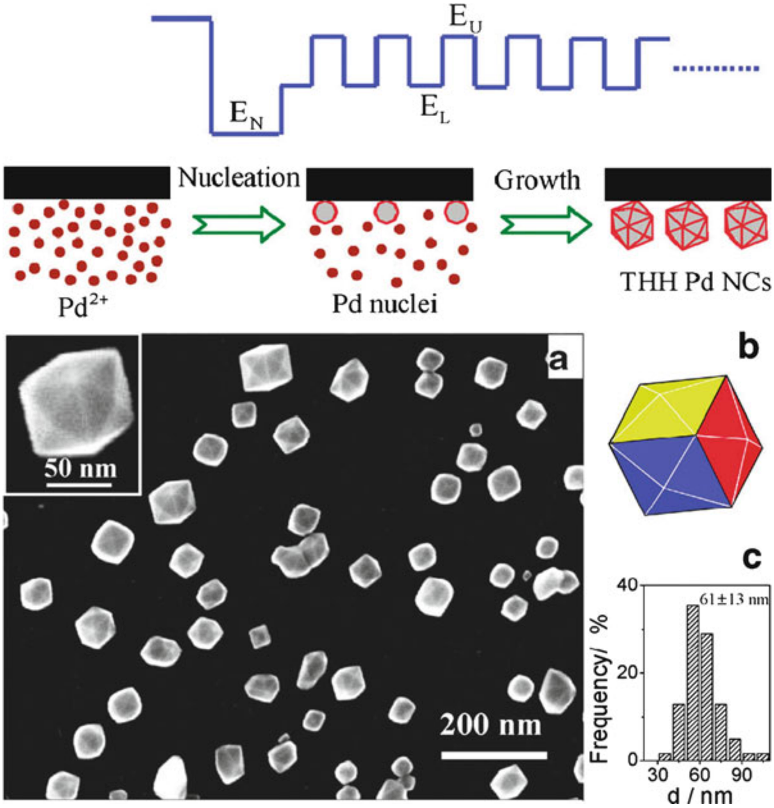

Fig. 2.7 A synthetic scheme and SEM images of tetrahexahedral Pd nanocrystals electrochemically deposited on the electrode (adapted from ref. [36])

metal, metal composite, and metal oxide materials. Instead of providing a comprehensive review of all of these examples, I will only introduce examples that show the potential and limitations of shaped nanocrystals in catalytic applications.

2.3.1 Pt_3Ni Nanooctahedra

In 2007, Markovic et al. reported a single-crystalline study showing that the $Pt_3Ni(111)$ surface is tenfold more active in the oxygen reduction reaction (ORR) than the corresponding Pt(111) surface and 90-fold more active than the current state-of-the-art Pt/C catalysts, as shown in Fig. 2.8 [40]. This beautiful study stimulated the synthesis of nanoparticles consisting of the $Pt_3Ni(111)$ surface and, 3 years later, the synthesis of Pt_3Ni nanooctahedra and the results for the ORR activity test were reported [26].

The authors emphasized the strong shape dependence of the Pt_3Ni nanoparticles on ORR activity. The shape dependence was clearly observed, but the enhancement

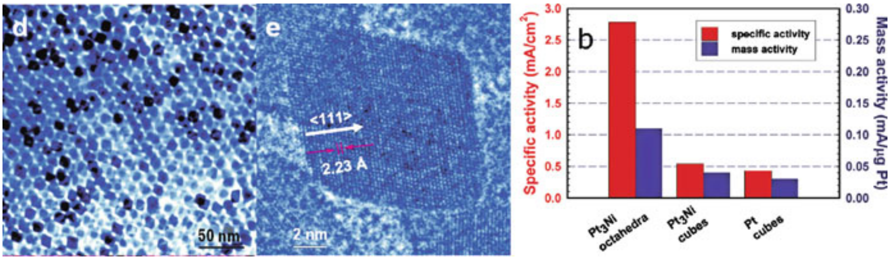

Fig. 2.8 TEM images of Pt_3Ni nanooctahedra and comparison of ORR activity (adapted from ref. [26])

in mass activity was rather disappointing. Mass activity of commercial Pt/C is usually ~0.1 A/mg_{Pt} for the ORR at 0.9 V (vs. RHE) in 0.1 M $HClO_4$ solution. The Pt_3Ni octahedra only showed mass activity comparable to commercial Pt/C, whereas the Pt_3Ni octahedra supported on carbon had higher mass activity (~0.3 A/mg_{Pt}). Considering the complicated synthetic conditions and potential shape degradation during the ORR, the synthesized Pt_3Ni octahedra do not seem to be attractive for practical applications.

The low mass activity might be the result of residual surface-capping agent (oleylamine) or shape deformation during the removal process of the surface-capping agent. The authors used Ar plasma to remove the surface-capping agent, but this might degrade the well-defined surfaces of the shaped nanoparticles.

2.3.2 Pt Nanodendrites

Dendritic-shaped Pt nanoparticles have been synthesized using amphiphilic polymers or block copolymers. We synthesized highly porous Pt nanoparticles using tetradecyltrimethylammonium bromide (TTAB) as the surface-capping agent. This agent has weaker interactions with the Pt surface, which better preserves the catalytically active sites [31]. Various sizes (13, 19, 30, 53 nm) of Pt nanodendrites were synthesized, and their catalytic activity was tested in the ORR [41]. Interestingly, the dendrites had a single-crystalline structure, rather than an agglomerated form composed of smaller nanoparticles. The dendrites showed a higher activity than commercial Pt/C; the mass activity was enhanced by a maximum of ~3 times at 0.9 V (vs. RHE), compared with commercial Pt/C (E-tek). Additionally, the long-term stability was tested by repeating the cyclovoltammogram 5,000 times in the range of 0.6–1.1 V in oxygen-saturated 0.1 M $HClO_4$ solution. The reduction in the electrochemically active surface area was lower in the nanodendrites than in the commercial Pt/C.

The reason of this enhanced activity and long-term stability was elucidated by taking extended X-ray absorption fine structure (EXAFS), X-ray absorption near edge structure (XANES), and high resolution X-ray diffraction (XRD) [42]. It

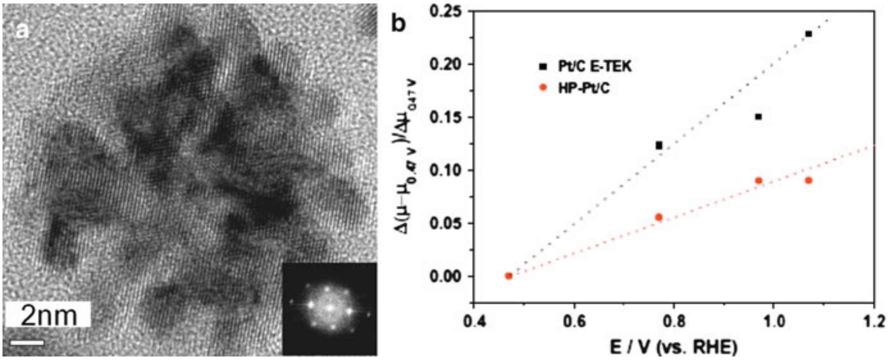

Fig. 2.9 HR-TEM image of the Pt dendrite and comparison of the change in absorption edge peaks of the XANES spectra as a function of potential (adapted from ref. [41, 42])

turned out that the abnormal shape of the dendrite (highly porous in spite of being a single crystal) induced greater compressive strain on the Pt surface. Bond length shortening occurred and d-band center was downshifted, resulting in increased ORR activity. The XANES study at various potentials also revealed the electron retention property of the dendrites. The Pt surface of the dendrites was oxidized less than the commercial Pt/C, minimizing the Pt dissolution at high potential and resulting in enhanced long-term stability. Figure 2.9 shows the HR-TEM image, which shows the single-crystalline nature of the nanodendrites and the XANES results at various potentials.

Our preliminary membrane-electrode assembly (MEA) test results, however, showed that Pt nanodendrites used as cathode catalysts did not necessarily guarantee higher performance as a single fuel cell. Although the result of a half-cell test showed that the mass activity of the Pt dendrites/C was enhanced by ~3 times, compared with commercial Pt/C, a full-cell test showed a current output only comparable to commercial Pt/C at 0.6 V. The porous shape induced higher ohmic and concentration resistance regardless of its lower activation overpotential. The Pt nanodendrites' three-phase boundary (gas reactant/Pt catalyst/polymer electrolyte) was not as good as that of commercial Pt/C. All of the studies reporting enhanced activity of shaped nanocrystals were actually performed in a half-cell system. Although the shaped nanocrystals can provide a good platform to study structure–activity relationships, the direct application of shaped nanocrystals in a practical fuel cell system would face many obstacles.

2.3.3 *Pt-Based Nanocubes*

Pt-based cubic nanoparticles have also been reported as electrocatalysts [18, 43]. They have especially high activity in H_2SO_4 solution. When $HClO_4$ solution was

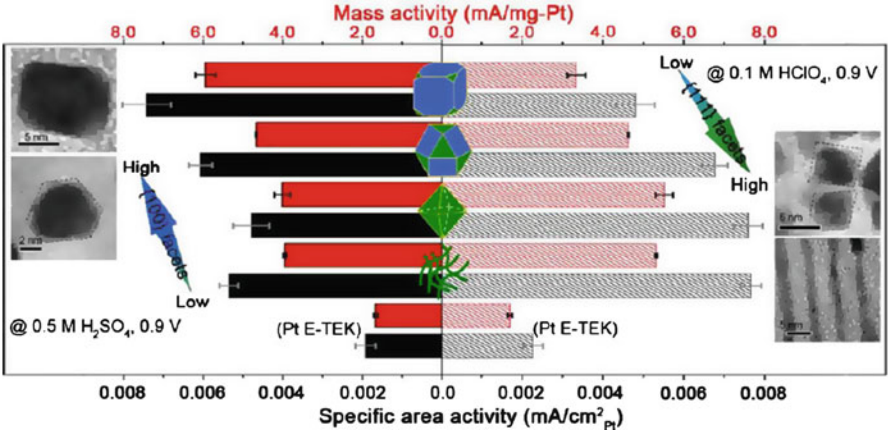

Fig. 2.10 The activity of shaped PtNiFe nanoparticles in ORR (adapted from ref. [43])

used as the electrolyte, the (111) surface showed higher activity, but when H_2SO_4 solution was used, the (100) surface had higher activity. The sulfate ions bind to the Pt(111) surface, strongly hindering the catalytic reaction on the surface, whereas $HClO_4$ does not have a strong interaction with the Pt surface. Because actual fuel cell systems use polymer electrolytes with excessive amounts of sulfate ions, such as Nafion, activity tests in H_2SO_4 solution might provide more practical results. Figure 2.10 shows the activity of PtNiFe nanoparticles in ORR in H_2SO_4 and $HClO_4$ electrolyte solutions. Although this graph shows the effect of the shapes and electrolytes well, the mass activity reported for the E-Tek catalyst is too small.

The shaped Pd nanocrystals were synthesized by overgrowing Pd on Pt nanocubes [28]. The cubic, cuboctahedral, and octahedral Pd nanocrystals were tested as electrocatalysts for formic acid oxidation. While Pd cubes showed the highest currents (~5 times of Pd octahedra), Pd octahedra demonstrated the least surface oxidation. PtFeCo branched nanocubes were also synthesized [44]. Co-rich branches were overgrown on Pt-based nanocubes. These branched nanocubes were tested as electrocatalysts for methanol oxidation. They showed enhanced activity due to less CO poisoning. The cubic Pt_xPd_{1-x} nanoparticles showed higher activity for the hydrogenation of nitrobenzene in the liquid-phase, compared with octahedral Pt_xPd_{1-x} nanoparticles [30]. In contrast, for $PtNi_2$ nanoparticles, the cubic shape showed poorer activity for the hydrogenation of benzalacetone in the liquid-phase compared with the truncated octahedral and octahedral shapes [20].

2.3.4 Pt Overgrowth on Shaped Nanocrystals

Underpotential deposition (UPD) has received much attention as a way to minimize Pt utilization. Copper is usually used as an intermediate species for Pt

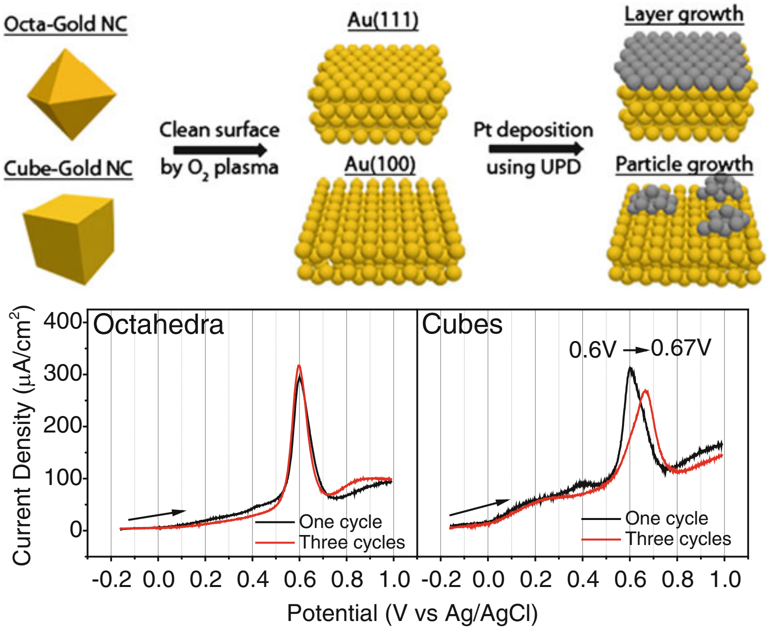

Fig. 2.11 A distinct platinum growth mode on shaped gold nanocrystals (adapted from ref. [45])

monolayer formation. Typically, copper is deposited on a gold surface as a monolayer because it is reduced on gold surfaces at a lower potential than the standard reduction potential of bulk copper. The copper can then be replaced by Pt via galvanic replacement. Because only the surface is used for electrocatalytic reactions, the deposition of a Pt monolayer on the support material can minimize the required amount of Pt. However, conflicting results have been reported on whether the Pt monolayer has enhanced or suppressed electrocatalytic activity when the monolayer was formed on a gold surface using the UPD technique. We have recently shown that the structure of overgrown Pt is affected by the crystalline structure of the underlying gold surface. When Pt was overgrown using the UPD technique on gold cubes with Au(100) facets or gold octahedra with Au(111) facets, Pt nanoparticles formed on the cubes, whereas Pt overlayers formed on the octahedra (Fig. 2.11) [45]. Simulation using density functional theory also confirmed that Pt overlayers were energetically favorable on the Au(111) surface, but Pt islands were more stable on the Au(100) surface.

CO stripping results showed that CO binds more strongly to Pt nanoparticles than Pt overlayers. For electrocatalytic oxidation of small organic molecules, such as methanol or formic acid, stronger binding to CO often results in poorer activity. The conflicting reports about the activity of Pt formed by the UPD technique might result from not knowing the effect of the underlying gold surface on the Pt nanostructure.

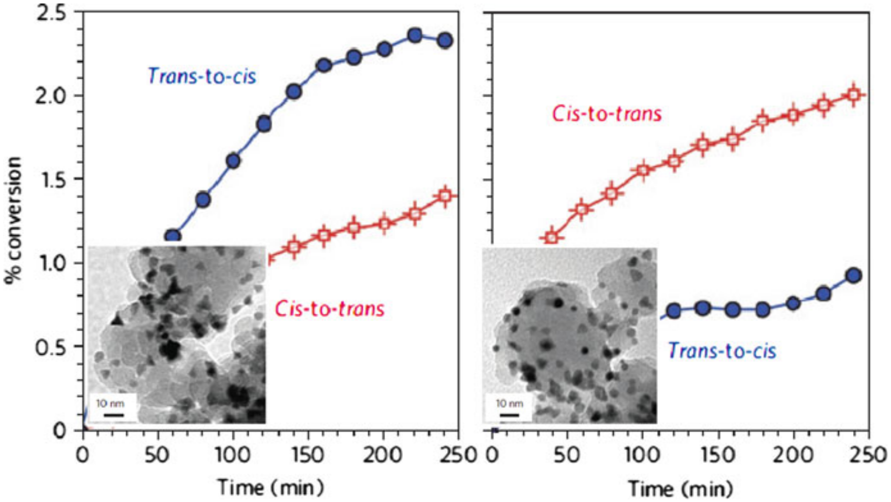

Fig. 2.12 Isomerization of 2-butene; *trans* to *cis* occurred more frequently on the tetrahedral Pt nanoparticles, whereas *cis* to *trans* occurred more frequently on the spherical Pt nanoparticles (adapted from ref. [47])

2.3.5 Selectivity Enhanced by Shape

Examples have been reported showing that selectivity can be controlled by changing the shape of the nanocrystals. The initial example was benzene hydrogenation using Pt cubes and cuboctahedra [46]. As explained earlier, the Pt(100) surface produces fully hydrogenated cyclohexane as a product of benzene hydrogenation, whereas the Pt(111) surface produces both fully and partially hydrogenated cyclohexene [5]. Shaped Pt nanoparticles were tested to determine if they produced the same results as seen in the single-crystalline surfaces. Pt cubes with Pt(100) facets produced only cyclohexane, but Pt cuboctahedra, which contain Pt(111) facets, produced cyclohexene as well. However, the amount of cyclohexene produced was much larger in the nanoparticle case, compared to the single-crystalline surface.

Zaera et al. successfully tuned the selectivity for the production of *cis*-olefins by isomerization [47]. They synthesized tetrahedral Pt nanoparticles with Pt(111) facets using PVP as the surface-capping agent. Then, the organic surface layer was removed by calcination and subsequent oxidation/reduction cycles in O_2 and H_2 atmospheres. When the calcination temperature was 475 K, the shape was preserved and the "*trans* to *cis*" formation occurred more frequently, as shown in Fig. 2.12. When the calcination temperature was 575 K, the tetrahedral shape degraded into the spherical shape and the "*cis* to *trans*" formation occurred more frequently than the "*trans* to *cis*."

Control over the reaction pathway was also observed in electrocatalytic reactions. In electrocatalytic formic acid oxidation, there are two pathways by which formic acid is oxidized: dehydration ($HCOOH \rightarrow H_2O + CO$) and dehydrogenation ($HCOOH \rightarrow H_2 + CO_2$). The dehydration pathway generates surface-poisoning CO

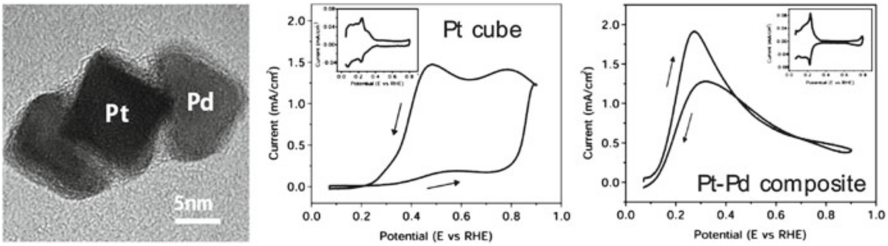

Fig. 2.13 TEM image of a Pt–Pd composite nanoparticle and cyclovoltammograms showing electrocatalytic formic acid oxidation for Pt cube and Pt–Pd composite nanoparticles (adapted from ref. [48])

species, often increasing the oxidation potential and decreasing the amount of current produced. In the case of the Pt cube, the formic acid is oxidized following a dehydration pathway, which generates almost no current in the forward scan. However, when Pd is locally overgrown on the Pt surface, as shown in Fig. 2.13, the pathway is shifted to dehydrogenation, producing a high current in the forward scan [48]. The peak potential is also significantly lowered.

The electrocatalytic hydrogenation of cyclohexenone was also tested for various shapes of Pt cubes, cuboctahedra, and dendrites [49]. The dendrites produced more fully hydrogenated cyclohexanol, whereas the cubes produced more partially hydrogenated cyclohexanone. Presumably, there are more stepped sites on the surface of the dendrites, which are more advantageous for hydrogenating C═O bonds, compared to the (100) surface.

2.3.6 Long-Term Stability Enhanced by Shape

Few studies have focused on the effect of the shape on long-term stability. As explained in Sect. 3.2, Pt dendrites have enhanced long-term stability in the electrocatalytic ORR because there is less surface oxidation at high potential [42]. A few other examples have shown the long-term stability of shaped metal oxide nanocrystals for catalytic reactions. Shen et al. reported that Co_3O_4 nanorods with (110) facets are very active for CO oxidation [50], but the oxygen-exposed (110) facets are easily degraded, showing a sudden reduction in activity 60 h later at room temperature. We recently reported the long-term stability of Cu/CeO_2 with copper deposited on shaped CeO_2 nanocrystals for preferential oxidation of CO in excess H_2 (PROX) [51], as shown in Fig. 2.14. When CeO_2 cubes, rods, and octahedra were compared, the octahedral shape showed the highest activity and the best long-term stability. While significant reduction in the activity was observed for both cubes and rods, the high activity remained unchanged for the octahedra after 100 h of reaction.

The long-term stability of the shaped nanocrystal catalysts should be obtained for their practical application. More studies need to focus on the stability over many hours of reaction using shaped nanocatalysts.

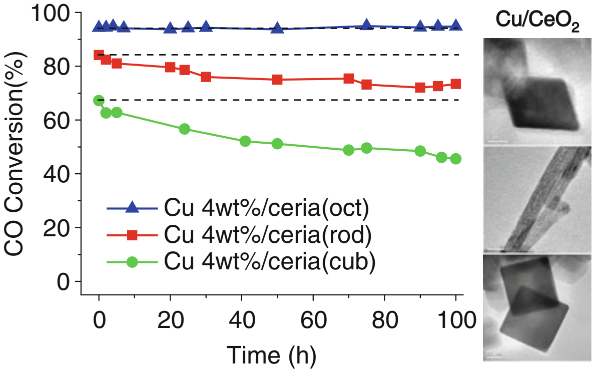

Fig. 2.14 PROX reaction for 100 h using Cu/shaped CeO_2 catalysts (adapted from ref. [51])

2.4 The Effect of the Surface-Capping Agent

The effect of residual surface-capping agents on catalytic properties should be considered carefully. Catalytic activity can often be observed only after removing the surface-capping agent to some extent, but completely removing the organic agents is not easily achieved. Not only do the capping agents occupy the surface of the catalysts but also they affect the chemical properties of the surface, such as the oxidation state.

2.4.1 How the Catalytic Activity Can Be Varied by the Surface-Capping Agents

Previously, we investigated how the surface-capping agent affects catalytic activity. Pt cubes of the same shape and similar sizes have been synthesized by using two different surface-capping agents, PVP (MW 55,000) and TTAB (MW 336). The catalytic activity of these Pt cubes was tested for electrocatalytic H adsorption, C_2H_4 hydrogenation, benzene hydrogenation, and *p*-nitrophenol hydrogenation [52]. The size of the reactants increased from H to *p*-nitrophenol. The surface-capping agents reside on the surface for the first three reactions, whereas the surface-capping agents spread out into the liquid medium for the *p*-nitrophenol hydrogenation. The long polymeric alkyl chain of PVP covered the Pt surface more than TTAB. When using PVP, there were fewer clean Pt atom ensembles for the adsorption of the reactants. However, when the surface-capping agents spread out, the length of the capping agent did not matter much (Fig. 2.15).

TTAB-capped Pt nanocubes had higher activity than PVP-capped cubes for the first three reactions. Furthermore, the activity difference became larger when the size of the reactants was larger. The activity ratio of the TTAB case to the PVP case

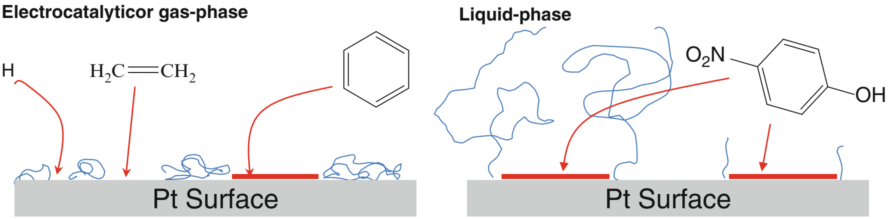

Fig. 2.15 The effect of the length of the surface-capping agents and the reaction medium

was 3.8 for H adsorption, 7.1 for C_2H_4 hydrogenation, and 13.4 for benzene hydrogenation. However, the activity was similar for the *p*-nitrophenol hydrogenation with an activity ratio of 0.98. For liquid-phase reactions, the length of the surface-capping agent had a negligible effect. This work clearly shows how the activity can be varied by the surface-capping agents and reaction conditions.

2.4.2 Removal of the Surface-Capping Agents

Various methods have been utilized to remove surface-capping agents, such as thermal annealing, repetitive oxidation/reduction, UV/ozone treatment, acetic acid washing, ultrasonication, and the imposition of high voltage. Stamenkovic et al. reported that when oleylamine-coated nanoparticles were annealed in an oxygen atmosphere at a mild temperature (185 °C), the activity for ORR was the highest [53]. Acetic acid washing or UV/ozone treatment showed much lower activity (2/3 and 2/5 of oxygen annealing, respectively). This result clearly confirms that the surface-capping agent affects the catalytic activity significantly enough to blur the real shape effect. In particular, this removal process often deforms the shape of the nanocrystals. Sharp corners, such as at the vertex of cubic nanoparticles, are typically rounded [54].

Furthermore, the removal of the surface-capping agent does not necessarily guarantee a “clean” surface; instead, there is a significant chance that remnants of the surface-capping agent remain on the surface. When the surface of TTAB-capped Pt nanoparticles was monitored by FT-IR diffuse reflectance infrared Fourier transform spectroscopy (DRIFT) over increasing temperatures, the alkyl chain could be easily removed, especially in an oxygen atmosphere, but the ammonium head group stayed on the surface above 350 °C regardless of the chemical environment [55] (Fig. 2.16).

2.4.3 In Situ Shaping Without Surface-Capping Agents

We developed a method to synthesize shaped Pt nanocrystals directly on three-dimensional supports without a surface-capping agent. When the Pt precursors were reduced in the presence of carbon supports with high surface areas, nucleation occurred on the supports and the nanoparticle was formed without surface-capping

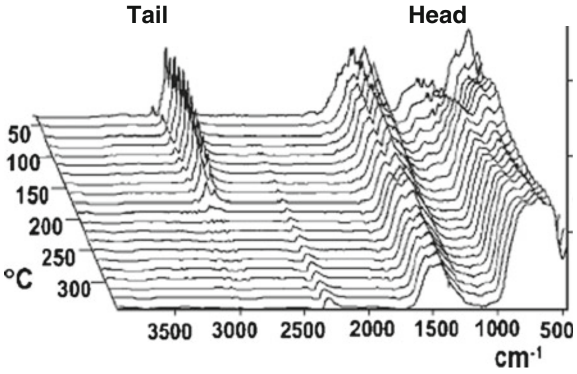

Fig. 2.16 FT-IR DRIFT results of TTAB-capped Pt nanoparticles treated in an oxygen atmosphere at various temperatures (adapted from ref. [55])

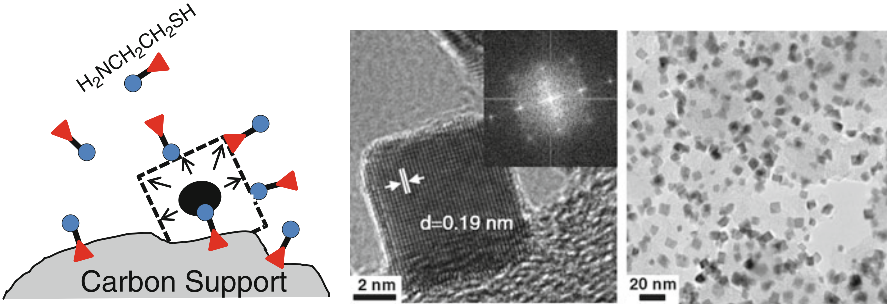

Fig. 2.17 In situ-shaped cubic Pt/C synthesized without a surface-capping agent (adapted from ref. [56])

agents. When cysteamine was added with the Pt precursor and carbon supports, it acted as an anchoring agent, providing nucleation sites on the carbon supports, and as a shaping agent, inducing a cubic shape (Fig. 2.17) [56]. But the cysteamine itself cannot be a surface-capping agent; it combines with the nanoparticles, producing large aggregates without carbon supports. As a result, the surface of in situ-shaped cubic Pt/C was catalytically active without any posttreatment for the removal of organic material. When the activity was compared to Pt nanocubes synthesized with oleylamine and oleic acid for the ORR, these in situ-shaped Pt cubes showed a higher activity.

2.4.4 Participating in Catalytic Reactions

Although the surface-capping agents are usually considered as trouble in catalytic applications, they can actually participate in catalytic reactions. Kim et al. synthesized Pt nanoparticles (1–2 nm in size) by using an enzyme (aminopeptidase) [57]

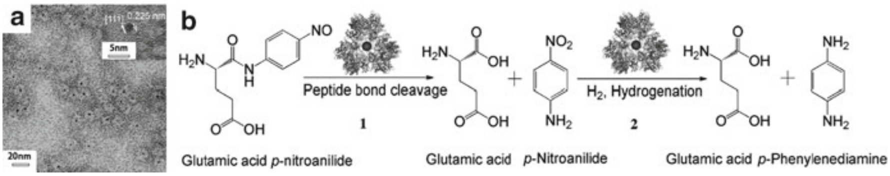

Fig. 2.18 Pt nanoparticles synthesized with PepA and their use in a cascade reaction (adapted from ref. [57])

as the surface-capping agent. The enzyme enabled the Pt nanoparticles to disperse in an aqueous solution and it acted as a biocatalyst. Glutamic acid *p*-nitroanilide was cleaved into separate molecules of glutamic acid and *p*-nitroanilide by the enzyme and then the *p*-nitroanilide was hydrogenated to *p*-phenylenediamine by the Pt nanoparticles residing inside the enzyme (Fig. 2.18).

Additionally, the surface-capping agents often prevent surface oxidation, preserving the metallic state of the surface. When dodecylamine-capped Pt nanoparticles were deposited on iron oxide supports for preferential oxidation of CO in excess H_2, these nanoparticles showed higher activity for CO at lower temperatures than ligand-free Pt nanoparticles due to less surface oxidation [58]. The organic layer might be used to tune the metal–support interaction for heterogeneous gas-phase catalytic reactions.

2.5 Issues to Be Resolved

Although the shaped nanocrystals have shown a high potential for the enhancement of catalytic activity, selectivity, and long-term stability, there are several issues that need to be resolved to expand their use to practical applications. The shaped nanocrystals are typically too large to effectively utilize expensive precious metals. The stability of the shaped nanocrystals should be carefully evaluated. The shape is often deformed too easily, especially at high temperatures where many practical gas-phase reactions occur. Shaped nanoparticles should also operate stably for long periods of time. Mass production of shaped nanocrystals is another important issue to be addressed properly. Indeed, much work on shaped nanoparticles is still needed to fundamentally understand their catalytic reactions and develop practical catalysts with better catalytic properties.

2.5.1 Size: Facet vs. Edge/Step/Vertex

The size of the shaped nanocrystals is usually large. Those larger than 100 nm are often observed for shaped Au or Ag nanocrystals. In the case of Pt, shaped nanocrystals are usually observed in the range of 5–10 nm. However, the typical size of

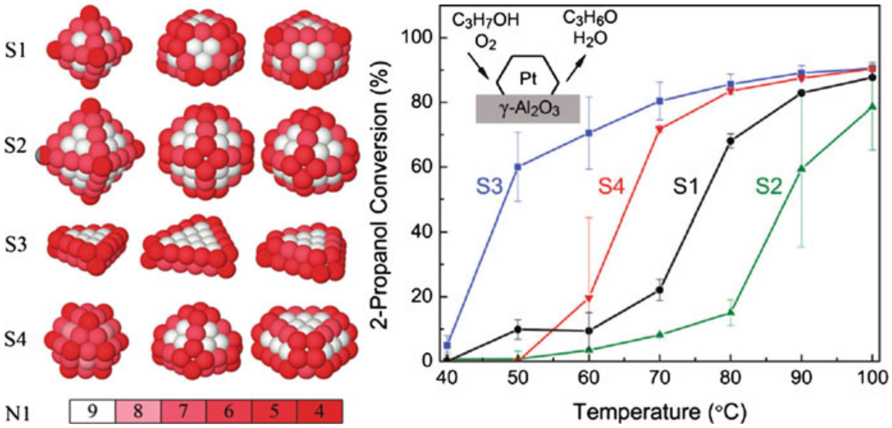

Fig. 2.19 Small shaped Pt nanoparticles (0.8–1 nm) and their catalytic activity for 2-propanol oxidation (adapted from ref. [59])

Pt nanoparticles used as practical catalysts is 1–3 nm. Large shaped nanoparticles would not be practically useful unless their size is reduced further, although the specific activity (activity per unit surface atom) is improved significantly. Cuenya et al. recently reported shape-dependent catalytic properties of Pt nanoparticles with a size of 0.8–1 nm [59]. They prepared these small nanoparticles by inverse micelle encapsulation using polystyrene-*block*-poly(2-vinylpyridine). Because direct observation of the shape by electron microscopy is almost impossible, they measured the coordination number via EXAFS and calculated the shape, as shown in Fig. 2.19. The oxidation of 2-propanol on these nanoparticles showed a large dependence on the shape of the nanoparticles. However, the activity was actually correlated to the average number of missing bonds on the nanoparticle surface. The activity was significantly affected by the undercoordinated atoms, not by the surface crystalline structure induced by the shape control. Furthermore, nanoparticles with sizes smaller than 5 nm would have a strong quantum effect, with an electronic structure significantly different from larger nanoparticles. Although surface structure has been studied mainly for shaped nanoparticles with larger sizes (>5 nm), different factors, such as coordination number and the change in electronic structure from interaction with supports, should be evaluated more carefully for smaller shaped nanoparticles (<5 nm). Additionally, a completely new strategy should be developed to synthesize these small shaped nanoparticles.

2.5.2 *Stability*

As explained before, the shape of nanoparticles should be preserved during the removal of the organic agent and the catalytic reaction process. Additionally, to expand the applicability of these shaped nanoparticles, they should have shape

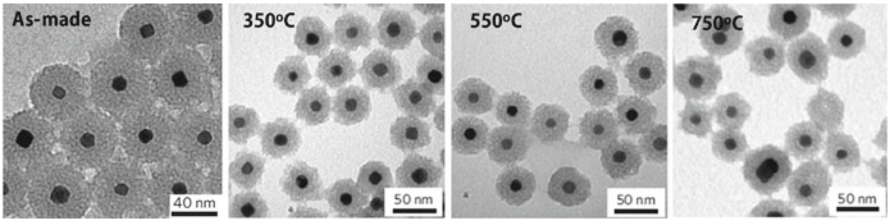

Fig. 2.20 Pt-cube/mesoporous-silica core/shell; the effect of temperature (adapted from ref. [61])

stability at higher reaction temperatures. Many gas-phase reactions occur in the temperature range of 300–500 °C. The cubic Pt nanoparticles (TTAB-capped, PVP-capped, and oleylamine-capped) with an average size of ~10 nm were degraded and lost their shape below 300 °C [60]. Although Wang et al. reported that the tetrahexahedral shape could be preserved up to 815 °C [35], the particle size was very large (over 200 nm). Somorjai et al. reported that Pt nanoparticles with a size smaller than 10 nm could be thermally stable up to 750 °C, with a mesoporous-silica shell around the individual Pt nanoparticles. Figure 2.20 shows TEM images of Pt/silica core/shell nanoparticles and the effect of thermal treatment at various temperatures. Although this work did not particularly mention the preservation of the shape, the TEM images showed that the silica coating contributed to preservation of the shape at higher temperatures.

2.5.3 Mass Production

The typical amount of the shaped nanoparticles synthesized per batch is less than 100 mg. When additional purification processing is needed, the amount obtained decreases even further. Some nanoparticles might also be lost during the washing process. The small amounts obtained might be enough to test the activity once in a laboratory, but the amount needs to be scaled up for more practical application. However, mass production of shaped nanoparticles is not easy. Although well-defined nanoparticles are reproducibly synthesized on a small scale, the shape purity becomes much worse when the synthesis occurs on a large scale. New strategies might be necessary to produce a large quantity of shaped nanoparticles.

References

1. Vang RT, Wang JG, Knudsen J, Schnadt J, Laegsgaard E, Stensgaard I, Besenbacher F (2005) The adsorption structure of NO on Pd(III) at high pressures studied by STM and DFT. J Phys Chem B 109:14262–14265
2. Davis SM, Zaera F, Somorjai GA (1984) Surface structure and temperature dependence of n-hexane skeletal rearrangement reactions catalyzed over platinum single crystal surfaces: marked structure sensitivity of aromatization. J Catal 85:206–223

3. Zaera F, Godbey D, Somorjai GA (1986) Methylcyclopentane conversion over platinum single crystal surfaces: evidence for the cyclic mechanism of n-hexane isomerization. J Catal 101:73–80
4. Solla-Gullon J, Vidal-Iglesias FJ, Lopez-Cudero A, Garnier E, Feliu JM, Aldaza A (2008) Shape-dependent electrocatalysis: methanol and formic acid electrooxidation on preferentially oriented Pt nanoparticles. Phys Chem Chem Phys 10:3689–3698
5. Bratlie KM, Kliewer CJ, Somorjai GA (2006) Structure effects of benzene hydrogenation studied with sum frequency generation vibrational spectroscopy and kinetics on Pt(111) and Pt(100) single-crystal surfaces. J Phys Chem B 110:17925–17930
6. Tao AR, Habas S, Yang PD (2008) Shape control of colloidal metal nanocrystals. Small 4:310–325
7. Schuth F (2011) Controlled nanostructures for applications in catalysis. Phys Chem Chem Phys 13:2447–2448
8. Lee K, Kim M, Kim H (2010) Catalytic nanoparticles being facet-controlled. J Mater Chem 20:3791–3798
9. Mazumder V, Lee Y, Sun SH (2010) Recent development of active nanoparticle catalysts for fuel cell reactions. Adv Funct Mater 20:1224–1231
10. Chen JY, Lim B, Lee EP, Xia YN (2009) Shape-controlled synthesis of platinum nanocrystals for catalytic and electrocatalytic applications. Nano Today 4:81–95
11. Narayanan R, El-Sayed MA (2005) Catalysis with transition metal nanoparticles in colloidal solution: nanoparticle shape dependence and stability. J Phys Chem B 109:12663–12676
12. Xia YN, Xiong YJ, Lim B, Skrabalak SE (2009) Shape-controlled synthesis of metal nanocrystals: simple chemistry meets complex physics? Angew Chem Int Ed Engl 48:60–103
13. Lu Y, Liu GL, Kim J, Mejia YX, Lee LP (2005) Nanophotonic crescent moon structures with sharp edge for ultrasensitive biomolecular detection by local electromagnetic field enhancement effect. Nano Lett 5:119–124
14. Zhu J, Somorjai GA (2001) Formation of platinum silicide on a platinum nanoparticle array model catalyst deposited on silica during chemical reaction. Nano Lett 1:8–13
15. Ahmadi TS, Wang ZL, Green TC, Henglein A, El-Sayed MA (1996) Shape-controlled synthesis of collodial platinum nanoparticles. Science 272:1924–1926
16. Sui YM, Fu WY, Yang HB, Zeng Y, Zhang YY, Zhao Q, Li YE, Zhou XM, Leng Y, Li MH, Zou GT (2010) Low temperature synthesis of Cu2O crystals: shape evolution and growth mechanism. Cryst Growth Des 10:99–108
17. Niu ZQ, Peng Q, Gong M, Rong HP, Li YD (2011) Oleylamine-mediated shape evolution of palladium nanocrystals. Angew Chem Int Ed Engl 50:6315–6319
18. Wang C, Daimon H, Onodera T, Koda T, Sun SH (2008) A general approach to the size- and shape-controlled synthesis of platinum nanoparticles and their catalytic reduction of oxygen. Angew Chem Int Ed Engl 47:3644–3647
19. Wu JB, Gross A, Yang H (2011) Shape and composition-controlled platinum alloy nanocrystals using carbon monoxide as reducing agent. Nano Lett 11:798–802
20. Wu YE, Cai SF, Wang DS, He W, Li YD (2012) Syntheses of water-soluble octahedral, truncated octahedral, and cubic Pt-Ni nanocrystals and their structure-activity study in model hydrogenation reactions. J Am Chem Soc 134:8975–8981
21. Song H, Kim F, Connor S, Somorjai GA, Yang PD (2005) Pt nanocrystals: shape control and Langmuir-Blodgett monolayer formation. J Phys Chem B 109:188–193
22. Rioux RM, Song H, Grass M, Habas S, Niesz K, Hoefelmeyer JD, Yang P, Somorjai GA (2006) Monodisperse platinum nanoparticles of well-defined shape: synthesise characterization, catalytic properties and future prospects. Top Catal 39:167–174
23. Chen M, Kim J, Liu JP, Fan HY, Sun SH (2006) Synthesis of FePt nanocubes and their oriented self-assembly. J Am Chem Soc 128:7132–7133
24. Sun SH, Murray CB, Weller D, Folks L, Moser A (2000) Monodisperse FePt nanoparticles and ferromagnetic FePt nanocrystal superlattices. Science 287:1989–1992
25. Zhang J, Fang JY (2009) A general strategy for preparation of Pt 3d-transition metal (Co, Fe, Ni) nanocubes. J Am Chem Soc 131:18543–18547

26. Zhang J, Yang HZ, Fang JY, Zou SZ (2010) Synthesis and oxygen reduction activity of shape-controlled Pt3Ni nanopolyhedra. Nano Lett 10:638–644
27. Kang YJ, Ye XC, Murray CB (2010) Size- and shape-selective synthesis of metal nanocrystals and nanowires using CO as a reducing agent. Angew Chem Int Ed Engl 49:6156–6159
28. Habas SE, Lee H, Radmilovic V, Somorjai GA, Yang P (2007) Shaping binary metal nanocrystals through epitaxial seeded growth. Nat Mater 6:692–697
29. Zhang YW, Grass ME, Kuhn JN, Tao F, Habas SE, Huang WY, Yang PD, Somorjai GA (2008) Highly selective synthesis of cataytically active monodisperse rhodium nanocubes. J Am Chem Soc 130:5868–5869
30. Huang X, Li Y, Li Y, Zhou H, Duan X, Huang Y (2012) Synthesis of PtPd bimetal nanocrystals with controllable shape, composition, and their tunable catalytic properties. Nano Lett 12:4265–4270
31. Lee H, Habas SE, Kweskin S, Butcher D, Somorjai GA, Yang PD (2006) Morphological control of catalytically active platinum nanocrystals. Angew Chem Int Ed Engl 45:7824–7828
32. Chen JY, Wiley B, McLellan J, Xiong YJ, Li ZY, Xia YN (2005) Optical properties of Pd-Ag and Pt-Ag nanoboxes synthesized via galvanic replacement reactions. Nano Lett 5:2058–2062
33. Min M, Kim C, Yang YI, Yi J, Lee H (2009) Surface-specific overgrowth of platinum on shaped gold nanocrystals. Phys Chem Chem Phys 11:9759–9765
34. Min M, Kim C, Yang YI, Yi J, Lee H (2011) Top-down shaping of metal nanoparticles in solution: partially etched Au@Pt nanoparticles with unique morphology. Chem Commun 47:8079–8081
35. Tian N, Zhou ZY, Sun SG, Ding Y, Wang ZL (2007) Synthesis of tetrahexahedral platinum nanocrystals with high-index facets and high electro-oxidation activity. Science 316:732–735
36. Tian N, Zhou ZY, Yu NF, Wang LY, Sun SG (2010) Direct electrodeposition of tetrahexahedral Pd nanocrystals with high-index facets and high catalytic activity for ethanol electrooxidation. J Am Chem Soc 132:7580–7581
37. Chen YX, Chen SP, Zhou ZY, Tian N, Jiang YX, Sun SG, Ding Y, Wang ZL (2009) Tuning the shape and catalytic activity of Fe nanocrystals from rhombic dodecahedra and tetragonal bipyramids to cubes by electrochemistry. J Am Chem Soc 131:10860–10861
38. Siegfried MJ, Choi KS (2005) Directing the architecture of cuprous oxide crystals during electrochemical growth. Angew Chem Int Ed Engl 44:3218–3223
39. Siegfried MJ, Choi KS (2008) Elucidation of an overpotential-limited branching phenomenon observed during the electrocrystallization of cuprous oxide. Angew Chem Int Ed Engl 47:368–372
40. Stamenkovic VR, Fowler B, Mun BS, Wang GF, Ross PN, Lucas CA, Markovic NM (2007) Improved oxygen reduction activity on Pt3Ni(111) via increased surface site availability. Science 315:493–497
41. Kim C, Oh JG, Kim YT, Kim H, Lee H (2010) Platinum dendrites with controlled sizes for oxygen reduction reaction. Electrochem Commun 12:1596–1599
42. Kim DS, Kim C, Kim JK, Kim JH, Chun HH, Lee H, Kim YT (2012) Enhanced electrocatalytic performance due to anomalous compressive strain and superior electron retention properties of highly porous Pt nanoparticles. J Catal 291:69–78
43. Chou SW, Shyue JJ, Chien CH, Chen CC, Chen YY, Chou PT (2012) Surfactant-directed synthesis of ternary nanostructures: nanocubes, polyhedrons, octahedrons, and nanowires of PtNiFe. Their shape-dependent oxygen reduction activity. Chem Mater 24:2527–2533
44. Kim S, Kim C, Lee H (2010) Shape- and composition-controlled Pt-Fe-Co nanoparticles for electrocatalytic methanol oxidation. Top Catal 53:686–693
45. Yang S, Park NY, Han JW, Kim C, Lee SC, Lee H (2012) A distinct platinum growth mode on shaped gold nanocrystals. Chem Commun 48:257–259
46. Bratlie KM, Lee H, Komvopoulos K, Yang PD, Somorjai GA (2007) Platinum nanoparticle shape effects on benzene hydrogenation selectivity. Nano Lett 7:3097–3101
47. Lee I, Delbecq F, Morales R, Albiter MA, Zaera F (2009) Tuning selectivity in catalysis by controlling particle shape. Nat Mater 8:132–138

48. Lee HJ, Habas SE, Somorjai GA, Yang PD (2008) Localized Pd overgrowth on cubic Pt nanocrystals for enhanced electrocatalytic oxidation of formic acid. J Am Chem Soc 130:5406–5407
49. Kim C, Lee H (2009) Shape effect of Pt nanocrystals on electrocatalytic hydrogenation. Catal Commun 11:7–10
50. Xie XW, Li Y, Liu ZQ, Haruta M, Shen WJ (2009) Low-temperature oxidation of CO catalysed by Co3O4 nanorods. Nature 458:746–749
51. Han J, Kim HJ, Yoon S, Lee H (2011) Shape effect of ceria in Cu/ceria catalysts for preferential CO oxidation. J Mol Catal A Chem 335:82–88
52. Kim C, Lee H (2009) Change in the catalytic reactivity of Pt nanocubes in the presence of different surface-capping agents. Catal Commun 10:1305–1309
53. Li DG, Wang C, Tripkovic D, Sun SH, Markovic NM, Stamenkovic VR (2012) Surfactant removal for colloidal nanoparticles from solution synthesis: the effect on catalytic performance. ACS Catal 2:1358–1362
54. Inaba M, Ando M, Hatanaka A, Nomoto A, Matsuzawa K, Tasaka A, Kinumoto T, Iriyama Y, Ogumi Z (2006) Controlled growth and shape formation of platinum nanoparticles and their electrochemical properties. Electrochim Acta 52:1632–1638
55. Borodko Y, Jones L, Lee H, Frei H, Somorjai G (2009) Spectroscopic study of tetradecyltrimethylammonium bromide Pt-C(14)TAB nanoparticles: structure and stability. Langmuir 25:6665–6671
56. Kim C, Kim SS, Yang S, Han JW, Lee H (2012) In situ shaping of Pt nanoparticles directly overgrown on carbon supports. Chem Commun 48:6396–6398
57. San BH, Kim S, Moh SH, Lee H, Jung DY, Kim KK (2011) Platinum nanoparticles encapsulated by aminopeptidase: a multifunctional bioinorganic nanohybrid catalyst. Angew Chem Int Ed Engl 50:11924–11929
58. Sonstrom P, Arndt D, Wang XD, Zielasek V, Baumer M (2011) Ligand capping of colloidally synthesized nanoparticles—a way to tune metal-support interactions in heterogeneous gas-phase catalysis. Angew Chem Int Ed Engl 50:3888–3891
59. Mostafa S, Behafarid F, Croy JR, Ono LK, Li L, Yang JC, Frenkel AI, Cuenya BR (2010) Shape-dependent catalytic properties of Pt nanoparticles. J Am Chem Soc 132:15714–15719
60. Kim C, Min M, Chang YW, Yoo KH, Lee H (2010) Chemical and thermal stability of Pt nanocubes synthesized with various surface-capping agents. J Nanosci Nanotechnol 10:233–239
61. Joo SH, Park JY, Tsung CK, Yamada Y, Yang PD, Somorjai GA (2009) Thermally stable Pt/mesoporous silica core-shell nanocatalysts for high-temperature reactions. Nat Mater 8:126–131

Chapter 3
Non-Colloidal Nanocatalysts Fabricated with Nanolithography and Arc Plasma Deposition

Sang Hoon Kim and Jeong Young Park

3.1 Introduction

In this chapter, we discuss the most recent advances in the preparation of nanocatalysts via dry processes. We describe the fabrication of metal nanoparticles using lithography and the synthesis of catalytic nanoparticles using noncolloidal techniques, including plasma deposition and lithographical techniques. Synthesis of oxide-supported metal catalysts via wet-chemical processes is well known in heterogeneous catalysis [1–3]. Impregnation, coprecipitation, deposition-precipitation, ion exchange, sol–gel, and colloidal processes are typical examples of wet processes. Typically, precursors of the active catalyst materials are dissolved and reacted in an aqueous or organic solution and the solution is mixed with ceramic supports to prepare the oxide-supported metal catalysts. In general, the wet-chemically produced oxide-supported metal catalysts need to undergo annealing processes at elevated temperature in order to eliminate the organic materials required for the wet processes, such as solvent, surfactant, or capping agents [4–6]. The annealing process can cause oxidation of the catalyst metal particles, causing catalytic activity deterioration. In order to overcome the shortcomings of wet-chemical processes, direct vaporization of metallic materials to deposit active materials on ceramic

---

S.H. Kim (✉)
Center for Materials Architecturing, Korea Institute of Science and Technology (KIST), Seoul 136-791, Republic of Korea

School of Science, University of Science and Technology (UST), Daejeon 305-333, Republic of Korea
e-mail: kim_sh@kist.re.kr

J.Y. Park
Graduate School of EEWS (WCU) and NanoCentury KI, Korea Advanced Institute of Science and Technology (KAIST), Daejeon, Republic of Korea

Center for Nanomaterials and Chemical Reactions, Institute for Basic Science, Daejeon 305-701, Republic of Korea

J.Y. Park (ed.), *Current Trends of Surface Science and Catalysis*,
DOI 10.1007/978-1-4614-8742-5_3,

supports has drawn considerable interest due to its simplicity, high reproducibility, and the possibility for large-scale production. Examples of such dry synthesis processes for nanocatalyst production are arc plasma deposition (APD) [7–9], e-beam lithography [10, 11], and laser vaporization [12, 13]. In this chapter, we introduce APD and nanolithography technologies for preparing catalyst materials and discuss recent advances in their application.

3.2 Nanocatalysts Fabricated with Lithography

3.2.1 Nanolithography for Fabrication of Nanodots and Nanowires

Lithography-based nanocatalyst fabrication is one of the main techniques developed for the production of catalysts with high throughput [14–16]. It has the advantage of precise control of particle size and interparticle distance. The two-dimensional (2D) array of nanocatalysts produced via lithography is also highly monodispersed. Lithography-based nanocatalysts can be formed on any substrate; therefore, it can form a controlled oxide–metal interface, which offers opportunities for studying the role of the interface between the catalytically active phase and the support in catalytic reactions. Moreover, a fabricated 2D array of nanodots or nanowires can be easily cleaned and crystallized for catalyst studies with various surface treatments.

Most importantly, the nanolithography routes exemplified in this section are applicable to the fabrication of any other 2D nanocatalysts on different substrates. The simplest route is electron beam lithography (EBL) [17–19], which utilizes high-resolution pattern writing with a focused electron beam, followed by electron-sensitive resist/etching. It can fabricate nanoparticles with a size of ~10 nm. However, nanofabrication with EBL is limited by low throughput and high cost. A new method called size reduction lithography (SRL) [20] can reduce the mold from 0.6 μm polysilicon to ~7 nm silicon nanowire. The nanowire pattern is transferred into polymethyl methacrylate (PMMA) under high pressure and high temperature using nano imprint lithography (NIL). A thermal oxide layer formed by oxygen–plasma etching upon the residual PMMA is then removed. In this way, a nanoscale mold is fabricated. Figure 3.1 presents the multiplication of pattern density by SRL. Pt atoms can be deposited by electron beam evaporation to form Pt nanowires. Thermal treatment in vacuum, hydrogen, or oxygen crystallizes the Pt nanowires [21, 22]. The major contaminant, carbon from PMMA, can be removed by thermal oxidation under low pressure (1×10^{-6} Torr) of NO_2 at 573 K. The adsorbed oxygen remaining after the carbon removal step can be removed by converting CO into CO_2.

Another method for fabricating catalytic nanodots is called mold-to-mold cross imprint (MTMCI) [24]. This technique is capable of producing high areal density nanodots of any metal on any surface. It includes three main steps. First, a silicon

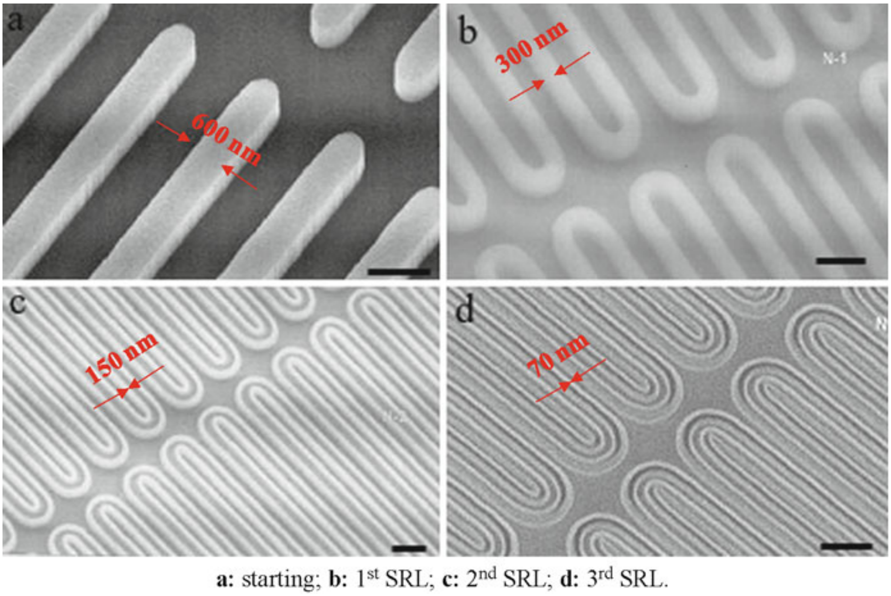

Fig. 3.1 Multiplication of pattern density by size reduction lithography. (**a**) After patterning a sacrificial poly-Si layer; (**b**) after SiO_2 deposition, a SiO_2 spacer etch using CF_4 plasma, and removal of the sacrificial poly-Si by KOH; (**c**) after poly-Si deposition, poly-Si spacer etch by Cl_2 and HBr, and removal of SiO_2 by HF; and (**d**) after SiO_2 deposition, SiO_2 spacer etch by CF_4 plasma, and removal of sacrificial poly-Si by KOH. Thus, 8 lines with a line width of 70 nm and interline spacing of 80 nm were generated after threefold reduction lithography. The scale bars in all images are 1 μm. (Reprinted with permission from ref. [23]. © Springer.)

wire mold is fabricated using spacer lithography. Second, a MTMCI technique is used to convert the silicon spacer nanowires into silicon nanopillars. The principle of the second step is to pattern a silicon spacer nanowire mold with another nanowire mold by imprinting one mold placed perpendicularly onto the other. Figure 3.2a shows the protocol for the fabrication of a silicon nanodot model using the MTMCI technique. In the second step, an array of silicon nanopillars is fabricated at the intersection of the silicon and chromium nanowires by etching the silicon. The silicon nanopillars thus formed have a size of 15 × 30 × 250 nm (width × height × length). Figure 3.2b is an array of silicon nanopillars, which acts as the final mold for fabricating the 2D catalytic nanodots on the substrate. The third step is imprinting the Pt nanodots (Fig. 3.3). The silicon nanopillar mold is imprinted into a PMMA layer on silicon oxide layers formed naturally on a commercially available silicon wafer. A thin layer of Cr is deposited via angled evaporation as a hard mask for the PMMA mold. Then, Pt atoms are deposited into the uncovered nanowell, forming Pt nanodots with dimensions of 15 × 30 × 5 nm. Figure 3.2c is an array of Pt nanodots on silicon oxide after removal of the residual PMMA. Compared to the cleaning and crystallization of Pt nanowires fabricated through SRL, similar cleaning routes [21, 22] are used for cleaning and crystallization of the Pt nanodots.

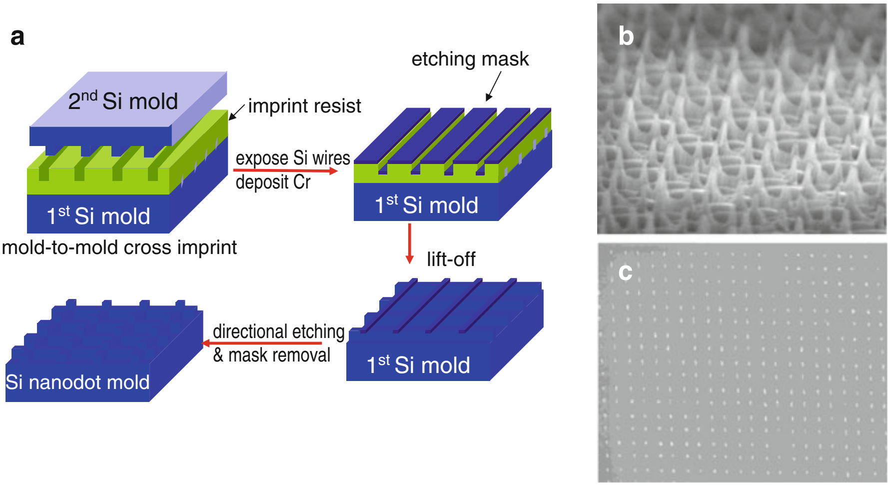

Fig. 3.2 (**a**) Scheme of mold-to-mold cross imprint (MTMCI) to fabricate a nanopillar mold. (**b**) SEM of a nanopillar mold (each nanopillar: 15 × 30 × 250 nm). (**c**) A homogeneous array of Pt nanodots (each nanodot: 15 × 30 × 5 nm) made by MTMCI. (Reprinted with permission from ref. [23]. © Springer.)

Fig. 3.3 Scheme of nanoimprint lithography. (Reprinted with permission from ref. [23]. © Springer.)

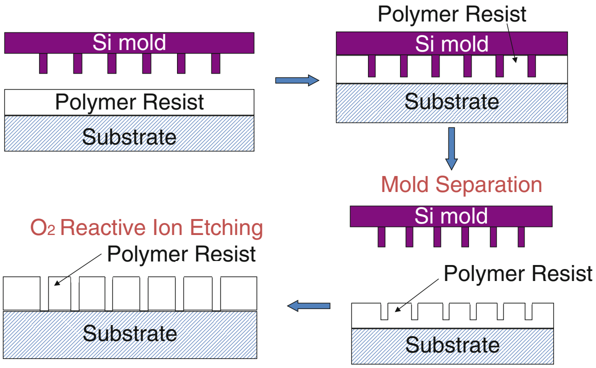

3.2.2 Catalytic Properties of Nanowires Fabricated with Lithography

Dense arrays of platinum nanowires deposited on the oxide thin-film surfaces of ZrO_2, SiO_2, Al_2O_3, and CeO_2 are fabricated by combining lithographic nanofabrication and nanoimprint technology [16]. These nanowire arrays have been used to study the effects of oxide support on the catalytic oxidation of CO. Figure 3.4 shows

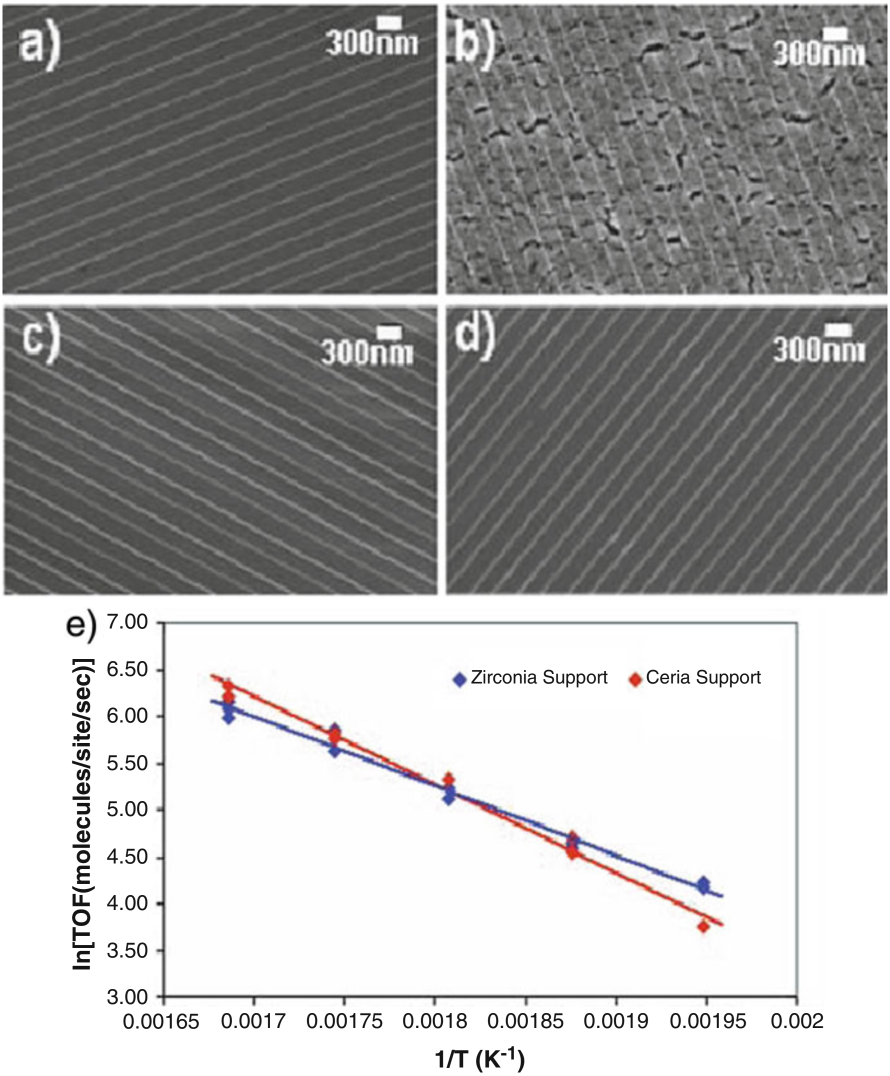

Fig. 3.4 SEM images of 20 nm wide Pt nanowires on different oxide supports. All wires are 5 nm in height. (**a**) Silica support, (**b**) ceria support, (**c**) alumina support, and (**d**) zirconia support. (**e**) Arrhenius plots measured for CO oxidation reactions on zirconia- and ceria-supported Pt nanowire arrays. (Reprinted with permission from ref. [16]. © Springer.)

SEM images of the nanowire arrays on different oxides. From the SEM images, the typical dimensions of a single platinum nanowire are 20 × 5 × 12 nm. Catalytic oxidation of CO to CO_2 over the various catalyst arrays was carried out at temperatures of 513–613 K. Figure 3.4e shows Arrhenius plots for the reaction on zirconia- and ceria-supported samples. Apparent activation energies for the zirconia- and ceria-supported wire arrays are 14.6 ± 0.2 and 18.8 ± 0.2 kcal/mol, respectively. The nanowires on silica have an activation energy of 12.6 ± 0.2 kcal/mol. Therefore, the nanocatalysts composed of metal nanowires and oxide supports reveal support dependence for both reaction turnover frequency (TOF) and the measured activation energy.

3.3 Nanocatalysts Fabricated Via Arc Plasma Deposition

3.3.1 Introduction to Arc Plasma Deposition

APD, or cathodic arc deposition, has been traditionally applied for preparing dense thin films of corrosion-resistant, protective, and decorative coatings, such as TiN, TiC, and CrN [25–27]. This method is usually regarded as physical vapor deposition (PVD), but it differs from other PVD methods in that energetic plasma ions condense to form dense films in APD, while in other PVD methods, it is the vapor of neutral atoms that condense [25].

In APD, very high current densities (~10^{12} A/m^2) let the cathode material directly evaporate from the surface. A plasma discharge then generates cathodic arcs within the vapor. The size of the arc spot is typically a few microns [26]. The plasma generated at the arc spots expands rapidly into the ambient vacuum. The final velocities of the generated ions are ~1–2 × 10^4 m/s and are largely independent of the cathode materials. These velocities correspond to the kinetic energies of about 20 eV for light elements and 200 eV for heavy elements [25]. The biggest obstacle for implementing the APD method has been that macrodroplets are also emitted simultaneously from the cathode spot along with the plasma ions and electrons. The droplets adhere to the film and act as defects. Another problem of the APD method is that it is not easy to control the arc generation location [28, 29]. In order to reduce or eliminate macrodroplets, various methods have been tried, such as steered arc [30], distributed arc [31], and filters [28, 32, 33].

Among these trials, pulsed coaxial APD offers macrodroplet-free plasma deposition without large-scale conventional magnetic filter systems in the vacuum chamber. Chun et al. developed the pulsed coaxial APD system shown in Fig. 3.5a [34]. A high-voltage pulse (a few kilovolts, tens of microseconds) is applied between the trigger and cathode cylinder. This voltage induces dielectric breakdown and trigger discharge. Then, the main discharge occurs sequentially between the cathode spot and the cylindrical anode, where a voltage of 50–300 V is applied. During arc discharge, a very large current (~2,000 A) flows through the cathode (Fig. 3.5b). Due to the large magnetic field induced by the current, plasma ions and electrons fly away from the cathode towards the substrate. Meanwhile, any macrodroplets, which are neutral, fly towards the anode and adhere to the anode surface. Because the duration of the arc is less than 1 ms, heating of the cathode material and generation of macrodroplets are minimized. As the arc plasma is generated between the cathode

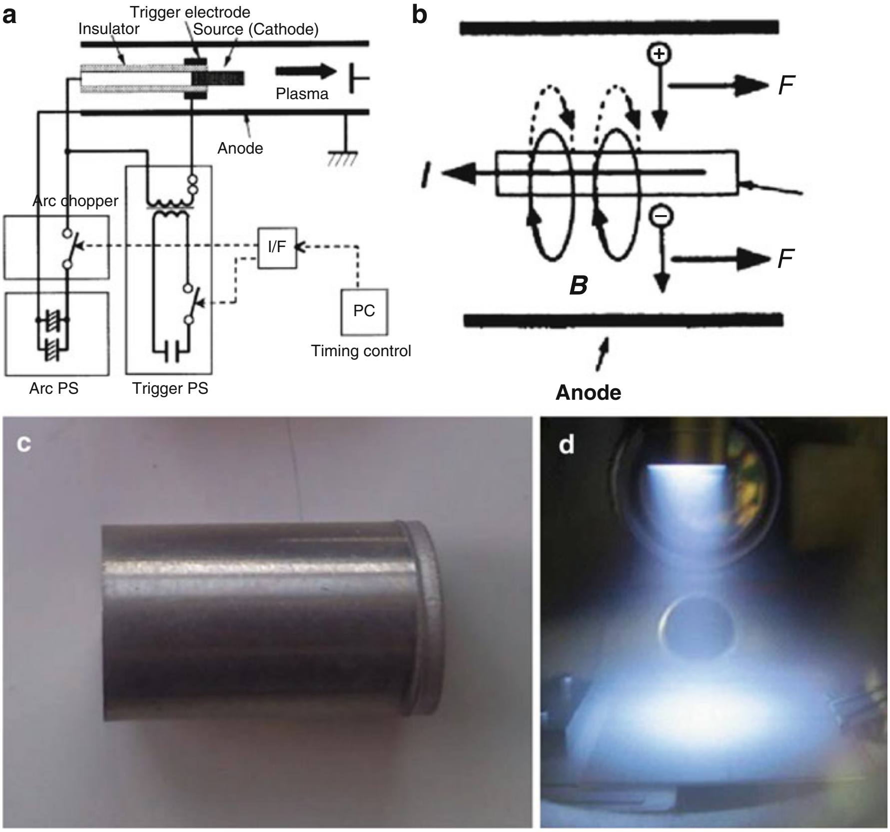

Fig. 3.5 Schematic diagram of (**a**) coaxial pulsed arc plasma deposition system and (**b**) quasi-stationary model of a generated arc plasma. *I* is the arc current, *B* is the magnetic field induced by *I*, and *F* is the electromagnetic force applied to the plasma ions and electrons. (Reprinted with permission from ref. [34]. © 2000 Elsevier Science S.A.) (**c**) Used cathode cylinder made of palladium. The plasma is generated from the circular rim on the right side. (**d**) A generated arc plasma. The plasma beam accelerates towards bottom of the image. (Courtesy of Ulvac-Riko, Inc.)

and anode surfaces, arc spots are limited to the protruded rim of the cathode cylinder. For example, a slightly used cathode cylinder is shown in Fig. 3.5c. In the figure, the rim on the right is used for plasma generation. Therefore, by controlling the length of the protrusion, arc spots can be limited to the rim of the protrusion. Figure 3.5d shows an actual arc plasma beam generated from the cathode (top). The accelerated plasma beam hits the bottom, where catalyst support materials are placed. In the case of powder-type catalyst supports, the powder is constantly stirred for effective dispersion of the deposited catalyst nanoparticles on the powder. In case of thin-film type catalyst supports, no stirring is needed.

This pulsed coaxial APD has been used to fabricate multilayer structures with subnanometer thickness control [34–36] without the need of filters, such as curved

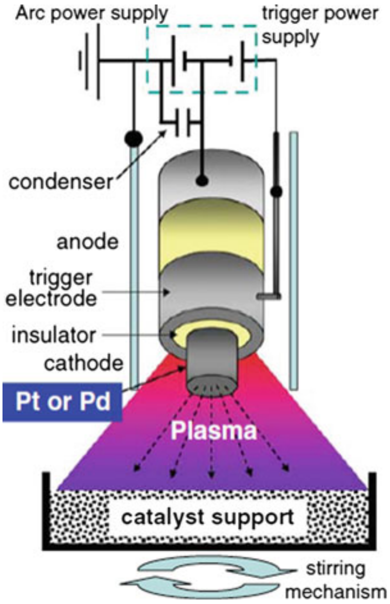

Fig. 3.6 Schematic of arc plasma deposition of nanoparticles on a catalyst support. In the case of powder-type catalyst supports, the powder is constantly stirred for effective dispersion. In the case of thin-film type catalyst supports, no stirring is needed. (Reprinted with permission from ref. [38]. © 2009 Springer Science+Business Media, LLC.)

ducts, to remove macrodroplets [37]. Another advantage of pulsed coaxial APD is that each pulse generates a very large number of nanoparticle ions a few nanometer in size (~1–5 nm). The amount of deposited materials or, for the two-dimensional case, coverage of the deposited materials can be easily controlled by the number of pulses.

As long as the material is solid and can be formed as a cylindrical cathode target for an APD system, any material can be dry deposited as nanoparticles without going through wet-chemical processes. Those deposited nanoparticles can be used as seed particles for growing nanotubes [39, 40] or for decorating underlying nanostructures to form complex nanocomposites with enhanced functionalities [41]. Among these new possibilities, using APD to dry deposit nanoparticles as nanocatalyst materials has drawn significant attention and interest is rapidly growing [42]. Figure 3.6 shows a schematic of depositing catalytic nanoparticles on catalyst supports. It is a dry process in a high vacuum chamber with a base pressure of ~10^{-7} Torr. Nanoparticles generated from the cathode surface are accelerated towards the bottom due to the high magnetic field induced by the high current flowing along the cathode axis, as discussed above.

Figure 3.7 shows a TEM image of individual Pt nanoparticles deposited by APD on an amorphous carbon film substrate. The dark dots are Pt nanoparticles and the gray background is the amorphous carbon substrate. The nanoparticles are ~1–5 nm in size and lattice structures are clearly seen in the particles. In the following sections, recent applications of APD for nanocatalyst preparation are discussed.

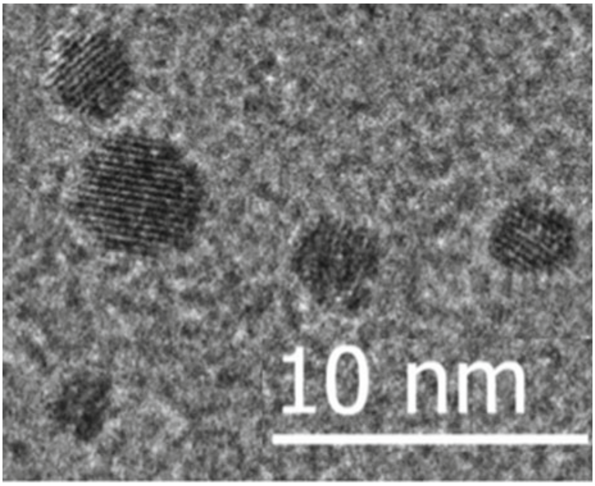

Fig. 3.7 Arc plasma-deposited Pt nanoparticles on amorphous carbon

3.3.2 Nanocatalysts on Two-Dimensional Supports Using APD

As a model for metal–oxide hybrid catalysts using strong metal–support interactions (SMSI) [43], thin-film type substrates have been employed to disperse catalyst nanoparticles [44–46]. Recently, Qadir et al. compared the catalytic activity of Pt nanoparticles prepared by conventional wet-chemistry methods and by APD on TiO_2 thin film substrates [9]. In the study, ~150 nm thick TiO_2 films were sputtered on Si wafers and used as catalytic supports. Approximately the same amount of Pt (0.12 mg) was deposited using APD (150 pulses, 100 V arc discharge voltage 1,080 μF discharge condenser capacity) and conventional impregnation. For impregnation, potassium hexachloroplatinate (K_2PtCl_6) was dissolved in distilled water and droplets were dropped and dried, then the sample was annealed at 500 °C for 5 h to remove organic substances. The catalytic activity was tested using CO oxidation in an ultra-high vacuum (UHV) batch reactor. As can be seen in Fig. 3.8, the catalytic activity of the dry-deposited Pt nanoparticles on the TiO_2 films was higher than that of the impregnated ones. The 150-pulse APD Pt was enough to have 100 % surface coverage. Therefore, it was assumed that the deposited Pt is thicker than one monolayer and that the layer is flat. From these assumptions, the number of active sites on the deposited Pt layer was calculated, and the turnover frequency (TOF) (Fig. 3.8a) and activation barrier for the reaction (Fig. 3.8b) were measured.

Still, it is not easy to find clues for the observed difference in catalytic activities from only these structural aspects. The XPS analysis in Fig. 3.9 shows that the impregnated and annealed Pt nanoparticles have inactive bulk oxide states, while the APD Pt nanoparticles are purely metallic. This oxide formation during annealing is considered the main reason for the difference in the catalytic activities. In order to improve catalytic activity, impregnated and annealed Pt nanoparticles on TiO_2 films were reduced under 100 Torr of hydrogen at 250 °C for 1 h to decrease the oxidation state. However, the catalytic activity after reduction was still lower than that of the

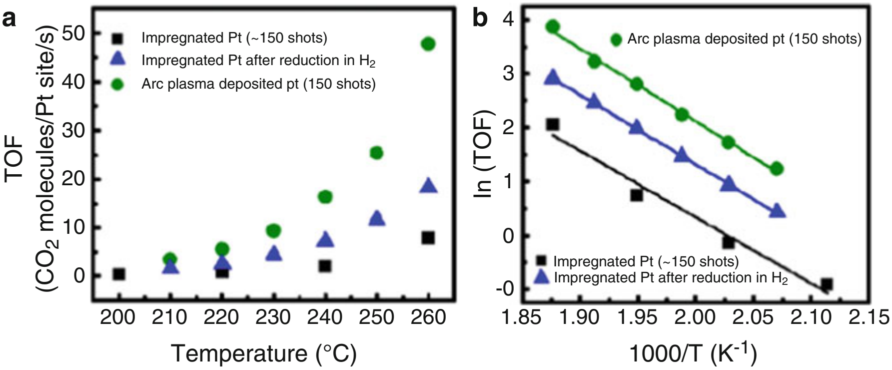

Fig. 3.8 Comparison of the catalytic activity of Pt nanoparticles on TiO_2 films prepared by APD and impregnation. (Reprinted with permission from ref. [9]. © 2012 American Chemical Society.)

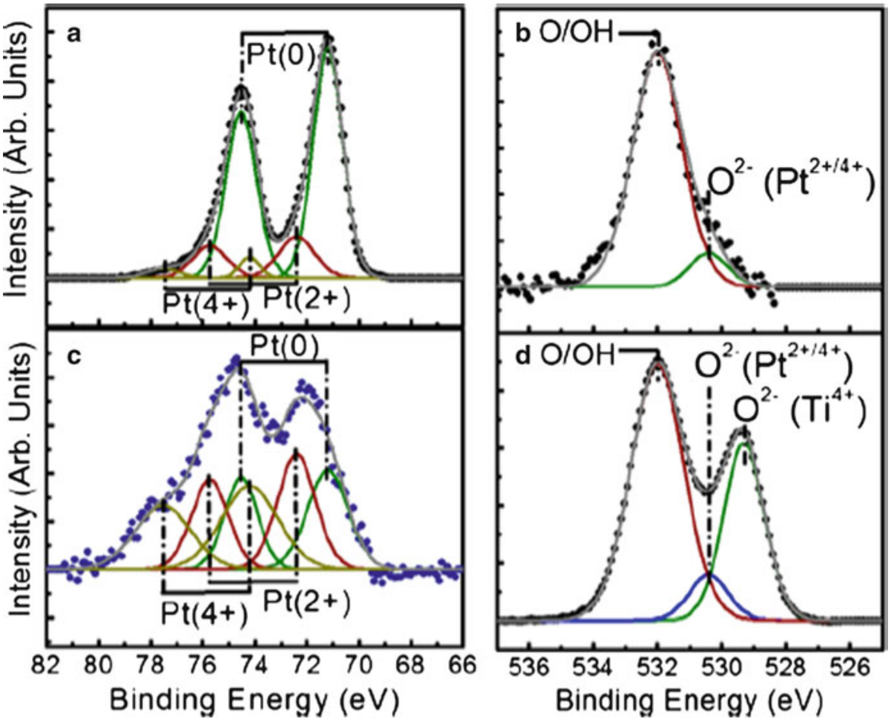

Fig. 3.9 XPS measurement of (**a**) Pt 4*f* and (**b**) O 1*s* peaks of 150 pulse APD Pt nanoparticles and (**c**) Pt 4*f* and (**d**) O 1*s* peaks of a similar amount of impregnated and annealed Pt nanoparticles on TiO_2 films. (Reprinted with permission from ref. [9]. © 2012 American Chemical Society.)

Fig. 3.10 Comparison of the HD formation rates vs. mean gold particle size for the same amount of deposited gold on $TiO_2(110)$. (Reprinted with permission from ref. [47]. © 2009 Wiley-VCH Verlag.)

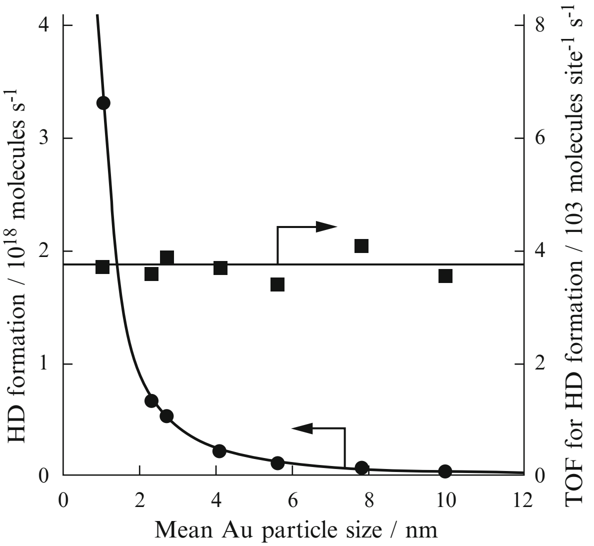

APD Pt nanoparticles (Fig. 3.8a). Furthermore, XPS survey spectra showed a very small peak for K on the impregnated Pt nanoparticles. The presence of K ions may have blocked active sites too [9]. This study showed that APD enabled the deposition of metallic Pt nanoparticles on TiO_2 films with neither oxidation due to annealing nor impurities commonly found in conventional wet-chemical processes.

Fujitani et al. examined hydrogen molecule dissociation at low temperature (425 K) on gold nanoparticles deposited on $TiO_2(110)$ single crystal surface via APD [47]. In the study, they deposited the same amount of gold nanoparticles with average diameters of ~1–10 nm by changing the discharge condenser capacity between 360 and 2,200 μF. They then exposed the prepared $Au/TiO_2(110)$ surface to the H_2 and D_2 exchange reaction and measured the rate of HD formation (Fig. 3.10). The rate of HD formation increased dramatically when the gold particle size was below 2 nm, while the TOF was more or less constant over the entire particle size range. TOFs were calculated by dividing the number of HD molecules formed per second by the total number of gold atoms at the periphery of the gold particles. Based on this measurement, the active sites for H_2 dissociation are along the periphery around the deposited gold particles. This study shows that it is possible to control the size of nanoparticles generated by APD in the nanometer range by controlling the parameters for arc plasma generation.

3.3.3 Nanocatalysts on Three-Dimensional Supports Using APD

For a two-dimensional substrate, we can assume the number of active sites or directly measure the coverage of catalyst particles. Therefore, quantitative analysis

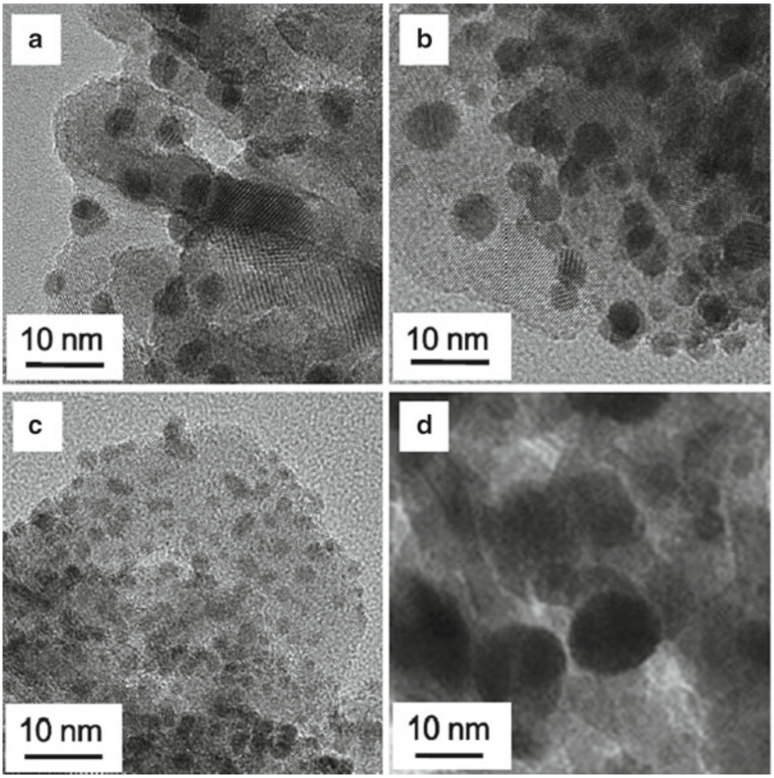

Fig. 3.11 TEM images of APD-deposited gold and platinum nanoparticles on TiO_2 powder. The arc discharge condenser capacity was 1,800 μF. (**a**) Au/TiO_2 at 200 V discharge voltage (**b**) Au/TiO_2 at 300 V discharge voltage (**c**) Pt/TiO_2 at 200 V discharge voltage and (**d**) Au/TiO_2 prepared by sol–gel method for comparison. (Reprinted with permission from ref. [8]. © 2013 Elsevier Science S.A.)

(e.g., TOF and active barrier calculations) is possible, as shown in the previous section, and two-dimensional substrates can be used as model catalyst supports. On the other hand, three-dimensional powder supports are much more widely used in industry, but it is not easy to do quantitative analysis using a powder support. Still, it is important to improve processes to incorporate catalyst nanoparticles on powder support, such as better dispersion of ever smaller nanoparticles or controlling the adhesion strength between catalytic nanoparticles and support powder materials. Recently, Kim et al. studied the catalytic activity of nanometer-sized Au and Pt particles deposited on TiO_2 powder via APD [8]. In the study, they controlled the size of the deposited nanoparticles by changing the arc discharge voltage, *V*, for generating plasma. Figures 3.11 and 3.12 show TEM images and the size distribution of the APD-deposited Au and Pt nanoparticles on TiO_2 powder, respectively. The metallic nanoparticles are seen as dark spots, while the catalyst support TiO_2 powder particles are seen as bright and extended shapes. Nanoparticles deposited by

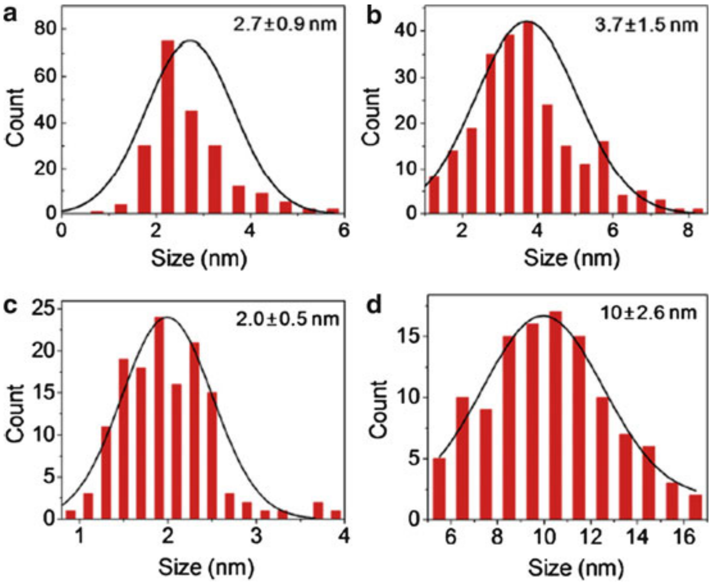

Fig. 3.12 Particle size distributions of the Au/TiO_2 and Pt/TiO_2 particles shown in Fig. 3.9. (**a**)–(**d**) corresponds to those in Fig. 3.9. (Reprinted with permission from ref. [8]. © 2013 Elsevier Science S.A.)

APD tend to increase in size with increasing *V*; this tendency can be seen in Fig. 3.11a, b. Although prepared using the same deposition conditions, the Au and Pt nanoparticles had different sizes (Fig. 3.11a, c). Figure 3.11d shows nanoparticles prepared using the wet-chemical sol–gel method for comparison. The sol–gel-prepared nanoparticles are ~10 nm in size—bigger than those prepared by APD, which are ~2–4 nm in size (Fig. 3.12).

Gold nanoparticles are well known for their high catalytic activity for CO oxidation [48, 49]. On the nanometer scale, the catalytic activity of gold nanoparticles increases with decreasing size [41, 50]. On the other hand, it is known that the catalytic activity of Pt nanoparticles is independent of particle size [49, 51]. The catalytic activity comparison for the samples shown in Fig. 3.13 reflects these tendencies. In the comparison, the overall CO oxidation efficiency followed the order of Au/TiO_2 200 V > Au/TiO_2 300 V > Au/TiO_2 sol–gel > Pt/TiO_2 200 V. Regardless of preparation method, be it dry or wet, particle size is the most important parameter for the catalytic activity of nano-sized gold. On the other hand, Pt/TiO_2 200 V had the lowest catalytic activity, as the catalytic activity was not very different from that of bulk Pt. The catalytic activity of gold increased with decreasing particle size and eventually surpassed Pt. Again, it was possible to control the size of the nanoparticles with the parameters for generating the arc plasma. However, it was within the same materials only. For different materials, the particles differed in size when using the same parameters for arc plasma generation.

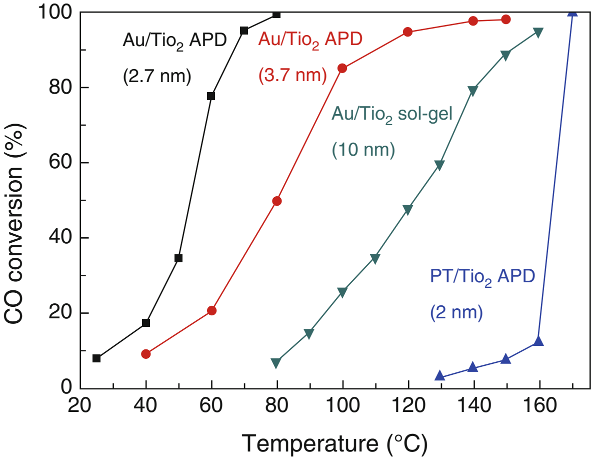

Fig. 3.13 Catalytic activity comparison for Au/TiO_2 and Pt/TiO_2. (Reprinted with permission from ref. [8]. © 2013 Elsevier Science S.A.)

Hinokuma et al. reported a similar study on dispersing Pt and Pd nanoparticles on γ-alumina powder using APD and conventional impregnation. They compared the catalytic activities for CO oxidation [38]. In the study, they found out that the average size of the Pt nanoparticles deposited by APD is ~2.5 nm and the size of the Pd nanoparticles is 6.8 nm. XPS measurements showed that the Pt nanoparticles were metallic regardless of the preparation method. As for the Pd nanoparticles, they were mostly in their oxide form (PdO) when prepared by impregnation. When prepared by APD, however, the metallic Pd had a higher fraction (60 %) than the Pd-oxide (40 %). As the APD process occurs in vacuum and directly vaporizes the metallic cathode materials, the deposited nanoparticles tend to be metallic. Figure 3.14 shows a comparison of the catalytic activities of Pt/alumina and Pd/alumina powders prepared by APD and impregnation. For comparison, they loaded the same amount (0.4 wt%) of Pt and Pd on γ-alumina powder and labeled “apg” for APD preparation and “imp” for impregnation. For the Pt/alumina samples, APD-prepared samples showed higher catalytic activity than impregnation-prepared samples due to their higher dispersion (Fig. 3.14a, *left*). However, after thermal aging in 10 % H_2O/air at 900 °C for 25 h, deactivation was more pronounced for the APD-prepared samples than for the impregnation-prepared sample (Fig. 3.14b, *left*). This observation indicates that the thermal stability of APD-dispersed Pt nanoparticles on γ-alumina is not so good. With TEM, they actually observed sintering of Pt nanoparticles up to 20 nm in size. For the Pd/alumina samples, the situation was somewhat different. The APD-prepared samples showed a slightly lower catalytic activity than the impregnation-prepared samples (Fig. 3.14a, *right*). They explained this difference by the higher catalytic activity of PdO than metallic Pd [52].

Hinokuma et al. continued their study to include prepared bimetallic Pd-Fe nanoparticles on ceria powder using APD and investigated their catalytic activity for CO oxidation [53]. In the study, they prepared bimetallic nanoparticles using two plasma guns in a chamber, one for Pd and one for Fe. They prepared the

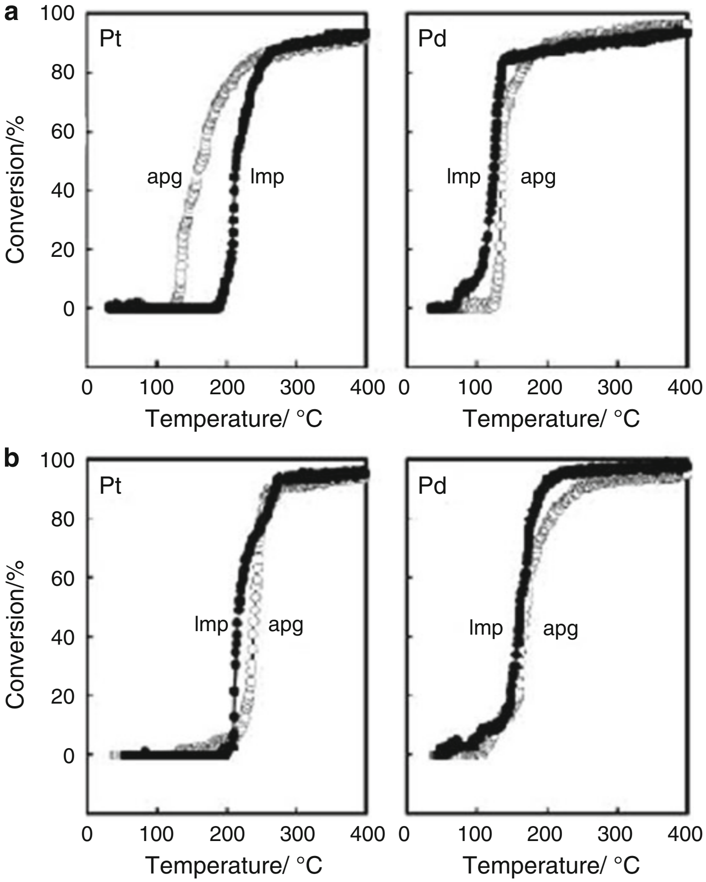

Fig. 3.14 Catalytic activity comparison for Pt/alumina and Pd/alumina (**a**) as prepared and (**b**) after thermal aging. Reprinted with permission from ref. [38]. © 2009 Springer Science+Business media, LLC

bimetallic nanoparticles using the two cathode guns synchronously (syn) and asynchronously (asyn). Synchronous pulses of Pd and Fe resulted in Pd-Fe bimetallic alloy nanoparticles, while asynchronous pulses resulted in individual Pd and Fe nanoparticles on the ceria support. They found out that Pd-Fe bimetallic nanoparticles showed slightly higher catalytic activity than the individual metal nanoparticles (Fig. 3.15a). They attributed these findings to better dispersion and a higher metallic fraction of Pd in the Pd-Fe alloy nanoparticles on ceria. The catalytic activity increased after thermal aging for both the synchronous- and asynchronous-prepared samples (Fig. 3.15b). The authors argued that, in contrast to the alumina case above, thermal aging helped stabilize the Pd–O–Ce bonding, keeping the dispersion of nanoparticles intact, which enabled higher catalytic activity after thermal aging [54].

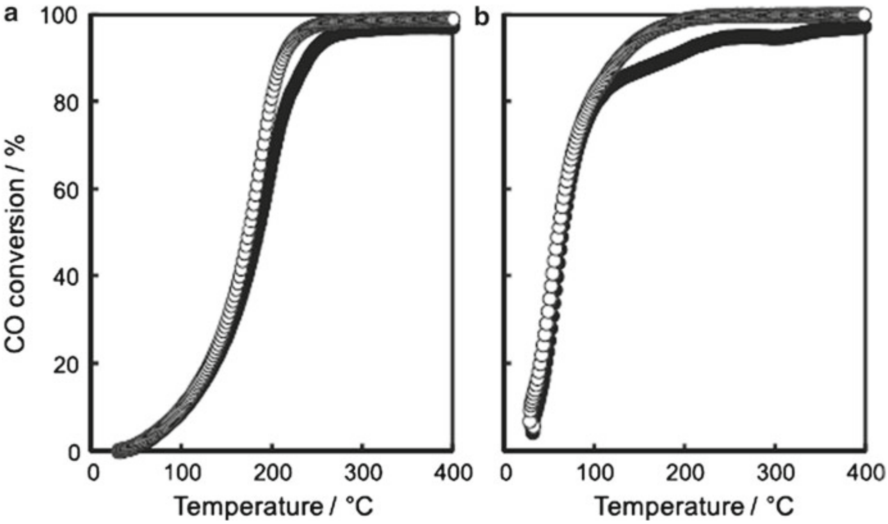

Fig. 3.15 Comparison of catalytic activity for Pd-Fe on ceria powder by APD. (*Open circles*) Pd-Fe/ceria (syn) and (*filled circles*) Pd-Fe/ceria (asyn), (**a**) before and (**b**) after thermal aging. Reprinted with permission from ref. [53]. © 2013 Elsevier Science S.A.

3.3.4 Some New Applications for Nanoparticles Prepared Via APD

Other than the familiar gas-phase catalytic reactions, examples of APD-deposited nanoparticle applications in some new fields are also emerging. In order to investigate photocatalytic antibacterial effects, Oveisi et al. deposited silver nanoparticles on mesoporous anatase titania films using APD [55]. The size of the deposited nanoparticles ranged between 3.7 and 5.6 nm by changing the number of arc plasma pulses. When a droplet of *E. coli* suspension is dropped on top of Ag nanoparticles dispersed on titania and irradiated with UV light, the survival fraction of *E. coli* cells decreased as the nanoparticle size decreased. In other words, smaller Ag nanoparticles were more effective for inactivating the bacteria. For sensing applications, Ito et al. reported detection of hydrogen peroxide using APD-deposited Pt nanoparticles on carbon electrodes in an electrochemical setup [56]. In the study, they varied the coverage of the Pt nanoparticles on glassy carbon surfaces by incrementally increasing the number of plasma pulses from 5 to 20. The average particle size was 2.7 nm. After annealing the Pt-deposited glassy carbon, only the Pt nanoparticles deposited using five APD pulses remained as individual particles, while Pt particles deposited using more APD pulses coalesced to form connected island shapes. After annealing, electrodes with individual Pt nanoparticles showed better sensitivity than electrodes with connected Pt islands for hydrogen peroxide detection.

3.4 Summary and Outlook

In this chapter, we have discussed the most recent advances in the preparation of catalyst nanoparticles on catalyst support using dry processes. These two-dimensional model catalyst arrays fabricated using nanolithography have been used to study the support dependence of CO oxidation reaction kinetics; they indicate that the most important factor affecting TOF is the interaction of the platinum and the support. The APD method was traditionally used for preparation of dense protective coating layers. However, with the advent of pulsed APD, new applications for preparing metallic nanoparticles in a direct and dry process are emerging. So far, applications are limited to the much studied gas-phase reactions—mostly the model CO oxidation reaction. However, we have also noticed that the scope of applications is widening, too (e.g., liquid-phase photocatalysts, electrode materials for fuel cells and secondary batteries, and sensor applications). The biggest advantage of APD is that it is relatively easy to generate a large number of particles a few nanometer in size. It is also easy to control the size of the generated nanoparticles, on the nanometer scale, by controlling APD parameters, such as the number of arc plasma pulse shots, arc discharge voltage, and arc discharge condenser capacitance. As for substrates for deposition, the APD method provides a simple and easy method for direct and dry deposition of metallic nanoparticles on a variety of substrates, such as two-dimensional thin films and three-dimensional powders. Therefore, the possibilities for new applications are enormous. We assume that more attention will be paid to this method with respect to generating dry nanoparticles for many new applications with the central focus remaining on catalyst materials.

Acknowledgments This work was supported by a grant from the future R&D Program funded by Korea Institute of Science and Technology (2E23900). This work was supported by the WCU (World Class University) program (31-2008-000-10055-0 and 2012R1A2A1A01009249) through the National Research Foundation, the Research Center Program (CA1201) of IBS (Institute for Basic Science), and from the Fundamental R&D Program for Core Technology of Materials funded by the Ministry of Knowledge Economy, Republic of Korea.

References

1. Ertl G, Knozinger H, Weitkamp J (1999) Preparation of solid catalysts. Wiley-VCH, Weinheim
2. Regalbuto JR (2007) Handbook of catalyst preparation. Taylor & Francis, Boca Raton
3. Somorjai GA, Park JY (2008) Colloid science of metal nanoparticle catalysts in 2D and 3D structures. Challenges of nucleation, growth, composition, particle shape, size control and their influence on activity and selectivity. Top Catal 49:126–135
4. Park J, Aliaga C, Renzas JR, Lee H, Somorjai G (2009) The role of organic capping layers of platinum nanoparticles in catalytic activity of CO oxidation. Catal Lett 129:1–6
5. Kuhn JN, Tsung C-K, Huang W, Somorjai GA (2009) Effect of organic capping layers over monodisperse platinum nanoparticles upon activity for ethylene hydrogenation and carbon monoxide oxidation. J Catal 265:209–215

6. Aliaga C, Park JY, Yamada Y, Lee HS, Tsung CK, Yang P, Somorjai GA (2009) Sum frequency generation and catalytic reaction studies of the removal of organic capping agents from Pt nanoparticles by UV-ozone treatment. J Phys Chem C 113:6150–6155
7. Agawa Y, Endo S, Matsuura M, Ishii Y (2010) Multi-functional materials and structures III, Pts 1 and 2, vol 123–125. Advanced materials research. Trans Tech Publications, Switzerland, pp 1067–1070
8. Kim SH, Jung C-H, Sahu N, Park D, Yun JY, Ha H, Park JY (2013) Catalytic activity of Au/TiO_2 and Pt/TiO_2 nanocatalysts prepared with arc plasma deposition under CO oxidation. Appl Catal Gen 454:53–58
9. Qadir K, Kim SH, Kim SM, Ha H, Park JY (2012) Support effect of arc plasma deposited Pt nanoparticles/TiO_2 substrate on catalytic activity of CO oxidation. J Phys Chem C 116: 24054–24059
10. Komanicky V, Iddir H, Chang K-C, Menzel A, Karapetrov G, Hennessy D, Zapol P, You H (2009) Shape-dependent activity of platinum array catalyst. J Am Chem Soc 131:5732–5733
11. Tsirlin T, Zhu J, Grunes J, Somorjai G (2002) AFM and TEM studies of Pt nanoparticle arrays supported on alumina model catalyst prepared by electron beam lithography. Top Catal 19: 165–170
12. Glaspell G, Hassan HMA, Elzatahry A, Abdalsayed V, Samy El-Shall M (2008) Nanocatalysis on supported oxides for CO oxidation. Top Catal 47:22–31
13. Yang Y, Saoud KM, Abdelsayed V, Glaspell G, Deevi S, El-Shall MS (2006) Vapor phase synthesis of supported Pd, Au, and unsupported bimetallic nanoparticle catalysts for CO oxidation. Catal Commun 7:281–284
14. Contreras AM, Grunes J, Yan XM, Liddle A, Somorjai GA (2005) Fabrication of platinum nanoparticles and nanowires by electron beam lithography (EBL) and nanoimprint lithography (NIL): comparison of ethylene hydrogenation kinetics. Catal Lett 100:115–124
15. Contreras AM, Grunes J, Yan XM, Liddle A, Somorjai GA (2006) Fabrication of 2-dimensional platinum nanocatalyst arrays by electron beam lithography: ethylene hydrogenation and CO-poisoning reaction studies. Top Catal 39:123–129
16. Contreras AM, Yan XM, Kwon S, Bokor J, Somorjai GA (2006) Catalytic CO oxidation reaction studies on lithographically fabricated platinum nanowire arrays with different oxide supports. Catal Lett 111:5–13
17. Jacobs PW, Ribeiro FH, Somorjai GA, Wind SJ (1996) New model catalysts: uniform platinum cluster arrays produced by electron beam lithography. Catal Lett 37:131–136
18. Jacobs PW, Wind SJ, Ribeiro FH, Somorjai GA (1997) Nanometer size platinum particle arrays: catalytic and surface chemical properties. Surf Sci 372:L249–L253
19. Yan XM, Contreras AM, Koebel MM, Liddle JA, Somorjai GA (2005) Parallel fabrication of sub-50-nm uniformly sized nanoparticles by deposition through a patterned silicon nitride nanostencil. Nano Lett 5:1129–1134
20. Yan XM, Kwon S, Contreras AM, Koebel MM, Bokor J, Somorjai GA (2005) Fabrication of dense arrays of platinum nanowires on silica, alumina, zirconia and ceria surfaces as 2-D model catalysts. Catal Lett 105:127–132
21. Grunes J, Zhu J, Anderson EA, Somorjai GA (2002) Ethylene hydrogenation over platinum nanoparticle array model catalysts fabricated by electron beam lithography: determination of active metal surface area. J Phys Chem B 106:11463–11468
22. Grunes J, Zhu J, Yang MC, Somorjai GA (2003) CO poisoning of ethylene hydrogenation over Pt catalysts: a comparison of Pt(111) single crystal and Pt nanoparticle activities. Catal Lett 86:157–161
23. Somorjai GA, Tao F, Park JY (2008) The nanoscience revolution: merging of colloid science, catalysis and nanoelectronics. Top Catal 47:1–14
24. Kwon S, Yan XM, Contreras AM, Liddle JA, Somorjai GA, Bokor J (2005) Fabrication of metallic nanodots in large-area arrays by mold-to-mold cross imprinting (MTMCI). Nano Lett 5:2557–2562
25. Anders A (2008) Cathodic arcs: from fractal spots to energetic condensation. Springer, New York

26. Randhawa H (1988) Cathodic arc plasma deposition technology. Thin Solid Films 167: 175–185
27. Randhawa H, Johnson PC (1987) A review of cathodic arc plasma deposition processes and their applications. Surf Coat Technol 31:303–318
28. Sanders DM, Anders A (2000) Review of cathodic arc deposition technology at the start of the new millennium. Surf Coat Technol 133:78–90
29. Takikawa H, Tanoue H (2007) Review of cathodic arc deposition for preparing droplet-free thin films. IEEE Trans Plasma Sci 35:992–999
30. Swift PD (1996) Macroparticles in films deposited by steered cathodic arc. J Phys D: Appl Phys 29:2025–2031
31. Shinno H, Fukutomi M, Fujitsuka M, Okada M (1985) In situ coating of low-z materials by reactive vacuum arc-deposition with a stabilized arc cathode. J Nucl Mater 133:749–753
32. Anders A (1999) Approaches to rid cathodic arc plasmas of macro- and nanoparticles: a review. Surf Coat Technol 120:319–330
33. Martin PJ, Bendavid A (2001) Review of the filtered vacuum arc process and materials deposition. Thin Solid Films 394:1–15
34. Chun S-Y, Chayahara A (2000) Pulsed vacuum arc deposition of multilayers in the nanometer range. Surf Coat Technol 132:217–221
35. Chun SY, Chayahara A (2000) Enhanced interfacial roughness in metallic multilayers prepared by pulsed cathodic arc deposition. Surf Coat Technol 127:282–284
36. Chun SY, Chayahara A, Posselt M (2004) Limitations on ultra-thin multilayers: pulsed cathodic arc and computer simulation. Surf Coat Technol 182:171–174
37. Li LH, Lu QY, Fu RKY, Chu PK (2008) Thickness uniformity and surface morphology of Fe, Ti, and Hf films produced by filtered pulsed cathodic arc deposition. Surf Coat Technol 203:887–892
38. Hinokuma S, Murakami K, Uemura K, Matsuda M, Ikeue K, Tsukahara N, Machida M (2009) Arc plasma processing of Pt and Pd catalysts supported on gamma-Al_2O_3 powders. Top Catal 52:2108–2111
39. Hiramatsu M, Nagao H, Taniguchi M, Amano H, Ando Y, Hori M (2005) High-rate growth of films of dense, aligned double-walled carbon nanotubes using microwave plasma-enhanced chemical vapor deposition. Jpn J Appl Phys Part 2—Lett Express Lett 44:L693–L695
40. Phokharatkul D, Ohno Y, Nakano H, Kishimoto S, Mizutani T (2008) High-density horizontally aligned growth of carbon nanotubes with CO nanoparticles deposited by arc-discharge plasma method. Appl Phys Lett 93:053112–053113
41. Chen JH, Lu GH (2006) Controlled decoration of carbon nanotubes with nanoparticles. Nanotechnology 17:2891–2894
42. Takei T, Akita T, Nakamura I, Fujitani T, Okumura M, Okazaki K, Huang J, Ishida T, Haruta M (2012). Heterogenous catalysis by gold. In: Gates Bruce C, Jentoft Friederike C (eds) Advances in catalysis, vol 55. Academic Press, Waltham, MA, USA, pp 1–126
43. Haller GL, Resasco DE (1989) Metal-support interaction: group VIII metals and reducible oxides. Adv Catal 36:173–235
44. Belton DN, Sun YM, White JM (1986) Chemisorption of CO, NO, and H_2 on transition metal-titania thin film model catalysts. J Catal 102:338–347
45. Grunwaldt J-D, Baiker A (1999) Gold/titania interfaces and their role in carbon monoxide oxidation. J Phys Chem B 103:1002–1012
46. Hayek K, Fuchs M, Klötzer B, Reichl W, Rupprechter G (2000) Studies of metal—support interactions with "real" and "inverted" model systems: reactions of CO and small hydrocarbons with hydrogen on noble metals in contact with oxides. Top Catal 13:55–66
47. Fujitani T, Nakamura I, Akita T, Okumura M, Haruta M (2009) Hydrogen dissociation by gold clusters. Angew Chem Int Ed 48:9515–9518
48. Valden M, Lai X, Goodman DW (1998) Onset of catalytic activity of gold clusters on titania with the appearance of nonmetallic properties. Science 281:1647–1650
49. Haruta M (2002) Catalysis of gold nanoparticles deposited on metal oxides. CATTECH 6:102–115

50. Anpo M, Onaka M, Yamashita H (2003) Science and technology in catalysis 2002: proceedings of the fourth Tokyo conference on advanced catalytic science and technology, Kodansha, Tokyo, 14–19 July 2002
51. Boronat M, Corma A (2010) Origin of the different activity and selectivity toward hydrogenation of single metal Au and Pt on TiO_2 and bimetallic Au-Pt/TiO_2 catalysts. Langmuir 26:16607–16614
52. Farrauto RJ, Hobson MC, Kennelly T, Waterman EM (1992) Catalytic chemistry of supported palladium for combustion of methane. Appl Catal Gen 81:227–237
53. Hinokuma S, Katsuhara Y, Ando E, Ikeue K, Machida M (2013) Pd-Fe/CeO_2 bimetal catalysts prepared by dual arc-plasma deposition. Catal Today 201:92–97
54. Hinokuma S, Fujii H, Okamoto M, Ikeue K, Machida M (2010) Metallic Pd nanoparticles formed by Pd-O-Ce interaction: a reason for sintering-induced activation for CO oxidation. Chem Mater 22:6183–6190
55. Oveisi H, Rahighi S, Jiang XF, Agawa Y, Beitollahi A, Wakatsuki S, Yamauchi Y (2011) Improved inactivation effect of bacteria: fabrication of mesoporous anatase films with fine Ag nanoparticles prepared by coaxial vacuum arc deposition. Chem Lett 40:420–422
56. Ito T, Kunimatsu M, Kaneko S, Hirabayashi Y, Soga M, Agawa Y, Suzuki K (2012) High performance of hydrogen peroxide detection using Pt nanoparticles-dispersed carbon electrode prepared by pulsed arc plasma deposition. Talanta 99:865–870

Chapter 4
Dendrimer-Encapsulated Metal Nanoparticles: Synthesis and Application in Catalysis

Wenyu Huang

4.1 Introduction

Dendrimers are a category of macromolecules that have a central core surrounded by hyperbranched repetitive units. Dendrimers have versatile structures and chemical properties because the core, the branches, and the external surface can have different functions. The hyperbranched structure of dendrimers distinguishes them from other macromolecules or polymers. For example, dendrimers have large number of end groups as well as higher concentrations of nanoporous channels and cavities because the number of dendrimer end groups increases faster than the surface area.

The pioneer work in dendrimer synthesis was carried out by Vögtle and co-workers who made the first branched molecule in 1978 [1]. Following this work, Tomalia and co-workers synthesized a series of branched molecules and named them “dendrimers” in 1985 [2], which later became the accepted term for this class of molecules. In 1986, Newkome and co-workers also reported a series of branched molecules and named them arborols [3]. Early on, dendrimers only contained organic building blocks and were considered to be organic molecules, which is still common in more recently designed and constructed dendrimer molecules. However, hybrid dendrimers have been realized that include other main group elements [4] and organometallic complexes [5, 6].

Dendrimers can be synthesized using divergent [2, 3, 7–9] or convergent [10–13] methods. Using the divergent method, an inside-out approach, the synthesis of dendrimers starts at the core and branches out using a series of organic or organometallic synthesis techniques. With the convergent method, the dendritic fragments (branches) are synthesized first and are then connected to a core with multiple link

---

W. Huang (✉)
Department of Chemistry, Iowa State University, 2760 Gilman Hall, Ames,
IA 50011-3111, USA
e-mail: whuang@iastate.edu

J.Y. Park (ed.), *Current Trends of Surface Science and Catalysis*,
DOI 10.1007/978-1-4614-8742-5_4,

sites to form hyperbranched dendrimer structures [13]. Both divergent and convergent synthesis methods have their limitations. Divergent methods require intensive purification and separation of the dendrimers at each step of the synthesis to achieve pure products, while convergent methods cannot be used to synthesize dendrimers of high generation (>8th) with a more crowded surface due to steric effects [14].

With the divergent and convergent synthesis methods, many organic and organometallic functional groups have been integrated into dendrimer molecules, such as amines, amides, carbosilanes, ferrocenes, porphyrins, and saccharides [15]. These functional groups introduce many interesting properties into dendrimers, such as a large number of binding sites for metal ions [16], a hydrophobic or hydrophilic microenvironment within the interior of the dendrimer [17, 18], or a biocompatible external surface [19]. Based on these unique properties, a broad spectrum of applications have been demonstrated in many research fields, such as chemical sensing [20], drug delivery [19], environmental remediation [21], as well as homogeneous and heterogeneous catalysis [15, 22–27].

Catalysis is one of the most common applications for dendrimers. Using dendrimers as homogeneous catalysts, active sites have been placed at the core, in the middle of the branch, or on the periphery of the molecule. These active sites include many organic functional groups and organometallic complexes incorporated into the dendrimer molecules. When these catalytic active sites are placed at the periphery, or surface, of the dendrimers, they can be directly accessed by reactants in solution and are generally more efficient than heterogeneous catalysts. Because the surface end groups of dendrimers at high generation are densely packed, the local concentration of catalytic sites is extremely high, which could lead to cooperative catalysis processes [28]. When these catalytic active sites are located at the core or in the middle of the branches, reactants have to enter the pores of a dendrimer prior to reaction. The diffusion limitation of these dendrimer pores could decrease the efficiency of the catalysts. However, the limitation induced by these dendrimer pores also introduces size selectivity for reactants of different sizes and geometries. Having catalytic active sites located inside of dendrimers, the catalysts could also be more stable against deactivation caused by excess ligands or bimetallic mechanisms [25]. The microcavities inside high-generation dendrimers could also provide a totally different reaction environment compared to the bulk solution and could therefore benefit catalytic reactions [29]. Moreover, many dendrimer catalysts can be separated from reactants and products by precipitation and two-phase catalysis. High-generation dendrimer catalysts with a spherical shape can also be isolated from reactions by membranes that only allow small reactant and product molecules to pass through. This membrane-based separation technique is called nanofiltration, which is used in continuous flow membrane reactors to recycle dendrimer catalysts [30].

In general, homogeneous catalysts are more efficient than heterogeneous catalysts. Heterogeneous catalysts, on the other hand, are insoluble in solution and can thus be easily separated from the reaction solution by filtration. Heterogeneous catalysis is also more robust in continuous flow processes, which is preferred for large-scale industrial production processes. Dendrimer-based homogeneous catalysts could be readily converted to their heterogeneous counterparts by immobilizing dendrimers on insoluble supports, such as silica, alumina, carbon-based materials, and many polymers [31–36]. The use of organic functional groups and organometallic complexes integrated inside dendrimers as the catalytic active sites has been reviewed many times with different foci [15, 25, 27, 37–41] and will not be covered in this review.

Another very important category of dendrimer catalysis is based on nanoparticles synthesized directly inside the dendrimers being the active component for catalytic reactions. The current review will focus on Polyamidoamine (PAMAM) dendrimer-encapsulated nanoparticles (DENs). This topic has been reviewed several times [22–24, 26, 42]. In this review, the techniques developed for the synthesis of mono- and bi-metallic DENs will only be briefly overviewed. The focus of this review is on the most recent advances in understanding the structure of DENs and newly developed applications of DENs in catalysis.

4.2 Synthesis of Dendrimer-Encapsulated Metal Nanoparticles

As templating and capping agents for nanoparticle synthesis, dendrimers behave fundamentally different from other capping agents such as oleylamine, oleic acid, PVP, and other surfactant-based molecules. These capping agents are usually tightly adsorbed on the surface of the nanoparticles to stabilize them, which could block surface atoms from reactants and lead to low catalytic activities [43–45]. On the contrary, nanoparticles synthesized inside the cavities of high-generation dendrimers rely more on steric confinement [46]. Therefore, most of the atoms on the surface of DENs are free of ligands and are catalytically active for reactant molecules as long as they can pass through the nanopores formed by the branches at the dendrimer periphery [47].

4.2.1 Synthesis of Monometallic DENs by Chemical Reduction

The dendrimer-mediated synthesis of metal nanoparticles was initiated by the pioneering work of Tomalia [48] and Crooks [49] on synthesizing copper nanoclusters in 1998. In 1999, Crooks and Zhao reported two studies on the synthesis of Pt [50] and Pd [51] nanoparticles with PAMAM Starburst dendrimers. In these two studies, the synthesized Pt and Pd nanoparticles were used in electrocatalytic oxygen reduction and homogeneous hydrogenation reactions, respectively.

PAMAM dendrimers are one of the most utilized dendrimers for the synthesis of nanoparticles. PAMAM dendrimers have tertiary amine and amide groups that can bind metal precursors at a tunable ratio as shown by Step (1) in Fig. 4.1 [52]. These metal precursors are reduced chemically to form metal nanoparticles inside the

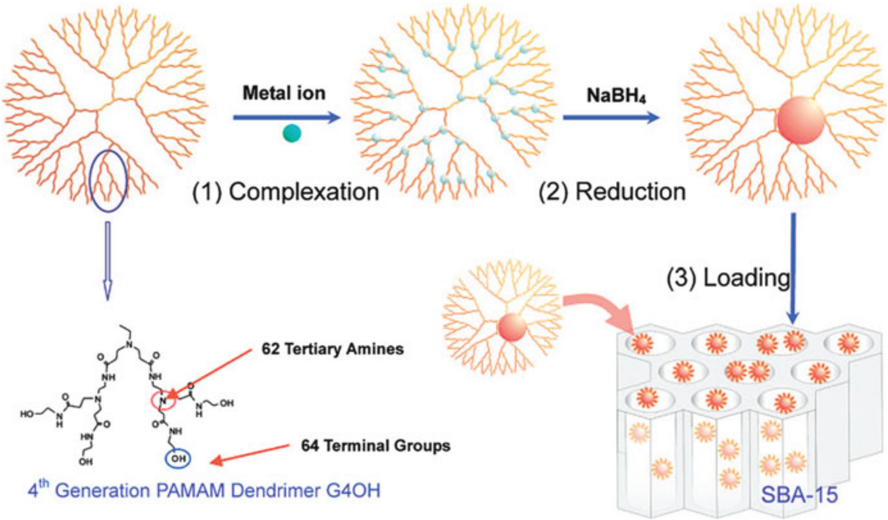

Fig. 4.1 Synthesis of dendrimer-encapsulated metal nanoparticles and the subsequent immobilization of the nanoparticles on mesoporous SBA-15 support. Reprinted with permission from ref. [52]. Copyright 2008 American Chemical Society

cavities of dendrimers, as shown by Step (2) in Fig. 4.1. These nanoparticles were named DENs. The PAMAM dendrimers act as both size-limiting agents and protection layers during the nanoparticle synthesis processes. Based on a similar synthesis mechanism, other kinds of dendrimers have also been used to synthesize DENs, such as the poly (propylene imine) (PPI) [53, 54], phenylazomethine (DPA) [55, 56], and triazole families [57, 58]. However, PAMAM dendrimers are the most broadly used dendrimers. For PAMAM dendrimers, the most used generations are from 4 to 6, because PAMAM dendrimers of generation 3 and less have no spherical shape and thus have no cavities to stabilize any formed nanoparticles. On the other hand, PAMAM dendrimers of generation 6 and above are very expensive due to the extensive purification steps required during synthesis.

It is worthwhile to point out that dendrimers can also be used as normal capping agents during the synthesis of nanoparticles that do not reside inside the cavities of dendrimers [59, 60]. These dendrimer-stabilized nanoparticles, capped with several dendrimer molecules, are usually much bigger than DENs and will not be discussed in this book chapter.

PAMAM dendrimer-templated synthesis of metal nanoparticles has been demonstrated for many metals, such as Cu, Pt, Pd, Au, Rh, and Ru [42]. Most of the syntheses were carried out in aqueous solution at an appropriate pH. For amine-terminated PAMAM dendrimers, the pH of the solution needs to be adjusted to 3 to protonate the terminal amine groups and prevent dendrimer cross-linking [61, 62]. Metal ions cannot bind to protonated amine groups; instead, they bind to the tertiary amines inside the PAMAM dendrimer.

4.2.2 Synthesis of DENs in Organic Solutions

Crooks' group developed new synthesis approaches to directly prepare DENs in organic solutions using PAMAM dendrimers functionalized with hydrophobic dodecyl terminal groups [63]. Similar approaches have also been applied to Fe and Ni DENs [64, 65], which cannot be synthesized in aqueous solution. The Fe and Ni DENs are stable without exposure to oxygen and water, but decompose within several minutes in the presence of oxygen and water. Bimetallic DENs containing Ni (e.g., NiSn [66] and NiAu [67]) have also been synthesized in organic solution.

4.2.3 Synthesis of DENs by Galvanic Redox Displacement

Dendrimer-templated synthesis of metal nanoparticles is a powerful technique and many metal DENs can be synthesized. However, the approach cannot be used to synthesize metal nanoparticles whose precursors (metal ions) have weak interactions with the dendrimers. For certain metal ions, such as Ag^+, another technique was developed based on galvanic redox displacement [68]. Using the galvanic redox displacement technique, Cu DENs were mixed with Ag^+. Since the standard reduction potential of Ag^+ is more positive than Cu^{2+}, Ag^+ will be reduced to form Ag(0), and Cu(0) will be oxidized to Cu^{2+}. Therefore, Cu DENs will be converted to Ag DENs using this technique. The conversion of Cu DENs to Au, Pt, or Pd DENs has also been demonstrated using the galvanic redox displacement technique [68].

4.2.4 Synthesis of Bimetallic DENs

Bimetallic DENs have also trigged great research interest because these nanoparticles often have enhanced catalytic activity, selectivity, and/or stability compared with corresponding single element nanoparticles. Two reviews have been published on bimetallic DENs [22, 23] and will not be discussed in detail in this review. Instead, the evolution of several synthesis techniques, including those developed after the two reviews, will be discussed.

As shown by Scheme **1** in Fig. 4.2, the first method for the synthesis of bimetallic DENs is called co-complexation, in which two metal ions are mixed with dendrimers at the same time and are reduced simultaneously after both of them form complexes with the dendrimers. Bimetallic DENs, such as Pd/Pt and Pd/Rh, have been synthesized by this method and have shown enhanced activity in the catalytic hydrogenation of 1,3-cyclooctadiene and allyl alcohol [69–72].

The second method is based on a sequential approach (Scheme **2** in Fig. 4.2). After the synthesis of monometallic DENs, the DENs were mixed with the second metal precursor and given time for complexation. After reduction, core-shell

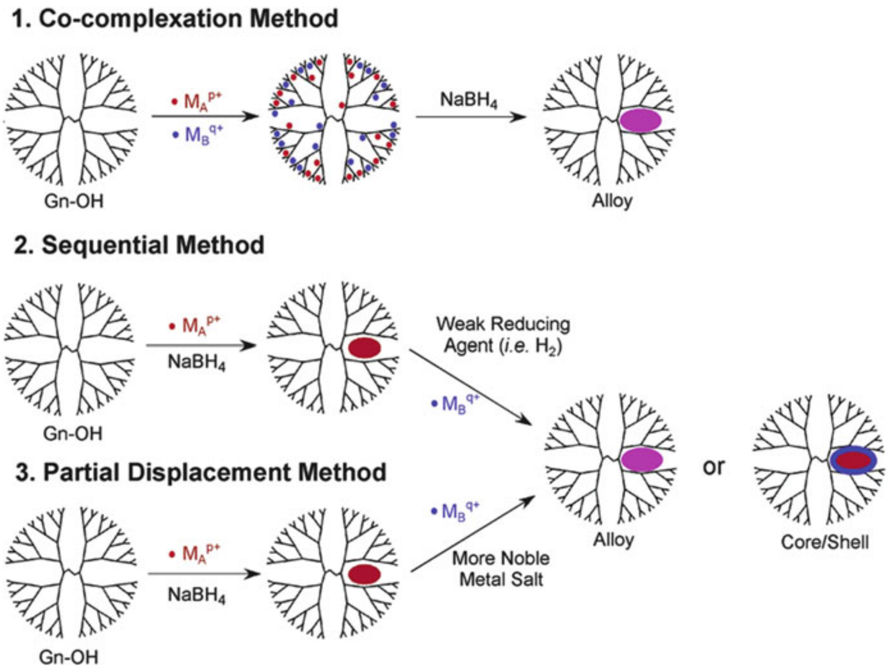

Fig. 4.2 Three different strategies for the synthesis of bimetallic DENs. Reprinted with permission from ref. [24]. Copyright 2005 American Chemical Society

bimetallic DENs can be formed. Bimetallic PdAu core-shell DENs were synthesized by the sequential reduction approach in Crooks' group. Initially, they tried to make both Pd@Au and Au@Pd core-shell DENs by changing the loading and reducing sequences of the Au and Pd precursors [73]. However, a recent study using extended X-ray absorption fine structure (EXAFS) spectroscopy suggested that Pd atoms always prefer to stay on the surface of PdAu DENs [74].

The third method is based on the galvanic redox displacement technique (Scheme **3** in Fig. 4.2). Following the development of the galvanic redox displacement technique to make single metal DENs, a partial displacement approach was proposed to synthesize bimetallic DENs, such as Ag/Cu, Au/Cu, Pd/Cu, and Pt/Cu [26]. Chandler and co-workers used this technique to synthesize $Pt_{16}Au_{16}$ DENs starting from Cu_{40} DENs [75]. However, the $Pt_{16}Au_{16}$ nanoparticles formed via this process are 1–7 nm in diameter. The enlarged particle size is most likely due to sintering induced by the high-temperature treatment used to remove the dendrimer capping for catalysis purposes.

Another recently developed technique used for synthesizing bimetallic DENs is based on under potential deposition (UPD). This is a technique based on the reductive electrodeposition of cations. This technique is extremely powerful in synthesizing core@shell nanoparticles where the shell is controlled at the atomic level [76–79]. Crooks et al. used UPD to deposit a monolayer of Cu onto Pt DENs containing averages of 55, 147, and 225 Pt atoms, pre-synthesized and deposited onto glassy carbon electrodes (GCE) [80]. The formation of Pt@Cu core@shell DENs is proved by cyclic voltammetry measurements and in situ electrochemical X-ray absorption spectroscopy (XAS). Because the reduction potential of metal cations at different facets of metal cores varies, the UPD method might be used to make core@shell nanoparticles with a facet-selective partial deposition of the shell metal [42]. By combining UPD with the galvanic redox replacement technique, Crooks and co-workers also demonstrated that Au@Pt DENs could be synthesized by replacing Cu with Pt in Au@Cu DENs [81]. The Au@Cu DENs were prepared by depositing Cu on Au DENs using the UPD method.

4.3 Recent Advancement in Understanding the Structure of DENs

Since the development of the dendrimer-templated synthesis of metal nanoparticles, there have been many fundamental questions raised about the synthesis processes and final structures of DENs. Many efforts have been devoted to answering these questions, which are the foundation of these dendrimer-based synthesis techniques. The answers to these questions could also explain the observed catalytic properties of DENs. In this section, we discuss several recent reports that provide deeper understanding of the synthesis and structure of DENs.

4.3.1 Metal Binding Sites for Pt^{2+} Ions

Through the use of UV–vis spectroscopy, earlier studies conclude that metal-ligand bonds are formed between Pt ions and tertiary amine groups in PAMAM dendrimers during the complexation step (Step 1 in Fig. 4.1) [26]. A ligand to metal charge transfer (LMCT) band at 250 nm was observed. The intensity of the band is proportional to the amount of Pt ions loaded into the PAMAM dendrimer [26, 50]. However, there are twice as many amide groups as tertiary amine groups inside PAMAM dendrimers that could also act as the binding sites for Pt ions. Figure 4.3 lists the most possible Pt^{2+} binding sites on PAMAM dendrimers. Pt^{2+} ions could form metal-ligand bonds with the lone pair of electrons on the N or O of the amide group, or on the N of the tertiary amine group.

A recent study using resonance Raman spectroscopy strongly suggests that the binding of Pt^{2+} ions to PAMAM dendrimers is through the amide N atoms (structure **1** in Fig. 4.3) [82]. In these experiments, 244 nm UV light from a continuous wave intracavity-doubled argon ion laser was used as the excitation source. Since the UV light could decompose PAMAM dendrimers, the sample was placed on a rotation disk to minimize over exposure at a given spot. Since the LMCT band of PtG4OH

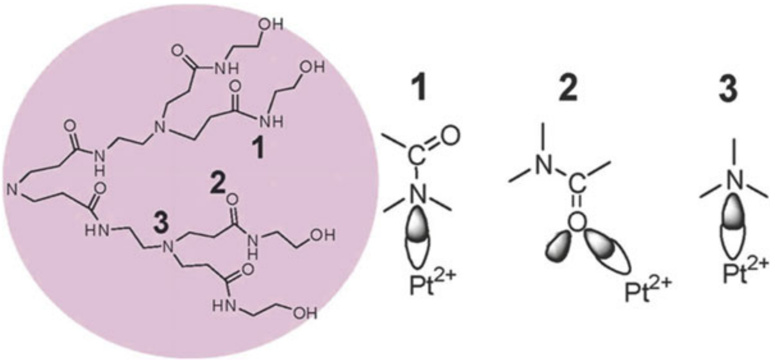

Fig. 4.3 A branch of a PAMAM dendrimer and possible coordination sites for Pt^{2+}. Reprinted with permission from ref. [82]. Copyright 2011 American Chemical Society

(K_2PtCl_4 mixed with fourth-generation PAMAM dendrimers) at 260 nm is partially overlapped with the 244 nm Raman excitation wavelength, resonance Raman spectra of PtG4OH will show enhanced vibration bands of those groups that are involved in the LMCT. Therefore, groups that are bonded to Pt^{2+} ions could be determined by comparing the intensity of the vibration bands in their resonance Raman spectra.

For pure G4OH, the Raman spectrum 1 in Fig. 4.4a indicates that there are four vibration bands located at 1,643 (amide I, C=O), 1,560 (amide II, ν(C–N) + δ (C–N–H)), 1,440, and 1,300 cm^{-1}. For PtG4OH, if Pt^{2+} ions are bonded to the PAMAM dendrimer through the tertiary amine groups, we should observe enhanced Raman peaks for symmetric and/or asymmetric tertiary amine vibration bands (located around 916 and 1,064 cm^{-1}, respectively) [83, 84]. However, the resonance Raman spectrum 2 in Fig. 4.4a for PtG4OH only shows two strongly enhanced vibration bands at 1,560 and 1,440 cm^{-1}, which can be attributed to amide II and H–N–Cα/C, respectively [85]. Therefore, the resonance Raman spectra strongly suggest that the tertiary amine groups in PAMAM dendrimers are not involved in forming metal-ligand bonds with Pt^{2+} ions, while the Pt^{2+} ions form complexes with the N in the amide group (amide II), as shown by structure **1** in Fig. 4.3.

Rh^{3+} ions behave similarly to Pt^{2+} ions, but the resonance Raman peaks at 1,560 and 1,440 cm^{-1} are much weaker, as shown by spectrum 3 in Fig. 4.4a, because the LMCT band for RhG4OH (Rh^{3+} mixed with fourth-generation PAMAM dendrimers) has much less overlap with the 244 nm Raman excitation (Fig. 4.4b).

4.3.2 Oxidation State of Pt DENs

During the synthesis of Pt DENs with PAMAM dendrimers, $NaBH_4$ is the most frequently used reducing agent. In a typical synthesis, 10- to 100-fold of $NaBH_4$ is used to completely reduce the metal precursors bonded in PAMAM dendrimers

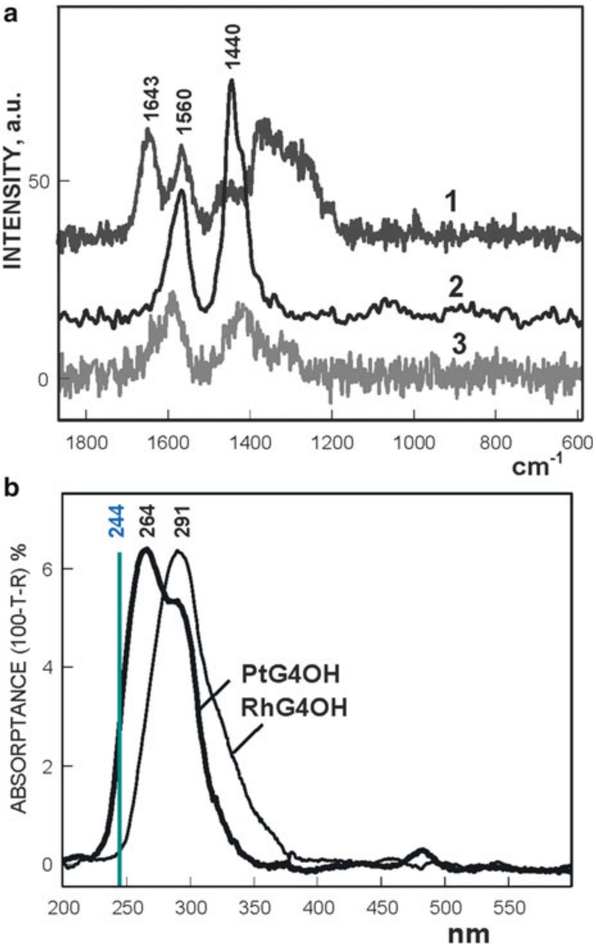

Fig. 4.4 (**a**) UV-Raman spectra of samples dried on aluminum foil. (1) G4OH, (2) PtG4OH, and (3) RhG4OH. (**b**) UV–vis spectrum of PtG4OH and RhG4OH. Reprinted with permission from ref. [82]. Copyright 2011 American Chemical Society

[26, 62, 86]. Since Pt is a noble metal and $NaBH_4$ is an efficient reducing agent, researchers initially believed that the Pt^{2+} ions in the DENs should be completely reduced into their metallic form. Early X-ray photoelectron spectroscopy (XPS) studies also suggested a full reduction of Pt^{2+} ions to Pt(0) in Pt_{60} DENs, which has the Pt $4f_{7/2}$ peak located at 71.3 eV [50]. Later, Ye et al. observed that the Pt $4f_{7/2}$ peak appeared at 73.0 eV for Pt_{30} DENs, which is 1.8 eV higher than the binding energy for Pt(0). The high binding energy for Pt_{30} DENs was blamed on their small size and the dendrimer ligands [87]. Ozturk et al. measured the XPS spectrum of Pt_{40} DENs deposited on a substrate with a thick layer and a thin layer [88]. The Pt $4f_{7/2}$ peak was observed at 74.6 eV for the thick layer of Pt_{40} DENs, while the Pt $4f_{7/2}$ peak was located at 73.3 eV for the thin layer. The high binding energy for Pt $4f_{7/2}$was attributed unreduced Pt^{2+} ions.

What is the real oxidation state of Pt in DENs? To answer this question, Somorjai et al. measured the XPS spectrum of Pt_{20} DENs, as shown in Fig. 4.5, which shows

Fig. 4.5 X-ray photoelectron spectrum of Pt_{20} DENs. For Pt nanoparticles, 93 % of the Pt was oxidized. Reprinted with permission from ref. [52]. Copyright 2008 American Chemical Society

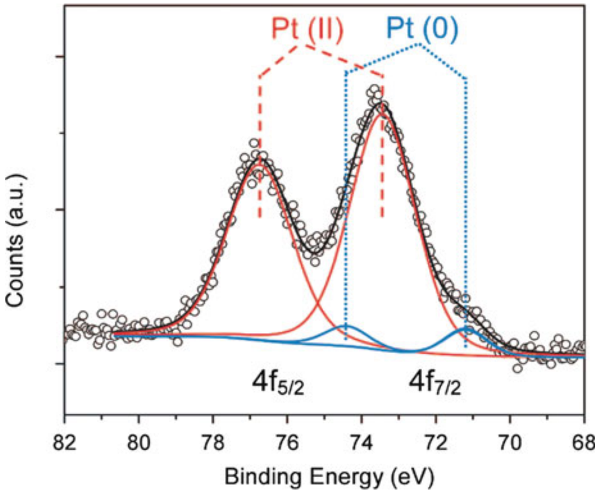

a main Pt $4f_{7/2}$ peak at 73.5 eV with a clear shoulder at 71.2 eV. Because of the presence of this shoulder, which corresponds to Pt(0), the authors concluded that the majority of the Pt in PAMAM dendrimer-encapsulated Pt nanoparticles was unreduced. Our result partially agrees with an EXAFS study, in which Amiridis et al. found that $NaBH_4$ cannot reduce H_2PtCl_6/G4OH and K_2PtCl_4/G4OH at all [89]. However, our XPS study shows that 7 % of the Ptis in its metallic format. We also observed an obvious color change of the solution from light yellow to brown after addition of $NaBH_4$ to K_2PtCl_4/G4OH, which is a slow process and usually takes more than 4 h. The appearance of the brown color in the solution is a sign of the formation of colloidal Pt nanoparticles. If Amiridis et al. did their EXAFS measurement correctly after adding $NaBH_4$ to K_2PtCl_4/G4OH, they would not observe any reduction of Pt^{2+} ions because of their slow reduction after coordination inside PAMAM dendrimers.

Another detailed study about the synthesis and properties of Pt DENs synthesized using the sixth-generation PAMAM dendrimer (G6OH) completely agrees with our results [90]. As shown in Fig. 4.6, the XPS spectra of G6OH$(Pt^{2+})_n$ complexes after reduction with $NaBH_4$ suggest an incomplete reduction of Pt^{2+}. Additionally, more Pt^{2+} ions are reduced after adding $NaBH_4$ at high Pt^{2+} loading. The earlier observation that a full reduction of Pt^{2+} ions to Pt(0) was present in G4OH(Pt_{60}) DENs [50] could be explained by the high loading of Pt^{2+} into the G4OH.

Combined with other techniques, such as transmission electron microscopy (TEM), EXAFS, and high-energy X-ray diffraction (XRD), a bimodal distribution was proposed, as shown in Fig. 4.7 [90]. The proposed model suggests that each Pt^{2+}/G6OH complex can only be fully reduced or fully intact after reduction with $NaBH_4$. The same work also suggests an autocatalytic mechanism in which Pt seeds form very slowly inside PAMAM dendrimers and a fast catalytic reduction of Pt^{2+}

Fig. 4.6 X-ray photoelectron spectra of G6OH$(Pt^{2+})_n$ complexes (**a**) before and (**b**) after reduction with $NaBH_4$. Reprinted with permission from ref. [90]. Copyright 2008 American Chemical Society

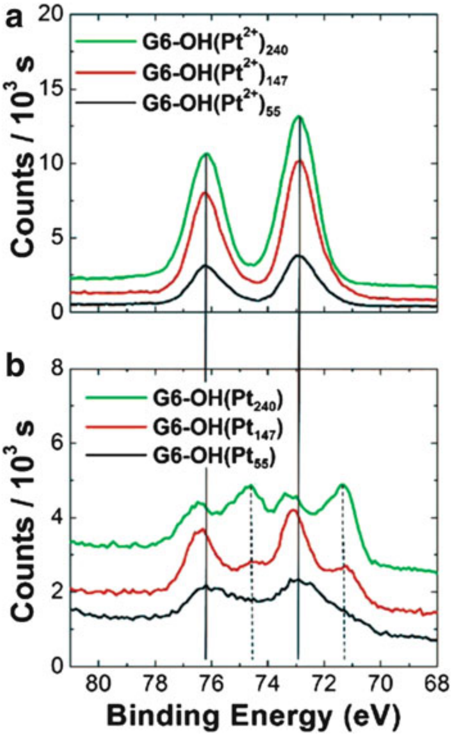

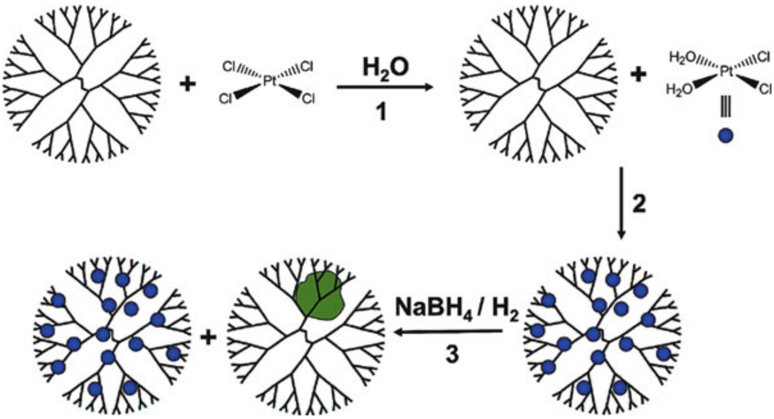

Fig. 4.7 A bimodal distribution of Pt^{2+}/dendrimer complexes after reduction with $NaBH_4$. Pt^{2+}/dendrimer complexes are either fully reduced or fully intact. Reprinted with permission from ref. [90]. Copyright 2008 American Chemical Society

ions only happens once a Pt seed forms inside the PAMAM dendrimer. This mechanism is quite reasonable to explain the partial reduction of Pt^{2+} ions within PAMAM dendrimers, but it doesn't explain why Pt seeds formed in some of the dendrimers but not in others. A recent work by Somorjai et al. suggests that the Pt^{2+} bonds to the N in the amide groups in a chelating configuration, which could make the reduction of these chelated Pt^{2+} ions difficult [82]. However, at a high metal ion loading, there will be a substantial amount of Pt^{2+} ions that can't bind with dendrimers in a chelating configuration. These Pt^{2+} ions are the first ions to be reduced after adding $NaBH_4$ and act as catalysts to reduce the chelated Pt^{2+} ions present within the same dendrimer.

4.3.3 Glass Nature of the Cluster

To fully understand the chemical and physical properties of DENs, it is important to know the lattice structure of these ultrasmall particles (<2 nm). A general question is whether these small particles have a periodic 3D structure and well-defined crystal facets as their bulk counterparts do. For big nanoparticles, high-resolution transmission electron microscopy (HRTEM) and XRD spectroscopy are two commonly used and powerful techniques to characterize lattice structure. However, the lattice structure of ultrasmall nanoparticles is largely unknown because HRTEM and XRD are either not applicable or can't provide meaningful information.

Recently, Frenkel et al. combined total XRD and atomic pair distribution function (PDF) analysis to study 147 atom Au clusters encapsulated in sixth-generation PAMAM dendrimers, G6-Au_{147} (1.6 nm in diameter) [91]. High-energy synchrotron radiation X-rays are required for the XRD experiments and PDF analysis because of the high flux and high energy that allow the measurement of the weak diffraction patterns of the G6-Au_{147} and that reach high wave vectors. As shown in Fig. 4.8a, the XRD of bulk Au shows a typical diffraction pattern for Au with sharp peaks. However, both dry and wet G6-Au_{147} nanoparticles show broad peaks in their XRD spectra. This indicates that they don't have a periodic crystal structure. Frenkel et al. reduced the XRD spectra to their corresponding atomic PDF spectra, as shown in Fig. 4.8b. The PDF of bulk Au shows sharp peaks that correspond to the different coordination spheres for an fcc crystal lattice. For dry and wet G6-Au_{147} nanoparticles, the first peak at 2.87 Å appears in the same position as bulk Au, which indicates that the Au in these nanoparticles is reduced to its metallic form. The PDF peaks of dry G6-Au_{147} nanoparticles are broader than those of bulk gold and decay to zero when the radial distance is larger than 15 Å. This indicates that there is no long-range periodicity in the dry G6-Au_{147} nanoparticles. For wet G6-Au_{147} nanoparticles, the PDF peaks at long radial distance are less distinguishable than those of the dry nanoparticles. This suggests that wet G6-Au_{147} nanoparticles have an even more random lattice structure.

Fig. 4.8 Experimental XRD (**a**) and the corresponding PDFs G(r) for 1.6-nm Au particles. (**b**) Best model PDFs (line in *red*) and an experimental PDF for 26-nm Pd particles (line in *blue*) are also shown. Reprinted with permission from ref. [91]. Copyright 2008 American Chemical Society

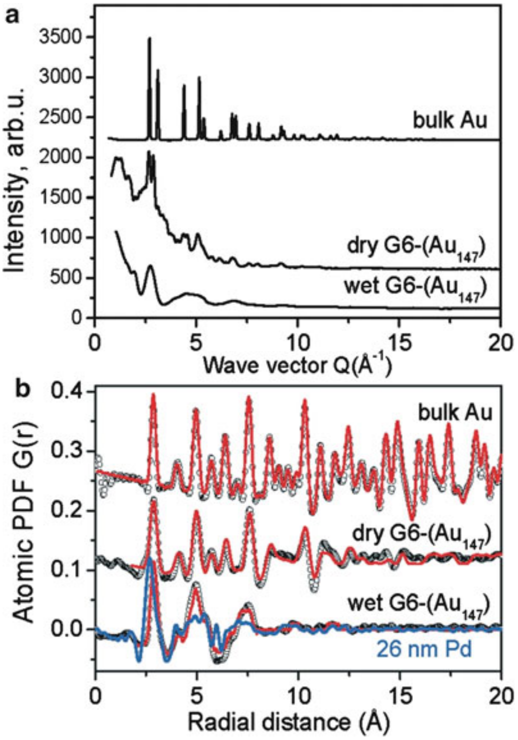

4.4 Newly Developed Applications of DENs in Catalysis

DENs have been applied in many homogeneous and heterogeneous catalytic reactions and show excellent activity and selectivity. DENs have also been used in electrocatalytic reactions. A recent review article covers most of these reactions [42]. In this section, we will only focus on several recent developments of using DENs in catalysis.

4.4.1 Removal of Dendrimers for Heterogeneous Catalysis

Dendrimer-templated synthesis of metal nanoparticles provides a powerful way to synthesize ultrasmall particles with an extremely narrow size distribution. Researchers in the field of heterogeneous catalysis quickly recognized this advantage and adopted this method to prepare oxide-supported metal catalysts with a narrow particle size distribution [75, 92–94]. However, it was found that removal of the PAMAM dendrimer capping agent by high-temperature treatments in oxygen and hydrogen is a necessary step for the supported DENs to show good catalytic

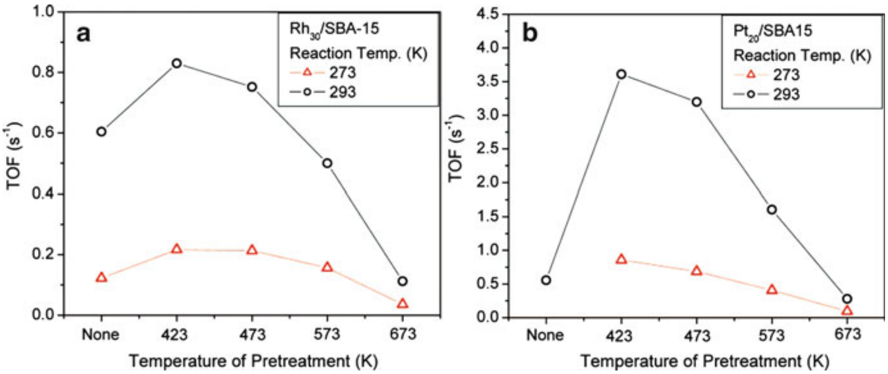

Fig. 4.9 Initial ethylene hydrogenation activity over (**a**) Rh_{30}/SBA-15 and (**b**) Pt_{20}/SBA-15 after reducing in 76 Torr of H_2 balanced with He at different temperature. The reaction mixture was 10 Torr C_2H_4,100 Torr H_2, and 650 Torr He. Reprinted with permission from ref. [52]. Copyright 2008 American Chemical Society

activity in heterogeneous catalysis [92, 93]. Unfortunately, DENs usually grow larger after these high-temperature treatments due to sintering [92, 95].

When DENs were used as catalysts in solution, Crooks et al. found that the presence of PAMAM dendrimers doesn't block the metal surface [24, 96, 97]. Once DENs were loaded onto oxides, it was proposed that the PAMAM dendrimer would collapse onto the surface of the metal nanoparticles and block their active sites [98]. However, Somorjai et al. found that it is not necessary to perform the high-temperature oxidation and reduction treatments for mesoporous silica (SBA-15) supported Rh and Pt DENs for them to show good activity for the ethylene hydrogenation reaction, as shown in Fig. 4.9 [52].

Figure 4.9b shows that the as-synthesized Pt nanoparticles, without any reduction pretreatment, have very low activity. Upon reduction at 423 K for 1 h, the activity of SBA-15 supported Pt DENs was enhanced sevenfold. If the reduction temperature was too high (573 and 673 K), the Pt DENs lost their activity, possibly due to sintering and carbon deposition, which decreases the surface area of the Pt DENs. The low activity of the as-synthesized Pt DENs could be attributed to their high oxidation state, which is not active for ethylene hydrogenation. From XPS measurement of the sample (Fig. 4.5), only 7 % of the Pt was reduced to the metallic state after treating Pt PAMAM dendrimer complexes with $NaBH_4$ for 8 h. This observation agrees with a detailed study performed by Crooks et al. [90]. The high oxidation state could also explain why Amiridis et al. couldn't observe any CO adsorption on Pt DENs without any high-temperature reduction treatment in the gas phase, as shown in Fig. 4.10 [93]. In this study, the Pt PAMAM dendrimer complexes were only reduced using H_2 for 1 h at room temperature. By the end of this treatment, the majority of the Pt ions would still remain in their high oxidation state [90] and would not adsorb CO molecules.

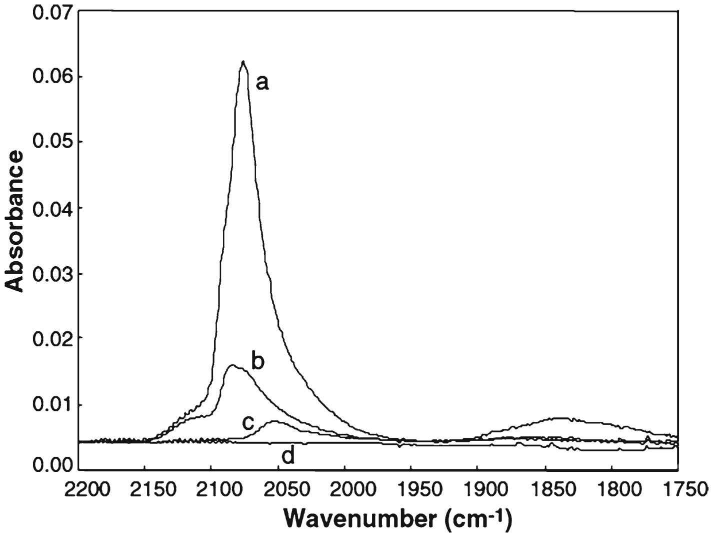

Fig. 4.10 Room temperature FTIR spectra of adsorbed CO on Pt-G4OH/SiO_2 following oxidation at (**a**) 425 °C, (**b**) 350 °C, and (**c**) 275 °C for 1 h and subsequent reduction at 200 °C for 1 h. The sample labeled (**d**) was only treated in a He environment for 1 h at 100 °C. Reprinted with permission from ref. [93]. Copyright 2004 Plenum Publishing Corporation

4.4.2 Understanding the Nanoparticle Size Effect in Catalysis

Catalysts with high activity and selectivity could dramatically reduce the energy required for many energy intensive catalytic processes. Many factors could affect the catalytic activity and selectivity of metal nanoparticles, such as particle size, shape, capping agent, and oxide support. With the help of dendrimers, monodisperse nanoparticles <1 nm in diameter can be synthesized repeatedly, which extends the study of size-induced activity and selectivity changes of metal nanoparticles to the sub-nm regime.

A recent study on the sequential hydrogenation of pyrrole to pyrrolidine and *n*-butylamine (Fig. 4.11a) showed a strong size effect on reaction selectivity [34]. The sizes of the Pt nanoparticles studied were 0.8, 1.2, 1.5, 2.0, 2.9, and 5 nm, of which 0.8, 1.2, and 2.0 nm nanoparticles were encapsulated by fourth-generation PAMAM dendrimers and the other nanoparticles were capped with PVP molecules. As shown in Fig. 4.11b, small nanoparticles (1.5 nm and less) produce a mix of pyrrolidine and *n*-butylamine, while nanoparticles of 2–5 nm produce more than 90 % of *n*-butylamine and less than 10 % of butane and ammonia (complete hydrogenation products of pyrrole). Since Pt nanoparticles 2 nm and larger show similar selectivity in pyrrole hydrogenation, it would be impossible to observe this size-induced selectivity change of Pt nanoparticles without these ultrasmall Pt DENs. The size effect of Pt nanoparticles on the selectivity of pyrrole hydrogenation is

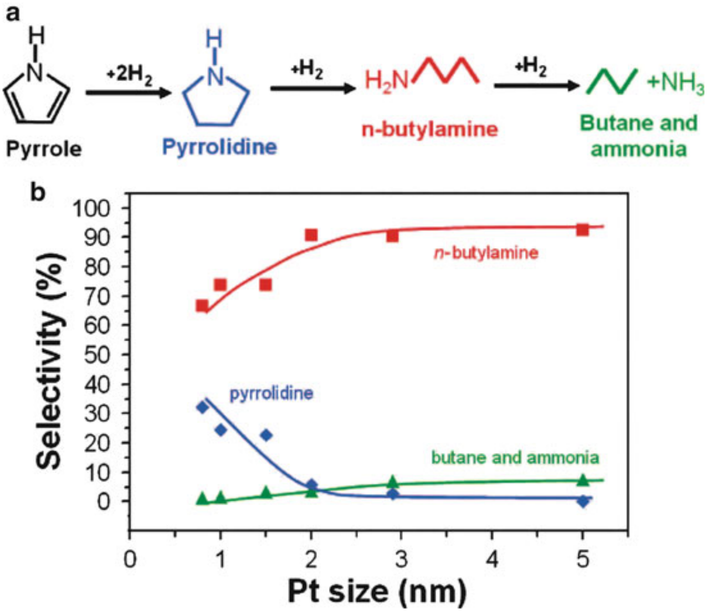

Fig. 4.11 (**a**) Pyrrole hydrogenation reaction network. (**b**) Pyrrole hydrogenation selectivity (color coordinated to (**a**)) as a function of Pt NP size ($T = 413$ K and 11 ± 2 % conversion). Feed was 4 Torr of pyrrole and 400 Torr of H_2 with the balance He. Reprinted with permission from ref. [34]. Copyright 2008 American Chemical Society

attributed to a stronger adsorbate-surface interaction between the *n*-butylamine and the smaller Pt nanoparticles.

Using Pd DENs of 1.3–1.9 nm, Crooks et al. also conducted an interesting study about the size effect on the activity for catalytic hydrogenation of allyl alcohol [97]. A clear correlation was observed between the size of the DENs and their catalytic activity in allyl alcohol hydrogenation, as shown in Fig. 4.12a. Nanoparticles 1.3, 1.4, and 1.5 nm in size show similar activity for the reaction. When nanoparticles are bigger than 1.5 nm (1.7 and 1.9 nm), activity increases with increasing particle size.

Electronic and/or geometric effects could be used to explain the size-induced activity changes for metal catalysts [99]. To understand which effect dominates, the authors plotted the size-dependent normalized turnover frequency (TOF) calculated based on the number of Pd atoms located at the facets, at the defect sites, the total surface atoms, and the number of Pd particles of different size (blue triangles), as shown in Fig. 4.12b. If the geometric effect dominates the observed size-induced activity changes, the TOF should remain constant for particles of different sizes. The TOFs calculated based on the total surface atoms, defect atoms, and number of particles increased monotonically, while the TOFs calculated based on face atoms remained constant for particle sizes larger than 1.5 nm. These results indicate that for Pd nanoparticles 1.5–1.9 nm in size, the geometric effect dominates the

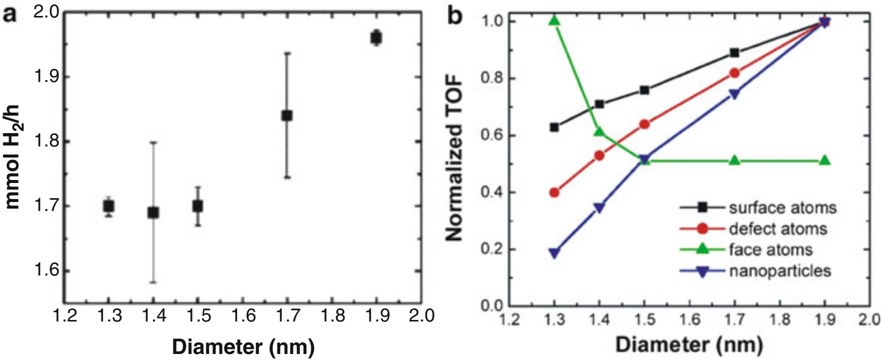

Fig. 4.12 (**a**) Plot of the rate of hydrogen consumption as a function of particle diameter. (**b**) Plots of normalized TOF (mol H_2/(mol active site-h)) as a function of particle diameter for three different types of possible active sites and for the total number of nanoparticles. Reprinted with permission from ref. [97]. Copyright 2006 American Chemical Society

size-induced activity changes and the active sites are face atoms. For Pd nanoparticles smaller than 1.5 nm, the size-induced activity changes are mostly due to the electronic effect.

4.4.3 Heterogenizing Homogeneous Catalysts and Their Use in a Continuous Flow Reactor

Converting homogeneous catalytic reactions to heterogeneous versions will benefit the pharmaceutical and fine chemical industries because heterogeneous catalysts are physically separated from reactants and products and can therefore be easily recycled. Dendrimers have been employed as a recoverable catalyst platform using specially designed techniques, such as nanofiltration, precipitation, and two-phase catalysis [25].

Recently, Pt DENs were used as an electrophilic catalyst in an intramolecular addition of phenols to alkynes (intramolecular hydroalkoxylation), as shown in Fig. 4.13b [100]. The Pt DENs were supported on a mesoporous silica material known as SBA-15 (Fig. 4.13a). Since the as-synthesized SBA-15 consists of micrometer-sized particles, the supported Pt DENs can be easily separated from the reaction solution by centrifugation. This reaction has only been catalyzed by homogeneous catalysts (e.g., $PtCl_2$) before this report. The use of the supported Pt DENs to catalyze this reaction was the first demonstration that a heterogeneous catalyst could also catalyze this conversion. It was also found that adding an oxidation agent, $PhICl_2$, would dramatically increase the benzofuran yield from 10 to 98 %, as shown in Fig. 4.13b. The authors proposed that $PhICl_2$ could render the surface of the Pt nanoparticles more electrophilic, which is required for the Pt DENs to be active for the hydroalkoxylation reaction.

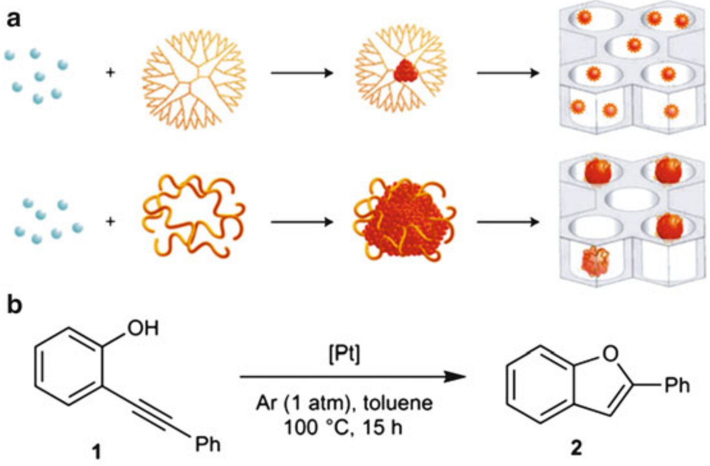

Catalyst	Yield
2.9 nm Pt/PVP/SBA-15 (2.5 mol%)	9%
Pt_{40}/G4OH/SBA-15 (4 mol%)	10%
2.9 nm Pt/PVP/SBA-15 (2.5 mol%), $PhICl_2$ (7.5 mol%)	>99%
Pt_{40}/G4OH/SBA-15 (4 mol%), $PhICl_2$ (12 mol%)	98%
$PtCl_2$ (5 mol%) (2 h)^{29}	97%

Fig. 4.13 Depiction of the two nanoparticle synthesis techniques used and the initial reactivity results for electrophilic catalysis. (**a**) In the top scheme, Pt ions are loaded onto a PAMAM dendrimer and reduced to form a dendrimer-encapsulated NP. Sonication deposits the NPs on the mesoporous silica, SBA-15, to generate the NP catalysts. In the bottom scheme, polyvinylpyrrolidone (PVP) encapsulates the NP. Deposition on SBA-15 follows to produce the catalyst. In both cases, the NPs are synthesized before loading onto SBA-15. (**b**) Hydroalkoxylation of **1** with Pt NPs. To obtain electrophilic activity from the Pt NPs, treatment with the mild oxidant $PhICl_2$ is required. Pt_{40}/G4OH/SBA-15 NPs must be further reduced under H_2 atmosphere at 100 °C for 24 h before reaction. This treatment generates catalytically active NPs that activate the π-bond in **1**, resulting in hydroalkoxylation to benzofuran **2**. Yields were determined by comparing peaks in NMR against an internal standard. Reprinted with permission from ref. [100]. Copyright 2009 Nature Publishing Group

The authors also designed and performed extensive experiments, such as three-phase and catalyst filtration tests, to prove the heterogeneous nature of the SBA-15 supported Pt DENs in the intramolecular hydroalkoxylation reaction. No leaching of the active catalytic species was detected in these tests. PVP-capped Pt nanoparticles were also tested for use in this reaction, but they could not be recycled.

Pd DENs also catalyzed the same intramolecular hydroalkoxylation reaction [101]. SBA-15 supported Pd DENs achieved 95 % yield of benzofuran in 15 h at 20 °C, while $PdBr_2$ and $PdCl_2$ only achieved 10 % yield under the same conditions. Even at 100 °C, $PdCl_2$ only gave 25 % yield of benzofuran after 15 h. After proving that there is no leaching of Pd during the reaction, the SBA-15 supported Pd DENs were applied in a continuous flow reactor. It was found that the presence of 5 mM

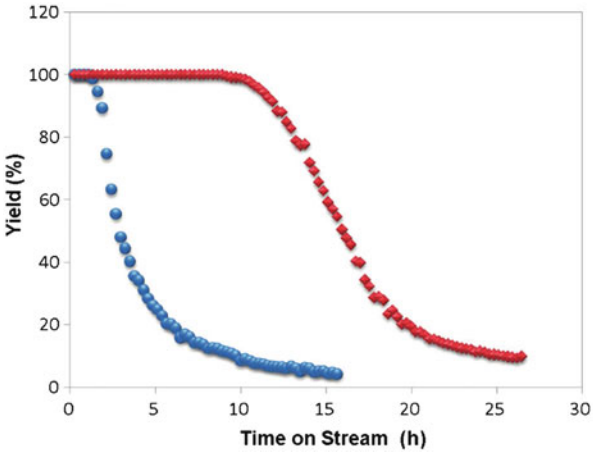

Fig. 4.14 Time on stream of product yield during the hydroalkoxylation of 2-phenylethynylphenol catalyzed by Pd_{40}/SBA-15. In the presence of 5 mM $PhICl_2$ in the reaction stream (a 50 mM solution of 2-phenylethynylphenolin toluene), the catalyst was more stable and deactivated relatively slowly (*red diamonds*), compared to the case when only the reactant flowed through the reactor (*blue dots*). The flow rate was0.6 mL/h. Reprinted with permission from ref. [101]. Copyright 2010 American Chemical Society

of $PhICl_2$ in the reaction feed was important for the catalyst to remain active (Fig. 4.14). However, the SBA-15 supported Pd DENs finally deactivated after 10 h of 100 % conversion. The deactivated catalyst could be regenerated by H_2 reduction at 100 °C followed by $PhICl_2$ oxidation at 20 °C. The authors also demonstrated that the continuous flow reactor could be used to probe other kinetic parameters of the reaction, such as activation energy. When using a batch mode reactor, multiple reactions had to be carried out at different temperatures to calculate the reaction activation energy. During these reactions, all parameters (e.g., stir speed, solution volume, and catalyst amount) had to be controlled as much as possible to achieve accurate reaction kinetic data. One of the benefits of measuring kinetic data of a reaction using a flow mode reactor is that every parameter can be precisely controlled and easily reproduced.

A mechanism study was performed by the same group of authors using EXAFS and near-edge X-ray absorption fine structure (NEXAFS), as well as reaction kinetic measurements [29]. Figure 4.15a shows the coordination number of Pt–Pt, Pt–Cl, and Pt–O measured using EXAFS. The average coordination numbers of Pt–Pt and Pt–Cl after hydrogen reduction are 5 and 0.2, respectively. After oxidation treatment by $PhICl_2$, the coordination number of Pt–Pt decreases to 1. Meanwhile, the coordination number of Pt–Cl increases to 2. These changes in coordination number of Pt–Pt and Pt–Cl indicate that Pt nanoclusters form after hydrogen reduction and that Pt nanoclusters were oxidized to form $PtCl_x^{y-}$ species after $PhICl_2$ oxidation. These changes are reversible upon further reduction and oxidation treatments. The NEXAFS results in Fig. 4.15b reveal that both Pt(II) and Pt(IV) exist after oxidation

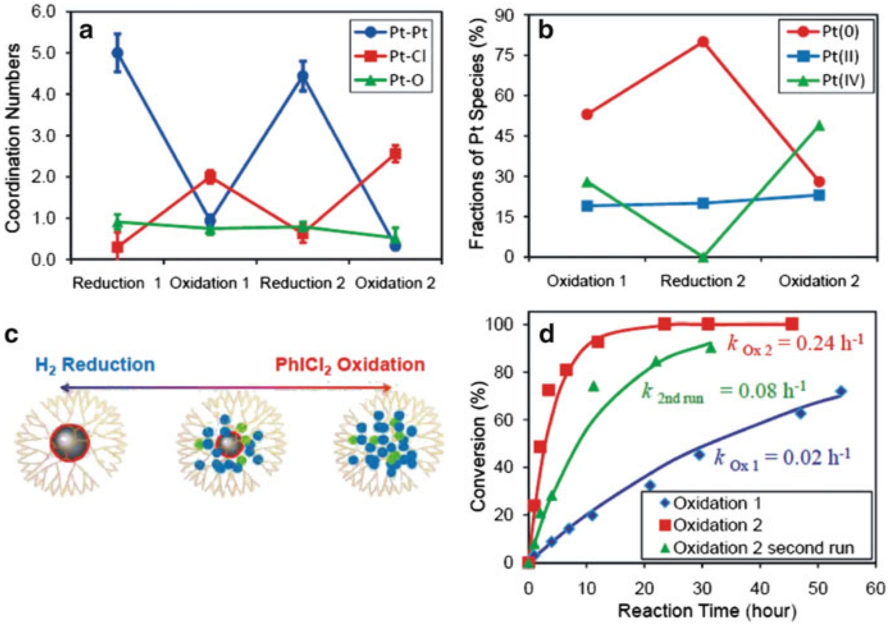

Fig. 4.15 (**a**) Average coordination numbers of Pt atoms in the supported Pt catalyst after a sequence of hydrogen reduction and $PhICl_2$ oxidation treatments in the toluene derived from EXAFS analysis. (**b**) The fractions of Pt(0), Pt(II), and Pt(IV) chloride species of the Pt catalyst derived from NEXAFS analysis. (**c**) A scheme based on the XAS results showing possible structures of the dendrimer-encapsulated Pt catalyst after reduction and oxidation treatment. The gray spheres represent the metallic Pt clusters. The surface Pt chlorides are indicated by *circles*. The small spheres represent the Pt(II) and Pt(IV) species formed after oxidation treatment. (**d**) The reaction conversion vs. reaction time for pre-oxidized samples with 1 wt% Pt loading: *Oxidation 1* and *Oxidation 2*. The rate constants, k_{ox1} and k_{ox2}, are obtained by fitting the conversion (*square* and *diamonds*) to the kinetic model for unimolecular reactions. The solid lines are the fitting curves. For *Oxidation 2*, a second oxidation step was performed after the first reaction run reached full conversion by adding fresh reactant into the reaction mixture. The conversion versus reaction time of the second run is given by *triangle*. $k_{\mathrm{second\ run}}$ is the rate constant of the second run. Reprinted with permission from ref. [29]. Copyright 2011 American Chemical Society

treatment. These species are the active catalytic species for the hydroalkoxylation of 2-phenylethynylphenol. The scheme in Fig. 4.15c was suggested to represent the reversible changes in the Pt DENs upon oxidation and reduction treatments. It was also discovered that after the second oxidation treatment, the reaction rate constant increased 12-fold, compared to that after the first oxidation treatment. This could be explained by the increase in the active Pt(II) and Pt(IV) species, as shown in Fig. 4.15b.

The solvent, toluene, plays an important role in the leaching-inhibition mechanism of the silica-supported Pt DENs catalyst. Since toluene is a nonpolar solvent, the Pt ions prefer to stay in the polar environment inside the PAMAM dendrimers

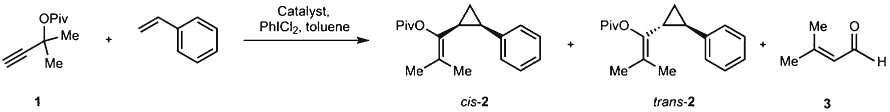

Fig. 4.16 Reaction scheme of propargyl pivalate **1** and styrene to form the *cis* and *trans-diastereomers* of cyclopropane **2**. Reprinted with permission from ref. [102]. Copyright 2012 Nature Publishing Group

and the dendrimers prefer to stay on the surface of the polar silica support. This design principle should be applicable to other liquid-phase heterogeneous catalytic systems to prevent leaching.

4.4.4 Increasing Diastereoselectivity and Chemoselectivity

Since highly selective chemical conversion processes generate less waste and use less energy, controlling the selectivity of chemical reactions using innovated catalysts is exceedingly important for conserving energy and protecting the environment. DENs provide a promising platform that can be used to catalyze chemical reactions with dramatically improved selectivity. Two recent examples using Au and Cu nanoparticles encapsulated in PAMAM dendrimers to control the diastereoselectivity and chemoselectivity of chemical reactions demonstrate the potential of DENs in selective catalytic processes.

Au nanoparticles encapsulated in the fourth-generation PAMAM dendrimer, G4OH, and supported on SBA-15 were used to catalyze the conversion of propargyl pivalate **1** and styrene to form the *cis*- and *trans*-diastereomers of cyclopropane **2** and 3-methyl-2-butenal **3**, as shown by the reaction scheme in Fig. 4.16 [102]. Using SBA-15 supported Au-G4OH as the catalyst, the diastereoselectivity of *cis*- to *trans*-cyclopropane **2** is 17 to 1, while a homogeneous catalyst, $AuCl_3$, only gives 3.5 to 1 *cis*- to *trans*-**2** selectivity of the two diastereomers.

Since the SBA-15 supported Au-G4OH is a heterogeneous catalyst, the authors also carried a cascade reaction (cyclopropanation rearrangement) in a liquid-phase flow reactor and found that the product distribution and reactivity can be controlled by the residence time of the reactants. Under high flow rate (short residence time) of the reactants, the cyclopropanation product is dominant with 100 % diastereoselectivity to the *cis*-configuration. Under low flow rate (long residence time), one of the rearranged products becomes dominant. This example demonstrates the use of a PAMAM dendrimer platform to heterogenize a homogeneous catalyst. Using the flow rate of reactants to control the selectivity of the cyclopropanation rearrangement reaction demonstrated a unique advantage of using a heterogeneous catalyst compared to its homogeneous counterpart.

Using Cu nanoparticles encapsulated in the sixth-generation PAMAM dendrimer, an excellent chemoselectivity of C=O versus C=C was demonstrated on the

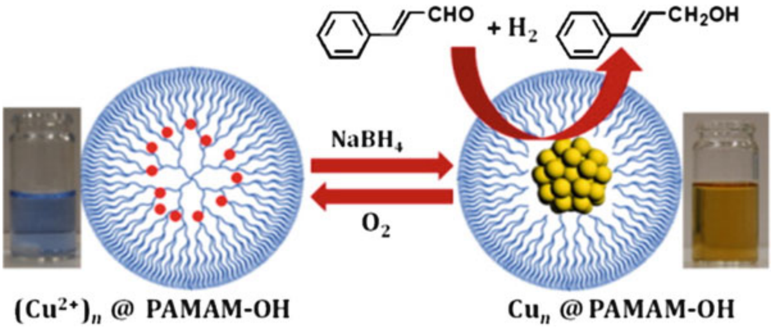

Fig. 4.17 A copper cluster encapsulated within a PAMAM dendrimer with hydroxyl surface groups (PAMAM–OH) acting as a chemoselective catalyst for hydrogenation of carbonyl and olefin groups in water. The activity was dependent on the molar ratio of the Cu^{2+} and PAMAM–OH used in the synthesis, which was ascribed to the size-specific chemical properties of the Cu clusters. The dendrimer-encapsulated Cu cluster was oxidized into Cu^{2+} ions under aerobic conditions, but it could be regenerated by reduction with $NaBH_4$ for use in catalytic applications. Reprinted with permission from ref. [103]. Copyright 2013 American Chemical Society

hydrogenation of cinnamaldehyde, as shown in Fig. 4.17 [103]. At 99 % conversion, the selectivity to cinnamyl alcohol is around 86 %. At 67 % conversion, the selectivity could reach 93 %. The Cu DENs also show extremely low activity for the hydrogenation of the nitro group. The hydrogenation of 4-nitrobenzaldehyde could reach 100 % selectivity to 4-nitrobenzyl alcohol. Since Cu DENs could easily be oxides due to the oxygen in air, the authors also demonstrated that a facile reduction by $NaBH_4$ could restore the activity of the catalyst. During the reversible oxidation and reduction conversions, there is no leaching of Cu^{2+} ions because they are coordinated more strongly with the PAMAM dendrimers than with the water molecules.

4.5 Summary and Outlook

We have discussed the most recent advancements in understanding DEN structures, including the metal binding sites inside the PAMAM dendrimer, the oxidation state of platinum after reduction by $NaBH_4$, and the glassy nature of the small nanoclusters synthesized inside dendrimers. We also discussed several newly developed applications of DENs in catalysis, including the necessity for removing dendrimer capping, the size effect of DENs on catalysis, heterogenizing a homogeneous catalyst, applications of DENs in liquid flow reactors, and the enhanced diastereoselectivity and chemoselectivity. A deep understanding of DEN structures is vitally important for synthesizing DENs of desired structures. The understanding of DEN structures also helps to design superior catalysts for important chemical conversions. Future efforts should be devoted to the development of more selective chemical conversion processes based on DENs and conversion of homogeneous batch reactions to heterogeneous flow reactions. More effort is also needed using in situ techniques to study DEN catalysts under operando conditions.

Acknowledgements This work was supported in part by the startup funds provided by Iowa State University and Ames National Laboratory, as well as a research fund from Iowa Energy Center. I am grateful to Dr. Chaoxian Xiao and Mr. Kyle Brashler for their help with this manuscript.

References

1. Buhleier E, Wehner W, Vogtle F (1978). Cascade-chain-like and nonskid-chain-like syntheses of molecular cavity topologies. Synthesis-Stuttgart 2:155
2. Tomalia DA, Baker H, Dewald J, Hall M, Kallos G, Martin S, Roeck J, Ryder J, Smith P (1985) A new class of polymers—starburst-dendritic macromolecules. Polym J 17:117
3. Newkome GR, Yao ZQ, Baker GR, Gupta VK, Russo PS, Saunders MJ (1986) Cascade molecules. 2. Synthesis and characterization of a benzene 9 3-arborol. J Am Chem Soc 108:849
4. Majoral JP, Caminade AM (1999) Dendrimers containing heteroatoms (Si, P, B, Ge, or Bi). Chem Rev 99:845
5. Cuadrado I, Moran M, Casado CM, Alonso B, Losada J (1999) Organometallic dendrimers with transition metals. Coord Chem Rev 193–5:395
6. Hearshaw MA, Moss JR (1999) Organometallic and related metal-containing dendrimers. Chem Commun 1:1–8
7. de Brabander-van den Berg EMM, Meijer EW (1993) Poly(propylene imine) dendrimers: large-scale synthesis by hetereogeneously catalyzed hydrogenations. Angew Chem Int Ed Engl 32:1308
8. Wörner C, Mülhaupt R (1993) Polynitrile- and polyamine-functional poly(trimethylene imine) dendrimers. Angew Chem Int Ed Engl 32:1306
9. Tomalia DA (1994) Starburst/cascade dendrimers: fundamental building blocks for a new nanoscopic chemistry set. Adv Mater 6:529
10. Miller TM, Neenan TX (1990) Convergent synthesis of monodisperse dendrimers based upon 1,3,5-trisubstituted benzenes. Chem Mater 2:346
11. Xu Z, Moore JS (1993) Rapid construction of large-size phenylacetylene dendrimers up to 12.5 nanometers in molecular diameter. Angew Chem Int Ed Engl 32:1354
12. Xu Z, Moore JS (1993) Synthesis and characterization of a high molecular weight stiff dendrimer. Angew Chem Int Ed Engl 32:246
13. Hawker CJ, Frechet JMJ (1990) Preparation of polymers with controlled molecular architecture. A new convergent approach to dendritic macromolecules. J Am Chem Soc 112:7638
14. Zeng FW, Zimmerman SC (1997) Dendrimers in supramolecular chemistry: from molecular recognition to self-assembly. Chem Rev 97:1681
15. Twyman LJ, King ASH, Martin IK (2002) Catalysis inside dendrimers. Chem Soc Rev 31:69
16. Vassilev K, Ford WT (1999) Poly(propylene imine) dendrimer complexes of Cu(II), Zn(II), and Co(III) as catalysts of hydrolysis of p-nitrophenyl diphenyl phosphate. J Polym Sci A Polym Chem 37:2727
17. Newkome GR, Moorefield CN, Baker GR, Johnson AL, Behera RK (1991) Alkane cascade polymers possessing micellar topology: micellanoic acid derivatives. Angew Chem Int Ed Engl 30:1176
18. Stevelmans S, van Hest JCM, Jansen JFGA, van Boxtel DAFJ, de Brabander-van den Berg EMM, Meijer EW (1996) Synthesis, characterization, and guest–host properties of inverted unimolecular dendritic micelles. J Am Chem Soc 118:7398
19. Kojima C, Kono K, Maruyama K, Takagishi T (2000) Synthesis of polyamidoamine dendrimers having poly(ethylene glycol) grafts and their ability to encapsulate anticancer drugs. Bioconjug Chem 11:910
20. Adronov A, Frechet JMJ (2000) Light-harvesting dendrimers. Chem Commun 1:1701
21. Bhattacharya P, Kim SH, Chen P, Chen R, Spuches AM, Brown JM, Lamm MH, Ke PC (2012) Dendrimer-fullerenol soft-condensed nanoassembly. J Phys Chem C 116:15775

22. Peng XH, Pan QM, Rempel GL (2008) Bimetallic dendrimer-encapsulated nanoparticles as catalysts: a review of the research advances. Chem Soc Rev 37:1619
23. Chandler BD, Gilbertson JD (2006) Dendrimer-Encapsulated Bimetallic Nanoparticles: Synthesis, Characterization, and Applications to Homogeneous and Heterogeneous Catalysis. In: Gade LH (ed) Dendrimer catalysis, vol 20, p 97 Springer-Verlag Berlin Heidelberg
24. Scott RWJ, Wilson OM, Crooks RM (2005) Synthesis, characterization, and applications of dendrimer-encapsulated nanoparticles. J Phys Chem B 109:692
25. van Heerbeek R, Kamer PCJ, van Leeuwen P, Reek JNH (2002) Dendrimers as support for recoverable catalysts and reagents. Chem Rev 102:3717
26. Crooks RM, Zhao MQ, Sun L, Chechik V, Yeung LK (2001) Dendrimer-encapsulated metal nanoparticles: synthesis, characterization, and applications to catalysis. Acc Chem Res 34:181
27. Astruc D, Chardac F (2001) Dendritic catalysts and dendrimers in catalysis. Chem Rev 101:2991
28. Broussard ME, Juma B, Train SG, Peng W-J, Laneman SA, Stanley GG (1993) A bimetallic hydroformylation catalyst: high regioselectivity and reactivity through homobimetallic cooperativity. Science 260:1784
29. Li Y, Liu JH-C, Witham CA, Huang W, Marcus MA, Fakra SC, Alayoglu P, Zhu Z, Thompson CM, Arjun A, Lee K, Gross E, Toste FD, Somorjai GA (2011) A Pt-cluster-based heterogeneous catalyst for homogeneous catalytic reactions: x-ray absorption spectroscopy and reaction kinetic studies of their activity and stability against leaching. J Am Chem Soc 133:13527
30. Kragl U, Dreisbach C (1996) Continuous asymmetric synthesis in a membrane reactor. Angew Chem Int Ed Engl 35:642
31. Castillo VA, Kuhn JN (2012) Role of the Ni:Fe ratio in ethylene hydrogenation activity for silica-supported Ni-Fe clusters prepared by dendrimer-templating. J Phys Chem C 116:8627
32. Bae H, Rao KN, Ha H (2011) Structural characterization and catalytic activity of Pt dendrimer encapsulated nanoparticles supported over Al2O3 for SCR of NOx. J Nanosci Nanotechnol 11:6136
33. Lopez-De Jesus YM, Vicente A, Lafaye G, Marecot P, Williams CT (2008) Synthesis and characterization of dendrimer-derived supported iridium catalysts. J Phys Chem C 112:13837
34. Kuhn JN, Huang WY, Tsung CK, Zhang YW, Somorjai GA (2008) Structure sensitivity of carbon-nitrogen ring opening: impact of platinum particle size from below 1 to 5 nm upon pyrrole hydrogenation product selectivity over monodisperse platinum nanoparticles loaded onto mesoporous silica. J Am Chem Soc 130:14026
35. Krishnan GR, Sreekumar K (2008) First example of organocatalysis by polystyrene-supported PAMAM dendrimers: highly efficient and reusable catalyst for Knoevenagel condensations. European J Org Chem 281:4763
36. Lu X, Imae T (2007) Dendrimer-mediated synthesis of water-dispersible carbon-nanotube-supported oxide nanoparticles. J Phys Chem C 111:8459
37. Chase PA, Gebbink R, van Koten G (2004) Where organometallics and dendrimers merge: the incorporation of organometallic species into dendritic molecules. J Organomet Chem 689:4016
38. Astruc D, Ornelas C, Aranzaes JR (2008) Ferrocenyl-terminated dendrimers: design for applications in molecular electronics, molecular recognition and catalysis. J Inorg Organomet Polym Mater 18:4
39. Astruc D, Ornelas C, Ruiz J (2008) Metallocenyl dendrimers and their applications in molecular electronics, sensing, and catalysis. Acc Chem Res 41:841
40. Astruc D (2012) Electron-transfer processes in dendrimers and their implication in biology, catalysis, sensing and nanotechnology. Nat Chem 4:255
41. Caminade A-M, Ouali A, Keller M, Majoral J-P (2012) Organocatalysis with dendrimers. Chem Soc Rev 41:4113
42. Myers VS, Weir MG, Carino EV, Yancey DF, Pande S, Crooks RM (2011) Dendrimer-encapsulated nanoparticles: new synthetic and characterization methods and catalytic applications. Chem Sci 2:1632

43. Somorjai GA, Aliaga C (2010) Molecular studies of model surfaces of metals from single crystals to nanoparticles under catalytic reaction conditions. Evolution from prenatal and postmortem studies of catalysts. Langmuir 26:16190
44. Burda C, Chen X, Narayanan R, El-Sayed MA (2005) Chemistry and properties of nanocrystals of different shapes. Chem Rev 105:1025
45. Lee H, Habas SE, Kweskin S, Butcher D, Somorjai GA, Yang P (2006) Morphological control of catalytically active platinum nanocrystals. Angew Chem 118:7988
46. Gomez MV, Giuerra J, Velders AH, Crooks RM (2009) NMR characterization of fourth-generation PAMAM dendrimers in the presence and absence of palladium dendrimer-encapsulated nanoparticles. J Am Chem Soc 131:341–350
47. Niu YH, Yeung LK, Crooks RM (2001) Size-selective hydrogenation of olefins by dendrimer-encapsulated palladium nanoparticles. J Am Chem Soc 123:6840
48. Balogh L, Tomalia DA (1998) Poly(amidoamine) dendrimer-templated nanocomposites. 1. Synthesis of zerovalent copper nanoclusters. J Am Chem Soc 120:7355
49. Zhao M, Sun L, Crooks RM (1998) Preparation of Cu nanoclusters within dendrimer templates. J Am Chem Soc 120:4877
50. Zhao MQ, Crooks RM (1999) Dendrimer-encapsulated Pt nanoparticles: synthesis, characterization, and applications to catalysis. Adv Mater 11:217
51. Zhao MQ, Crooks RM (1999) Homogeneous hydrogenation catalysis with monodisperse, dendrimer-encapsulated Pd and Pt nanoparticles. Angew Chem Int Ed 38:364
52. Huang W, Kuhn JN, Tsung C-K, Zhang Y, Habas SE, Yang P, Somorjai GA (2008) Dendrimer templated synthesis of one nanometer Rh and Pt particles supported on mesoporous silica: catalytic activity for ethylene and pyrrole hydrogenation. Nano Lett 8:2027
53. Yeung LK, Crooks RM (2001) Heck heterocoupling within a dendritic nanoreactor. Nano Lett 1:14
54. Niu YH, Crooks RM (2003) Preparation of dendrimer-encapsulated metal nanoparticles using organic solvents. Chem Mater 15:3463
55. Satoh N, Nakashima T, Kamikura K, Yamamoto K (2008) Quantum size effect in TiO2 nanoparticles prepared by finely controlled metal assembly on dendrimer templates. Nat Nanotechnol 3:106
56. Nakamula I, Yamanoi Y, Yonezawa T, Imaoka T, Yamamoto K, Nishihara H (2008). Nanocage catalysts-rhodium nanoclusters encapsulated with dendrimers as accessible and stable catalysts for olefin and nitroarene hydrogenations. Chem Comm 44:5716
57. Ornelas C, Aranzaes JR, Salmon L, Astruc D (2008) "Click" dendrimers: synthesis, redox sensing of Pd(OAc)(2), and remarkable catalytic hydrogenation activity of precise Pd nanoparticles stabilized by 1,2,3-triazole-containing dendrimers. Chemistry 14:50
58. Diallo AK, Ornelas C, Salmon L, Aranzaes JR, Astruc D (2007) "Homeopathic" catalytic activity and atom-leaching mechanism in Miyaura-Suzuki reactions under ambient conditions with precise dendrimer-stabilized Pd nanoparticles. Angew Chem Int Ed 46:8644
59. Peng C, Li K, Cao X, Xiao T, Hou W, Zheng L, Guo R, Shen M, Zhang G, Shi X (2012) Facile formation of dendrimer-stabilized gold nanoparticles modified with diatrizoic acid for enhanced computed tomography imaging applications. Nanoscale 4:6768
60. Liu H, Sun K, Zhao J, Guo R, Shen M, Cao X, Zhang G, Shi X (2012) Dendrimer-mediated synthesis and shape evolution of gold-silver alloy nanoparticles. Colloids Surf A Physicochem Eng Asp 405:22
61. Niu YH, Sun L, Crooks RA (2003) Determination of the intrinsic proton binding constants for poly(amidoamine) dendrimers via potentiometric pH titration. Macromolecules 36:5725
62. Scott RWJ, Ye HC, Henriquez RR, Crooks RM (2003) Synthesis, characterization, and stability of dendrimer-encapsulated palladium nanoparticles. Chem Mater 15:3873
63. Knecht MR, Garcia-Martinez JC, Crooks RM (2005) Hydrophobic dendrimers as templates for Au nanoparticles. Langmuir 21:11981
64. Knecht MR, Garcia-Martinez JC, Crooks RM (2006) Synthesis, characterization, and magnetic properties of dendrimer-encapsulated nickel nanoparticles containing <150 atoms. Chem Mater 18:5039

65. Knecht MR, Crooks RM (2007) Magnetic properties of dendrimer-encapsulated iron nanoparticles containing an average of 55 and 147 atoms. New J Chem 31:1349
66. Gates AT, Nettleton EG, Myers VS, Crooks RM (2010) Synthesis and characterization of NiSn dendrimer-encapsulated nanoparticles. Langmuir 26:12994
67. Chandler BD, Long CG, Gilbertson JD, Pursell CJ, Vijayaraghavan G, Stevenson KJ (2010) Enhanced oxygen activation over supported bimetallic Au–Ni catalysts. J Phys Chem C 114:11498
68. Zhao MQ, Crooks RM (1999) Intradendrimer exchange of metal nanoparticles. Chem Mater 11:3379
69. Chung YM, Rhee HK (2003) Partial hydrogenation of 1,3-cyclooctadiene using dendrimer-encapsulated Pd-Rh bimetallic nanoparticles. J Mol Catal A Chem 206:291
70. Chung YM, Rhee HK (2003) Pt-Pd bimetallic nanoparticles encapsulated in dendrimer nanoreactor. Catal Lett 85:159
71. Scott RWJ, Datye AK, Crooks RM (2003) Bimetallic palladium-platinum dendrimer-encapsulated catalysts. J Am Chem Soc 125:3708
72. Chung YM, Rhee HK (2004) Synthesis and catalytic applications of dendrimer-templated bimetallic nanoparticles. Catal Surv Asia 8:211
73. Scott RWJ, Wilson OM, Oh SK, Kenik EA, Crooks RM (2004) Bimetallic palladium-gold dendrimer-encapsulated catalysts. J Am Chem Soc 126:15583
74. Weir MG, Knecht MR, Frenkel AI, Crooks RM (2010) Structural analysis of PdAu dendrimer-encapsulated bimetallic nanoparticles. Langmuir 26:1137
75. Lang H, Maldonado S, Stevenson KJ, Chandler BD (2004) Synthesis and characterization of dendrimer templated supported bimetallic Pt-Au nanoparticles. J Am Chem Soc 126:12949
76. Zhang J, Lima FHB, Shao MH, Sasaki K, Wang JX, Hanson J, Adzic RR (2005) Platinum monolayer on nonnoble metal–noble metal core–shell nanoparticle electrocatalysts for O2 reduction. J Phys Chem B 109:22701
77. Wang JX, Inada H, Wu L, Zhu Y, Choi Y, Liu P, Zhou W-P, Adzic RR (2009) Oxygen reduction on well-defined core–shell nanocatalysts: particle size, facet, and pt shell thickness effects. J Am Chem Soc 131:17298
78. Zhai J, Huang M, Dong S (2007) Electrochemical designing of Au/Pt core shell nanoparticles as nanostructured catalyst with tunable activity for oxygen reduction. Electroanalysis 19:506
79. Li X, Liu J, He W, Huang Q, Yang H (2010) Influence of the composition of core–shell Au–Pt nanoparticle electrocatalysts for the oxygen reduction reaction. J Colloid Interface Sci 344:132
80. Carino EV, Crooks RM (2011) Characterization of Pt@Cu core@shell dendrimer-encapsulated nanoparticles synthesized by Cu underpotential deposition. Langmuir 27:4227
81. Yancey DF, Carino EV, Crooks RM (2010) electrochemical synthesis and electrocatalytic properties of Au@Pt dendrimer-encapsulated nanoparticles. J Am Chem Soc 132:10988
82. Borodko Y, Thompson CM, Huang W, Yildiz HB, Frei H, Somorjai GA (2011) spectroscopic study of platinum and rhodium dendrimer (PAMAM G4OH) compounds: structure and stability. J Phys Chem C 115:4757
83. Goldfarb TD, Khare BN (1967) Infrared spectra of solid and matrix-isolateD (CH3)3N (CD3)3N and (SIH3)3N. J Chem Phys 46:3379
84. Murphy WF, Zerbetto F, Duncan JL, McKean DC (1993) Vibrational spectrum and harmonic force field of trimethylamine. J Phys Chem 97:581
85. Lee S-H, Krimm S (1998) Ab initio-based vibrational analysis of α-poly(L-alanine). Biopolymers 46:283
86. Garcia-Martinez JC, Scott RWJ, Crooks RM (2003) Extraction of monodisperse palladium nanoparticles from dendrimer templates. J Am Chem Soc 125:11190
87. Ye HC, Scott RWJ, Crooks RM (2004) Synthesis, characterization, and surface immobilization of platinum and palladium nanoparticles encapsulated within amine-terminated poly(amidoamine) dendrimers. Langmuir 20:2915
88. Ozturk O, Black TJ, Perrine K, Pizzolato K, Williams CT, Parsons FW, Ratliff JS, Gao J, Murphy CJ, Xie H, Ploehn HJ, Chen DA (2005) Thermal decomposition of generation-4

polyamidoamine dendrimer films: decomposition catalyzed by dendrimer-encapsulated Pt particles. Langmuir 21:3998

89. Alexeev OS, Siani A, Lafaye G, Williams CT, Ploehn HJ, Amiridis MD (2006) EXAFS characterization of dendrimer-Pt nanocomposites used for the preparation of Pt/gamma-Al2O3 catalysts. J Phys Chem B 110:24903
90. Knecht MR, Weir MG, Myers VS, Pyrz WD, Ye HC, Petkov V, Buttrey DJ, Frenkel AI, Crooks RM (2008) Synthesis and characterization of Pt dendrimer-encapsulated nanoparticles: effect of the template on nanoparticle formation. Chem Mater 20:5218
91. Petkov V, Bedford N, Knecht MR, Weir MG, Crooks RM, Tang W, Henkelman G, Frenkel A (2008) Periodicity and atomic ordering in nanosized particles of crystals. J Phys Chem C 112:8907
92. Lang HF, May RA, Iversen BL, Chandler BD (2003) Dendrimer-encapsulated nanoparticle precursors to supported platinum catalysts. J Am Chem Soc 125:14832
93. Deutsch DS, Lafaye G, Liu DX, Chandler B, Williams CT, Amiridis MD (2004) Decomposition and activation of Pt-dendrimer nanocomposites on a silica support. Catal Lett 97:139
94. Beakley LW, Yost SE, Cheng R, Chandler BD (2005) Nanocomposite catalysts: dendrimer encapsulated nanoparticles immobilized in sol-gel silica. Appl Catal Gen 292:124
95. Lafaye G, Siani A, Marecot P, Amiridis MD, Williams CT (2006) Particle size control in dendrimer-derived supported ruthenium catalysts. J Phys Chem B 110:7725
96. Ye HC, Crooks RM (2005) Electrocatalytic O-2 reduction at glassy carbon electrodes modified with dendrimer-encapsulated Pt nanoparticles. J Am Chem Soc 127:4930
97. Wilson OM, Knecht MR, Garcia-Martinez JC, Crooks RM (2006) Effect of Pd nanoparticle size on the catalytic hydrogenation of allyl alcohol. J Am Chem Soc 128:4510
98. Albiter MA, Crooks RM, Zaera F (2010) Adsorption of carbon monoxide on dendrimer-encapsulated platinum nanoparticles: liquid versus gas phase. J Phys Chem Lett 1:38
99. Bond GC (1985) The origins of particle size effects in heterogeneous catalysis. Surf Sci 156(pt 2):966
100. Witham CA, Huang WY, Tsung CK, Kuhn JN, Somorjai GA, Toste FD (2009) Converting homogeneous to heterogeneous in electrophilic catalysis using monodisperse metal nanoparticles. Nat Chem 2:36
101. Huang W, Liu JH-C, Alayoglu P, Li Y, Witham CA, Tsung C-K, Toste FD, Somorjai GA (2010) Highly active heterogeneous palladium nanoparticle catalysts for homogeneous electrophilic reactions in solution and the utilization of a continuous flow reactor. J Am Chem Soc 132:16771
102. Gross E, Liu JH-C, Toste FD, Somorjai GA (2012) Control of selectivity in heterogeneous catalysis by tuning nanoparticle properties and reactor residence time. Nat Chem 4:947
103. Maity P, Yamazoe S, Tsukuda T (2013) Dendrimer-encapsulated copper cluster as a chemoselective and regenerable hydrogenation catalyst. ACS Catal 3:182

Chapter 5
Core–Shell Nanoarchitectures as Stable Nanocatalysts

Sang Hoon Joo, Jae Yeong Cheon, and Joon Yong Oh

The recent merging of catalysis with colloidal chemistry has dramatically enhanced the molecular-scale design and synthesis of heterogeneous catalysts. The development of stable catalysts, along with their enhanced activity and selectivity, has been a key issue in catalysis research. In this chapter, we review the recent progress in nanochemistry-based approaches to stable nanocatalysts. We present synthesis strategies for core– and yolk–shell-structured stable nanocatalysts. We next summarize the enhanced catalytic properties of such nanocatalysts in terms of thermal and chemical stabilities, as well as their catalytic activity and selectivity. Finally, we highlight future challenges and perspectives for stable nanocatalysts.

5.1 Introduction

Recent developments in nanotechnology have motivated a revolution in the preparation of heterogeneous catalysts [1–5]. The synthetic capability of colloidal nanochemistry permits the synthesis of catalytic metal nanoparticles (NPs) with precisely tailored size, shape, and composition [6–11]. Hence, these nanomaterials have been effectively used as nanoscale analogues of model catalysts, such as metal single crystals, allowing the identification of atomic-scale factors responsible for the activity and selectivity in catalytic reactions. In parallel with the pursuit of higher activity and selectivity, the development of thermally and chemically stable catalysts has been a long-standing issue in the field of catalysis. Industrial catalytic reactions are predominantly carried out under high temperature and/or

---

S.H. Joo (✉) • J.Y. Cheon • J.Y. Oh
School of Nano-Bioscience and Chemical Engineering, KIER-UNIST Advanced Center for Energy and Low Dimensional Carbon Materials Center, Ulsan National Institute of Science and Technology (UNIST), UNIST-gil 50, Ulsan 689-798, Republic of Korea
e-mail: shjoo@unist.ac.kr

J.Y. Park (ed.), *Current Trends of Surface Science and Catalysis*,
DOI 10.1007/978-1-4614-8742-5_5,

pressure. Under such demanding conditions, catalytic NPs dispersed on an oxide support are subjected to aggregation and sintering, leading to a decrease in the active sites available for catalytic reactions, which consequently reduces the life cycle of a catalyst. To mitigate the sintering problem, various strategies have been explored in traditional catalysts, including the addition of co-catalysts, formation of multi-metallic alloys, and exploitation of the strong metal–support interaction (SMSI) [12–14].

Ideally, if an individual NP can be encapsulated in a thermally stable inorganic shell layer, the geometric confinement of the metal NPs at the core can provide a physical barrier that prevents their mobility under high temperature or pressure, thereby suppressing sintering or aggregation of the NPs. Significantly, additional advantageous effects other than the enhanced stability can evolve in this core–shell nanostructure. For instance, if the core metal is coated with a catalytically active metal oxide, such as CeO_2, maximizing the contact area between the metal and the support could significantly enhance the metal–support interaction. In 2004, Alivisatos and Somorjai first recognized the individual nanoreactor concept by preparing a Pt NP encapsulated within a CoO layer [15], made possible by colloidal nanochemistry. Since then, several types of core–shell nanostructures for multifunctional nanocatalysts have emerged [16–19]. The most straightforward route to this endeavor is the direct coating of an individual metal NP with a porous oxide layer, generating metal/metal oxide core–shell-structured nanocatalysts. The yolk–shell nanocatalysts are prepared by the formation of a dense oxide layer on a single NP, followed by selective partial etching of metal particles or a metal oxide layer. The overcoating strategies have also been extended to traditional supported catalysts, affording metal oxide/metal/metal oxide-multilayered nanocatalysts. Figure 5.1 presents schematic models of the three classes of nanocatalysts. These core–shell-structured nanocatalysts have been utilized in various gas- and liquid-phase catalytic reactions and have shown superior stability over catalysts without coated layers, while maintaining similar catalytic activity. Furthermore, in some instances, the beneficial effects of nanoscale confinement were manifested as enhanced activity and selectivity in the core–shell-structured nanocatalysts.

In this chapter, we present recent advances in the design and synthesis of stable core–shell (or yolk–shell) nanocatalysts and their application in catalytic reactions. These nanocatalysts are classified into three classes: (1) core–shell catalysts; (2) yolk–shell catalysts; and (3) supported catalysts coated with shell layers. We introduce each class of nanocatalysts in the following sections; we highlight representative examples of the synthetic strategies for each class of nanocatalyst, followed by their catalytic properties. We conclude this chapter with future perspectives and challenges related to the design of core–shell catalysts. The core–shell nanostructures with compositions other than metal/metal oxides for applications in spectroscopy, magnetism, and biology are beyond the scope of this paper; they are covered in other recent excellent reviews [20–22].

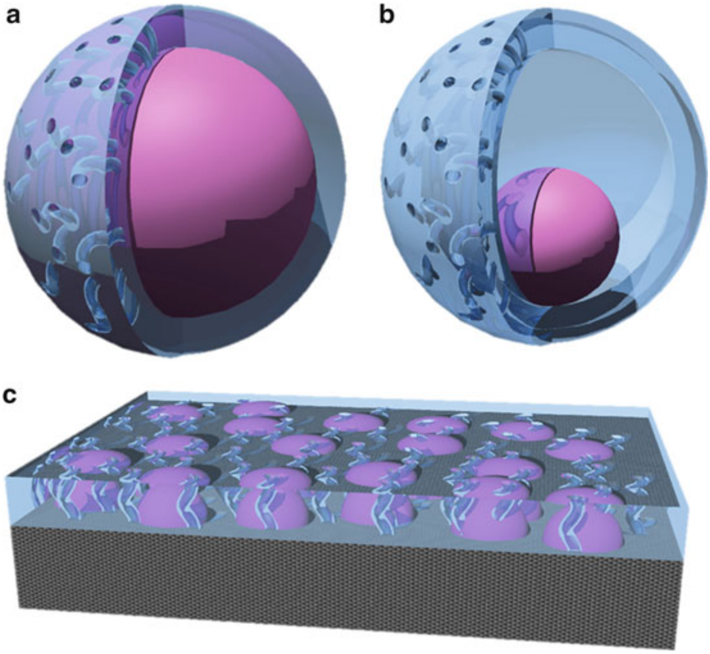

Fig. 5.1 Schematic representations of three types of stable nanocatalysts: (**a**) core–shell and (**b**) yolk–shell nanostructures. (**c**) Supported catalysts covered with a shell layer

5.2 Metal/Metal Oxide Core–Shell Nanocatalysts

5.2.1 Core–Shell Nanocatalysts with a Silica Shell

Among metal oxide compositions, the chemistry of silica is the most widely studied and well established, from the classical Stöber synthesis of a silica sphere [23] to the recently developed surfactant-mediated synthesis of mesoporous silica [24, 25]. These developments were mainly enabled by the availability of stable silica precursors, their controllable hydrolysis and condensation, and the stable oxidation state of silica. Based on previously established chemistries, sol–gel or microemulsion methods were used to synthesize silica-shell-based core–shell NPs.

Somorjai and his co-workers reported a straightforward route to platinum–mesoporous silica core–shell (Pt@mSiO_2) NPs that are thermally stable at high temperatures [26]. The synthesis of the core–shell Pt@mSiO_2 NPs was performed in three steps (Fig. 5.2): (1) synthesis of the Pt NPs using tetradecyltrimethyl ammonium bromide (TTAB) surfactant as the capping agent; (2) silica polymerization around the Pt cores via the sol-gel method, which generated the as-synthesized Pt@SiO_2 mesostructures; and (3) removal of the TTAB molecules using calcination to

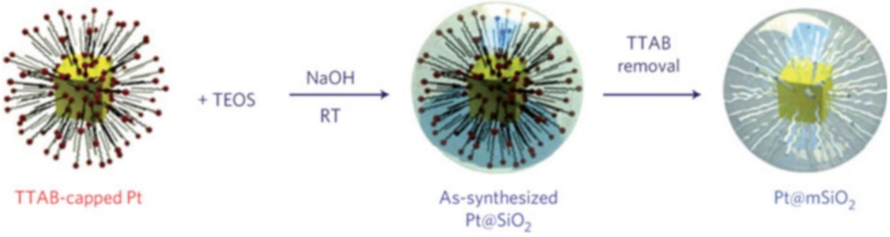

Fig. 5.2 Schematic representation of the synthesis of core–shell Pt@mSiO$_2$NPs. Adapted from ref. [26]

produce the Pt@mSiO$_2$ core–shell NPs. The key point of this synthetic scheme is the use of a cationic surfactant (in this case, TTAB) both as a capping agent for the synthesis of the metallic core NPs and as the structure-directing agent for the growth of the silica shell layers. TEM images and nitrogen adsorption analysis revealed that the silica shell layer in the final Pt@mSiO$_2$ NPs was mesoporous (Fig. 5.3a, b). In the core–shell structure of the Pt@mSiO$_2$ NPs, the reacting molecules can directly access the Pt cores through the mesopores within the silica shells, and the product molecules can readily exit through these mesopores. The Pt cores were engaged in the silica shells at temperatures up to 750 °C in air (Fig. 5.3c). In catalytic reaction applications, the Pt@mSiO$_2$ NP catalysts exhibited catalytic activity similar to the TTAB-capped Pt NPs for ethylene hydrogenation and CO oxidation (Fig. 5.3d). Importantly, after CO oxidation performed at up to 300 °C, the morphology of the Pt@mSiO$_2$ core–shell particles was essentially preserved, whereas that of the bare Pt NPs or Pt NPs supported on mesoporous silica experienced a significant degree of deformation or aggregation of particles (Fig. 5.4). We note that the high thermal stability of the Pt@mSiO$_2$ NPs enabled the study of ignition behavior during the Pt NP-catalyzed CO oxidation process. The high thermal stability and the uniform mesoporous shell structure suggest that the Pt@mSiO$_2$ core–shell NPs are a NP system that allows for catalytic reactions or surface chemical processes to occur at high temperature.

Similar or modified synthetic strategies for thermally stable core–shell nanocatalysts were also reported by other groups. McFarland's group reported the synthesis of core–shell Pd@SiO$_2$ NPs as active and sinter-resistant nanocatalysts [27]. They used a microemulsion method to prepare Pd@SiO$_2$ NPs. In this synthesis, a mixture of tetraethyl-orthosilicate (TEOS) and *n*-octyldecyltrimethoxysilane (C$_{18}$-TMS) was used as the silica source, with C$_{18}$-TMS being used as the porogen to endow porosity to the silica layer. Under high-temperature calcination at 700 °C, the core–shell Pd@SiO$_2$ NPs maintained their original shape with minimal sintering of the core Pd particles, whereas the traditional silica-supported Pd (Pd/SiO$_2$) catalyst exhibited noticeable aggregation of the Pd particles. During CO oxidation, the Pd@SiO$_2$ nanocatalysts initially showed a higher light-off temperature compared to the Pd/SiO$_2$ catalysts, indicating a low activity of the Pd@SiO$_2$ core–shell nanocatalyst. After calcination at 700 °C for 6 h in air, the Pd@SiO$_2$ nanocatalyst retained its

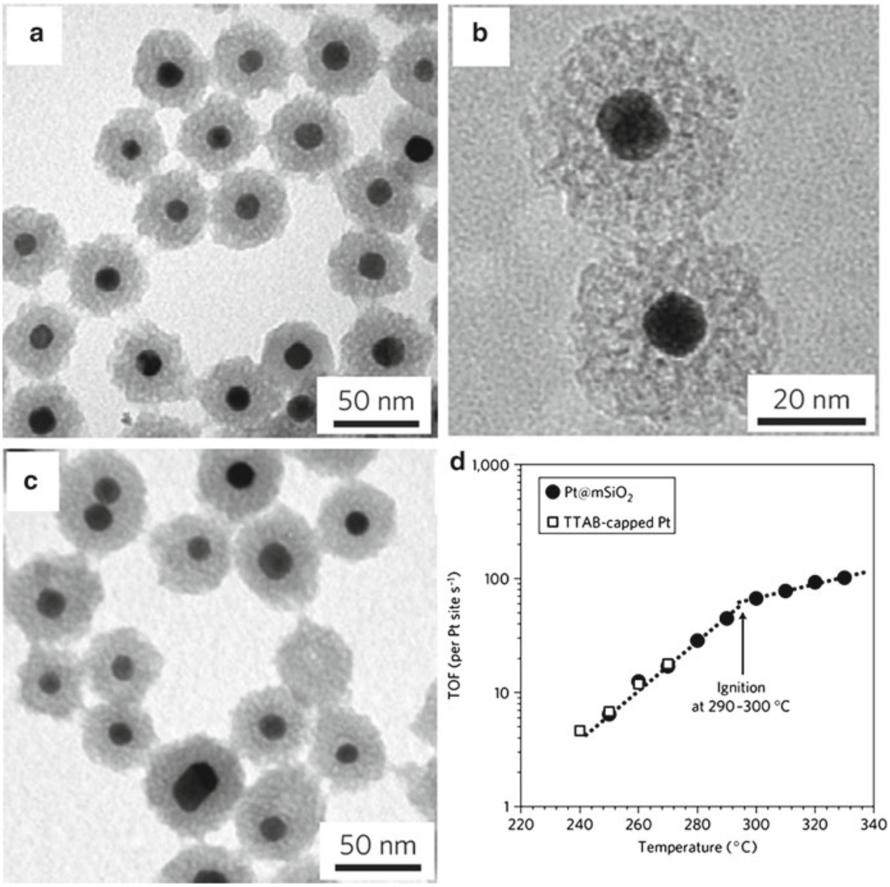

Fig. 5.3 TEM images of Pt@mSiO$_2$core–shell NPs after calcination at (**a**, **b**) 350 °C and (**c**) 750 °C. (**d**) CO oxidation activity of TTAB-capped Pt and Pt@mSiO$_2$ NPs. Adapted from ref. [26]

activity, whereas the supported Pd/SiO$_2$ catalyst showed a significant shift to a much higher light-off temperature. These results are consistent with the enhanced sintering stability of the Pd@SiO$_2$ nanocatalysts at high temperature. We note that for acetylene hydrogenation, the fresh Pd@SiO$_2$ catalyst was active at a much lower temperature than the fresh Pd/SiO$_2$ catalyst. Moreover, after calcination at 700 °C for 6 h in air, the light-off curve of the Pd@SiO$_2$ catalyst showed only a slight shift, whereas that of the control Pd/SiO$_2$ catalyst significantly increased, indicating the sintering of the latter. Although a definite reason for the better performance of the Pd@SiO$_2$ nanocatalyst was not suggested, the acetylene hydrogenation results suggest that the core–shell geometry can provide both a physical barrier for the sintering-resistant effect but can also potentially alter the catalytic pathway. McFarland's group later extended the microemulsion strategy to core–shell NPs composed of ferromagnetic magnetite cores and silica shells (Fe$_3$O$_4$@SiO$_2$) [28]. The core–shell

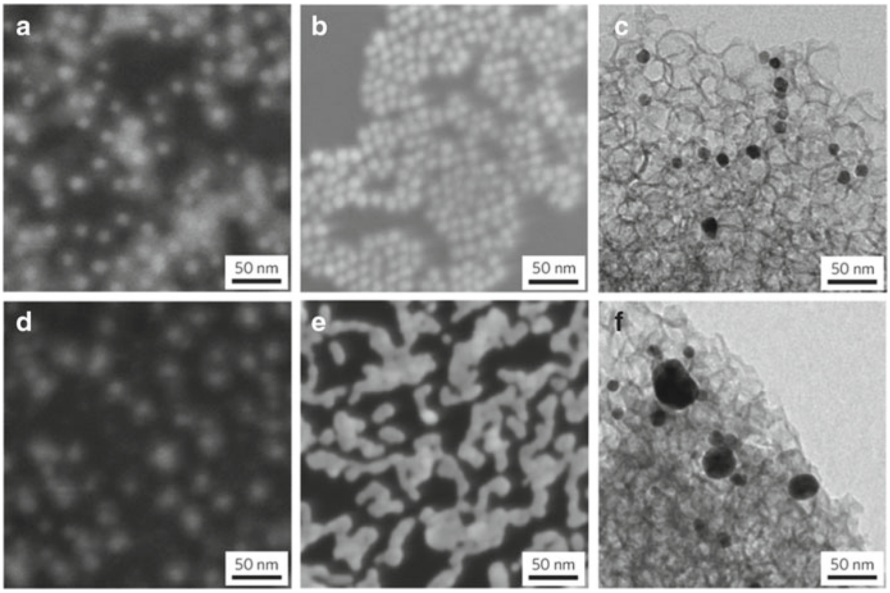

Fig. 5.4 Comparison of morphology changes before and after CO oxidation. SEM images of (**a**, **d**) core–shell Pt@mSiO_2 NPs and (**b**, **e**) TTAB-capped Pt NPs on a silicon wafer, and TEM images of (**c**, **f**) TTAB-capped Pt nanoparticles dispersed on an MCF mesoporous silica support, (**a**–**c**) before and after CO oxidation at (**d**) 330 °C and at (**e**, **f**) 300 °C. Adapted from ref. [26]

Fe_3O_4@SiO_2 nanocatalysts were active for CO oxidation and the chemical looping combustion of methane at temperatures as high as 700 °C. Significantly, the Fe_3O_4@SiO_2 NPs retained their magnetism following the reaction, which provides potential for use in magnetic separation and capture in moving-bed reactor applications. The core magnetite within the silica shell was resistant to sintering and transition to the bulk phase at temperatures as high as 700 °C. These catalysts can be used in high-temperature applications where catalyst recovery by magnetic separation is required.

The use of core–shell catalysts for high-temperature reactions was also extended to the ammonia decomposition reaction, as reported by Schüth and his co-workers [29]. They first synthesized hematite NPs with controlled particle size (35, 47, and 75 nm) using the hydrothermal reaction, followed by the formation of a porous silica shell by means of base-catalyzed hydrolysis of TEOS using cetyltetramethylammonium bromide (CTABr) as the porogen. After calcination, the α-Fe_2O_3@SiO_2 core–shell nanocatalysts were obtained. In ammonia decomposition, the α-Fe_2O_3@SiO_2 nanocatalysts had high reaction rates at temperatures above 600 °C, while maintaining stability up to 800 °C. A reference material that consisted of similar components, but without a core–shell structure, exhibited an inferior stability and long-term activity compared to the core–shell-structured catalysts. In their work, in situ XRD measurements under reaction conditions over the α-Fe_2O_3@SiO_2

nanocatalysts revealed the presence of body-centered iron and FeN_x, which are considered the most active iron phases for ammonia decomposition.

The use of core–shell nanocatalysts for the decomposition of ammonia was also explored by Au and his co-workers. They prepared core–shell-structured microcapsule-like $Ru@SiO_2$ NPs [30]. Although the porosity of the silica shells of $Ru@SiO_2$ NPs were not clearly verified, they were demonstrated as efficient materials for CO_x-free hydrogen production via ammonia decomposition. The active Ru core particles retained good stability even at high temperatures (up to 650 °C) owing to the protection provided by the inert SiO_2 nanoshell. Au and his co-workers later extended the same synthetic strategy to other core–shell metal/metal oxide compositions (metal = Fe, Co, Ni, and Ru; metal oxides = SiO_2, Al_2O_3, and MgO) and investigated the structural parameters of the core–shell nanocatalysts for NH_3 decomposition [31]. The core–shell particles were also effective for partial oxidation of methane to synthesis gas. Au and his co-workers [32] and Ji and his co-workers [33] prepared $Ni@SiO_2$ and $CoNi@SiO_2$ core–shell particles, respectively, and demonstrated that these core–shell particles were active for partial oxidation of methane. As demonstrated in other examples, the silica shell layers effectively prevented aggregation of the core particles. The silica coating strategy was also extended for composition with metal oxide cores. Along this line, Kaliaguine and his co-workers used the core–shell-structured $LaMn_{0.7}Fe_{0.3}O_{3.15}@mSiO_2$ particles as oxygen carriers for chemical looping combustion [34]. The core–shell $LaMn_{0.7}Fe_{0.3}O_{3.15}@mSiO_2$ particles showed unchanged morphology after multiple redox cycles without losing catalytic activity.

5.2.2 Non-Siliceous Oxide Shells

The role of silica shells in $metal@SiO_2$ core–shell nanocatalysts is mostly related to the stabilization of metal particles against demanding thermal or chemical environments. If the silica shells are replaced with catalytically active metal oxides, such as CeO_2 or TiO_2, additional catalytic properties are expected to evolve. For instance, the noble metals supported by ceria-based materials are among the systems long known to exhibit SMSI effects [35]. These catalysts have been shown to provide high activity for hydrogenation reactions, water–gas shift (WGS) reactions, CO and hydrocarbon oxidation, etc. Hence, if the noble metal NPs are encapsulated within shells composed of such metal oxides, the degree of metal–support interaction through the enlarged contact area between the metal cores and the ceria shells would be enlarged, which could result in enhanced catalytic activity. Nevertheless, the preparation of core–shell catalysts with non-siliceous oxide shells is not as straightforward as that of the silica shell. Compared to silica, other metal oxides are often more susceptible to hydrolysis, redox reactions, or phase transitions, accompanied by thermal breakdown of the structural integrity. Recent developments in nanochemistry, combined with judicious control of the synthetic parameters, however, enabled successful preparations of core–shell nanocatalysts with non-siliceous shell layers.

For this purpose, Tsang's group recognized an opportunity to prepare Pt@CeO_2 core–shell nanocatalysts and demonstrated that the latter were highly active and selective in the WGS reaction but were completely inert for methanation [36]. The group synthesized Pt@CeO_2 core–shell nanocatalysts using a modified microemulsion method in the presence of CTABr surfactant. In this method, the auto-redox reactions of Pt(IV) [$(NH_4)_2PtCl_6$] and Ce(III) [$Ce(NO_3)_3$] species generated a reduced Pt NP core and an oxidized CeO_2 NP shell layer, respectively. Although the distinct core–shell geometry shown in M@SiO_2 was difficult to observe in the resulting particles, a detailed HR-TEM study revealed that the core was enriched with Pt inside each ceria particle. The TEM image of the Pt@CeO_2 particle was structurally similar to that of the Pt/ceria supported catalyst in the SMSI state where the metal particle was decorated by a few-angstrom-thick ceria (prepared above 500 °C under reduced conditions) [37]. The Pt@CeO_2 nanocatalysts showed very low activity for methanation in contrast to the conventionally prepared coprecipitated Pt/CeO_2. The inactivity of these materials for methanation was ascribed to the fact that the ceria shell can substantially reduce metal exposure. However, the core–shell catalysts showed comparable WGS activity with the Cu/ZnO and Pt/CeO_2 catalysts but without any methane formation, suggesting that the nature of the active sites for methanation may not be the same as that for WGS or that some metal sites may have been blocked by the ceria.

The Fornasiero and Gorte group carried out extensive work with metal@CeO_2 core–shell nanocatalysts using a newly developed synthesis scheme [38–41]. They prepared Pd@CeO_2 core–shell nanostructures that were easily dispersed in common organic solvents [38, 39]. The method involved the synthesis of Pd NPs protected by a monolayer of 11-mercaptoundecanoic acid. The carboxylic groups on the NP surfaces were used to direct the self-assembly of a cerium(IV) tetrakis (decyloxide) precursor around the metal particles, followed by controlled hydrolysis to form CeO_2. Although this method required multiple steps and the use of a rather complex cerium precursor, well-defined core–shell nanocatalysts could be generated (Fig. 5.5). They showed that the Pd@CeO_2 supported on Al_2O_3 showed activity for CO oxidation, WGS reaction, and methanol steam-reforming reactions, suggesting accessibility of the Pd phase in the nanocomposites [38].

The same group later demonstrated the dramatic effect of core–shell geometry in high-temperature methane oxidation [39]. They used a modular approach in which the Pd@CeO_2 core–shell particles were deposited onto a hydrophobically modified alumina support (H-Al_2O_3). The resulting Pd@CeO_2/H-Al_2O_3 catalyst showed outstanding catalytic performance. Complete conversion of methane was observed for a gas stream with 0.5 vol% CH_4 and 2.0 vol% O_2 in Ar at a space velocity of 200,000 mL g^{-1} h^{-1} at approximately 400 °C (Fig. 5.6a). In comparison, all the other reference samples (Pd/CeO_2 and Pd/CeO_2/Al_2O_3) prepared by the conventional incipient wetness catalyst method only achieved complete CH_4 conversion above 700 °C, more than 300 °C higher than that found in the Pd@CeO_2/H-Al_2O_3 catalyst. The enhanced reactivity of the Pd@CeO_2/H-Al_2O_3 catalyst was claimed as the result of the strong Pd/CeO_2 interaction among the core–shell Pd@CeO_2 units. By contrast, such metal–support interactions were not as optimal in the Pd/CeO_2 or Pd/

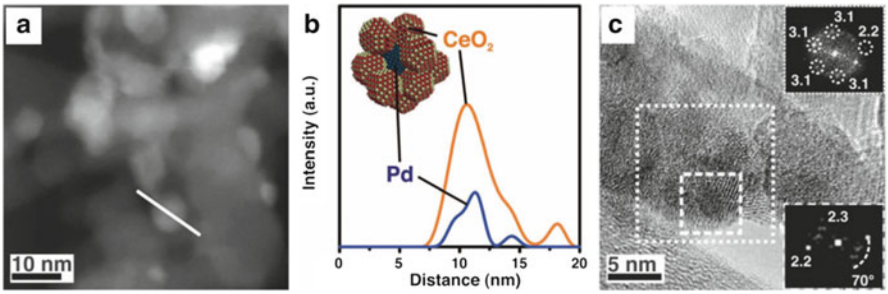

Fig. 5.5 TEM investigations of Pd@CeO_2 core–shell nanostructures dispersed on hydrophobic alumina. (**a**) High magnification HAADF-STEM image of the Pd@CeO_2/H-Al_2O_3 catalysts calcined at 500 °C and (**b**) the corresponding EDS line profile, together with a model. (**c**) High-resolution TEM image of a single Pd@CeO_2 structure on the Pd@CeO_2/H-Al_2O_3 catalysts calcined at 500 °C. The digital diffraction patterns of the particles in the *white squares* are reported in the *top-right* and *bottom-right* insets, together with representative bond distances (Å) and bond angles for the Pd and ceria. Adapted from ref. [39]

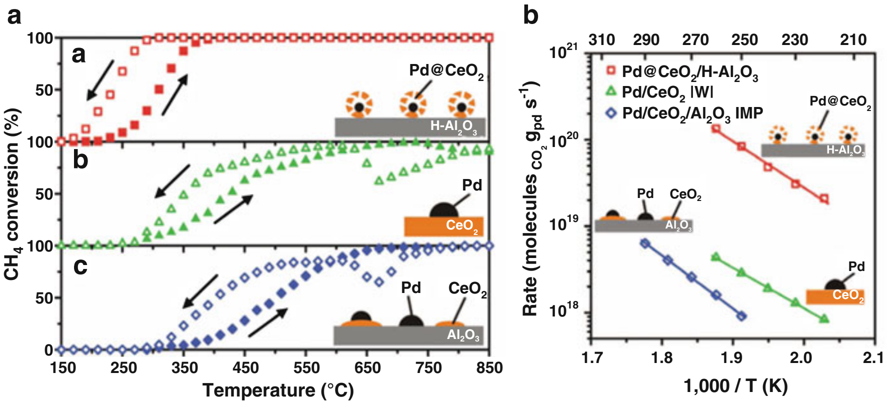

Fig. 5.6 (**a**) Heating and cooling (10 °C min^{-1}) light-off curves of CH_4 conversion versus temperature for the three catalysts used: (A) Pd@CeO_2/H-Al_2O_3 core–shell, (B) Pd/CeO_2, and (C) Pd/CeO_2/Al_2O_3 catalysts. (**b**) Kinetic rate data for CH_4 oxidation on the three catalysts. Adapted from ref. [39]

CeO_2/Al_2O_3 catalysts, resulting in lower activities compared to that of the Pd@CeO_2/H-Al_2O_3 catalyst. The kinetic rate data further corroborated the very high intrinsic activity of the Pd@CeO_2/H-Al_2O_3 catalyst compared to that of the reference catalysts (Fig. 5.6b). The reaction rates of the Pd@CeO_2/HAl_2O_3 sample were approximately 40 times higher than those of Pd/CeO_2-IWI and 200 times higher than those of Pd/CeO_2/Al_2O_3-IMP.

The group extended this synthesis scheme to core–shell structures with different compositions using Au, Pd, and Pt as cores and CeO_2, TiO_2, and ZrO_2 as shells [40, 41]. For instance, they encapsulated preformed Au NPs inside a porous ceria layer to yield Au@CeO_2 core–shell NPs [40]. The core–shell nanocatalyst with an Au loading of 1 wt% showed good activity under real preferential oxidation conditions and better activity than the catalysts with higher metal loadings or prepared through optimized deposition–precipitation methods described in the literature. Under simulated aging, the Au (1 wt%)@CeO_2 sample exhibited minor deactivation (mainly associated with the formation of carbonates) that can be reversed by a mild regenerative oxidative treatment to fully restore its initial activity. By contrast, the other catalysts showed either unavoidable reversible carbonate poisoning or irreversible deactivation because of the metal sintering/agglomeration phenomena.

Formation of the ceria shell utilizing the classical sol–gel methods was commonly hampered by the low hydrolysis ability of Ce cations in water or alcohol solutions. In this regard, Tang and his co-workers developed a self-template method for core–shell NPs with a ceria shell [42]. They exploited hydrothermal reactions to prepare the Au@CeO_2 core–shell NPs using $HAuCl_4$ and $CeCl_3$ as the precursors in an aqueous solution containing glucose and urea. In this synthesis, the Au^{3+} ions were first reduced by the glucose in the solution to yield Au NPs. Then, the condensation of glucose in the solution under hydrothermal conditions led to the formation of an amorphous carbon sphere with a diameter of 100–200 nm, where the Au NP was located at the center; the Ce^{3+} ions were embedded in the carbogenic layer. Finally, the carbon submicrospheres were used as sacrificial templates to generate Au@CeO_2 core–shell NPs via calcination in air. The prepared particles showed a distinct core–shell morphology, although the size was larger than that of the previous versions of the metal/ceria core–shell NPs. When these Au@CeO_2 submicrospheres were used as catalysts for CO oxidation, they exhibited considerably enhanced catalytic activity and stability compared to conventionally supported Au/CeO_2 catalysts, as revealed by their significantly lower light-off temperature.

Kayama and his co-workers developed a synthetic scheme that exploited a one-pot selective redox reaction using cerium(III) and silver(I) to produce core–shell Ag@CeO_2 NPs [43]. Co-precipitation by the addition of a cerium(III) nitrate and silver(I) nitrate aqueous solution to aqueous ammonia (equimolar to nitrate) yielded core–shell-structured NPs, where the Ag NPs at the core were surrounded by aggregates of the ceria particles. The core–shell Ag@CeO_2 nanocatalyst showed a lower conversion temperature for carbonaceous soot oxidation compared to the conventionally synthesized supported Ag/CeO_2 catalyst and CeO_2, demonstrating that its higher activity originated primarily from the enhanced metal–support interaction.

The synergistic effect of the ceria coating was not limited to enhancing catalytic activity; Kaneda's group demonstrated a highly chemoselective reaction by utilizing the core–shell Ag@CeO_2 nanocatalyst [44]. They synthesized the core–shell Ag@CeO_2 NPs by combining the reverse micelle technique and the redox reaction between silver(I) and cerium(III). The Ag@CeO_2 nanocatalyst comprised a core Ag NP that is 10 nm in diameter and a shell assembled with spherical CeO_2 NPs with a diameter of 3–5 nm. In this structure, the shell has nanospaces among the CeO_2 NPs that permit access of reactants to the active center of the Ag NPs. The Ag@CeO_2 catalyst showed remarkable improvement in chemoselectivity, compared to the Ag NPs supported on CeO_2 (Ag/CeO_2), for the reduction of both nitrostyrenes to aminostyrenes and epoxides to alkenes using H_2 (Fig. 5.7). The group suggested that the heterolytic cleavage of H_2 occurred at the interface between the Ag and CeO_2 NPs,

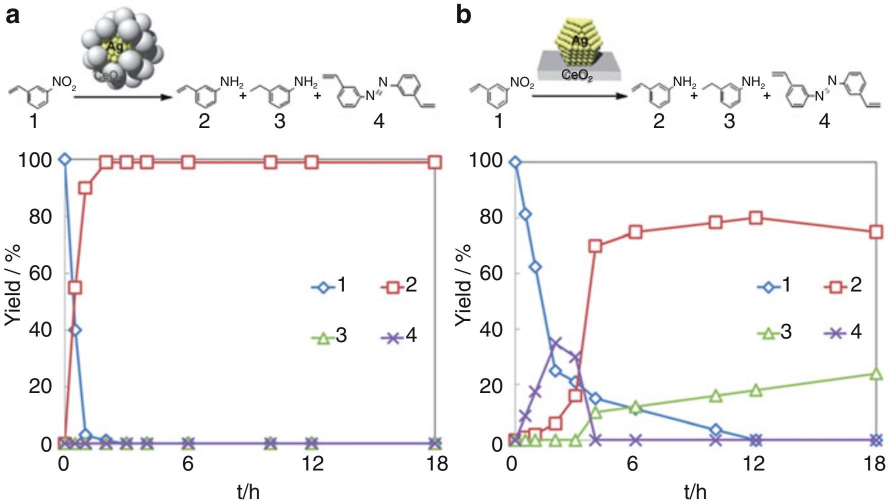

Fig. 5.7 The reduction of one with H_2 versus time using (**a**) core–shell Ag@CeO_2 and (**b**) supported Ag/CeO_2 catalysts. Adapted from ref. [44]

whereas the homolytic cleavage of H_2 occurred at the top of the Ag NPs. In the Ag@CeO_2 nanocatalyst, the interface area between Ag and CeO_2 can be maximized. This property enabled the exclusive formation of the heterolytically cleaved hydrogen species through the combined effect of the Ag and CeO_2, which suppressed the unfavorable formation of homolytically cleaved hydrogen species on bare Ag NPs. In addition, Ag@CeO_2 was easily separated from the reaction mixture and was reusable without loss of catalytic activity or selectivity.

The core–shell NPs with non-siliceous metal oxide coatings other than ceria were also explored, including SnO_2 [45], TiO_2 [46], Cu_2O [47], and ZnO [48]. For instance, Xie and her co-workers prepared Au@SnO_2 core–shell NPs, formed by the synthesis of Au NPs and subsequent formation of AuSn intermetallics, followed by oxidation, to yield Au@SnO_2 core–shell NPs [45]. Interestingly, the Au@SnO_2 core–shell nanocatalysts showed superior catalytic activity compared to the non-encapsulated supported Au/SnO_2 catalyst. By using X-ray photoelectron spectroscopy, they found that the interactions between the Au NPs and oxide support in the well-encapsulated Au@SnO_2 core–shell NPs were stronger than those in the non-encapsulated Au/SnO_2 catalyst, indicating a synergetic confinement effect in such nanoscale catalyst/support core-shell systems.

5.3 Metal/Metal Oxide Yolk–Shell Nanocatalysts

The yolk–shell nanostructure is a modified form of the core–shell configuration. The yolk–shell structure is distinguished from the core–shell structure in that the former has a hollow inner space between the core and the shell layers. Compared to the core–shell nanostructure, where the shell is directly interfaced at the metal surface, the cavity between the core and the shell in the yolk–shell structure provides a larger exposed metal surface for the reactants and enables the reactants to interact more homogeneously with the surface. Compared to the synthesis of core–shell NPs, the yolk–shell structure requires an additional etching step that generates hollow void spaces. The most widely used method of the yolk–shell nanostructure relies on the formation of a core–shell structure, followed by partial etching of the core or shell layers. A similar, yet alternative, scheme involves the formation of a core-shell1-shell2 triple-layered structure, followed by the etching of an intermediate shell layer to yield the yolk–shell nanostructure.

The group of Alivisatos and Somorjai developed the initial hollow yolk–shell structure nanoreactor concept [15]. They synthesized a Pt@CoO yolk–shell nanostructure in which a platinum nanocrystal a few nanometers in size was encapsulated in a hollow CoO shell. The synthesis of these nanoreactors consisted of three steps: synthesis of platinum NPs, deposition of cobalt on the platinum to form Pt@Co core–shell nanocrystals, and transformation of the cobalt into CoO hollow structures by bubbling oxygen gas. In the final step, oxidation removed the cobalt atoms from the platinum particle surface via the nanoscale Kirkendall effect, which led to the formation of a platinum yolk/CoO shell structure. The size of the Pt@CoO NPs could be tunable by changing the diameter and number of platinum seeds, and by changing the amount of cobalt precursor. The catalytic activity of the resulting Pt@CoO NPs was investigated using the hydrogenation of ethylene as a model reaction. Without any pretreatment, the Pt@CoO NPs were found to be active for C_2H_4 hydrogenation at temperatures as low as 208 K. The steady-state turnover frequency for ethane formation at 227 K was comparable to the rates of the conventionally supported Pt/SiO_2 catalyst and pure platinum powders. A route appeared for the ethylene and hydrogen to enter into the CoO shell interior; thus, catalytic reactions could occur on the platinum surfaces. The grain boundaries on the shell were the most probable entry points for ethylene and hydrogen diffusion into the shell, as well as for the ethane to diffuse outward.

Following the work of Alivisatos and Somorjai, various versions of yolk–shell nanostructures have emerged. Song and his co-workers prepared a variety of M@SiO_2 yolk–shell nanostructures and exploited them in various liquid- and gas-phase reactions [49–53]. Their synthesis approach relied primarily on partial etching of the metal core or silica shell. For the synthesis of Au@SiO_2 yolk–shell NPs [49], the pre-synthesized Au NPs were first coated with an SiO_2 layer using the Stöber method to generate the Au@SiO_2 core–shell NPs. The latter were subsequently converted to hollow Au@SiO_2 yolk–shell NPs by partial etching of the Au core with potassium cyanide (KCN) (Fig. 5.8). The average size of the Au cores can be readily tuned using different amounts of KCN. The Au@SiO_2 yolk–shell frameworks were successfully employed in the catalytic reduction of *p*-nitrophenol, in which they exhibited a size-dependent reaction property (Fig. 5.9). Song's group utilized a similar approach to synthesize Ni@SiO_2 yolk–shell NPs for the high-temperature methane reforming reaction [50]. The etching of Ni@SiO_2 core–shell NPs with hydrochloric acid yielded yolk–shell-structured Ni@SiO_2 NPs. The

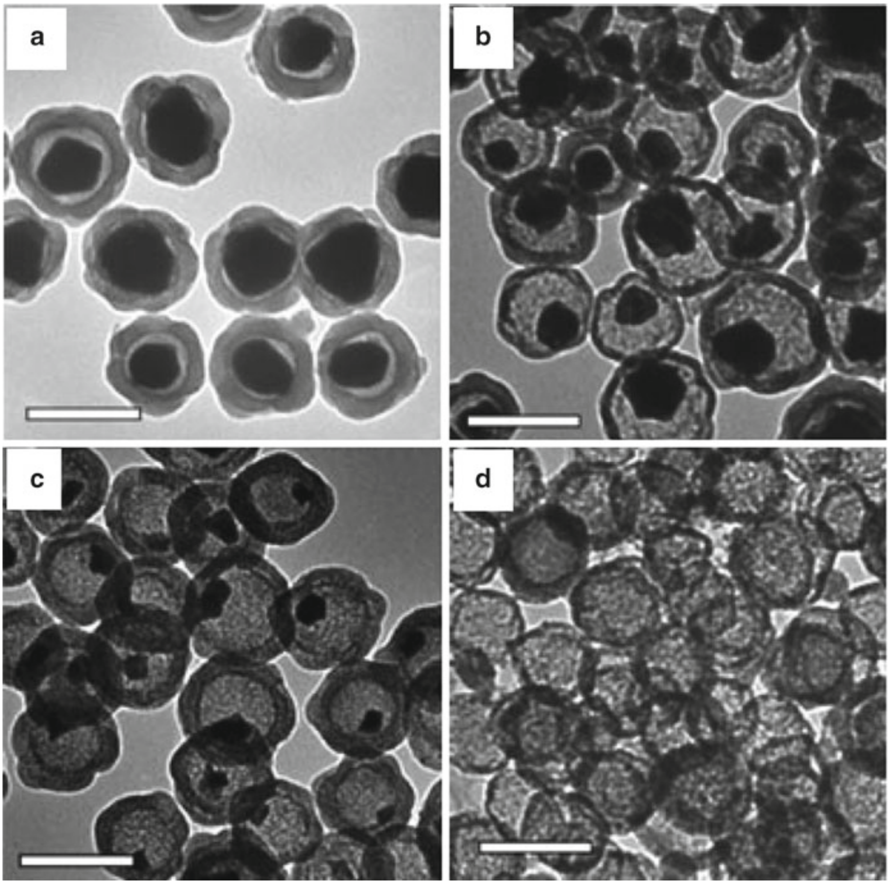

Fig. 5.8 TEM images of Au@SiO_2 yolk–shell NPs (**a**–**c**) and silica hollow shells (**d**). Au core diameters are (a) (104 ± 9) nm, (b) (67 ± 8) nm, and (c) (43 ± 7) nm. The scale bars represent 200 nm. Adapted from ref. [49]

particle size of the Ni cores in Ni@SiO_2 was tailored by the concentration of the etchant. In the methane reforming reaction, the Ni@SiO_2 yolk–shell catalyst exhibited a continuous conversion rate of methane and hydrogen and a significantly enhanced stability at high temperatures, leading to high recyclability without loss of catalytic activity. These reaction properties were superior to those of the supported Ni/MCF catalysts and comparable to state-of-the-art commercial catalysts.

The same group also synthesized Ni@SiO_2 [51], Pd@SiO_2 [52], and Co@SiO_2 [53] yolk–shell nanostructures with tiny metal cores using the microemulsion method. The hollow yolk–shell structure in the Pd@SiO_2 NPs was generated via hydrothermal etching of the silica in the Pd@SiO_2 core–shell structure. The Pd@SiO_2 yolk–shell catalysts exhibited extremely high initial turnover frequency, as well as excellent reusability (more than ten times) in Suzuki coupling reactions.

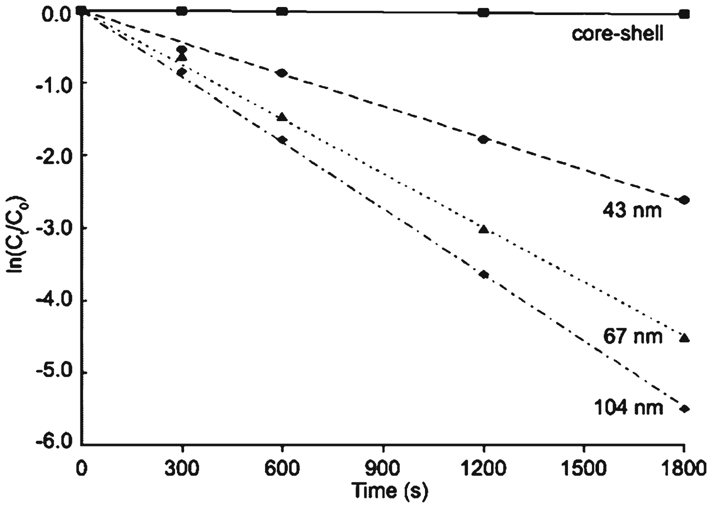

Fig. 5.9 Plot of $\ln(C_t/C_0)$ versus time for Au@SiO$_2$ yolk–shell nanocatalysts with different core sizes in *p*-nitrophenol reduction reaction. Adapted from ref. [49]

The Co@SiO$_2$ yolk–shell structure was obtained by thermal reduction of CoO@ SiO$_2$ core–shell particles via volume contraction of CoO to Co. The Co@SiO$_2$ yolk–shell nanocatalysts exhibited high activity and reusability for phenoxycarbonylation of iodobenzene. In addition, the magnetic property of the cobalt cores permitted facile separation of the catalysts from the products.

The etching of the shell layer instead of the metal cores can also generate yolk–shell NPs. Yin's group reported a "surface-protected etching" strategy that enabled conversion of Au@SiO$_2$ core–shell NPs into hollow Au@SiO$_2$ yolk–shell structures [54]. In this method, poly(vinylpyrrolidone) was used to protect the near surface layer, and NaOH was used to selectively etch the interior of the silica spheres. Etching initially yields porous structures and eventually removes the core to leave behind hollow silica spheres with porous shells (Fig. 5.10). By controlling the extent of etching, it was demonstrated that the permeation rate of the chemical species through the shells could be controlled. In the 4-nitrophenol reduction reaction, the hollow Au@SiO$_2$ yolk–shell NPs exhibited catalytic conversions, which were enhanced as the degree of the etching increased. Furthermore, the Au@SiO$_2$ yolk–shell NPs showed excellent reusability for 4-nitrophenol reduction, as the initial activity was maintained after cycling 12 times. In contrast, the bare Au NPs underwent a dramatic decrease in conversion after just 1 cycle due to severe aggregation of the Au NPs.

An alternative method to the yolk–shell structure is the use of a sacrificial intermediate layer, which is etched away to generate hollow spaces. This general scheme was realized by Schüth and his co-workers using the Au@ZrO$_2$ yolk–shell NPs as an example (Fig. 5.11) [55]. They first synthesized 15–17 nm Au NPs using sodium citrate as the reductant, followed by coating a silica layer on the individual Au

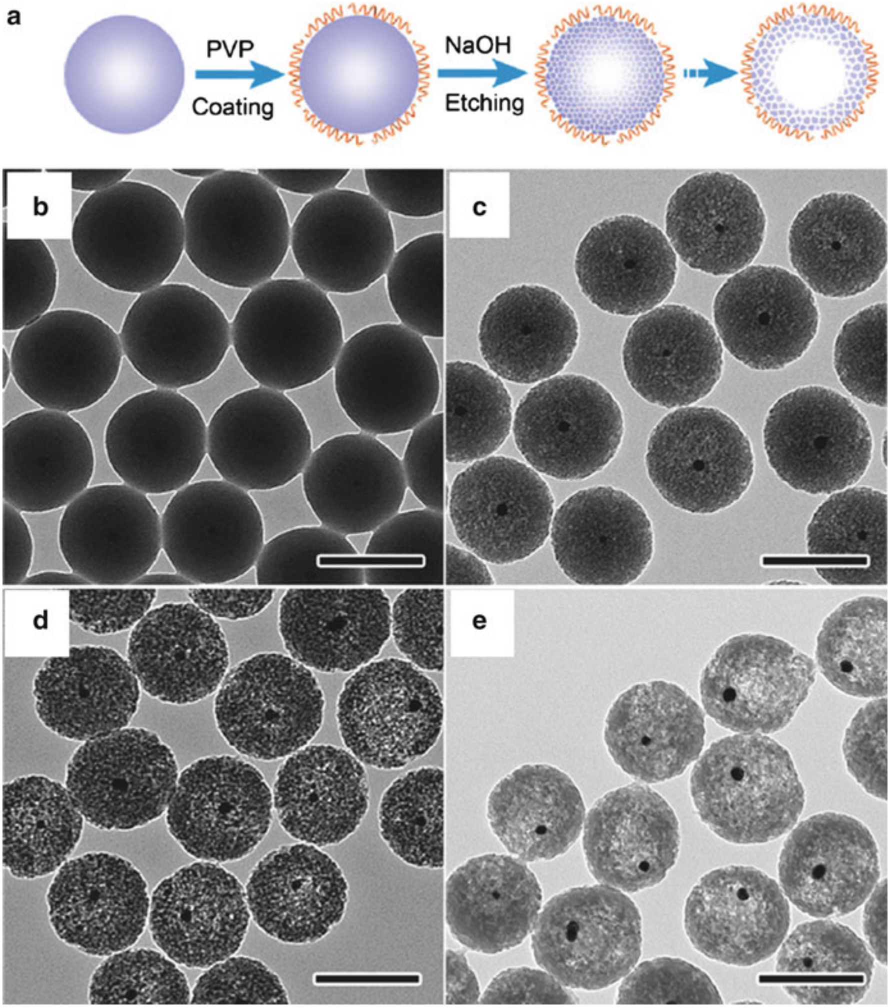

Fig. 5.10 (**a**) Schematic illustration of the concept of "surface-protected etching" for transforming solid silica spheres into permeable shells. (**b**–**e**) TEM images showing the structural evolution of Au@SiO$_2$ core–shell NPs: (**b**) the original samples; and (**c**–**e**) the samples after etching by NaOH for (**c**) 2 h; (**d**) 2 h 45 min; and (**e**) 3 h. Before etching, the silica particles have been refluxed in an aqueous solution of PVP for 3 h. All scale bars are 200 nm. Adapted from ref. [54]

particles using the modified Stöber method. Subsequently, the Au@SiO$_2$ core–shell nanospheres were coated with a zirconia layer by reacting them with zirconium butoxide under the presence of a surfactant (Lutensol AO5), followed by calcination at 900 °C. During the final calcination step, crystalline ZrO$_2$ NPs with a diameter of 10 nm were formed, with pores approximately 3–4 nm in size generated among the ZrO$_2$ particles. In the final step, the silica was removed from the composite by treating with an NaOH solution, yielding Au@ZrO$_2$ yolk–shell NPs. In the CO

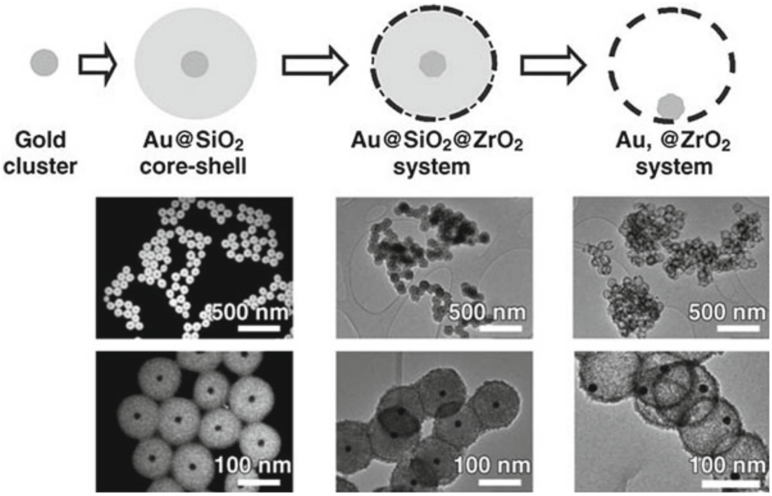

Fig. 5.11 Schematic representation and TEM images (*left*: dark field; *middle* and *right*: bright field) of the products obtained after each step during the synthesis of Au@ZrO_2 yolk-shell NPs. Adapted from ref. [55]

Fig. 5.12 Catalytic performance of the samples for CO oxidation. The activities of the catalysts were measured in a plug-flow reactor using 50 mg of catalyst in a gas mixture of 1 % CO in air at a flow rate of 67 cm^3 mil^{-1}, which corresponds to a space velocity of 80,000 cm^3 h^{-1} g_{cat}^{-1}. Adapted from ref. [55]

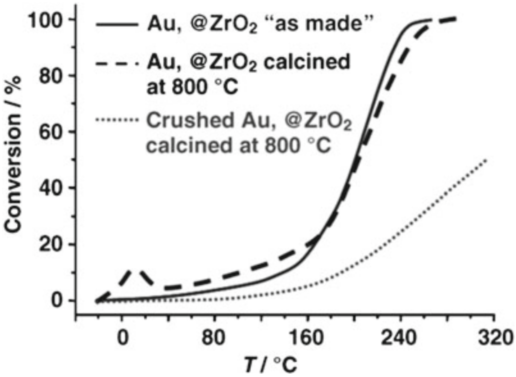

oxidation reaction, the yolk–shell Au@ZrO_2 catalysts showed a half-conversion temperature of 200 °C, which was remarkable considering the large size of the Au particles (Fig. 5.12).

The Au@ZrO_2 yolk–shell NPs showed a sintering resistance, as demonstrated by the almost identical morphology of the particles after thermal treatment at 800 °C. Schüth's group later demonstrated that the Au size can be reduced down to 5 nm using a simple NaCN etching process [56]. Zheng and his co-workers demonstrated that the Au@ZrO_2 and Au@TiO_2 yolk–shell structures could be prepared from small (~6 nm) Au NPs, based on Schüth's synthetic strategy [57]. A strategy utilizing a sacrificial, intermediate silica layer was also adopted by Zaera and his co-workers to produce Au@TiO_2 yolk–shell NPs, which demonstrated superior sintering resistance, compared to the supported Au/TiO_2 catalyst prepared by the conventional method [58].

In the yolk–shell nanostructures, the shell composed of porous carbon can also be synthesized. Ikeda and his co-workers reported two strategies for the M@C hollow yolk–shell structures [59–61]. The first strategy [59, 60] involved the following steps: (1) preparation of metal (Pt or Rh) NPs; (2) coating of individual metal NPs with a nonporous silica layer, (3) overgrowing a second silica layer on the preexisting metal@SiO_2 particles with C_{18}-TMS surfactant, followed by calcination to generate a mesoporous silica layer; (4) backfilling the mesopores with a carbon source (phenol-formaldehyde resin) and carbonization; and (5) etching the silica using hydrogen fluoride to generate the hollow yolk–shell Pt@C [59] or Rh@C [60] nanostructures. The Pt@C yolk–shell nanocatalyst showed very high catalytic activity for the hydrogenation of nitrobenzene and various olefins, surpassing that of the activated carbon-supported Pt catalyst. The second route for the synthesis of yolk–shell Pt@C nanostructures was achieved in a simpler way [61]. In this method, the TiO_2 NPs functioned as molds for hollow carbon but also induced simultaneous deposition of Pt NPs and phenolic polymers by photocatalytic reduction of a platinum(IV) precursor and oxidation of a phenol, respectively. The simultaneous formation of Pt NPs and an organic layer on the TiO_2 NP and the subsequent carbonization and etching of the TiO_2 template produced hollow yolk–shell Pt@C nanostructures. The yolk–shell Pt@C nanocatalysts also exhibited enhanced catalytic activity in liquid-phase hydrogenation and sintering resistance, compared to the conventional Pt/activated carbon catalyst.

The facile synthesis route to hollow yolk–shell structures without requiring the etching step was reported by Mou and his co-workers [62]. They exploited a water-in-oil microemulsion as a template where reduction of the gold precursor and polymerization of the silica precursor occurred, resulting in a structure composed of an Au NP (2.8–4.5 nm) entrapped inside a hollow silica shell. The size of the gold nanocatalysts can be readily controlled by the concentration of the gold precursor (chloroauric acid). More importantly, these Au@SiO_2 yolk–shell nanocatalysts showed catalytic activity in the 4-nitrophenol reduction reaction, both in the absence and presence of a thiol compound, meso-2,3-dimercaptosuccinic acid, indicating that the silica shell can provide a beneficial effect against poisoning by strongly adsorbing molecules from the reaction solution.

The shell layers in the above-described core–shell or yolk–shell nanostructures are composed of amorphous materials (SiO_2 and carbon) or aggregates of tiny nanocrystalline (few nanometer-sized) particles (CeO_2, ZrO_2, SnO_2, and TiO_2). If a shell layer can be constructed with a well-defined crystalline material, such as zeolite or metal–organic frameworks (MOFs), more precise control of the molecular-level properties can be expected. Very recently, Tsung's group realized such an opportunity to develop a general synthetic strategy for the yolk–shell M@ZIF-8 nanostructures (ZIF-8 is a type of MOF) [63]. The synthesis of this new yolk–shell material was performed by coating the NP cores with a layer of Cu_2O, a sacrificial template, followed by a layer of polycrystalline ZIF-8. The Cu_2O surface layer assisted in the formation of the ZIF-8 coating layer and was etched off simultaneously during this process (Fig. 5.13). In the hydrogenation of ethylene, cyclohexene, and cyclooctene over the Pd@ZIF-8 catalysts, the microporous ZIF-8 shell layer provided excellent molecular-size selectivity. Pd@ZIF-8 displayed high activity for ethylene and cyclohexene hydrogenation, whereas no activity was found for cyclooctene hydrogenation. In addition, by determining the differences in the activation energies of cyclohexene hydrogenation over the yolk– and core–shell-structured Pd@ZIF nanostructures, the effect of the hollow space between the core and shell layers on the catalysis was also investigated.

5.4 Supported Catalysts Coated with Shell Layers

The construction of core– or yolk–shell nanoarchitectures relies on the encapsulation of an individual metal NP with a shell layer. As demonstrated in the above examples, these catalysts were effective as nanoscale model catalysts that show thermal and chemical stabilities, as well as enhanced catalytic activity and selectivity. Recent works demonstrated that the principles acquired from these model catalysts are applicable to more complex model catalytic systems, and even to industrial supported catalysts.

In this regard, Park and his co-workers reported the facile synthesis of silica-supported platinum NPs with an ultrathin titania coating ($Pt/SiO_2@TiO_2$) [64]. This hybrid nanocatalyst was prepared by the deposition of uniform platinum NPs (2.5 nm) on the surface of a uniform silica sphere (25 nm), followed by sol–gel formation of a thin titania layer (Fig. 5.14). The $Pt/SiO_2@TiO_2$ catalysts showed thermal stability, retaining their original morphology after calcination at 600 °C. In the CO oxidation reaction, the $Pt/SiO_2@TiO_2$ catalyst exhibited lower activation energy than the Pt single crystal and $Pt@SiO_2$ core–shell catalyst, indicating possible involvement of the metal–support interaction between the Pt NPs and the TiO_2 layer.

Similar synthetic approaches to triple-layer nanocatalysts were reported by a number of groups [65–70]. Yin and his co-workers extended their “surface-protected etching” technique, based on using NaOH as an etchant, to prepare triple-layer model catalytic systems [65]. For this method, a monolayer of the metal nanocatalyst is first immobilized on the surface of silica sphere colloids using coupling agents. The core–satellite structures are then coated with another layer of silica of the desired thickness to fix the position of metal nanoparticles. Finally, the etching technique is applied to make the outer shell mesoporous, exposing the catalyst particles to outside chemical species. They also prepared a similar nanostructure with a super paramagnetic Fe_3O_4 NP at the center of the initial silica colloids. The inclusion of magnetic components allows facile separation and purification during synthesis using external magnetic fields.

Asefa and his co-workers coated a silica layer on a silica sphere-supported Pd catalyst (Pd/SiO_2), followed by partial etching of the outer silica layer using NaOH,

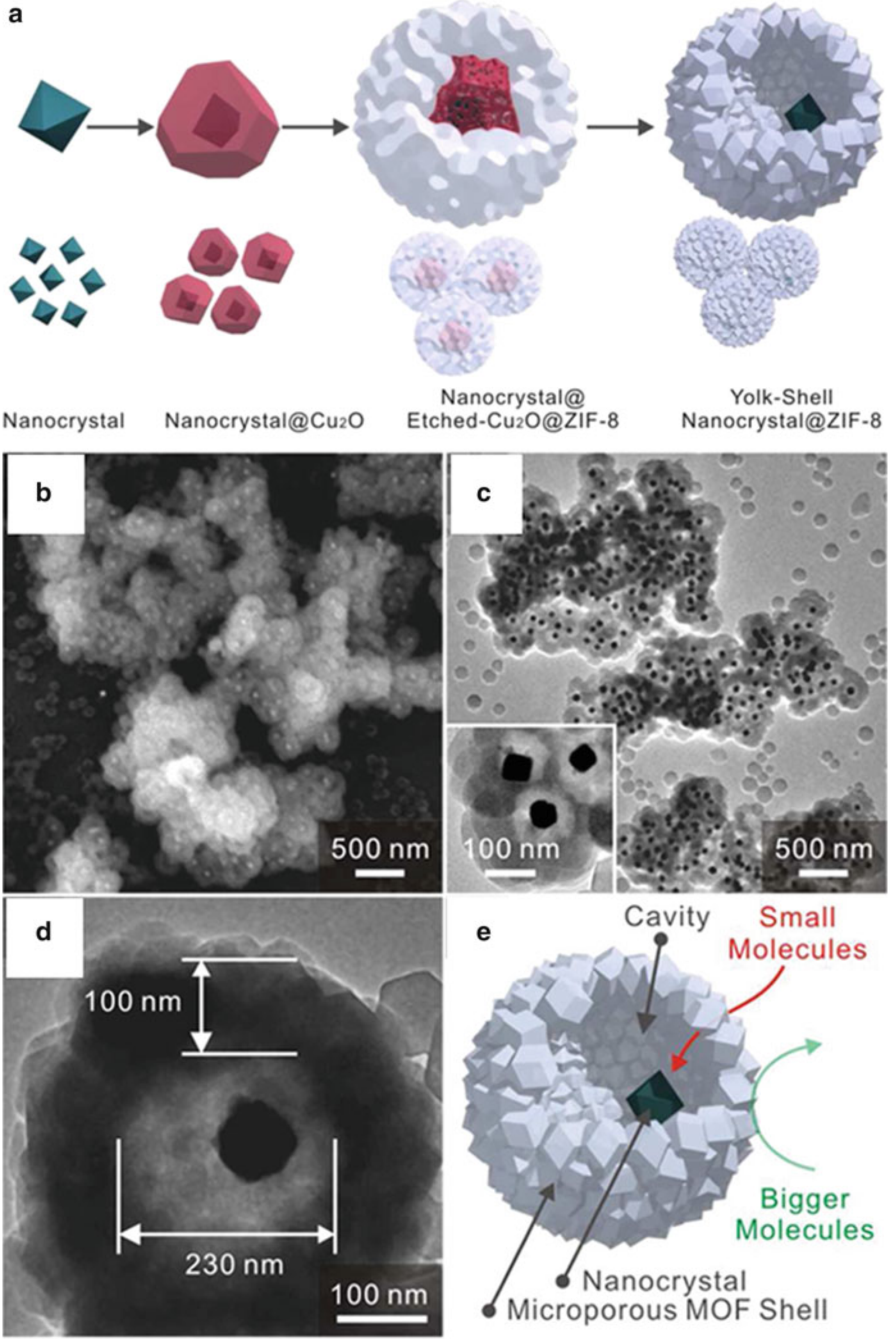

Fig. 5.13 (**a**) Schematic representation of the growth procedure, (**b**) SEM and (**c**, **d**) TEM images for the nanocrystal@ZIF-8 yolk–shell nanostructures. The cores are Pd octahedra with edge sizes of 60 nm, and the shells are microporous ZIF-8 with a thickness of ~100 nm. (**e**) Schematic sketch of the final yolk–shell nanostructure. Adapted from ref. [63]

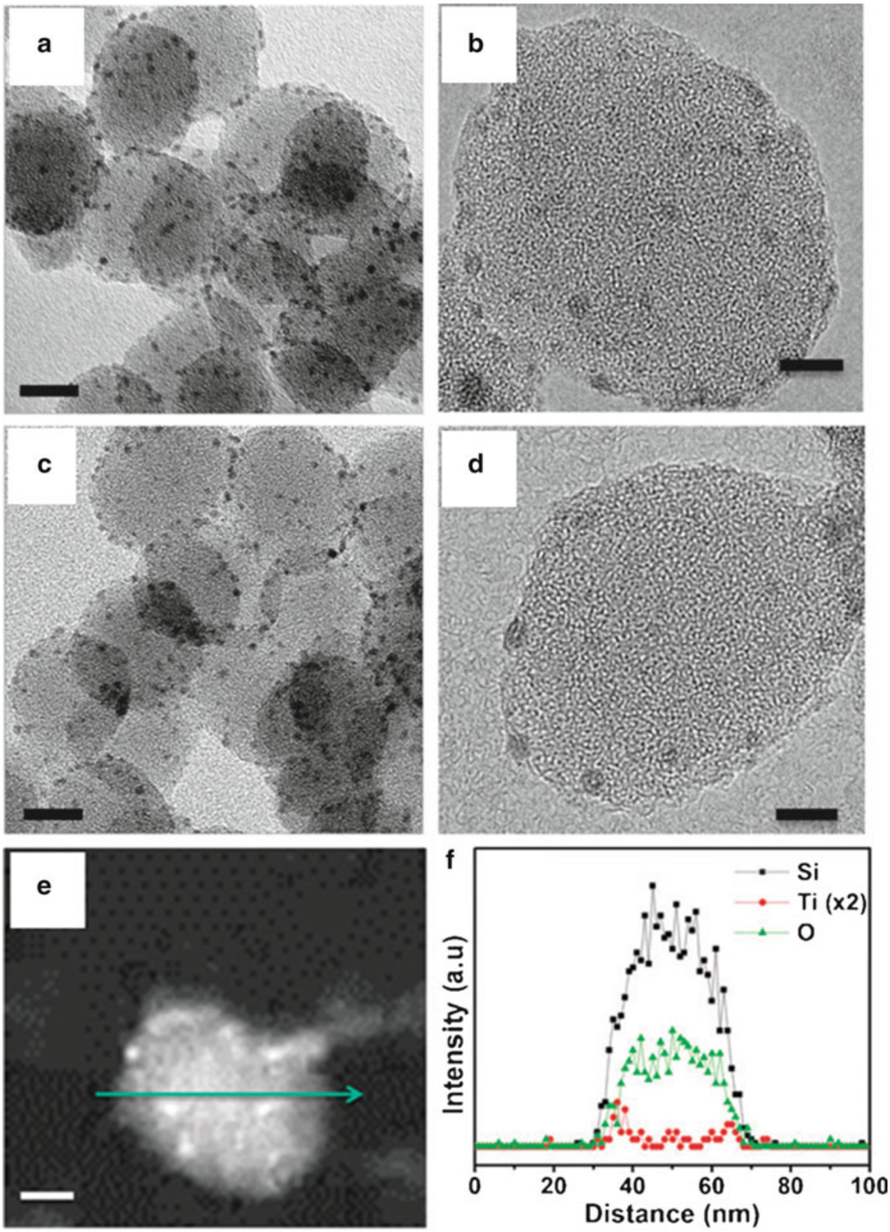

Fig. 5.14 TEM and thermal stability of Pt/SiO_2@TiO_2 nanocatalysts. (**a**, **b**) Pt/SiO_2@TiO_2NPs, (**c**, **d**) Pt/SiO_2@TiO_2NPs after calcination at 600 °C in air. (**e**, **f**) ADF STEM images and corresponding EDS line spectra of a single Pt/SiO_2@TiO_2NPs to prove the existence of the ultrathin TiO_2 layer. The bars represent (**a**, **c**, **e**) 10 nm and (**b**, **d**) 5 nm. Adapted from ref. [64]

yielding Pd/SiO_2@SiO_2 nanocatalysts [66]. This nanocatalyst exhibited high catalytic activity and turnover numbers in the hydrogenation reaction and C–C coupling reactions. Moreover, these heterogeneous nanocatalysts were stable, showing negligible Pd leaching and aggregation, and can be recycled multiple times without loss of catalytic activity. Asefa's group further extended this strategy using a zirconia shell layer to produce Pd/SiO_2@ZrO_2 nanocatalysts [67]. Zaera and his co-workers prepared Pt/SiO_2@SiO_2 nanocatalysts for gas-phase reactions via a similar synthetic protocol [68]. The resulting encapsulated platinum nanoparticles were shown to resist sintering during calcination at temperatures as high as 800 °C, whereas the unprotected catalysts sintered by 600 °C. Xia's group utilized TiO_2 nanofibers as a support to generate a triple-layer nanocatalyst [69]. Their nanocatalyts consist of Pt nanoparticles that are supported on a TiO_2 nanofiber and coated with a mesoporous SiO_2 sheath. This nanocatalyst could resist sintering up to 750 °C in air, while retaining the catalytic activity of the Pt nanoparticles. Liu and her co-workers also developed a high-temperature stable nanocatalyst using carbon nanotubes as a support material [70].

A very recent work reported by Stair and his co-workers demonstrated an important application of the surface coating method developed in colloidal model catalysts to a real industrial catalyst [71]. They utilized an atomic layer deposition (ALD) process that can precisely control the thickness of the surface layer at a sub-nm level. They overcoated palladium NPs supported on an Al_2O_3 catalyst with 45 layers of alumina through an ALD process in which the catalysts were exposed to trimethylaluminum and water at 200 °C. When these catalysts were used for 1 h in oxidative dehydrogenation of ethane to ethylene at 650 °C, they were found by thermo gravimetric analysis to contain less than 6 % of the coke formed on the uncoated catalysts. Scanning transmission electron microscopy showed no visible morphology changes after reaction at 675 °C for 28 h (Fig. 5.15). The yield of ethylene improved on all ALD Al_2O_3-overcoated Pd catalysts (Fig. 5.16).

5.5 Summary and Future Perspectives

In this review, recent progress in the synthesis of core–shell-structured NPs for catalytic applications has been presented. Since the first realization of the nanoreactor concept, various versions of core–shell-structured nanocatalysts have emerged within a very short period of time, driven by advances in nanochemistry. Core–shell and yolk–shell nanocatalysts have shown enhanced thermal and chemical stability, thus preventing aggregation and sintering of small metal NPs. In core–shell (yolk–shell) structures where the shell layer was composed of metal oxides that show metal–support interaction, enhanced catalytic activity was observed. Furthermore, recent examples demonstrated that reactant size selectivity could be achieved by making shell layers with a crystalline, microporous MOF material.

Although the field of core–shell nanocatalyst has progressed rapidly, it is still in its infancy. Thus, continued efforts are required for further development of possible

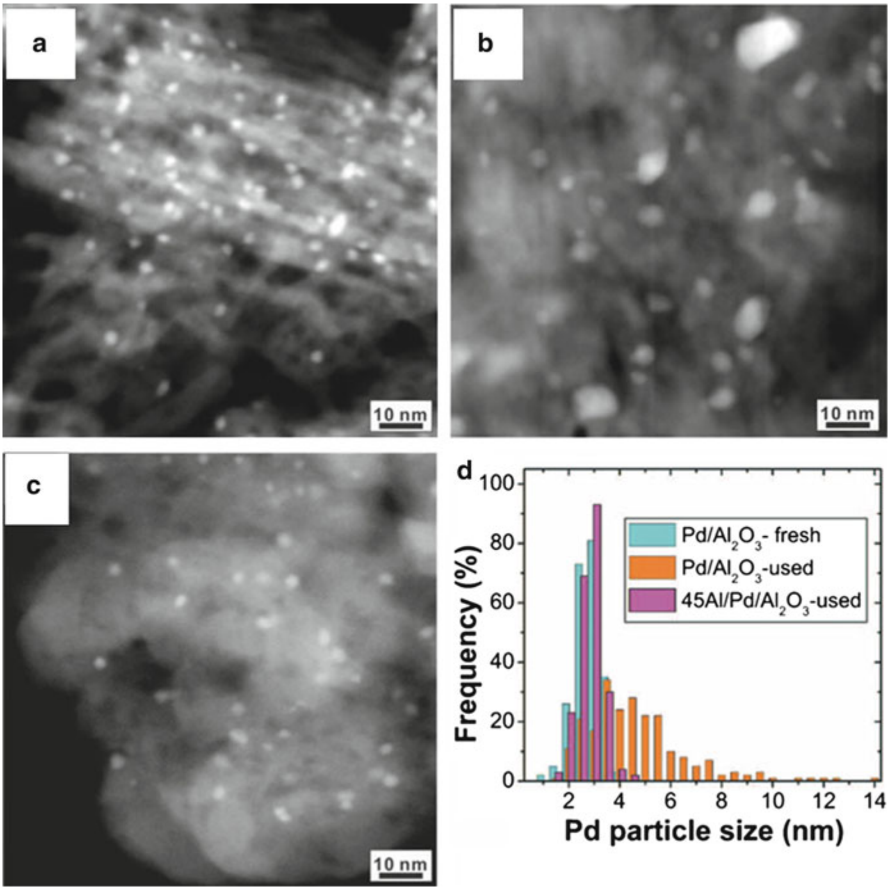

Fig. 5.15 STEM images of fresh and used samples after oxidative dehydrogenation of ethane reaction testing. (**a**) The fresh Pd/Al_2O_3 sample. (**b**) The used Pd/Al_2O_3 sample at 675 °C for 30 min. (**c**) The used 45Al/ Pd/Al_2O_3 sample at 675 °C for ~1,700 min. (**d**) Pd particle size distributions of these three samples. Adapted from ref. [71]

applications for and fundamental studies of core–shell nanocatalysts. A large-scale synthesis strategy for the core–shell catalysts suitable for industrial applications should be developed. Insights on enhanced thermal stability and activity largely rely on core–shell model nanocatalysts. However, synthesis of these nanocatalysts is, in most cases, rather complex and requires a multistep process. Hence, the development of a simple and economical process can be pivotal. The fundamental side of the core–shell nanocatalysts is a largely unexplored area. Other than the enhanced catalytic stability and activity, new catalytic properties may evolve in the confined space within the core–shell or yolk–shell geometry. In addition, state-of-the-art in situ characterization techniques may enhance our understanding of the phenomena occurring in the core–shell nanocatalysts. For instance, the use of in situ

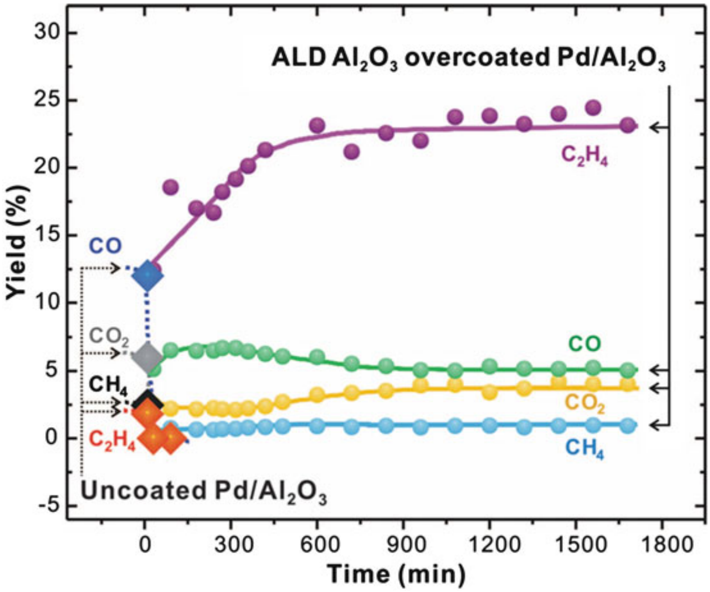

Fig. 5.16 Products yield on the Pd/Al_2O_3 samples with and without ALD-assisted Al_2O_3 overcoating during oxidative dehydrogenation of ethane reaction as a function of reaction time under identical reaction conditions. *Diamonds* with a *dashed line* are product yields on the uncoated Pd/Al_2O_3 sample; *circles* with *solid lines* are product yields on the 45Al/Pd/Al_2O_3 sample. Adapted from ref. [71]

environmental TEM might enable imaging of the interface between the core and shell layers, which will help in understanding the sintering-resistant behavior of these nanocatalysts.

On a final note, we point out that nanoscience has remarkably advanced the preparation of heterogeneous catalysts to the stage of their rational design beyond the traditional “trial-and-error” methods. In this review, some aspects of such rational approaches to creating stable nanocatalysts are highlighted. In the near future, the extension of such design concepts will lead to the control of activity and selectivity in catalytic reactions, which appears quite challenging.

Acknowledgements This work was supported by the Basic Science Research Program through the National Research Foundation (NRF) of Korea, funded by the Ministry of Education, Science and Technology (NRF-2010-0005341). S.H.J. is a TJ Park Junior Faculty Fellow.

References

1. Bell AT (2003) The impact of nanoscience on heterogeneous catalysis. Science 299:1688–1691
2. Schlögl R, Abd Hamid SB (2004) Nanocatalysis: mature science revisited or something really new? Angew Chem Int Ed 43:1628–1637
3. Somorjai GA, Contreras AM, Montano M, Rioux RM (2006) Clusters, surfaces, and catalysis. Proc Natl Acad Sci U S A 103:10577–10583

4. Somorjai GA, Frei H, Park JY (2009) Advancing the frontiers in nanocatalysis, biointerfaces, and renewable energy conversion by innovations of surface techniques. J Am Chem Soc 131:16589–16605
5. Li Y, Somorjai GA (2010) Nanoscale advances in catalysis and energy applications. Nano Lett 10:2289–2295
6. Narayanan R, El-Sayed M (2005) Catalysis with transition metal nanoparticles in colloidal solution: nanoparticle shape dependence and stability. J Phys Chem B 109:12663–12676
7. Somorjai GA, Tao F, Park JY (2008) The nanoscience revolution: merging of colloid science, catalysis and nanoelectronics. Top Catal 47:1–14
8. Lee K, Kim M, Kim H (2010) Catalytic nanoparticles being facet-controlled. J Mater Chem 20:3791–3798
9. Jia CJ, Schuth F (2011) Colloidal metal nanoparticles as a component of designed catalyst. Phys Chem Chem Phys 13:2457–2487
10. Lee IK, Albiter MA, Zhang Q, Ge J, Yin YD, Zaera F (2011) New nanostructured heterogeneous catalysts with increased selectivity and stability. Phys Chem Chem Phys 13:2449–2456
11. An K, Somorjai GA (2012) Size and shape control of metal nanoparticles for reaction selectivity in catalysis. ChemCatChem 4:1512–1524
12. Bartholomew CH (2001) Mechanisms of catalyst deactivation. Appl Catal A 212:17–60
13. De Rogatis L, Cargnello M, Gombac V, Lorenzut B, Montini T, Fornasiero P (2010) Embedded phases: a way to active and stable catalysts. ChemSusChem 3:24–42
14. Cao A, Lu R, Veser G (2010) Stabilizing metal nanoparticles for heterogeneous catalysis. Phys Chem Chem Phys 12:13499–13510
15. Yin Y, Rioux RM, Erdonmez CK, Hughes S, Somorjai GA, Alivisatos AP (2004) Formation of hollow nanocrystals through the nanoscale Kirkendall effect. Science 304:711–714
16. Park JC, Song HJ (2010) Metal@silica yolk-shell nanostructures as versatile bifunctional nanocatalysts. Nano Res 4:33–49
17. Zhang Q, Lee IK, Ge J, Zaera F, Yin YD (2010) Surface-protected etching of mesoporous oxide shells for the stabilization of metal nanocatalysts. Adv Funct Mater 20:2201–2214
18. Liu J, Qiao SZ, Chen JS, Lou XW, Xing X, Lu GQ (2011) Yolk/shell nanoparticles: new platforms for nanoreactors, drug delivery and lithium-ion batteries. Chem Commun 47: 12578–12591
19. Liu S, Bai SQ, Zheng Y, Shah KE, Han MY (2012) Composite metal-oxide nanocatalysts. ChemCatChem 4:1462–1484
20. Guerrero-Martinez A, Perez-Juste J, Liz-Marzan LM (2010) Recent progress on silica coating of nanoparticles and related nanomaterials. Adv Mater 22:1182–1195
21. Wei S, Wang Q, Zhu J, Sun L, Lin H, Guo Z (2011) Multifunctional composite core-shell nanoparticles. Nanoscale 3:4474–4502
22. Ghosh Chaudhuri R, Paria S (2012) Core/shell nanoparticles: classes, properties, synthesis mechanisms, characterization, and applications. Chem Rev 112:2373–2433
23. Stöber W, Fink A, Bohn E (1968) Controlled growth of monodisperse silica spheres in the micron size range. J Colloid Interface Sci 26:62–69
24. Kresge CT, Leonowicz ME, Roth WJ, Vartuli JC, Beck JS (1992) Ordered mesoporous molecular sieves synthesized by a liquid-crystal template mechanism. Nature 359:710–712
25. Wan Y, Zhao D (2007) On the controllable soft-templating approach to mesoporous silicates. Chem Rev 107:2821–2860
26. Joo SH, Park JY, Tsung CK, Yamada Y, Yang P, Somorjai GA (2009) Thermally stable Pt/mesoporous silica core–shell nanocatalysts for high-temperature reactions. Nat Mater 8: 126–131
27. Park JN, Forman JA, Tang W, Cheng J, Hu YS, Lin H, McFarland EW (2008) Highly active and sinter-resistant Pd-nanoparticle catalysts encapsulated in silica. Small 10:1694–1697
28. Park JN, Zhang P, Hu YS, McFarland EW (2010) Synthesis and characterization of sintering-resistant silica-encapsulated Fe_3O_4 magnetic nanoparticles active for oxidation and chemical looping combustion. Nanotechnology 21:225708

29. Feyen M, Weidenthaler C, Guttel R, Schlichte K, Holle U, Lu AH, Schüth F (2011) High-temperature stable, iron-based core–shell catalysts for ammonia decomposition. Chem Eur J 17:598–605
30. Li Y, Yao L, Song Y, Liu S, Zhao J, Ji W, Au CT (2010) Core–shell structured microcapsular-like Ru@SiO_2 reactor for efficient generation of CO_x-free hydrogen through ammonia decomposition. Chem Commun 46:5298–5300
31. Yao LH, Li YX, Zhao J, Ji WJ, Au CT (2010) Core–shell structured nanoparticles (M@SiO_2, Al_2O_3, MgO; M=Fe, Co, Ni, Ru) and their application in CO_x-free H_2 production via NH_3 decomposition. Catal Today 158:401–408
32. Li L, He S, Song Y, Zhao J, Ji W, Au CT (2012) Fine-tunable Ni@porous silica core–shell nanocatalysts: synthesis, characterization, and catalytic properties in partial oxidation of methane to syngas. J Catal 288:54–64
33. Li L, Lu P, Yao Y, Ji W (2012) Silica-encapsulated bimetallic Co–Ni nanoparticles as novel catalysts for partial oxidation of methane to syngas. Catal Commun 26:72–77
34. Sarshar Z, Sun Z, Zhao D, Kaliguine S (2012) Development of sinter-resistant core–shell $LaMn_xFe_{1-x}O_3$@mSiO_2 oxygen carriers for chemical looping combustion. Energy Fuel 26:3091–3102
35. Bernal S, Kaspar J, Trovarelli A (1999) Preface—recent progress in catalysis by ceria and related compounds. Catal Today 50:173
36. Yeung CMY, Kai MK, Fu QJ, Thompsett D, Petch MI, Tsang SC (2005) Engineering Pt in ceria for a maximum metal-support interaction in catalysis. J Am Chem Soc 127:18010–18011
37. Tauster SJ, Fung SC, Garten RL (1978) Strong metal-support interactions group 8 noble metals supported on TiO_2. J Am Chem Soc 100:170–175
38. Cargnello M, Wider NL, Montini T, Gorte RJ, Fornasiero P (2010) Synthesis of dispersible Pd@CeO_2 core-shell nanostructures by self-assembly. J Am Chem Soc 132:1402–1409
39. Cargenllo M, Jaen DJJ, Garrido JCH, Bakhmutsky K, Montini T, Gamez JJC, Gorte RJ, Fornasiero P (2012) Exceptional activity for methane combustion over modular Pd@CeO_2 subunits on functionalized Al_2O_3. Science 337:713–717
40. Cargnello M, Gentilini C, Montini T, Fonda E, Mehraeen S, Chi M, Collado MH, Browning ND, Polizzi S, Pasquato L, Fornasiero P (2010) Active and stable embedded Au@CeO_2 catalysts for preferential oxidation of CO. Chem Mater 22:4335–4345
41. Bakhmutsky K, Wieder NL, Cargnello M, Galloway B, Fornasiero P, Gorte RJ (2012) A versatile route to core–shell catalysts: synthesis of dispersible M@Oxide (M=Pd, Pt; Oxide=TiO_2, ZrO_2) nanostructures by self-assembly. ChemSusChem 5:140–148
42. Qi J, Chen J, Li G, Li S, Gao Y, Tang Z (2012) Facile synthesis of core–shell Au@ CeO_2nanocomposites with remarkably enhanced catalytic activity for CO oxidation. Energy Environ Sci 5:8937–8941
43. Kayama T, Yamzaki K, Shinjoh H (2010) Nanostructured ceria-silver synthesized in a one-pot redox reaction catalyzes carbon oxidation. J Am Chem Soc 132:13154–13155
44. Mitsudome T, Mikami Y, Matoba M, Mizugaki T, Jitsukawa K, Kaneda K (2012) Design of a silver–cerium dioxide core–shell nanocomposite catalyst for chemoselective reduction reactions. Angew Chem Int Ed 51:136–139
45. Yu K, Wu Z, Zhao Q, Li B, Xie Y (2008) High-temperature-stable Au@SnO_2 core/shell supported catalyst for CO oxidation. J Phys Chem C 112:2244–2247
46. She ZW, Liu S, Zhang SY, Shah KW, Han MY (2011) Synthesis and multiple reuse of eccentric Au@TiO_2 nanostructures as catalysts. ChemCommun 47:6689–6691
47. Kong L, Chen W, Ma D, Yang Y, Liu S, Huang S (2012) Size control of Au@Cu_2O octahedra for excellent photocatalytic performance. J Mater Chem 22:719–724
48. Aguirre ME, Rodriguez HB, San Roman E, Feldhoff A, Grela MA (2011) Ag@ZnO core-shell nanoparticles formed by the timely reduction of Ag^+ ions and zinc acetate hydrolysis in N, N-dimethylformamide: mechanism of growth and photocatalytic properties. J Phys Chem C 115:24967–24974

49. Lee J, Park JC, Song H (2008) A nanoreactor framework of a Au@SiO_2 yolk/shell structure for catalytic reduction of *p*-nitrophenol. Adv Mater 20:1523–1528
50. Park JC, Bang JU, Lee J, Ko CH, Song H (2010) Ni@SiO_2 yolk-shell nanoreactor catalysts: high temperature stability and recyclability. J Mater Chem 20:1239–1246
51. Park JC, Lee HJ, Kim JY, Park KH, Song H (2010) Catalytic hydrogen transfer of ketones over Ni@SiO_2 yolk-shell nanocatalysts with tiny metal cores. J Phys Chem C 114:6381–6388
52. Park JC, Heo E, Kim A, Kim M, Park KH, Song H (2011) Extremely active Pd@pSiO_2 yolk-shell nanocatalysts for Suzuki coupling reactions of aryl halides. J Phys Chem C 115: 15772–15777
53. Park JC, Lee HJ, Jung HS, Kim M, Kim HJ, Park KH, Song H (2011) Gram-scale synthesis of magnetically separable and recyclable Co@SiO_2 yolk-shell nanocatalysts for phenoxycarbonylation reactions. ChemCatChem 3:755–760
54. Zhang Q, Zhang T, Ge J, Yin Y (2008) Permeable silica shell through surface-protected etching. Nano Lett 8:2867–2871
55. Arnal PM, Comotti M, Schüth F (2006) High-temperature-stable catalysts by hollow sphere encapsulation. Angew Chem Int Ed 45:8224–8227
56. Guttel R, Paul M, Schüth F (2010) Ex-post size control of high-temperature–stable yolk–shell Au,@ZrO_2 catalysts. Chem Commun 46:895–897
57. Huang X, Guo C, Zuo J, Zheng N, Stucky GD (2009) An assembly route to inorganic catalytic nanoreactors containing sub-10-nm gold nanoparticles with anti-aggregation properties. Small 3:361–365
58. Lee I, Joo JB, Yin Y, Zaera F (2011) A yolk@shell nanoarchitecture for Au/TiO_2 catalysts. Angew Chem Int Ed 50:10208–10211
59. Ishino S, Harada T, Okamoto N, Sakata T, Mori H, Kuwabata S, Torimoto T, Matsumura M, Ikeda S (2006) Ligand-free platinum nanoparticles encapsulated in a hollow porous carbon shell as a highly active heterogeneous hydrogenation catalyst. Angew Chem Int Ed 45: 7063–7066
60. Harada T, Ikeda S, Ng YH, Sakata T, Mori H, Torimoto T, Matsumura M (2008) Rhodium nanoparticle encapsulated in a porous carbon shell as an active heterogeneous catalyst for aromatic hydrogenation. Adv Funct Mater 18:2190–2196
61. Ng YH, Ikeda S, Harada T, Higashida S, Sakata T, Mori H, Matsumura M (2007) Fabrication of hollow carbon nanospheres encapsulating platinum nanoparticles using a photocatalytic reaction. Adv Mater 19:597–601
62. Wu SH, Tseng CT, Lin YS, Lin CH, Hung Y, Mou CY (2011) Catalytic nano-rattle of Au@ hollow silica: towards a poison-resistant nanocatalyst. J Mater Chem 21:789–794
63. Kuo CH, Tang Y, Chou LY, Sneed BT, Brodsky CN, Zhao Z, Tsung CK (2012) Yolk–shell nanocrystal@ZIF-8 nanostructures for gas-phase heterogeneous catalysis with selectivity control. J Am Chem Soc 134:14345–14348
64. Reddy AS, Kim SM, Jeong HY, Jin SY, Qadir K, Jung K, Jung CH, Yun JY, Cheon JY, Yang JM, Joo SH, Terasaki O, Park JY (2011) Ultrathin titania coating for high-temperature stable SiO_2/Pt nanocatalysts. Chem Commun 47:8412–8414
65. Ge J, Zhang Q, Zhang T, Yin Y (2008) Core–satellite nanocomposite catalysts protected by a porous silica shell: controllable reactivity, high stability, and magnetic recyclability. Angew Chem Int Ed 47:8924–8928
66. Wang Y, Biradar AV, Duncan CT, Asefa T (2010) Silica nanosphere-supported shaped Pd nanoparticles encapsulated with nanoporous silica shell: efficient and recyclable nanocatalysts. J Mater Chem 20:7834–7841
67. Wang Y, Biradar AV, Asefa T (2012) Assembling nanostructures for effective catalysis: supported palladium nanoparticle multicores coated by a hollow and nanoporous zirconia shell. ChemSusChem 5:132–139
68. Lee I, Zhang Q, Ge J, Yin Y, Zaera F (2011) Encapsulation of supported Pt nanoparticles with mesoporous silica for increased catalyst stability. Nano Res 4:115–123

69. Dai Y, Lim B, Yang Y, Cobley CM, Li W, Cho EC, Grayson B, Fanson PT, Campbell CT, Sun Y, Xia Y (2010) A Sinter-resistant catalytic system based on platinum nanoparticles supported on TiO_2 nanofibers and covered by porous silica. Angew Chem Int Ed 49:8165–8168
70. Sun Z, Zhang H, Zhao Y, Huang C, Tao R, Liu Z, Wu Z (2011) Thermal-stable carbon nanotube-supported metal nanocatalysts by mesoporous silica coating. Langmuir 27: 6244–6251
71. Lu J, Fu B, Kung MC, Xiao G, Elam JW, Kung HH, Stair PC (2012) Coking- and sintering-resistant palladium catalysts achieved through atomic layer deposition. Science 335: 1205–1208

Chapter 6
Shape-Controlled Bimetallic Nanocatalysts in Fuel Cells: Synthesis and Electrocatalytic Studies

Yawen Zhang and Jun Gu

6.1 Introduction

Since the demand for electric energy is growing and fossil fuels are gradually diminishing, it is urgent for scientists to find clean and efficient sources of electrical energy as alternatives to combustion-based power. Direct methanol fuel cells (DMFCs) and proton exchange membrane fuel cells (PEMFCs) are promising next-generation electric energy sources that convert the chemical energy stored in the fuel (i.e., methanol and hydrogen) directly to electrical energy [1, 2]. However, some current problems with fuel cells cannot be ignored. Large amounts of noble metals, especially Pt, are used as catalysts for both the cathodic and anodic reactions of DMFCs and PEMFCs, which dramatically increase the cost of the fuel cells. Moreover, the cathodic reaction of DMFCs and PEMFCs (i.e., the oxygen reduction reaction (ORR)) suffers from high overpotential on the Pt surface and the activity of the anodic reaction of DMFCs (i.e., the methanol oxidation reaction (MOR)) on the Pt surface is strongly suppressed by CO poisoning. Developing bimetallic crystals as catalysts in fuel cells can, on the one hand, reduce the usage of Pt, and, on the other hand, provide catalysts with higher activity and durability [3–5].

Many types of bimetallic catalysts have been used to investigate electrocatalytic performance, including single-crystal surfaces [6], sputtered particles [5, 7], carbon-supported catalysts fabricated by impregnation reduction, and colloidal nanocrystals (NCs). Bimetallic single crystals are indispensable when investigating facet-specific electrocatalytic properties; sputtered bimetallic particles can be used as model catalysts with a clean surface to study the effect of composition on

---

Y. Zhang (✉) • J. Gu
Beijing National Laboratory for Molecular Sciences, State Key Laboratory of Rare Earth Materials Chemistry and Applications, PKU-HKU Joint Laboratory in Rare Earth Materials and Bioinorganic Chemistry, College of Chemistry and Molecular Engineering, Peking University, Beijing 100871, China
e-mail: ywzhang@pku.edu.cn

J.Y. Park (ed.), *Current Trends of Surface Science and Catalysis*,
DOI 10.1007/978-1-4614-8742-5_6,

electrocatalytic performance. These materials, however, are not suitable for practical applications because of their low specific surface area and high cost. Yet, the actual active sites are currently unclear for impregnation-reduction nanoparticles due to the large variation in their composition, size, and morphology. Colloidal bimetallic NCs (BMNCs) with uniform composition, size, and morphology possess both practical and theoretical value, which could maximize the proportion of noble metal atoms as highly active sites.

Most electrocatalytic reactions are sensitive to the structure of the metal surface. For instance, ORR activity varies dramatically on different facets of the Pt_3Ni alloy [6]. In the case of Pt-Cu alloy NCs with a dealloyed Pt surface, the ORR activity also changes when tuning the lattice strain of the Pt shells by changing the composition of the alloy cores [8]. As more experimental results are summarized, researchers today are trying to design the composition and structure of BMNCs according to electrocatalytic reaction and then design a synthetic approach to obtain BMNCs with the desired composition and structure. Structure identification links studies on electrocatalytic properties and rational design of the synthesis. Therefore, in this review, we will first classify BMNCs according to structure. Next, the formation processes of BMNCs with different structures will be introduced, together with commonly used experimental methods for synthesizing BMNCs. Then we will discuss in detail the key factors in controlling the structure of BMNCs, including the reduction rate of metal precursors, usage of facet-specific capping agents, and the combination of underpotential deposition (UPD) and the galvanic replacement reaction. The mechanisms for how the composition and structure of BMNCs affect their electrocatalytic activity will also be discussed. Finally, a brief summary and prospect in this field will be presented.

6.2 Classification of Bimetallic Nanocatalysts in Fuel Cells

According to the function of two compositions of BMNCs in the electrocatalytic reaction, BMNCs can be divided into mono-functional catalysts and bi-functional catalysts. In mono-functional catalysts, reagents are only adsorbed on one kind of metal atoms; in bi-functional catalysts, both kinds of metal atoms on the surface serve as adsorption sites for different reagents. The alloy BMNCs of Pt and early transition metals as ORR catalysts are mono-functional catalysts, in which reagent and intermediates are only adsorbed on the Pt sites and the early transition metals are introduced to modulate the electronic structure of the Pt and improve the ORR activity [5, 6, 8]. Pt-Ru catalysts used for methanol electro-oxidation, however, are considered as bi-functional catalysts where Pt atoms serve as the adsorption sites of the C-species and Ru atoms serve as the adsorption sites of the O-species [9, 10]. If BMNCs are to serve as bi-functional catalysts, the synthetic approach should be specially designed to optimize the ratio of the exposed sites of each of the two metal atoms.

When considering the distribution of different elements, there are two main classes of BMNCs: alloy and heterostructure. More specifically, there are two types

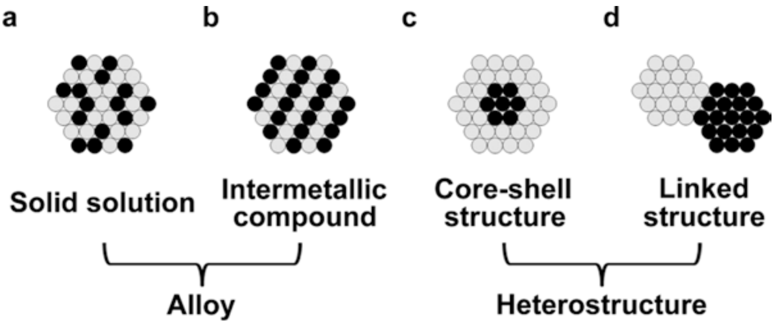

Fig. 6.1 Classification of BMNCs according to their element distribution. *Grey* and *black balls* represent metal atoms of different elements

of alloy BMNCs and two types of heterostructured BMNCs, as illustrated in Fig. 6.1. Figure 6.1a shows solid solution of different metals where atoms of different kinds are randomly arranged, and Fig. 6.1b shows an intermetallic compound where atoms of each metal occupy specific sites. In the formation of heterostructured BMNCs, epitaxial layered growth leads to core–shell structures (Fig. 6.1c) and island growth leads to linked structures (Fig. 6.1d) [11]. In most cases, simultaneous reduction of the precursors of the two metals favors the formation of alloy BMNCs and stepwise reduction results in heterostructured BMNCs. The heat of mixing of two metals is another important factor. A negative heat of mixing facilitates the formation of alloy BMNCs [12]. For instance, the heat of mixing of Pt and Ni is quite negative. Consequently, Pt-Ni alloy BMNCs could be obtained even if the Pt and Ni precursors were reduced stepwise [13].

Intermetallic compounds with a certain formula and crystal structure are thermodynamically more stable than the disordered solid solution with the same element ratio and exhibit different electrocatalytic activities and durabilities. Annealing can drive the transformation from disordered alloys to ordered intermetallic compounds. In the example of Fe-Pt-alloy BMNCs, Fe atoms and Pt atoms distribute randomly in face-center-cubic (FCC) Fe-Pt and in order in face-center-tetragonal (FCT) Fe-Pt. FCC Fe-Pt NCs could transform to FCT Fe-Pt during thermal treatment and the ORR activity and durability increased after this transformation [14]. A similar phenomenon was also found in surface-dealloyed Pt-Co alloy NCs as catalyst of ORR [15].

Whether layered growth or island growth will be employed in the formation of heterostructured BMNCs is mainly determined by the interfacial energy of the two metals. Two factors (i.e., lattice mismatch and the bond strength between the two metals) contribute to the interfacial energy. In some pioneering work on the syntheses of Au-Ag (lattice mismatch: 0.25 %) [16] and Pt-Pd (lattice mismatch: 0.77 %) [17] core–shell BMNCs, researchers considered a small lattice mismatch as the most important condition necessary for layered growth. Tian and co-workers first proposed that strong bonding between the two metals was another key factor when they synthesized Au@Pd NCs with a lattice mismatch of 4.88 % [18]. Since the chemical bonding between Au and Pt is much weaker than that between Au and Pd,

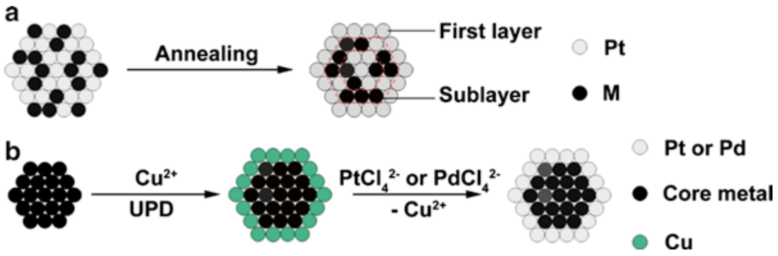

Fig. 6.2 Schemes of two methods to fabricate Pt (or Pd) skin on BMNCs. (**a**) Pt monolayer forms on the alloy of Pt and an early transition metal through the dealloying process during annealing. (**b**) A Cu monolayer forms through UPD, followed by the galvanic replacement reaction between the Cu and $PtCl_4^{2-}$ or $PdCl_4^{2-}$ ions

Pt could not grow epitaxially on Au cores, even though the lattice mismatch is 4.08 %. Recently, Pd@Cu NCs could also be prepared despite the large lattice mismatch (i.e., 7.1 %) between Pd and Cu [19].

A new type of core–shell BMNC, metallic NC coated with Pt skin, shows great promise in electrocatalysis. The *d*-band structure of the surface Pt atoms can be modulated through charge transfer and lattice strain between the core and shell in this structure, allowing for optimization of the electrocatalytic performance [20]. There are two commonly used methods to fabricate Pt skin on BMNCs, as shown in Fig. 6.2. The first method is the spontaneous segregation of alloy NCs of Pt and early transition metals via annealing [5, 8, 21]. Stamenkovic and co-workers investigated a series of annealed Pt-M (M = Ti, V, Fe, Co, Ni) alloy NCs [5]. The first layer of the alloy NCs was composed of Pt atoms only and the sublayer was rich in M atoms; the annealed alloy NCs exhibited higher ORR activity than the sputtered alloy. The second method, developed by Adzic and co-workers, is based on the UPD of Cu on various metals [22–24]. UPD means metal ions, M^{n+}, can be reduced and deposited as an M monolayer on a foreign metal substrate at a potential higher than the highest potential needed to reduce the M^{n+} ions to M bulk [25]. First, core-metal NCs were supported on a glassy carbon electrode (GCE) and Cu monolayers were deposited on the cores through UPD. The electrode was then immersed in a solution of K_2PtCl_4 or K_2PdCl_4. Pt or Pd monolayers formed through galvanic replacement between the Cu monolayers and $PtCl_4^{2-}$ or $PdCl_4^{2-}$. This method can be used to further fabricate metallic NCs with a certain number of Pt or Pd layers.

BMNCs can also be classified according to morphology. Among various polyhedrons of FCC metals, those with a fivefold twinned structure exhibit I_h symmetry or D_{5h} symmetry, such as icosahedrons and decahedrons; single-crystalline polyhedrons exhibit O_h symmetry or T_d symmetry, such as cubes, octahedrons, and tetrahedrons. The electrocatalytic properties of BMNCs are sensitive to their morphologies. First, twinned defects in dodecahedrons and icosahedrons can cause lattice compression and affect the electronic structure of the surface atoms [26]. Moreover, the catalytic performance of BMNCs is strongly dependent on the exposed facets [6]. NCs with different shapes expose different facets and exhibit

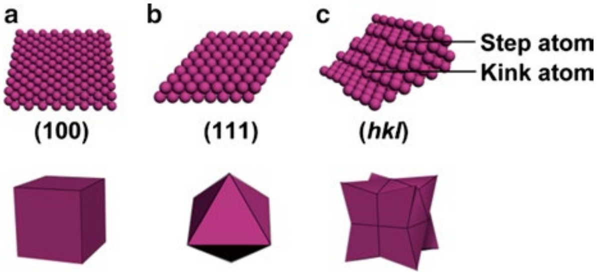

Fig. 6.3 Surface atomic arrangement of polyhedrons of FCC metal. (**a**) The cube exposes the (100) facet; (**b**) the octahedron exposes the (111) facet; (**c**) the hexoctahedron exposes the (*hkl*) facet. Step and kink atoms are marked

different atomic arrangements on the surface. Figure 6.3 shows the surface atomic arrangements of some fcc polyhedrons. The two former examples show two typical low-index facets (i.e., the (100) and (111) facets) and the last example shows a high-index facet with the index of (*hkl*) (*h*, *k*, and *l* are neither zero nor equal to each other), which is rich in step and kink atoms. The coordination number of the step and kink atoms on the high-index facets is very unsaturated, allowing for a strong adsorption capability for various species on these atoms.

6.3 Synthetic Routes to Bimetallic Nanocatalysts

Generally, two steps are needed from metal precursors to metallic NCs: nucleation and growth. As early as LaMer's work in the 1950s, people had distinguished these two steps in the formation of colloidal particles [27]. Two critical monomer concentrations, solubility and supersaturation, were pointed out. When the monomer concentration reaches supersaturation, nuclei will be generated, and when the concentration is higher than solubility, the nuclei will grow. In the case of metallic colloidal NCs, the metal monomers come from the decomposition and reduction of metal precursors. The formation process of BMNCs is much more complicated than the cases investigated by LaMer. BMNCs can be generated from the growth of nuclei as well as the aggregation of tiny metallic crystallites. Moreover, since the synthesis of BMNCs involves more than one kind of metal and precursor, UPD and the galvanic replacement reaction must be considered. Therefore, we categorize the synthesis of BMNCs into four types: continuous growth, crystallite coalescence, seeded growth, and the galvanic replacement reaction, as illustrated in Fig. 6.4 [28]. Continuous growth is similar to the classical synthesis of colloidal particles discussed by LaMer, except that two kinds of precursors are involved. Crystallite coalescence starts with explosive nucleation and rapid consumption of monomers. Then, the continuous growth of numerous nuclei is suppressed and the as-formed nuclei coalesce to reduce the high surface energy of tiny nuclei. In the seeded growth process,

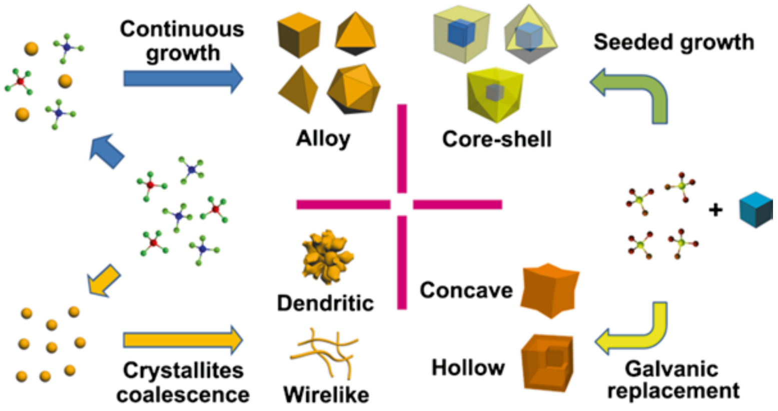

Fig. 6.4 Schemes of four basic routes for formation of colloidal BMNCs. Modified with permission from ref. [28]

foreign seeds are introduced so that the nucleation step is skipped. The galvanic replacement process is a unique process for the formation of BMNCs, in which the metal core reduces the precursor and the reduced metal atoms deposit on the surface of the same core. The core-metal atoms diffuse outward and the depositing metal atoms diffuse inward during the replacement reaction and a hollow structure may form in the center of the core due to the Kirkendall effect [29]. Previously synthesized metal seeds were required for seeded growth and the galvanic replacement reaction; in the galvanic replacement reaction, the reduction potential of the seeds must be lower than that of the other metal precursor.

Colloidal BMNCs can be prepared in many kinds of solvents, including water, polyol, and fatty amine. In water-phase synthesis, surfactants (e.g., cetyltrimethylammonium bromide (CTAB)) or polymers (e.g., poly(vinylpyrrolidone) (PVP)) serve as stabilizers for BMNCs and some ions (e.g., halide ions) or neutral molecules (e.g., CO) are used to control the exposed facets of BMNCs. The hydrothermal [30] and polyol [31] methods can be viewed as improvements of the water-phase synthesis under atmosphere, where the synthetic temperature can go above 100 °C. High temperature can increase the decomposition and reduction rate of the metal precursors, which facilitates nucleation and results in small (<10 nm) BMNCs. Furthermore, BMNCs obtained from these methods exhibit good crystallinity and uniform morphology. However, a major disadvantage of the water-phase or polyol-phase syntheses is that precursors of early transition metals are hard to reduce due to the etching effect caused by a high concentration of protons. BMNCs containing early transition metals can be prepared in a mixed solvent of fatty amine and fatty acid through the reduction or decomposition of metal precursors, such as acetylacetonates and carbonyls [13, 32, 33]. Fatty amine and fatty acid simultaneously serve as solvent and capping agents. BMNCs synthesized with this method exhibit uniform size and morphology, but these BMNCs with a hydrophobic surface are not suitable for electrocatalysis in an aqueous solution. Hence, complicated extra procedures are needed to effectively remove the fatty amine and fatty acid adsorbed on the surface of the NCs and etching of the early transition metals must be avoided. Recently, many solvothermal methods were developed to synthesize water-soluble BMNCs [34]. Dimethylformamide (DMF) can serve as a superior solvent for the solvothermal synthesis of BMNCs containing early transition metals; other surfactants are not needed in this method [35, 36].

6.4 Key Factors to Control the Morphology of Bimetallic Nanocrystals

Although there are many different colloidal methods for BMNC synthesis, the basic ideas for morphology control are similar. Different reaction routes will lead to different morphologies of the products, as shown in Fig. 6.4. Some key factors guide the reaction route and determine the morphology of product BMNCs. These factors include the reaction rate of the metal precursors, facet-specific capping agents, and UPD followed by the galvanic replacement reaction. Herein, we will discuss in detail the effects of these key factors.

6.4.1 Reduction Rate of Metal Precursors

The reduction rate can be modulated through the control of temperature, reduction potential of the metal precursors, and reducing capacity of the reductant. Raising the temperature results in increased reduction rates and nuclei population, and leads to the formation of smaller NCs. The reduction potential of certain kinds of metal ions can be tuned by changing the concentration and introducing different ligands. Decreasing the concentration of metal ions or introducing ligands that strongly coordinate with the metal ions can lower the reduction potential of the metal precursor and, thus, slow down the reduction rate. $NaBH_4$ and hydrazine are the most commonly used strong reductants in the synthesis of BMNCs. The reduction rate is so fast in the presence of these strong reductants that only aggregate NCs smaller than 5 nm can be obtained. Numerous mild reductants have been explored to gradually reduce the metal precursor. In organic solvent synthesis, fatty amine [13, 32], polyol [37], and DMF [35, 36] can simultaneously serve as solvent, capping agent, and reductant. In the aqueous phase, ascorbic acid [38], formaldehyde [30, 39], and some capping agents, including PVP [40] and citric acid [41], are often used as reductants. The reducing capacity of many reductants in the aqueous phase is suppressed in acidic conditions because protons are the product of the oxidation of these reductants. Equation 6.1 takes formaldehyde as an example.

$$HCHO + \mathrm{H_2O} \rightarrow 4\,\mathrm{H}^+ + CO_2 \uparrow + 4\,\mathrm{e}^- \tag{6.1}$$

Generally, when the reduction rate is slow, the nucleation and growth stage will be near equilibrium, and when the reduction rate is sped up, the near-equilibrium state will be broken. Near-equilibrium nucleation and growth lead to multi-twinned [39] and phase-separated BMNCs [42], while BMNCs with branched [38, 43] or thermodynamically unstable morphologies [44] can be obtained under conditions far from the equilibrium regime.

Nucleation under near-equilibrium conditions favors the formation of fivefold twinned metallic NCs when the (111) facets are stabilized [45]. Neglecting the edge and corner energy, the total free energy of a metallic NC can be written as:

$$G_{NC} = G_{Bulk} + \sum \sigma_i A_i + \sum E_{Twin} \tag{6.2}$$

In this equation, G_{NC} represents the total free energy of a metallic NC (monometallic or alloy) and G_{Bulk} represents the free energy of the bulk metal with the same amount of metal atoms. σ_i and A_i are the surface free energy and area of facet i. $\sum \sigma_i A_i$ and $\sum E_{\mathrm{Twin}}$ stand for the sum of the surface free energy and twinned defect formation energy, respectively. $\sigma_{(111)}$ is lower than other $\sigma_{(hkl)}$ for many FCC metals under diverse conditions, but the total surface area of an octahedron or a tetrahedron which only exposes the (111) facets is much larger than a spherical particle with the same volume. Therefore, in the case of an ideal single crystal ($\sum E_{\mathrm{Twin}} = 0$), truncated octahedrons possess the lowest $\sum \sigma_i A_i$ value. However, NCs with the fivefold twinned structure, such as icosahedron, only expose the (111) facets and possess a lower surface area compared to tetrahedron and octahedron with the same volume. An icosahedron can be considered as a suitable combination of 20 tetrahedrons. Tetrahedrons are compressed when they are accommodated into an icosahedron, so the $\sum E_{\mathrm{Twin}}$ term has a large contribution to the total free energy of the particle and this term increases significantly when the size of the particle increases. Hence, the energetic relationship between a single crystal NC and fivefold twinned NC reverses as the size of the NC increases. When the NC is smaller than a critical size, $(\sum \sigma_i A_i + \sum E_{\mathrm{Twin}})_{\text{five-twinned}}$ is smaller than $(\sum \sigma_i A_i)_{\text{single-crystal}}$ and the fivefold twinned NC is more thermodynamically favored, and when the NC grows over this critical size, $(\sum \sigma_i A_i + \sum E_{\mathrm{Twin}})_{\text{five-twinned}}$ will increase over $(\sum \sigma_i A_i)_{\text{single-crystal}}$ and the single-crystal NC is more stable. If the reduction rate of the metal precursors is slow enough to keep the nucleation and growth stages near equilibrium, the fivefold twinned nuclei will form first. However, when the nuclei grow beyond a critical size, the twinned defect structure will be retained because the energy barrier for the transition from a twinned NC to a single-crystalline NC is too high. If the reduction rate is so fast that nuclei grow beyond the critical size within a short period of time, single-crystalline NCs will be obtained. For instance, when K_2PtCl_4 and Na_2PdCl_4 were reduced by formaldehyde in the presence of $Na_2C_2O_4$, Pt-Pd alloy NCs exposing the (111) facets could be obtained. The reduction rate was tuned by changing the concentration of formaldehyde. Single-crystalline tetrahedrons formed at a high reduction rate [30] and fivefold twinned icosahedrons formed at a low reduction rate [39], as shown in Fig. 6.5.

If the reduction rate is high enough to keep the monomer concentration higher than supersaturation, as described by LaMer's model, numerous tiny nuclei will form and few monomers will be left for further growth. These tiny nuclei tend to

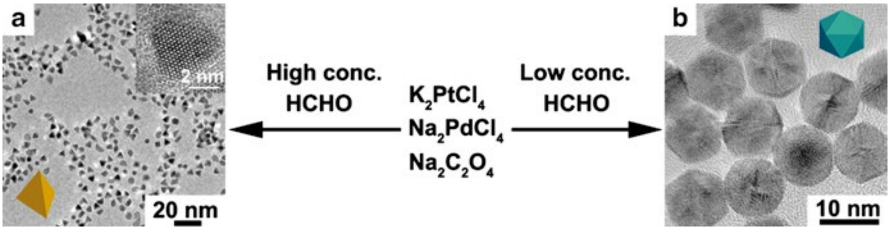

Fig. 6.5 (**a**) Transmission electron microscopy (TEM) and high-resolution TEM (HRTEM) images of Pt-Pd alloy tetrahedrons obtained at a high concentration of formaldehyde and (**b**) TEM image of Pt-Pd alloy icosahedrons obtained at a low concentration of formaldehyde. (**a**) and (**b**) are modified with permission from ref. [30, 39], respectively

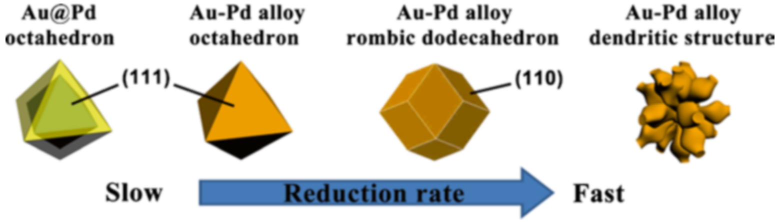

Fig. 6.6 Schemes of Au-Pd BMNCs obtained at different reduction rates of $HAuCl_4$ and Na_2PdCl_4. Modified with permission from ref. [28]

coalesce to lower surface energy. If these nuclei coalesce along one direction, nanowires will form [37]. Dendritic BMNCs could also be obtained through the coalescence route in the presence of micelles formed by block copolymers as soft templates. For instance, Au@Pd@Pt nanodendrites could be synthesized by using block copolymer Pluronic F127 as the template [46].

Figure 6.6 shows Au-Pd BMNCs obtained by reducing $HAuCl_4$ and Na_2PdCl_4 at different reduction rates, which reflect the influence of reduction rate on the BMNC structure. Au@Pd core–shell octahedrons were obtained when only cetyltrimethylammonium chloride (CTAC) served as the weak reductant. When ascorbic acid was added as a stronger reductant, Au-Pd alloy octahedrons formed [42]. Further increasing the concentration of ascorbic acid would lead to the formation of thermodynamically unfavored Au-Pd alloy rhombic dodecahedrons exposing twelve (110) facets [44]. If a stronger reductant, such as hydrazine, was used, Au-Pd alloy nanodendrites could be obtained through the coalescence route [43].

6.4.2 Facet-Specific Capping Agents

Facet-specific capping agents are ions or neutral molecules adsorbed specifically on certain facets of the metal, and are indispensable for the synthesis of BMNCs exposing well-defined facets. In water-phase synthesis, Br^- and I^- ions are the most

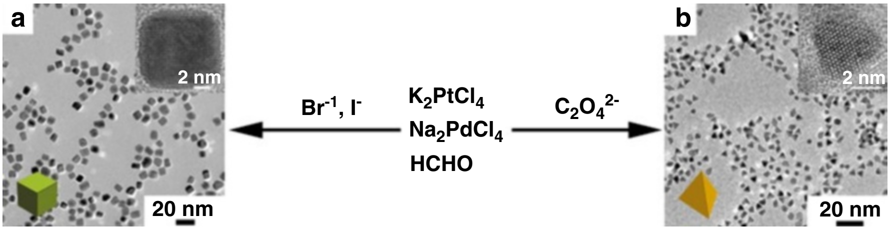

Fig. 6.7 (**a**) TEM and HRTEM images of Pt-Pd alloy cubes obtained with Br^- and I^- ions as capping agents and (**b**) TEM and HRTEM images of Pt-Pd alloy tetrahedrons obtained with $C_2O_4^{2-}$ ions as capping agents. (**a**) and (**b**) are modified with permission from ref. [30]

commonly used capping agents, which are selectively adsorbed on the (100) facets of diverse metals [17, 30], while oxalate [30] and citrate ions [41] are often used as specific capping agents for the (111) facets. In organic solvents, amine, carboxylic acid, and CO often serve as capping agents, but a lot of experimental evidences show that these capping agents stabilize different facets under different conditions [13, 33, 47]. For instance, CO stabilizes the (100) facets of Pt and the (111) facets of Pt_3Ni alloy. Both Pt_3Ni octahedrons and cubes could be obtained with high selectivity in the presence of CO in octadecylamine (OM) by changing the feeding sequence of different precursors [13].

The morphology of BMNCs can evolve through different processes, including the growth of nuclei, oxidative etching, and galvanic replacement reaction; all of these processes can be guided by introducing proper capping agents. Capping agents influence the growth stage of metallic NCs from both thermodynamic and kinetic aspects. Facet-specific capping agents can be selectively adsorbed on certain facets of metallic NCs and lower the surface energy. The relative surface energy of different facets decides the most thermodynamically stable morphology of the NCs. From a kinetic perspective, the relative coverage of capping agents on different facets is decided by the binding energy of the capping agent on each facet. Facets with a lower coverage of capping agents are more accessible to newly reduced monomers and, thus, the growth rate in the direction perpendicular to these facets is faster than that in other directions, leading to these facets diminishing. Consequently, facets strongly bound by capping agents will be retained in the growth stage [48]. The intrinsic mechanisms of these two aspects are different, but the results are always similar. If the capping agents are adsorbed stronger on one set of facets, the coverage of the capping agent on these facets will be higher and the surface energy will decrease more. From any aspect, these facets are preferentially exposed in the final product. Figure 6.7 shows Pt-Pd alloy cubes and tetrahedrons obtained via the hydrothermal method [30]. Cubes only exposing the (100) facets were obtained in the presence of Br^- and I^- ions, which specifically bind to the (100) facets, and tetrahedrons only exposing the (111) facets formed in the presence of oxalate ions, which selectively stabilize the (111) facets.

Capping agents also influence the oxidative etching process. Oxidative etching means that zero-valent metal atoms are oxidized by oxygen dissolved in solution.

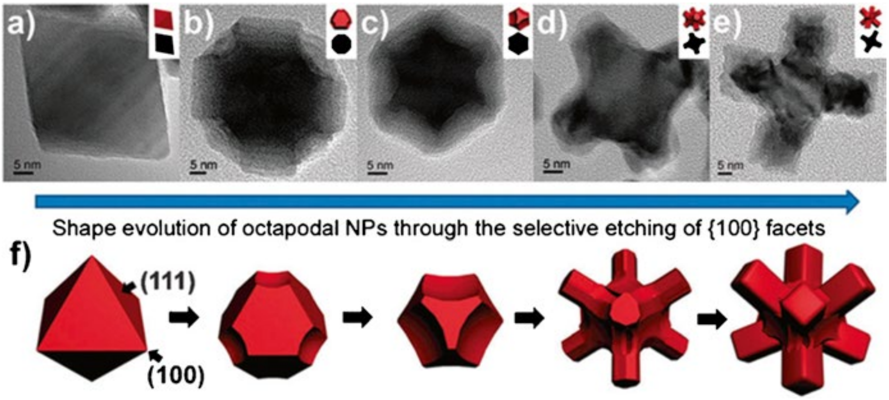

Fig. 6.8 Shape evolution of Au-Pd alloy BMNCs from octahedron to octapod in the presence of O_2 and Br^- ions. (**a**–**e**) The TEM images of the nanostructures obtained at (**a**) 10 min, (**b**) 15 min, (**c**) 20 min, (**d**) 2 h, and (**e**) 4 h. Reprinted with permission from ref. [49]

Capping agents that strongly coordinate with metal ions significantly promote the oxidative etching of zero-valent metal atoms. Equation 6.3 shows an example of the oxidative etching of Pd.

$$Pd + \frac{1}{2}\mathrm{O}_2 + 4Br^- + 2\mathrm{H}^+ \rightarrow PdBr_4^{2-} + \mathrm{H}_2\mathrm{O} \tag{6.3}$$

Due to the selective adsorption of these capping agents on certain facets, the oxidative etching process is promoted on certain directions. Au-Pd alloy octapods could be prepared using this approach, as shown in Fig. 6.8 [49]. In this synthetic reaction, Au-Pd alloy octahedrons formed through the reduction of $NaAuBr_4$ and K_2PtCl_4 in the first step. Br^- ions generated from the reduction of $AuBr_4^-$ were selectively adsorbed on the (100) facets of the alloy NCs and promoted the oxidative etching along the (100) direction. Consequently, the morphology of the alloy NCs evolved from octahedron to (100) facet-concaved truncated octahedrons and, finally, to octapods.

Similar to oxidative etching, the galvanic replacement reaction can also be guided by facet-specific capping agents. Pd-Pt concave cubes and octapods can be prepared based on this idea [50]. Galvanic replacement between Pd nanocubes and H_2PtCl_6 was designed in the presence of Br^- ions. Six (100) facets of Pd nanocubes were blocked by Br^- ions while eight corners on the (111) direction were accessible. Therefore, the dissolution of Pd atoms occurred preferentially on the (100) facets and the deposition of Pt atoms occurred on eight corners. Figure 6.9 shows the scheme of structure evolution from Pd nanocubes to Pd-Pt concave cubes and octapods.

In addition, surfactants as capping agents are indispensable for preparing bimetallic nanorods and nanowires. In the synthesis of Pt-Ag alloy nanowires in a

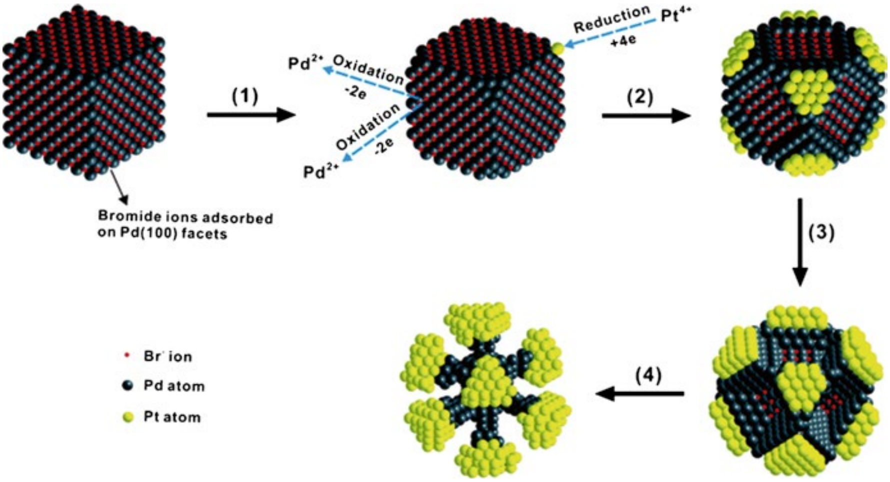

Fig. 6.9 Scheme of the galvanic replacement reaction between Pd nanocubes and $PtCl_6^{2-}$ ions in the presence of Br^- as the capping agent. Reprinted with permission from ref. [50]

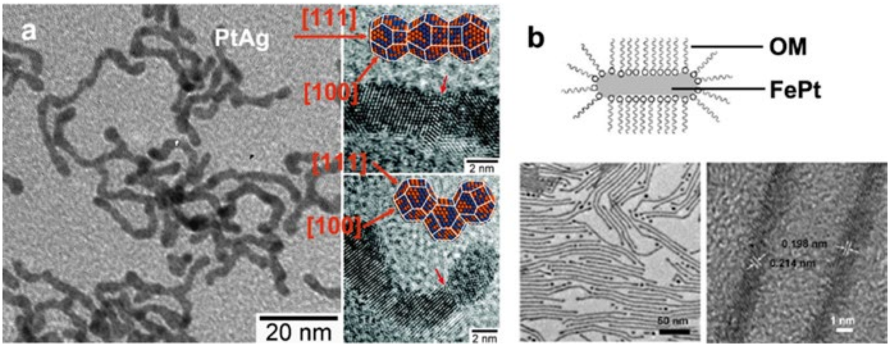

Fig. 6.10 (**a**) TEM and HRTEM images of Pt-Ag alloy nanowires formed by oriented coalescence of Pt-Ag crystallites along the [111] direction. Modified with permission from ref. [37]. (**b**, *top*) Scheme showing the reversed micelle formed by OM in the synthesis of Fe-Pt-alloy nanowires and (**b**, *bottom*) TEM and HRTEM images of Fe-Pt-alloy nanowires. Modified with permission from ref. [32]

mixed solvent of OM and oleic acid (OA), the coverage of OM was higher on the (100) facets than on the (111) facets, leading to the oriented coalescence of Pt-Ag crystallites along the [111] direction, as shown in Fig. 6.10a [37]. OM could also form rod-shaped reversed micelles, which served as the soft templates for the formation of Fe-Pt nanorods, as shown in Fig. 6.10b [32].

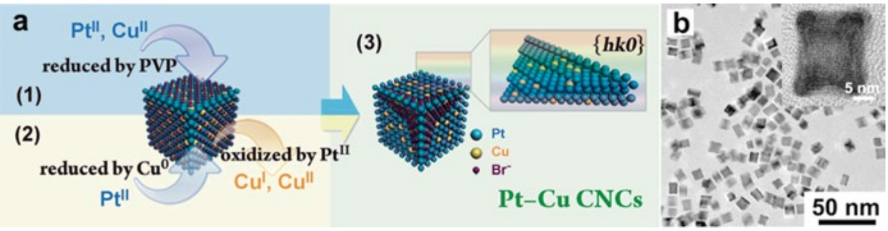

Fig. 6.11 (**a**) Scheme of the formation of Pt-Cu concave nanocubes. (**b**) TEM and HRTEM images of Pt-Cu concave nanocubes. Modified with permission from ref. [40]

6.4.3 *Combination of Underpotential Deposition and the Galvanic Replacement Reaction*

UPD and the galvanic replacement reaction are two unique processes in the synthesis of BMNCs. Due to the UPD phenomenon that a monolayer of a non-noble metal can form on the surface of a noble metal at a potential much higher than the equilibrium potential required to reduce non-noble metal ions, non-noble metal precursors are easier to be reduced together with noble metal precursors. Thus, a series of noble metal-based bimetallic NCs could be synthesized through this co-reduction approach, as long as the weighted average electronegativity of the two metals is higher than a critical value, such as 1.93 in octadecylamine [51]. The zero-valent non-noble metal atoms can then reduce the noble metal precursor and be replaced by the noble metal atoms. In this combination of UPD and the galvanic replacement reaction, non-noble metal ions serve as mediators for the reduction of the noble metal precursors, which greatly influence the morphology of the final product.

Cu^{2+} ions are usually used as this mediator. For instance, Au-Pd alloy NCs were hard to prepare due to the large reduction potential gap between $AuCl_4^-/Au$ and Pd^{2+}/Pd. The equilibrium reduction potential of Cu^{2+}/Cu is lower than that of Pd^{2+}/Pd, but the potential for UPD of Cu on the surface of Au is within the as-mentioned reduction potential gap of Au and Pd. When $AuCl_4^-$, Pd^{2+}, and Cu^{2+} ions were added together, Au nuclei formed first. Then a Cu monolayer deposited on the Au nuclei, followed by galvanic replacement between the Cu and Pd^{2+} or $AuCl_4^-$. Au-Pd alloy hexoctahedrons could be obtained through this approach [52]. A Cu-mediated combination of UPD and galvanic replacement could also be used to fabricate concave structures, including Pt-Cu and Pt-Pd-Cu concave nanocubes, as shown in Fig. 6.11 [40]. In the first step, $PtCl_4^{2-}$ ions were reduced by PVP and Cu atoms deposited on Pt surface through UPD. Pt-Cu alloy cubes then formed in the presence of Br^- ions. Whereafter, Cu reduced the $PtCl_4^{2-}$ and Pd^{2+} ions in the solution. Because Br^- ions blocked most of the sites on the (100) facets of the cubes, the Pt and Pd atoms preferentially deposited on the edges and corners of the Pt-Cu alloy cubes. Finally, Pt-Cu and Pt-Pd-Cu concave nanocubes could form. The surface of the concave nanocubes was rich in Pt and Pd, and the cores were rich in Cu.

6.5 Impact of Composition and Structure on Electrocatalytic Performance

Pt- and Pd-based metallic NCs are the most commonly used catalysts for both the cathodic (ORR) and anodic reactions (MOR) of DMFCs. Especially, Pt-based bimetallic NCs exhibit high activity and stability in acidic electrolytes. The main problems with Pt monometallic NCs as cathodic and anodic catalysts are that a high overpotential is needed for ORR and that the active sites are easy to be poisoned by intermediates in MOR, respectively. Designing and synthesizing Pt-based BMNCs with proper composition and morphology is the key to addressing these problems. A lot of experimental and theoretical work has been devoted to investigate the dependence of electrocatalytic performance on the composition, morphology, and size of Pt-based bimetallic NCs. This section will briefly introduce this structure–activity relationship of BMNCs used for electrocatalysis.

6.5.1 Relationship Between Adsorption Strength and Electrocatalytic Activity

A general heterogeneous catalytic reaction is composed of three steps: adsorption of reactants, reaction on the surface of the catalyst, and desorption of products. If only one adsorbed intermediate is involved, weak adsorption of this intermediate results in low coverage of reactants while strong adsorption leads to a high energy barrier for the desorption step. Therefore, the catalytic activity exhibits a volcano-shaped relationship dependent on the adsorption energy. Proper adsorption energy, neither too strong nor too weak, is the most important feature of catalysts with high activity.

When multistep surface reactions are involved, the adsorption energy of a certain kind of atom or small molecule, called a descriptor, is usually used as the *x-coordinate* of the volcano model. Herein, we use ORR as an example [4, 53, 54]. ORR is generally considered a four-step reaction, as shown in Fig. 6.12a. The black line shows the potential energy curve of ORR at 0 V vs. a reversible hydrogen electrode (RHE) and the energy difference of every step x is marked with ΔG_x. No ORR current can be observed at the equilibrium potential of 1.23 V vs. RHE, because extra energy is still needed for some steps at this potential, as shown by the red line in Fig. 6.12a. Therefore, the step with the smallest ΔG_x is the rate-limiting step that decides the upper limit potential for ORR, as shown with the blue line in Fig. 6.12a. Due to scaling relations where the adsorption energy of every intermediate involved in ORR is approximately linear to the dissociated adsorption energy of oxygen, marked with E_O, every ΔG_x exhibits a linear relationship to E_O [55, 56]. Hence, ΔG_1 and ΔG_4 form a volcano with E_O as the descriptor, as shown in Fig. 6.12b. Pt is the monometallic catalyst nearest to the top of the volcano, and the fourth step, the desorption of HO*, is the rate-limiting step for ORR on Pt. Weakening the adsorption of OH on the Pt surface (i.e., decreasing the adsorption energy of oxygen by a certain extent) can enhance the ORR activity of the catalyst.

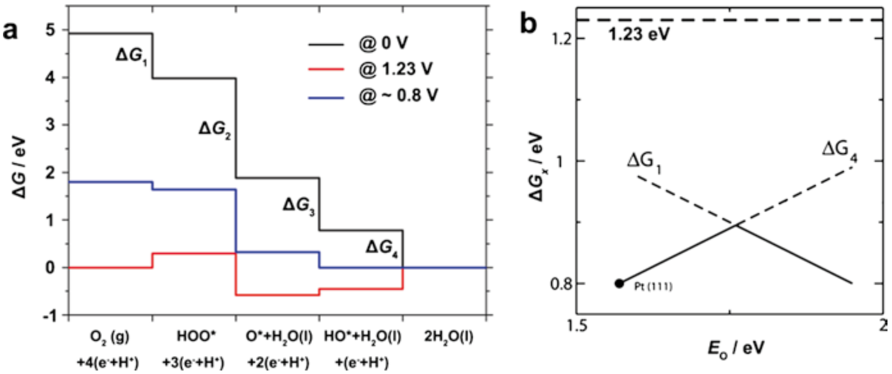

Fig. 6.12 (**a**) Schematic potential energy curve of ORR at an electrode potential of 0 V vs. RHE (*black line*), 1.23 V vs. RHE (equilibrium electrode potential, *red line*), and at ~0.8 V vs. RHE ($\Delta G_4/e$, *blue line*). Energy difference of every step at 0 V vs. RHE is marked with ΔG_x. (**b**) Dependency of ΔG_1 and ΔG_4 on the dissociated adsorption energy of oxygen. The fourth step limits the activity of ORR on the Pt(111) facet. The *dashed line* indicates the equilibrium electrode potential of ORR. Modified with permission from ref. [53]

MOR is more complicated than ORR. Two different kinds of paths, a direct path and an indirect path, are considered as the linkage between methanol and the oxidation products (i.e., CO_2 and H_2O). *CO species are involved in the indirect path, but not involved in the direct path [57]. Due to the strong adsorption of CO on the Pt surface, the rate-limiting step for the indirect path on the Pt surface is the oxidation of *CO. Moreover, the high coverage of *CO also suppresses the direct path. To increase the MOR activity of Pt-based catalysts, we need to weaken the adsorption of CO on the Pt sites and introduce some oxygen adsorption sites to help with stripping the CO on the Pt sites.

6.5.2 Mechanisms of Tuning Adsorption Energy

According to the *d*-band theory developed by Norskov and co-workers, adsorption energy is related to the local *d*-band center position of the surface atoms on the metallic catalysts. A shallow local *d*-band, compared to the Fermi level, leads to strong adsorption and a deep local *d*-band leads to weak adsorption [58, 59]. Therefore, BMNCs should be designed to possess the proper local *d*-band center position and, consequently, proper adsorption energy. The local *d*-band position of surface atoms can be tuned through two mechanisms: electron transfer between different kinds of metal atoms and changing the *d*-state overlap between two neighboring atoms, as shown in Fig. 6.13 [20]. The former mechanism changes the occupancy of the local *d*-band and the latter mechanism changes the width of the local *d*-band.

Electrons can migrate from metal atoms with lower electronegativity to those with higher electronegativity, as shown in Fig. 6.13a. In alloys of Pt and early transition

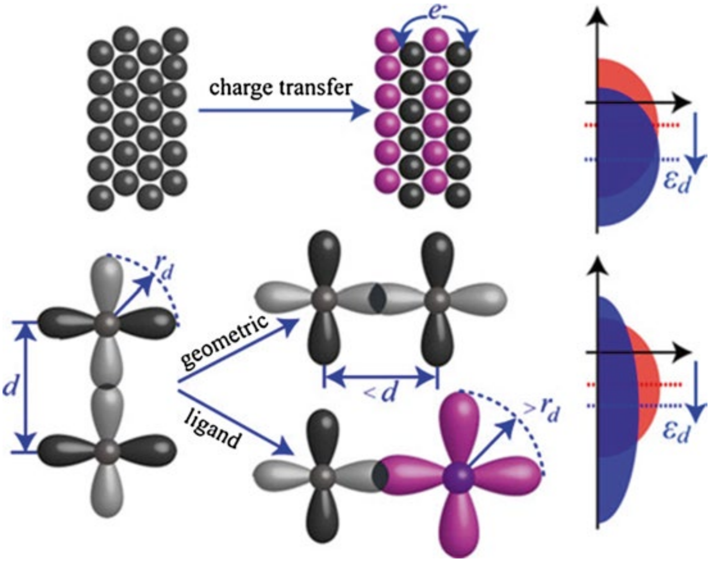

Fig. 6.13 Two mechanisms fortuning the center position of local *d*-band. (*top*) Charge transfer from one element to another results in a change in occupancy of the local *d*-band. (*bottom*) Change in the *d*-state overlap between two neighboring atoms leads to a change in *d*-band width. Reprinted with permission from ref. [20]

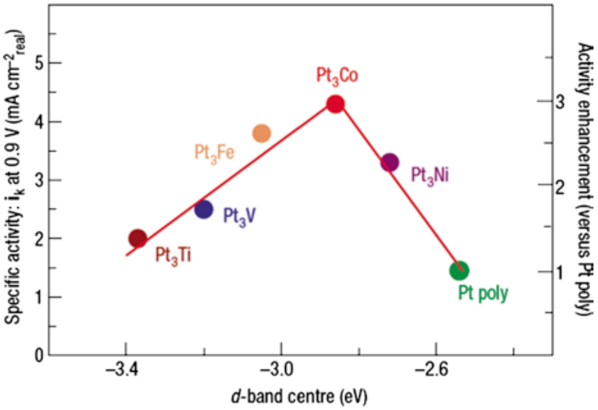

Fig. 6.14 Relationship between the experimentally measured specific activity for ORR on surface-dealloyed Pt_3M alloy BMNCs in 0.1 M $HClO_4$ at 333 K vs. the local *d*-band center position of Pt. Reprinted with permission from ref. [5]

metals, for instance, electrons migrate from the early transition metals to the Pt atoms. As a result, the occupancy of the local *d*-band of the surface Pt atoms increases and the adsorption energy on the Pt sites decreases. This phenomenon can be utilized to weaken the adsorption energy of HO* for Pt-based ORR catalysts [4, 5]. As shown in Fig. 6.14, the local *d*-band went lower as Pt was alloyed with a more active transition metal, and a clear volcano-shape relationship between ORR

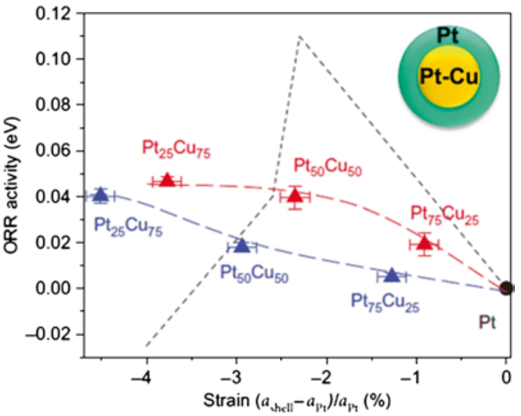

Fig. 6.15 The relationship between experimental ORR activity (in units of $kT\ \ln(J_{\text{alloy}}/J_{\text{Pt}})$, $T = 298$ K) of dealloyed Pt-Cu BMNCs after annealing at 800 °C (*red triangles*) and 950 °C (*blue triangles*) and the lattice strain of the Pt shell. The *inset* shows a scheme of a dealloyed Pt-Cu BMNC. The *dashed line* shows the DFT prediction of the ORR activity for a Pt(111) single-crystalline slab under isotropic strain. Modified with permission from ref. [8]

activity and the local *d*-band position can be seen. Among these alloys, Pt_3M (M = Fe, Co, Ni) alloys with a dealloyed Pt surface layer exhibited significant enhanced ORR activity, compared to polycrystalline Pt [5].

The enhancement of ORR activity in the alloys of Pt and early transition metals does not result entirely from the electron transfer effect. Since the lattice distance of the alloy is much smaller than that of pure Pt, the dealloyed Pt surface layer is significantly compressed, leading to an increase in the *d*-orbital overlap between the two neighboring atoms and the broadening of the local *d*-band, as shown in Fig. 6.13b. In this situation, the *d*-band center has to go lower to prevent changing the band occupancy, and the adsorption energy of OH decreases. Strasser and co-workers investigated a series of Pt-Cu NCs with Pt-Cu alloy cores and a dealloyed Pt surface [8]. Figure 6.15 shows how the composition of the alloy cores aroused the lattice compression of the dealloyed Pt surface and, furthermore, improved the ORR activity of the BMNCs. Lattice compression can not only be introduced through a mismatch between the core and surface lattices but also arise from the multi-twinned structure. Tetrahedrons need to be compressed when they are accommodated into an icosahedron; therefore, the lattice of icosahedrons is shrunken compared with that of tetrahedrons [39, 60]. Both kinds of BMNCs only exposed the (111) facets, while, for instance, the Pt-Pd alloy icosahedrons exhibit a higher MOR specific activity than the Pt-Pd alloy tetrahedrons due to lattice shrinkage. Lattice shrinkage led to the *d*-band sinking, causing weakening of the CO adsorption on the metal surface [39].

More importantly, catalytic activity is very sensitive to the exposed facets of the metallic catalysts. The coordination numbers of the surface atoms vary on different facets. Surface atoms with a high coordination number, such as atoms on the (111) facets for FCC metals, possess a broad local *d*-band and, thus, a small adsorption energy; the adsorption energy is large on the surface atoms with a low coordination

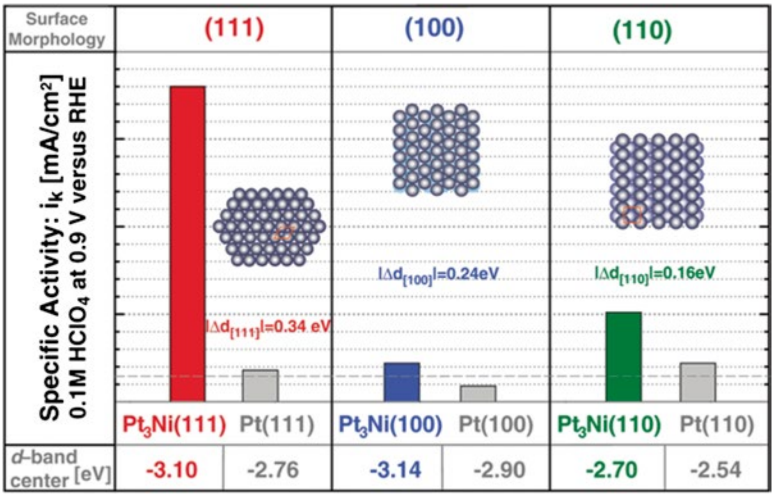

Fig. 6.16 Specific activity of ORR measured at 0.9 V vs. RHE in $HClO_4$ (0.1 M) at 333 K on three low-index facets of Pt_3Ni, as compared with the corresponding facets of Pt. The specific activity of polycrystalline Pt is also marked by a *horizontal dashed grey line*. The values of the experimental *d*-band center position of each facet are also listed. Reprinted with permission from ref. [6]

number, such as atoms on the (110) facets for FCC metals. Especially, the coordination numbers of step and kink atoms are significantly lower than that of atoms on the terrace. Therefore, step and kink atoms are more active for adsorption but desorption is more difficult. Facets with a high Miller index are rich in step and kink atoms and, consequently, are very active for adsorption. Figure 6.16 shows the dependence of ORR activity on the exposed facet of the Pt_3Ni alloy [6]. The surface morphology of different facets strongly influenced the local *d*-band center position and the ORR activity exhibited a dramatic difference on different facets. The ORR specific activity on the (111) facet of Pt_3Ni was about nine times of that on the (100) facet and four times of that on the (110) facet.

In addition, when two kinds of metals atoms are simultaneously exposed on the surface, species adsorbed on different sites may interact with each other and this interaction affects the adsorption energy of these species. For instance, on a Pt-M (M = Re, Os, Ir, etc.) surface, oxygen atoms tend to be adsorbed on the M sites, and the as-formed M-O species repulsed OH from being adsorbed on the surrounding Pt sites. This effect benefits Pt catalysts for ORR due to the weak adsorption of OH on this bimetallic surface [9, 61].

6.6 Summary

Starting with the structure classification of BMNCs, this review has summarized the synthetic strategies for synthesizing BMNCs with rational design, and the influence of structure and composition of BMNCs on their electrocatalytic activity.

BMNCs with different structures can form through four different routes: continuous growth, crystallite coalescence, seeded growth, and the galvanic replacement reaction. Some key factors, including the reduction rate of metal precursors, usage of facet-specific capping agents, and the combination of UPD and the galvanic replacement reaction, determine the formation route and guide the structure evolution of BMNCs. Furthermore, the electrocatalytic activity of BMNCs can be enhanced through electron transfer between different atoms, the tuning of surface structure of BMNCs, and the interaction between adsorbates on different metal atoms.

However, more effort is needed to further increase the energy exchange efficiency and reduce the cost of fuel cells by exploiting the shape-tunable BMNCs. In the field of synthetic chemistry, it is still challenging to prepare water-soluble BMNCs containing non-noble metals of uniform size and morphology. The function of surfactants (added during the synthesis process) in electrocatalytic reactions is poorly investigated, and more effort should be devoted to developing surfactant-free synthetic methods. New designs for BMNCs are also needed to increase the stability of non-noble metals in the acidic electrolyte. In the long run, a combination of in situ and/or *operando* studies of the molecular electrocatalytic mechanisms using various spectroscopic and microscopic methods and understanding the elemental reaction steps and the associated transition states using theoretical simulations, such as first-principles calculations, will greatly contribute to the rational design and development of active, durable, and economical BMNC nanocatalysts for real applications in fuel cells.

Acknowledgment This work was supported by the NSFC (Grant Nos. 21025101 and 21271011). Y.W.Z. particularly appreciates the financial aid of China National Funds for Distinguished Young Scientists from the NSFC.

References

1. Debe MK (2012) Electrocatalyst approaches and challenges for automotive fuel cells. Nature 486:43
2. Wagner FT, Lakshmanan B, Mathias MF (2010) Electrochemistry and the future of the automobile. J Phys Chem Lett 1:2204
3. Markovic NM, Schmidt TJ, Stamenkovic V, Ross PN (2001) Oxygen reduction reaction on Pt and Pt bimetallic surfaces: a selective review. Fuel Cells 1:105
4. Greeley J, Stephens IEL, Bondarenko AS, Johansson TP, Hansen HA, Jaramillo TF, Rossmeisl J, Chorkendorff I, Norskov JK (2009) Alloys of platinum and early transition metals as oxygen reduction electrocatalysts. Nat Chem 1:552
5. Stamenkovic VR, Mun BS, Arenz M, Mayrhofer KJJ, Lucas CA, Wang G, Ross PN, Markovic NM (2007) Trends in electrocatalysis on extended and nanoscale Pt-bimetallic alloy surfaces. Nat Mater 6:241
6. Stamenkovic VR, Fowler B, Mun BS, Wang G, Ross PN, Lucas CA, Markovic NM (2007) Improved oxygen reduction activity on $Pt_3Ni(111)$ via increased surface site availability. Science 315:493
7. Hwang SJ, Kim S-K, Lee J-G, Lee S-C, Jang JH, Kim P, Lim T-H, Sung Y-E, Yoo SJ (2012) Role of electronic perturbation in stability and activity of Pt-based alloy nanocatalysts for oxygen reduction. J Am Chem Soc 134:19508

8. Strasser P, Koh S, Anniyev T, Greeley J, More K, Yu C, Liu Z, Kaya S, Nordlund D, Ogasawara H, Toney MF, Nilsson A (2010) Lattice-strain control of the activity in dealloyed core–shell fuel cell catalysts. Nat Chem 2:454
9. Adzic RR, Zhang J, Sasaki K, Vukmirovic MB, Shao M, Wang JX, Nilekar AU, Mavrikakis M, Valerio JA, Uribe F (2007) Platinum monolayer fuel cell electrocatalysts. Top Catal 46:249
10. Petrii OA (2008) Pt–Ru electrocatalysts for fuel cells: a representative review. J Solid State Electr 12:609
11. Bauer E, Vandermerwe JH (1986) Structure and growth of crystalline superlattices: from monolayer to superlattice. Phys Rev B Condens Matter 33:3657
12. Johnson RA (1989) Alloy models with the embedded-atom method. Phys Rev B Condens Matter 39:12554
13. Zhang J, Yang H, Fang J, Zou S (2010) Synthesis and oxygen reduction activity of shape-controlled Pt_3Ni nanopolyhedra. Nano Lett 10:638
14. Kim J, Lee Y, Sun SH (2010) Structurally ordered Fe-Pt nanoparticles and their enhanced catalysis for oxygen reduction reaction. J Am Chem Soc 132:4996
15. Wang DL, Xin HLL, Hovden R, Wang HS, Yu YC, Muller DA, DiSalvo FJ, Abruna HD (2013) Structurally ordered intermetallic platinum–cobalt core–shell nanoparticles with enhanced activity and stability as oxygen reduction electrocatalysts. Nat Mater 12:81
16. Song JH, Kim F, Kim D, Yang PD (2005) Crystal overgrowth on gold nanorods: tuning the shape, facet, aspect ratio, and composition of the nanorods. Chem Eur J 11:910
17. Habas SE, Lee H, Radmilovic V, Somorjai GA, Yang P (2007) Shaping binary metal nanocrystals through epitaxial seeded growth. Nat Mater 6:692
18. Fan F-R, Liu D-Y, Wu Y-F, Duan S, Xie Z-X, Jiang Z-Y, Tian Z-Q (2008) Epitaxial growth of heterogeneous metal nanocrystals: from gold nano-octahedra to palladium and silver nanocubes. J Am Chem Soc 130:6949
19. Jin M, Zhang H, Wang J, Zhong X, Lu N, Li Z, Xie Z, Kim MJ, Xia Y (2012) Copper can still be epitaxially deposited on palladium nanocrystals to generate core–shell nanocubes despite their large lattice mismatch. ACS Nano 6:2566
20. Xin H, Holewinski A, Schweitzer N, Nikolla E, Linic S (2012) Electronic structure engineering in heterogeneous catalysis: identifying novel alloy catalysts based on rapid screening for materials with desired electronic properties. Top Catal 55:376
21. Gan L, Heggen M, Rudi S, Strasser P (2012) Core–shell compositional fine structures of dealloyed Pt_xNi_{1-x} nanoparticles and their impact on oxygen reduction catalysis. Nano Lett 12:5423
22. Zhang J, Mo Y, Vukmirovic MB, Klie R, Sasaki K, Adzic RR (2004) Platinum monolayer electrocatalysts for O_2 reduction: Pt monolayer on Pd(111) and on carbon-supported Pd nanoparticles. J Phys Chem B 108:10955
23. Karan HI, Sasaki K, Kuttiyiel K, Farberow CA, Mavrikakis M, Adzic RR (2012) Catalytic activity of platinum monolayer on iridium and rhenium alloy nanoparticles for the oxygen reduction reaction. ACS Catal 2:817
24. Gong K, Su D, Adzic RR (2010) Platinum-monolayer shell on $AuNi_{0.5}Fe$ nanoparticle core electrocatalyst with high activity and stability for the oxygen reduction reaction. J Am Chem Soc 132:14364
25. Herrero E, Buller LJ, Abruna HD (2001) Underpotential deposition at single crystal surfaces of Au Pt, Ag and other materials. Chem Rev 101:1897
26. Wang RM, Dmitrieva O, Farle M, Dumpich G, Ye HQ, Poppa H, Kilaas R, Kisielowski C (2008) Layer resolved structural relaxation at the surface of magnetic FePt icosahedral nanoparticles. Phys Rev Lett 100:017205
27. Lamer VK, Dinegar RH (1950) Theory production and mechanism of formation of monodispersed hydrosols. J Am Chem Soc 72:4847
28. Gu J, Zhang Y-W, Tao F (2012) Shape control of bimetallic nanocatalysts through well-designed colloidal chemistry approaches. Chem Soc Rev 41:8050
29. Huang X, Zhang H, Guo C, Zhou Z, Zheng N (2009) Simplifying the creation of hollow metallic nanostructures: one-pot synthesis of hollow palladium/platinum single-crystalline nanocubes. Angew Chem Int Ed 48:4808

30. Yin A-X, Min X-Q, Zhang Y-W, Yan C-H (2011) Shape-selective synthesis and facet-dependent enhanced electrocatalytic activity and durability of monodisperse sub-10 nm Pt-Pd tetrahedrons and cubes. J Am Chem Soc 133:3816
31. Park JY, Zhang Y, Grass M, Zhang T, Somorjai GA (2008) Tuning of catalytic CO oxidation by changing composition of Rh–Pt bimetallic nanoparticles. Nano Lett 8:673
32. Wang C, Hou Y, Kim J, Sun S (2007) A general strategy for synthesizing FePt nanowires and nanorods. Angew Chem Int Ed 46:6333
33. Wu J, Gross A, Yang H (2011) Shape and composition-controlled platinum alloy nanocrystals. Using carbon monoxide as reducing agent. Nano Lett 11:798
34. Wu Y, Cai S, Wang D, He W, Li Y (2012) Syntheses of water-soluble octahedral, truncated octahedral, and cubic Pt–Ni nanocrystals and their structure–activity study in model hydrogenation reactions. J Am Chem Soc 134:8975
35. Carpenter MK, Moylan TE, Kukreja RS, Atwan MH, Tessema MM (2012) Solvothermal synthesis of platinum alloy nanoparticles for oxygen reduction electrocatalysis. J Am Chem Soc 134:8535
36. Cui C, Gan L, Li H-H, Yu S-H, Heggen M, Strasser P (2012) Octahedral PtNi nanoparticle catalysts: exceptional oxygen reduction activity by tuning the alloy particle surface composition. Nano Lett 12:5885
37. Peng Z, You H, Yang H (2010) Composition-dependent formation of platinum silver nanowires. ACS Nano 4:1501
38. Lim B, Jiang M, Camargo PHC, Cho EC, Tao J, Lu X, Zhu Y, Xia Y (2009) Pd-Pt bimetallic nanodendrites with high activity for oxygen reduction. Science 324:1302
39. Yin A-X, Min X-Q, Zhu W, Wu H-S, Zhang Y-W, Yan C-H (2012) Multiply twinned Pt–Pd nanoicosahedrons as highly active electrocatalysts for methanol oxidation. Chem Commun 48:543
40. Yin A-X, Min X-Q, Zhu W, Liu W-C, Zhang Y-W, Yan C-H (2012) Pt–Cu and Pt–Pd–Cu concave nanocubes with high-index facets and superior electrocatalytic activity. Chem Eur J 18:777
41. Jiang M, Lim B, Tao J, Camargo PHC, Ma C, Zhu Y, Xia Y (2010) Epitaxial overgrowth of platinum on palladium nanocrystals. Nanoscale 2:2406
42. Hong JW, Kim D, Lee YW, Kim M, Kang SW, Han SW (2011) Atomic-distribution-dependent electrocatalytic activity of Au-Pd bimetallic nanocrystals. Angew Chem Int Ed 50:8876
43. Lee YW, Kim M, Kim Y, Kang SW, Lee J-H, Han SW (2010) Synthesis and electrocatalytic activity of Au–Pd alloy nanodendrites for ethanol oxidation. J Phys Chem C 114:7689
44. Lee YW, Kim M, Kang SW, Han SW (2011) Polyhedral bimetallic alloy nanocrystals exclusively bound by {110}facets: Au–Pd rhombic dodecahedra. Angew Chem Int Ed 50:3466
45. Xia Y, Xiong Y, Lim B, Skrabalak SE (2009) Shape-controlled synthesis of metal nanocrystals: simple chemistry meets complex physics? Angew Chem Int Ed 48:60
46. Wang L, Yamauchi Y (2010) Autoprogrammed synthesis of triple-layered Au@Pd@Pt core-shell nanoparticles consisting of a Au@Pd bimetallic core and nanoporous Pt shell. J Am Chem Soc 132:13636
47. Wang Y, Sun Z, Kumbhar A, Luo Z, Wang C, Zhang J, Porter N, Xu C, Sun K, Martens B, Fang J (2013) Is CO adequate to facilitate the formation of Pt_3M (M=Fe, Ni and Co) nanocubes? Chem Commun 49:3955
48. Wang ZL (2000) Transmission electron microscopy of shape-controlled nanocrystals and their assemblies. J Phys Chem B 104:1153
49. Hong JW, Lee YW, Kim M, Kang SW, Han SW (2011) One-pot synthesis and electrocatalytic activity of octapodal Au–Pd nanoparticles. Chem Commun 47:2553
50. Zhang H, Jin M, Wang J, Li W, Camargo PHC, Kim MJ, Yang D, Xie Z, Xia Y (2011) Synthesis of Pd-Pt bimetallic nanocrystals with a concave structure through a bromide-induced galvanic replacement reaction. J Am Chem Soc 133:6078
51. Wang D, Peng Q, Li Y (2010) Nanocrystalline intermetallics and alloys. Nano Res 3:574
52. Zhang L, Zhang J, Kuang Q, Xie S, Jiang Z, Xie Z, Zheng L (2011) Cu^{2+}-assisted synthesis of hexoctahedral Au-Pd alloy nanocrystals with high-index facets. J Am Chem Soc 133:17114

53. Rossmeisl J, Karlberg GS, Jaramillo T, Norskov JK (2009) Steady state oxygen reduction and cyclic voltammetry. Faraday Discuss 140:337
54. Koper MTM (2011) Thermodynamic theory of multi-electron transfer reactions: implications for electrocatalysis. J Electroanal Chem 660:254
55. Man IC, Su H-Y, Calle-Vallejo F, Hansen HA, Martinez JI, Inoglu NG, Kitchin J, Jaramillo TF, Norskov JK, Rossmeisl J (2011) Universality in oxygen evolution electrocatalysis on oxide surfaces. ChemCatChem 3:1159
56. Abild-Pedersen F, Greeley J, Studt F, Rossmeisl J, Munter TR, Moses PG, Skulason E, Bligaard T, Norskov JK (2007) Scaling properties of adsorption energies for hydrogen-containing molecules on transition-metal surfaces. Phys Rev Lett 99:016105
57. Ferrin P, Mavrikakis M (2009) Structure sensitivity of methanol electrooxidation on transition metals. J Am Chem Soc 131:14381
58. Kitchin JR, Norskov JK, Barteau MA, Chen JG (2004) Modification of the surface electronic and chemical properties of Pt(111) by subsurface 3d transition metals. J Chem Phys 120:10240
59. Hammer B, Norskov JK (2000) Theoretical surface science and catalysis—calculations and concepts. In: Gates BC, Knozinger H (eds) Advances in catalysis, vol 45: impact of surface science on catalysis, vol 45. Academic, San Diego, p 71
60. Wu JB, Qi L, You HJ, Gross A, Li J, Yang H (2012) Icosahedral platinum alloy nanocrystals with enhanced electrocatalytic activities. J Am Chem Soc 134:11880
61. Zhang JL, Vukmirovic MB, Sasaki K, Nilekar AU, Mavrikakis M, Adzic RR (2005) Mixed-metal Pt monolayer electrocatalysts for enhanced oxygen reduction kinetics. J Am Chem Soc 127:12480

Part III

In Situ Surface Characterization to Bridge Pressure Gaps

Chapter 7
Role of Surface Oxides on Model Nanocatalysts in Catalytic Activity of CO Oxidation

Jeong Young Park, Kamran Qadir, and Sun Mi Kim

7.1 Introduction

Rapid advances in the nanosciences and colloidal chemistry have generated new opportunities in the fields of physical and chemical science, including tuning the size, shape, and composition of noble metals at nanoscale, which have revealed many interesting properties. Studies identifying molecular factors that affect catalytic activity provide the means to control catalytic activity, a significant achievement in catalysis. Several molecular factors, including structural and electronic effects, metal–support interactions, and the presence of a surface oxide layer, have been reported as candidates for improving catalytic activity. Among these factors, the oxide layer on the metal surface is considered to play an important role in determining catalytic activity and there are a growing number of studies in this area. Understanding the chemical reactivity of a metal oxide is a rather complicated issue, requiring significant research to date. Here, we outline recent experimental work on the role of surface oxide on metal nanoparticles (NPs) that determines the catalytic activity of heterogeneous catalysis, including the effect of oxidation states of nanoparticles on the catalytic activity for model catalysts of single crystals and nanoparticles, with several examples, including Pt, Rh, Ru, and Pd.

J.Y. Park (✉) • K. Qadir • S.M. Kim
Graduate School of EEWS (WCU) and NanoCentury KI, Korea Advanced Institute of Science and Technology (KAIST), Daejeon 305-701, Republic of Korea

Center for Nanomaterials and Chemical Reactions, Institute for Basic Science, Daejeon 305-701, Republic of Korea
e-mail: jeongypark@kaist.ac.kr

J.Y. Park (ed.), *Current Trends of Surface Science and Catalysis*,
DOI 10.1007/978-1-4614-8742-5_7,

7.2 Pt Oxide

The platinum metal is an established noble metal catalyst that has been studied extensively due to its high catalytic activity and stability for the CO oxidation reaction. For oxidation of CO, studies on platinum single crystals report a surface reconstruction [1, 2] when a critical CO concentration is reached. Hendriksen et al. reported the observation of a roughening of the single crystal platinum surface, which was attributed to a switch from the metal surface to an oxide surface that coincided with a sudden increase in catalytic activity [3]. Ackermann et al. revealed an interrelation between the structure and reactivity of surface oxides on Pt(110) during catalytic CO oxidation using surface X-ray diffraction [4]. However, the fundamental mechanisms that occur during the catalytic reaction, which are strongly linked to the structure of platinum, remain elusive and there is an ongoing debate regarding the influence of surface structure on CO oxidation kinetics. To fully understand and model these phenomena, we need further in situ characterization of adsorbed oxygen and oxide phases of Pt(110) in O_2 and CO, and under reaction conditions.

Research into whether there is oxide formation during the reaction and whether this oxide is responsible for the reactivity is progressing. Recently, Butcher et al. investigated the formation of nanometer-sized islands of multilayered α-PtO_2-like surface oxide along with chemisorbed oxygen and its interaction with CO molecules using various in situ techniques, including ambient pressure X-ray photoelectron spectroscopy (AP-XPS), high-pressure scanning tunneling microscopy (HP-STM), and density functional theory (DFT) calculations [5]. Figure 7.1a shows the Pt4*f* spectrum of a clean Pt single crystal surface taken using AP-XPS at the different O_2 pressure conditions carried out by Butcher et al. Depending upon the exposure to an elevated oxygen pressure, it was found that only chemisorbed oxygen or α-PtO_2-like nanoscale surface oxide is observed on the clean Pt(110) crystal surface. The $Pt4f_{7/2}$ region for clean Pt(110) can be fitted with two peaks ((i), 230 eV photon energy) corresponding to bulk Pt (71.2 ± 0.1 eV) and surface Pt with a surface core level shift (CLS) of −0.4 eV (70.8 ± 0.1 eV) [6]. The surface peak arises from under-coordinated Pt atoms in the topmost atomic layer, indicating a clean surface. Increasing the pressure to 0.05 Torr O_2 (ii) leads to an increase in the intensity of the Pt4*f* peak at 71.9 eV due to Pt surface atoms bound to chemisorbed Oxygen (Chem-O). Increasing the pressure to 0.5 Torr (iii) further increases the Chem-O peak intensity, relative to that of the bulk Pt peak, and a third peak at 73.4 eV arises, which is assigned to a surface oxide (Surf-O). STM images inset in Fig. 7.1 under similar conditions show a roughened surface with nanometer islands.

Figure 7.1b shows the change in O and CO coverage on a Pt(110) surface at 270 K exposed to 0.5 Torr O_2, then 10^{-6} Torr CO, revealing a correlation between the structure and reactivity of the surface oxide. As shown in Fig. 7.1b, the coverage of CO increases while the total coverage of O_2, including Chem-O and Surf-O, decreases with reaction time. This result implies that the α-PtO_2-like nanoscale surface oxide is catalytically active for the CO oxidation reaction, which is consistent

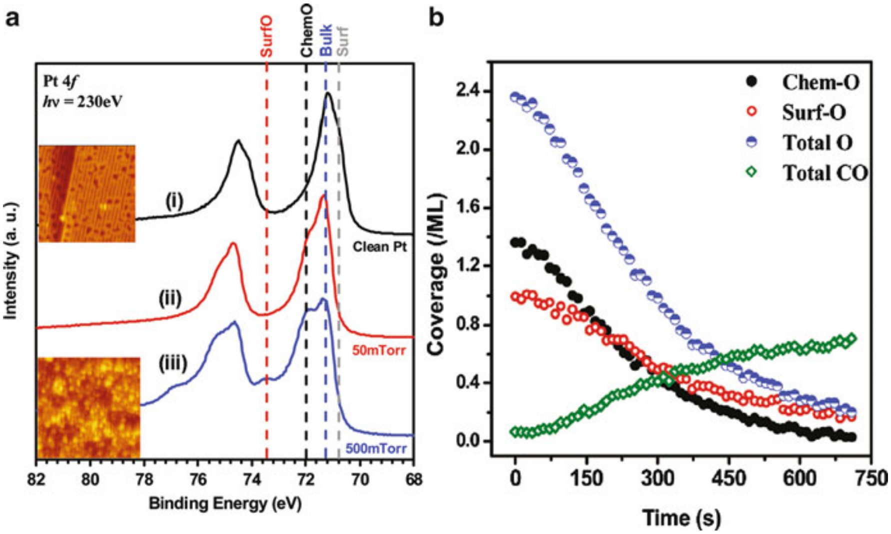

Fig. 7.1 (**a**) (i) The Pt4*f* spectrum taken after sputtering and annealing in UHV is composed of a peak from bulk Pt at 71.2 eV and a surface peak at lower binding energy (70.8 eV, CLS = −0.4 eV). (ii) Under 0.05 Torr O_2 an additional peak at 71.9 eV (CLS = 0.7 eV) appears. (iii) When the O_2 pressure is increased to 0.5 Torr, a third peak at 73.4 eV is observed. STM images taken under similar conditions are *inset*: clean surface (*top*) and under 0.2 Torr O_2 (*bottom*) at 423 K. (**b**) O and CO coverage of a Pt(110) surface exposed to 0.5 Torr O_2 and then exposed to 10^{-6} Torr CO at 270 K

with previous theoretical calculations where there are small energy barriers for CO oxidation at the reconstructed Pt-(110)-(12 × 2)-22O surface and at the (1010) facet of α-PtO_2, while the energy barrier is large on the perfect α-PtO_2(0001) surface. However, Butcher et al. mentioned that it is unclear whether the O atoms in the α-PtO_2 react directly with CO or if the α-PtO_2 destabilized at interfaces with CO-covered Pt and that O from this phase decomposes into chemisorbed O on neighboring Pt sites. Another possibility is that the α-PtO_2 reacts only at the boundary of α-PtO_2 and metallic Pt [7].

Hendriksen et al. also found an interrelation between surface structure and the catalytic activity of a Pt(110) model catalyst at semirealistic reaction conditions for CO oxidation by using a novel, high-pressure–high-temperature scanning tunneling microscope (STM), which was set up as a flow reactor [3]. They measured the mass spectrometer signals of O_2, CO, and CO_2 partial pressures directly from the reaction cell and STM images. By controlled switching from CO-rich to O_2-rich flow, the Pt(110) surface was oxidized or reduced. The sudden increase in reactivity was observed with a change of the Pt surface, indicating the formation of a surface oxide. The surface appeared to be less smooth and the stripes along the fast scan direction disappeared. After the increase in reactivity, a characteristic roughness developed gradually on a time scale of several minutes. Continuous, controlled switching from a CO-rich to an O_2-rich flow reproduced this phenomenon. Hendriksen et al.

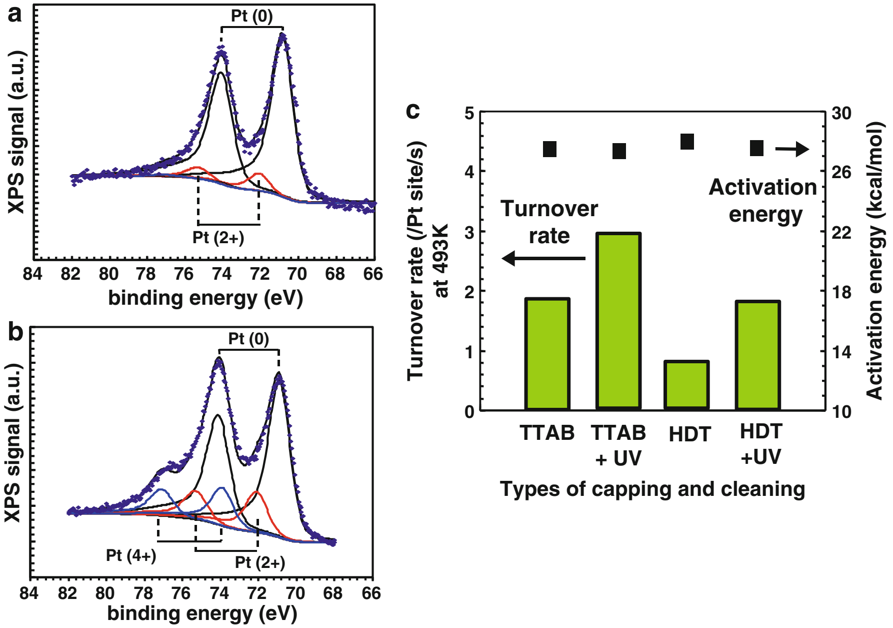

Fig. 7.2 XPS plots of Pt4*f* of Pt nanoparticles with TTAB capping measured (**a**) before and (**b**) after 2 h of UV-ozone cleaning. The Pt^{2+} (PtO) and Pt^{4+} (PtO_2) oxidation peaks are represented with *red* and *blue curves*. The chemical shift of the Pt4*f* core level of PtO and PtO_2 relative to pure Pt are about 1.2 and 3.0 eV. (**c**) Turnover rate and activation energy measured on TTAB and HDT before and after UV-ozone cleaning

concluded that the Pt(110) surface switches reversibly between a metallic state and an oxidic state depending on the applied reaction conditions (CO-rich or O_2-rich) and shows higher catalytic activity when the surface is oxidized.

An interesting question is whether there is a similarity between the surface oxide formed on Pt crystal surfaces and the oxide formed on Pt nanoparticles. For Pt nanoparticles, Park et al. recently carried out CO oxidation on several platinum nanoparticle systems capped with various organic molecules to investigate the role of capping agents on catalytic activity [8]. X-ray photoelectron spectroscopy (XPS) analysis revealed that the Pt nanoparticles are oxidized by the UV-ozone cleaning used to remove the organic capping agent, resulting in increased catalytic activity.

Figure 7.2 shows plots of the Pt4*f* peaks of tetradecyltrimethylammonium bromide (TTAB)-capped nanoparticles before and after 2 h of UV-ozone cleaning. The $Pt4f_{7/2}$ core level is fitted at 70.9 eV and the chemical shifts of the Pt4*f* core level of the natural oxidation states (Pt^{2+} from PtO and Pt^{4+} from PtO_2) relative to pure Pt are about 1.2 and 3.0 eV. As shown in Fig. 7.2a, the Pt4*f* peak of bare TTAB-capped nanoparticles exhibits an oxidation state of Pt^{2+}. After UV-ozone cleaning, the XPS Pt4*f* peak reveals higher oxidation states, which indicate the formation of Pt^{4+}. In accordance with the XPS results above, the turnover rate also increased after UV-ozone cleaning, as shown in Fig. 7.2c, for both TTAB- and hexadecylamine (HDT)-coated Pt nanoparticles. While the turnover rate increased by 60%–100 % for TTAB- and HDT-coated Pt nanoparticles, the activation energy remained the same (between 27 and 28 kcal/mol), within the error of measurement (1 kcal/mol). They assumed this is not only due to the removal of the capping layers, which leads to more reactive sites, but also due to the higher oxidation states of the Pt surface after UV-ozone cleaning. Thus, their results offer proof that the oxidized Pt nanoparticle has catalytically active properties. This argument is also consistent with recent CO oxidation results on core–shell Pt/mesoporous silica nanoparticles that exhibit partial oxidation of Pt. The turnover rate of CO oxidation on these core–shell Pt/mesoporous silica nanoparticles was found to be as high as that on bare Pt nanoparticles [9].

In conclusion, these observations show that the surface oxide formed on Pt crystal surfaces and on Pt nanoparticles is catalytically active for the CO oxidation reaction. Whether the oxidized Pt surface is catalytically active, however, is still up for some debate. Therefore, studies to bridge the connection between surface structures and catalytic performance are now needed to clearly understand how surface oxide layers affect the catalytic activity of CO oxidation.

7.3 Rh Oxide

To further understand the reactivity of transition metal and transition metal–oxide surfaces is of paramount importance because transition metal-based catalysts form the basis of much of modern chemistry. However, the role of surface oxides in the catalytic activity of Rh metals is still not well understood. Earlier studies reported that the oxide surfaces are generally inactive due to low adsorption probability for CO while the metallic surface is catalytically active by allowing coadsorption of CO and O. Many single Rh crystal studies revealed that the reaction is neither structure- nor particle size-sensitive, and that well-ordered, ultrathin oxide films formed on Rh surfaces lead to lower reaction rates [10, 11]. However, recent studies employing in situ spectroscopic techniques revealed that the catalytic activity over various metals improves in conjunction with the formation of a thin oxide film, indicating that the active phase is an oxide structure [12–17]. Gustafson et al. provided strong evidence, through combined SXRD and reactivity (mass spectrometry) studies of the Rh(111) surface, that an O-Rh-O tri-layer surface oxide is much more active than metallic Rh at low temperature (~500 K) CO oxidation, whereas Rh bulk oxide was not active at all [14]. They also found that an increase in CO_2 production coincides with the RhO_2 surface oxide film formed on vicinal Rh surfaces as well as on Rh nanoparticles. However, the formation of bulk Rh_2O_3 corundum oxide on all close-packed single crystal Rh surfaces poisons the reaction irrespective of the exact Rh substrate orientation [18]. For colloidal Rh nanoparticles, it was found that smaller nanoparticles are more reactive than larger ones during catalytic CO oxidation. Using in situ analysis via ambient pressure XPS, Grass et al. demonstrated that smaller, 2 nm Rh nanoparticles oxidize to a larger extent than 7 nm nanoparticles during reaction at 423–473 K. The thick oxide around the smaller nanoparticles correlated with enhanced activity of these nanoparticles [19]. In the case of electron beam-prepared Rh NPs, which were precovered with oxygen, a strong particle size dependence was observed for CO desorption, dissociation, and transient CO oxidation [20, 21].

Chemically modifying the surface of Rh nanoparticles can generate an active oxide overlayer of optimized stoichiometry and/or thickness on Rh nanoparticles and is, therefore, an appealing subject as it allows for the design of catalysts with high catalytic activity and stability. Such chemical modification can be accomplished via UV-ozone surface treatment of nanoparticles. Exposure to UV-ozone can alter the nanoparticle surface in two ways: first, by partial removal of the organic capping layer, thus unblocking some of the active reaction sites buried under it and, secondly, by changing the nature of the oxide over layer though oxidation state changes [8, 22].

Recently, Kim et al. carried out CO oxidation on 2 and 6.5 nm Rh nanoparticles capped by poly(vinylpyrrolidone) (PVP) before and after UV/O_3 surface treatment [51]. Figure 7.3 shows the catalytic activity, Arrhenius plot, and summary of catalytic turnover rates at 443 K for the CO oxidation reaction on two-dimensional arrays of 2 and 6.5 nm Rh nanoparticles before and after UV-ozone treatment. As shown in Fig. 7.3a, the smaller Rh nanoparticles before UV-ozone treatment show a higher activity than the larger Rh nanoparticles and it is also clear that the turnover frequency (TOF) of the 2 and 6.5 nm Rh nanoparticles increased by a factor of two or three after UV-ozone treatment. The activation energies for 2 and 6.5 nm Rh nanoparticles were obtained from Arrhenius plots of catalytic activity (Fig. 7.3b). Figure 7.3c shows a summary of the catalytic turnover rates at 443 K and the activation energies measured on the Rh nanoparticles before and after UV-ozone surface treatment. The activation energy decreased from 29.4 to 27.8 kcal/mol for the 2 nm Rh nanoparticles and decreased from 31.3 to 28.5 kcal/mol for the 6.5 nm Rh nanoparticles after UV-ozone treatment, as shown in Fig. 7.3c.

To indentify the change in oxidation state of the surface oxide layer formed on Rh NPs by UV-ozone treatment, we carried out XPS characterization for each Rh sample before and after 2 h of UV-ozone treatment. The Rh3*d* peak spectra of 2 and 6.5 nm particles are shown in Fig. 7.4. Before UV-ozone treatment, the 2 nm Rh NPs have two Rh^{X+} and Rh^{*X+} surface oxide peaks, the energy levels of which are 308.5 and 309.4 eV, respectively. The two Rh peaks are derived from Rh atoms in two different oxidation states or coordinated to a different number of oxygen atoms. The 6.5 nm Rh NPs have only one Rh^{*X+} surface oxide peak before UV-ozone treatment, however. After UV-ozone treatment, the peak area of the Rh^{X+} and Rh^{*X+} in both NPs increased, which changed from 0.88 to 1.22 for the 2 nm Rh nanoparticles and from 0.18 to 0.38 for the 6.5 nm Rh nanoparticles.

To more clearly confirm the correlation between catalytic activity and the amount of surface oxide layer formed on two different-sized Rh nanoparticles, we carried out the CO oxidation reaction as a function of UV-ozone exposure time. Figure 7.5a shows that the catalytic activity of the 2 and 6.5 nm Rh nanoparticles

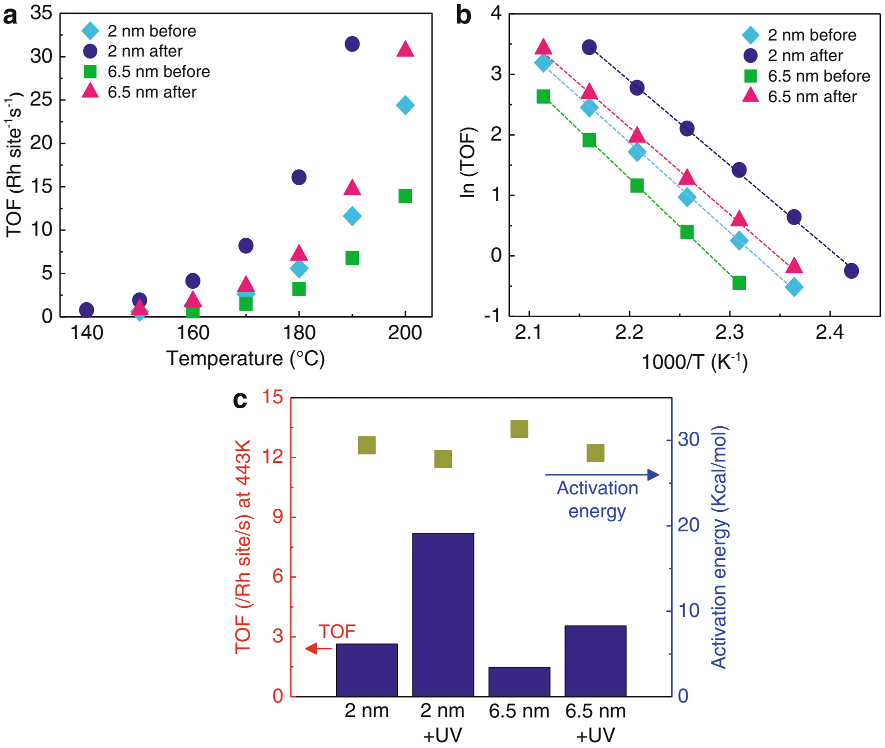

Fig. 7.3 Catalytic activity of the CO oxidation reaction on two-dimensional arrays of Rh NPs. (**a**) Turnover frequency (TOF) of Rh NPs with temperature, (**b**) Arrhenius plots of Rh NPs, and (**c**) summary of TOFs and activation energies of the CO oxidation reaction measured on Rh NPs before and after UV-ozone surface treatment

increased as the UV-ozone surface treatment time increased, which is closely related to the amount of surface oxide formed on the metal core, as revealed by XPS analysis. The Rh nanoparticles showed the largest growth of the surface oxide layer on the metal core after 2 h of UV-ozone surface treatment than for 10 or 24 h, resulting in the largest increment in the catalytic activity. It implies that the majority of the catalytically active surface oxide is very quickly formed by UV-ozone surface treatment in the initial step. The rate of surface oxide formation then decreases gradually until reaching steady state. Thus, we can conclude that the increased catalytic activity of the Rh NPs after UV-ozone exposure is correlated with the increase in the portion of the surface oxide layer formed on the Rh metallic core and that the surface oxide layer formed by UV-ozone surface treatment has catalytically active properties.

Why does metal oxide exhibit higher activity for CO oxidation than the corresponding metal? To demonstrate the role of the surface oxide layer on CO oxidation on Rh metal or metal oxide, Grass et al. assumed that the reactivity of the surface

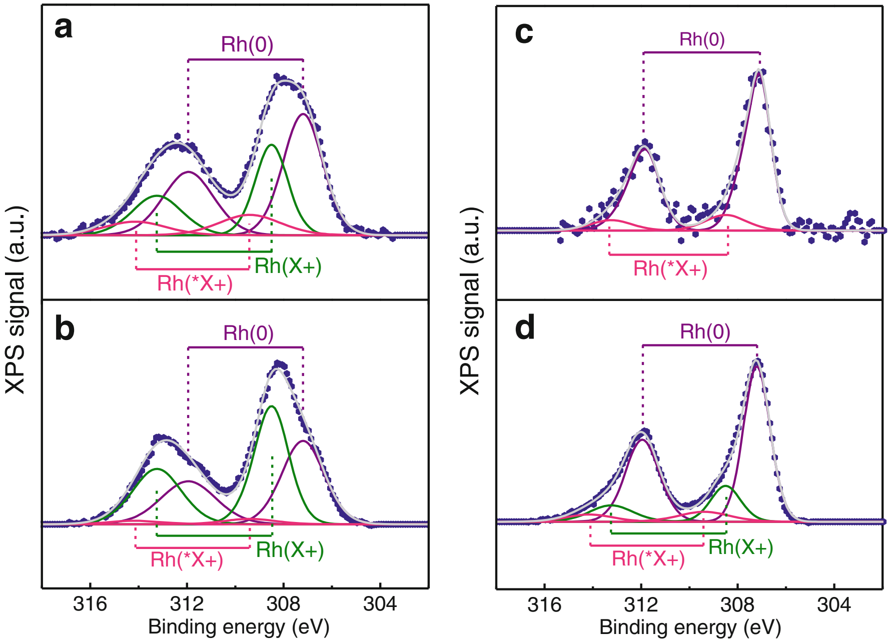

Fig. 7.4 XPS plots of Rh3*d* measured on 2 and 6.5 nm Rh NPs before and after UV-ozone treatment. 2 nm Rh NPs (**a**) before and (**b**) after UV-ozone treatment and 6.5 nm Rh NPs (**c**) before and (**d**) after UV-ozone treatment

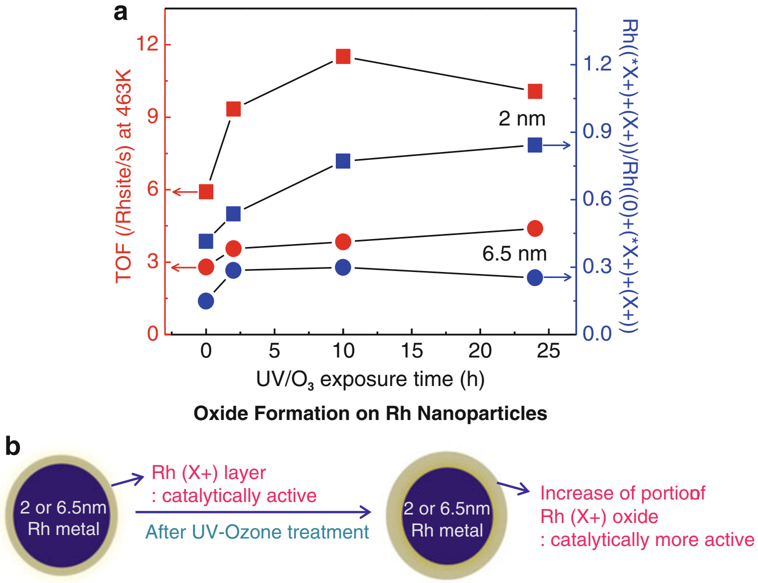

Fig. 7.5 (**a**) Correlation between the TOF and the surface oxide layer ratio of 2 and 6.5 nm Rh NPs as a function of UV-ozone exposure time. (**b**) Scheme of oxide formation on Rh

oxide layer on Rh NPs originates from an interface existing between the oxide surface and the metallic core that induces a strain on the oxide, which makes it less stable and, thus, more reactive. Gong et al. suggest that the geometric effect of metal oxides plays an important role in reducing the reaction barrier, which is related to the chemisorption energy of CO and O in the initial state (IS) [23]. The stronger the chemisorption in the initial state, the higher the reaction barrier. However, the increased reactivity of metal oxides does not simply explain the increase in chemisorption energy because the reaction barrier is not always proportional to the chemisorption energy. It may be reasonable to mention that the position of oxygen on the metals or metal oxides in the IS is a more fundamental reason for the increased reactivity. In the IS, the oxygen atom on the metal oxide is on the top site of a cus-metal atom and is still close to the top site in the transition state (TS). Therefore, the geometric difference of metal oxides plays an important role in reducing the barrier, resulting in the enhanced catalytic activity as the surface oxide layer on the Rh nanoparticles grows.

In conclusion, CO oxidation reactions on Rh nanoparticle catalysts were carried out before and after UV-ozone treatment. As illustrated in Fig. 7.5b, formation of the catalytically active oxide on the Rh metal core by UV-ozone treatment results in increased catalytic activity. These results suggest an intriguing way to tune the catalytic activity of metal catalysts by engineering the surface oxide layer.

7.4 Ru Oxide

7.4.1 CO Oxidation on Ru: From Single Crystals Towards Nanoparticles

Among the transition metal catalysts studied so far under catalytic CO oxidation, Ru has exhibited unusual behavior [24–36]. Under ultrahigh vacuum conditions, Ru single crystal surfaces have shown the least catalytic activity among noble metals [27]. However, we see a complete reversal of this trend when reaction conditions are oxidizing and under high pressure [28]. In such a state, Ru becomes much more active. During the last decade, this anomaly has driven researchers to extensively investigate Ru-based catalysts under CO oxidation. The initial focus of the studies reported thus far is based on Ru single crystal surfaces [24–27, 30, 32–36]. Studies dealing with model catalytic systems, such as two-dimensional nanoparticle arrays or three-dimensional oxide-supported Ru nanoparticles, have been reported sporadically and were recently investigated for the role of surface oxide in altering its catalytic activity under CO oxidation [33–36]. Here, we briefly review the role of surface oxide on Ru-based catalysts, summarizing Ru single crystals and presenting very recent trends reported on the subject.

Assmann et al. investigated the nature of catalytically active oxides formed on Ru(0001) and $Ru\left(10\bar{1}0\right)$ surfaces under oxidizing, reducing, and CO oxidation reaction conditions [35, 36]. The initial oxidation of the Ru(0001) single crystal surface proceeds as follows: First, oxygen adsorbs dissociatively, forming distinct O overlayers, which are inactive in oxidizing CO molecules owing to strong O–Ru bonding. Then below 500 K, no oxide forms even under high O_2 pressures (e.g., 10^{-2} mbar). Finally at 650 K, oxide formation occurs via autocatalysis, generating an ultrathin $RuO_2(110)$ layer on Ru(0001) of ~ 1 nm thickness. This oxide is reported to be extraordinarily active in oxidizing CO molecules. As the temperature exceeds 800 K, the RuO_2 film grows thicker under oxidizing conditions and becomes rough. From CO adsorption and reaction experiments, they conclude that this type of oxide is essentially inactive and, under CO oxidation reaction conditions, it deactivates. A similar observation is also reported for $Ru\left(10\bar{1}0\right)$ surfaces. When exposed excessively to oxygen at 650 K, a similar ultrathin RuO_2 film forms that is oriented along the (100) direction and is equally active in the oxidation of CO [29, 37]. This film, under oxidizing conditions and temperatures exceeding 800 K, grows thicker and irreversibly transforms into a reconstructed c(2 × 2) phase which is unable to convert CO to CO_2 [38].

The initial roughening of the RuO_2 film on Ru(0001) is being studied using STM to find the reason for its deactivation [36]. Figure 7.6 visualizes the initial roughening of the $RuO_2(110)$ surface. The flat regions in Fig. 7.6a are catalytically active $RuO_2(110)$ areas. The line profile, which shows the rough part of the surface ~8 nm in height above the flat region, exposes $RuO_2(100)$ facets, as seen in Fig. 7.6d. When we zoom in to the $RuO_2(100)$ facets, we identify catalytically inactive c(2 × 2) regions separated by narrow strips of $RuO_2(100)$ (see Fig. 7.6b, c). Similar STM images were also reported for the growth of $RuO_2(100)$ on $Ru\left(10\bar{1}0\right)$ [38]. These c(2 × 2) patches are inactive; thus, the rough RuO_2 film deactivates gradually. A thick RuO_2 film completely deactivates when covered by such c(2 × 2) domains.

On the other hand, under reducing conditions, the $RuO_2(110)$ surface will be the first surface to be depleted of the bridging O atoms. CO molecules, owing to their relatively high binding energy at the site (180 kJ/mol), adsorb strongly on these vacancies and stabilize the mildly reduced $RuO_2(110)$ surface. Such a surface is still active for CO oxidation [31]. Under reducing conditions, however, as the temperature exceeds 450 K, the mildly reduced oxide decomposes into metallic and oxide phases [38] and, finally, the $RuO_2(110)$ film is covered by a catalytically inactive Ru(0001)-O overlayer.

After investigating the Ru oxide formed on Ru single crystal surfaces under catalytic CO oxidation, a brief overview of the most recent studies on model catalytic systems, ranging from two-dimensional nanoparticle arrays to three-dimensional micro- or nanoparticles supported on an oxide support, is presented below. The studies highlight efforts to understand the surface oxide generated at nanoscale, its catalytic reactivity under CO oxidation, and the utilization of this knowledge for technological catalysts.

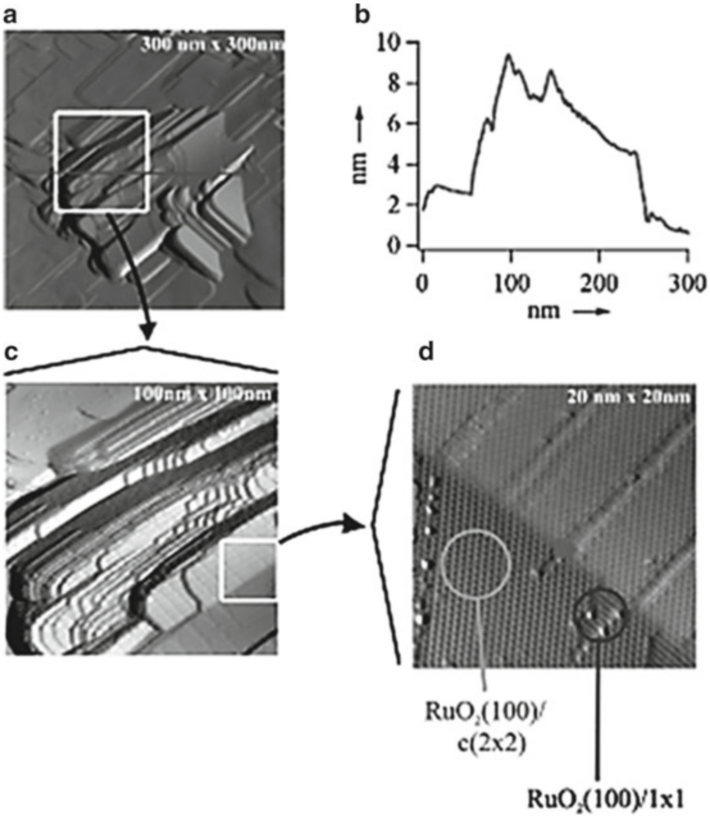

Fig. 7.6 The initial roughening of a RuO_2(110) film on Ru(0001). (**a**) STM image (300 × 300 nm). (**c**, **d**) Close-up images of the rough region STM image: (**c**) 100 × 100 nm, (**d**) 20 × 20 nm indicating that the facets are oriented along the (100) direction and reconstructed into a c(2 × 2) phase. (**b**) A line profile across the faceted region along the line shown in (**a**)

7.4.2 Ru Oxide Powder and Supported Ru Catalysts

After examining Ru single crystal surfaces, as mentioned above, the same group investigated polycrystalline RuO_2 powder catalysts and supported Ru catalysts [36]. These RuO_2 particles (~1 μm) preferentially expose the (110) and (100) facets. As shown in Fig. 7.7, under net oxidizing conditions ($CO/O_2 > 2$) during catalytic CO oxidation, the active RuO_2(100) facets transformed into the inactive RuO_2(100)-c(2 × 2) phase. Additionally, the RuO_2(110) facets roughened as well, thus transforming into RuO_2(100) facets, which eventually reconstructed into the inactive RuO_2(100)-c(2 × 2) phase. Under net reducing conditions ($CO/O_2 > 2$), the RuO_2 particles deactivated due to the presence of Ru(0001)-O domains on the surface. They found that the catalyst is at its highest active state when an ultrathin (1–2 nm)

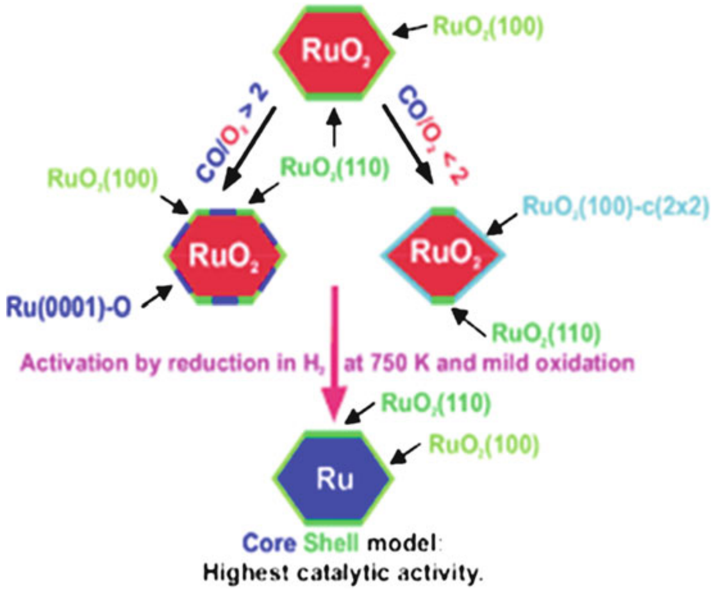

Fig. 7.7 Core–shell model for RuO_2 powder catalysts. The degree of surface oxidation is determined by the CO/O_2 reactant feed ratio and the temperature. The inactive $RuO_2(100)$-c(2×2) (*light blue*) surface facets are formed under oxidizing conditions ($CO/O_2 < 2$), whereas the low-activity metallic ruthenium surfaces (Ru(0001)-O) (*dark blue*) are exposed under net reducing conditions ($CO/O_2 > 2$). The most active state is an ultrathin RuO_2 (*light* and *dark green*; thickness 1–2 nm) layer supported on a metallic ruthenium core. This state is achieved by complete reduction of the RuO_2 particle followed by mild re-oxidation below 500 K

RuO_2 layer is formed around the metallic core (they achieved such a state after completely reducing the RuO_2 particle, followed by mild re-oxidation below 500 K). Under mild reaction conditions, the ruthenium particle will oxidize by growing a $RuO_2(110)$ layer on the Ru(0001) facets and a $RuO_2(100)$ layer on the $Ru\left(10\bar{1}0\right)$ facets. This RuO_2/Ru core–shell particle (see Fig. 7.7) reveals the highest activity for CO oxidation.

7.4.3 Size Effect Under Catalytic Carbon Monoxide Oxidation for Ru Nanoparticles

Tuning the metal particle size affects its inherent catalytic activity. This phenomenon is the subject of continuous interest owing to its significance from both fundamental and practical viewpoints [39–42]. This trend is found to be a function of various molecular–scale factors, such as alteration in surface structure, electronic states, oxidation states, and metal–support interactions [43–47]. In particular, sizes ranging from 1 to 10 nm are highly relevant to the size effects. Particle size effect studies have implications in rational catalyst design. A surface oxide around a metal

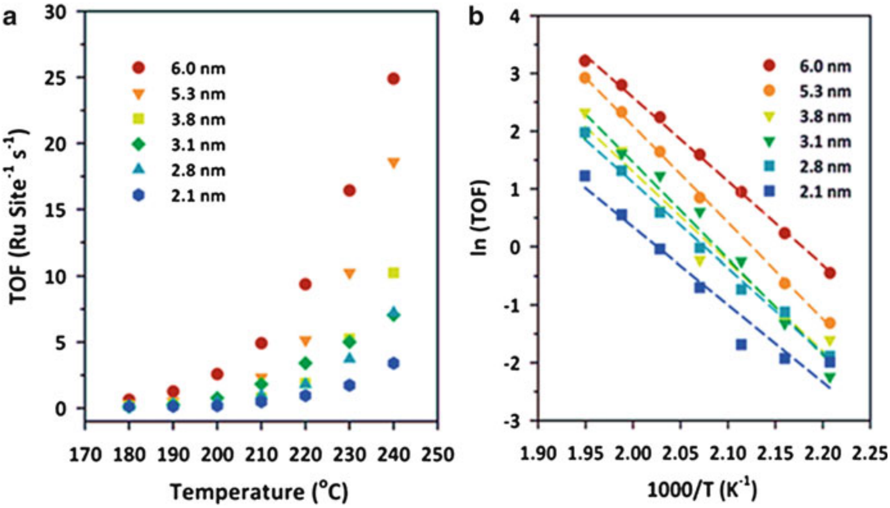

Fig. 7.8 CO oxidation activity of 2D model catalysts based on Ru NPs. (**a**) Change of CO oxidation activity with temperature and (**b**) Arrhenius plots for CO oxidation

core was suggested as a catalytically active species and was recently identified by advanced in situ analytical techniques, including AP-XPS, scanning tunneling microscopy, XRD, and X-ray absorption spectroscopy [3, 4, 19, 48, 49].

Ru nanoparticles exhibited the trend of increasing catalytic activity with increasing Ru particle size for CO oxidation under high-pressure and oxidizing reaction conditions [50]. Figure 7.8 shows the changes in TOF with reaction temperature and Arrhenius plots for CO oxidation on different sizes of Ru NP catalysts. As can be seen, the 2D catalyst based on 6 nm Ru NPs exhibits eight fold higher TOF than the 2.1 nm Ru catalyst at 513 K. The same trend is reported for 2.1, 3.1, and 5 nm Ru nanoparticles deposited inside SBA-15 mesoporous silica. This shows that it is a general observation for both 2D and 3D Ru model catalysts.

An active oxide layer on Ru single crystals or reduced RuO_2 powder is maintained under oxidizing conditions, where such an oxide is unstable on Ru nanoparticles. Joo et al. suggested that the stability of Ru oxide on nanoparticles changes in a fashion similar to that reported by Assmann et al. Smaller nanoparticles will undergo higher oxidation than larger ones, thus exposing more catalytically inactive species [36]. The stability of such an oxide on Ru nanoparticles can be correlated with the particle size effect found for Ru.

7.4.4 Engineering Ru Oxide on Nanoparticles through UV-Ozone Surface Treatment

Kim et al. carried out CO oxidation on Ru nanoparticles capped by PVP before and after UV-ozone surface treatment, respectively [51]. UV-ozone surface treatment

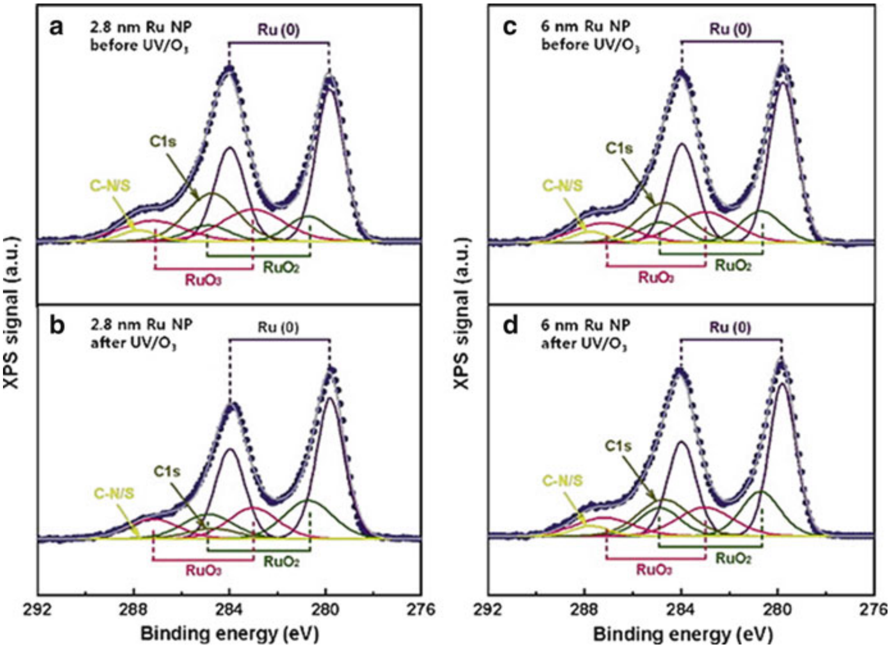

Fig. 7.9 XPS plots of Ru3*d* measured on 2.8 and 6 nm Ru nanoparticles before and after UV-ozone treatment. 2.8 nm Ru NPs (**a**) before and (**b**) after UV-ozone treatment and 6 nm NPs (**c**) before and (**d**) after UV-ozone treatment

allows the partial removal of organic capping layers and simultaneously generates an oxide layer on the surface [22, 51–53]. XPS showed an increase in oxidation states, which influenced the catalytic activity of the Ru nanoparticles, as described in the next section. XPS of the Ru nanoparticles showed that Ru3*d* comprises two types of surface oxide peaks, RuO_2 and RuO_3, at binding energies of 280.7 and 283 eV, respectively [54, 55]. As can be seen in Fig. 7.9, the RuO_2 peak shows an enhancement in peak area after UV-ozone treatment for both the 2.8 and 6 nm Ru nanoparticles. The ratio of RuO_2 to Ru(0) increased from 0.24 to 0.47 for 2.8 nm and from 0.29 to 0.42 for 6 nm Ru NPs after UV-ozone treatment. Afterwards, CO oxidation was carried out on the Ru nanoparticles to establish a correlation between oxidation state modification via UV-ozone treatment and activity of the nanoparticles.

As can be seen in Fig. 7.10, the larger Ru nanoparticles are more reactive than the smaller Ru nanoparticles. These results are consistent with the reports of several research groups, as described earlier, that larger Ru nanoparticles show higher catalytic activity due to enhanced stability of the core–shell-type surface oxide layer on the Ru metallic core [36, 48, 50]. We also see that the TOF of Ru nanoparticles decreases after UV-ozone treatment. The activation energy of the 2.8 nm Ru nanoparticles remained the same, within the error of measurement, while that of the 6 nm Ru nanoparticles increased from 33.2 to 38.7 kcal/mol after UV-ozone

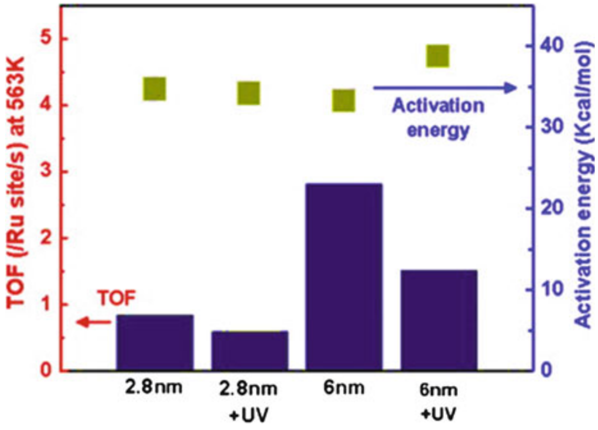

Fig. 7.10 Summary of TOF and activation energy of the CO oxidation reaction measured on Ru NP catalysts before and after UV-ozone surface treatment

treatment. The reaction rates, 0.17 and 0.55 mol/g/s at 563 K, were based on the mass of the 2.8 and 6 nm Ru nanoparticles before UV-ozone treatment, respectively. The decrease in catalytic activity of the Ru NPs after UV-ozone treatment is due to the formation of an inactive bulk oxide layer on the Ru metallic core.

7.4.5 Catalytic Activity of CO Oxidation on Ru Nanoparticles and Ru Oxides Probed with Ambient Pressure XPS

Ambient pressure XPS permits in situ investigation of the surface structure of catalysts. Catalytic oxidation, reduction, and CO oxidation were carried out on Ru nanoparticle arrays and the surface oxidation states were measured and monitored using AP-XPS to understand the relationship between the oxidation states and catalytic activity under realistic conditions [48]. AP-XPS showed that the smaller Ru nanoparticles form bulk RuO_2 on the surface, which is responsible for the lower catalytic activity.

To assess the catalytically active oxide species formed in situ during reaction conditions, the nanoparticles were subjected to catalytic CO oxidation under net oxidizing conditions using 200 mTorr O_2 and 80 mTorr CO (CO/O_2: 0.4) to correlate the observed trend of increasing catalytic activity with the nature of the oxide formed around the nanoparticles. Figure 7.11 shows AP-XPS spectra of Ru3*p* acquired at various temperatures during catalytic CO oxidation. At the lower reaction temperature of 232 K, both the 2.8 and 6 nm Ru nanoparticles show mild surface oxide formation. Both of the RuO_2/Ru^{4+} and RuO_x/Ru^{X+} oxide peaks are very small. The oxide, however, grows progressively as the temperature increases. During the course of CO oxidation over nanoparticles at various temperatures, the smaller 2.8 nm Ru nanoparticles show a higher proportion of surface oxide formation. Ru3*p* shows more significant oxide formation on the smaller nanoparticles than on the larger ones, particularly at 473 K.

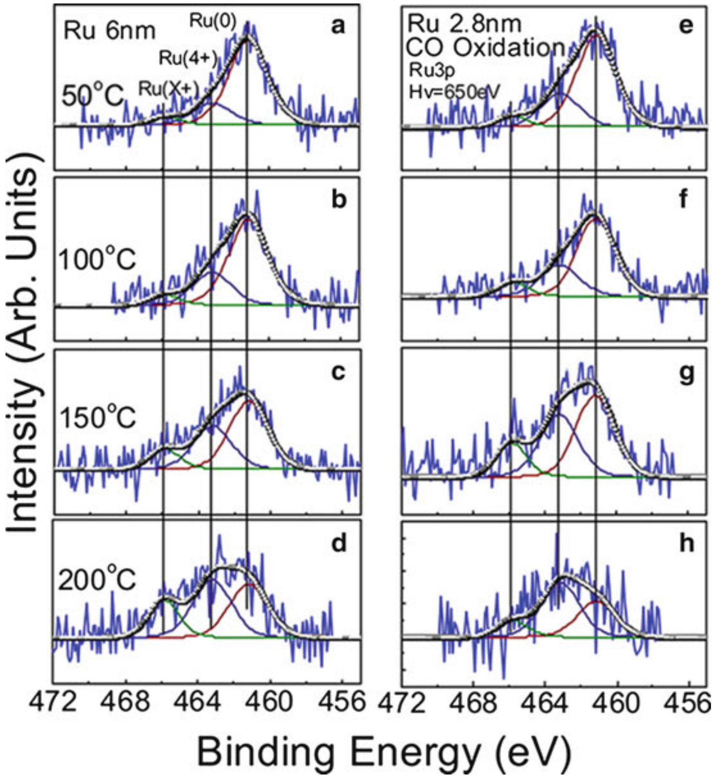

Fig. 7.11 AP-XPS spectra of Ru3*p* of Ru nanoparticles under CO oxidation (200 mTorr O_2 and 80 mTorr CO) with increasing temperature, showing spectra of 6 nm Ru nanoparticles acquired at (**a**) 323, (**b**) 373, (**c**) 423, and (**d**) 473 K, and spectra of 2.8 nm Ru nanoparticle acquired at (**e**) 323, (**f**) 373, (**g**) 423, and (**h**) 473 K (650 eV incident photon energy). Ru3*p* spectra show a thicker oxide formation around the smaller 2.8 nm Ru nanoparticles

Thus, it is clear that under net oxidizing conditions (CO/O_2: 0.4), the smaller nanoparticles show greater oxidation than the larger ones. Figure 7.12 shows the resulting trend of oxidation for both 2.8 and 6 nm Ru nanoparticles. The ratios for the smaller nanoparticles are higher than that for the larger Ru nanoparticles due to the high degree of oxidation during the CO oxidation reaction.

The Ru nanoparticles exhibit a trend of increasing catalytic activity with increasing Ru nanoparticle size for CO oxidation under high-pressure and oxidizing reaction conditions. It is confirmed from AP-XPS findings that the smaller nanoparticles are forming inactive bulk oxide on their surfaces and that a larger amount of the catalytically inactive species is exposed. Thus, the decrease in catalytic activity of the Ru nanoparticles with decreasing nanoparticle size is correlated with the formation of the inactive bulk oxide layer on the Ru metallic core. These results are consistent with previous reports, described above, and show that the stability of core–shell nanoparticles with a thin shell of active oxide increases as the nanoparticle size increases.

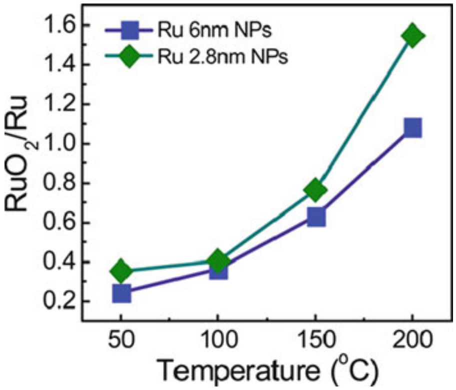

Fig. 7.12 Peak area ratios of the RuO_2 peak with respect to the Ru metallic peak (Ru^{4+}/Ru^0), as calculated from AP-XPS spectra of Ru3*p* for Ru nanoparticles under CO oxidation reaction conditions of 200 mTorr O_2 and 80 mTorr CO (CO/O_2: 0.4)

7.5 Pd Oxide

7.5.1 Pd Oxide on Single Crystal Surfaces

Palladium is widely used as an active component of catalysts in numerous industrial reactions. Therefore, a large number of research groups all over the world have investigated the catalytic activity of palladium species in both real and model catalytic systems [56–64]. The catalytic oxidation activity of palladium particles depends on the oxidation state of the metal [65–70]. The latter is in turn influenced by the oxygen pressure and temperature of the system.

Previously, it was reported that CO oxidation over Pd exhibits a hyperactive state under oxygen-rich conditions with a rate higher than those near stoichiometric reaction conditions [25]. The hyperactive surface was proposed to be a surface phase that contains primarily chemisorbed atomic oxygen on the metallic Pd surface and a low coverage of CO, based on the significant change of CO adsorption during infrared reflection absorption spectroscopy (IRAS) investigations [25, 65]. Additionally, the surface chemistry of the oxygen interaction with Pd surfaces has been reported to be very complicated, mainly due to diffusion of oxygen into the subsurface and/or the formation of bulk and metastable Pd_xO_y, depending on the experimental conditions [66, 71–74]. Furthermore, there is no oxygen poisoning observed with palladium in an auto converter, even under oxygen-rich conditions. Many groups reveal that the active surface is not a palladium oxide, but a chemisorbed oxygen-rich palladium surface exhibits hyperactivity for CO oxidation. Additionally, changes in the gas-phase compositions of CO and CO_2 at the hyperactive state, monitored by the infrared absorption intensity of gas-phase CO and CO_2, indicate that CO is depleted at the hyperactive state [75]. There still exists some controversy in the literature over the specific activity of Pd vs. Pd oxide for CO oxidation at moderate temperatures. Thus, significant efforts have been directed towards studying the nature and activity of various oxide surfaces for catalytic CO oxidation to correlate the oxidation state with its inherent activity [76]. Some studies have shown that in the case of the Pd(100) surface, the active surface is metallic Pd for CO oxidation with a CO/O_2 ratio near the stoichiometric one of 2/1, whether starting with a metallic or an oxidized surface [76].

7.5.2 CO Oxidation on Polycrystalline Palladium

The polycrystalline Pd metal surface imitates a system that is similar to the exposed facets of a real catalyst. Using STM, temperature-programmed desorption (TPD), and low energy electron diffraction (LEED), Altman et al. [77] carried out detailed studies of the mechanism of oxide formation and distinguished three states involving four surface oxygen phases on Pd(111) and four states with five surface oxygen phases on Pd(100). The key process involves chemisorbed oxygen, surface oxide, and bulk oxide as the O_2 dosing amount and temperature increase. Chen et al. have shown that neither the surface oxide nor bulk oxide is present on the Pd(100) and polycrystalline Pd for CO oxidation at ~525 K, even under oxygen-rich conditions. Even though a very high rate (TOF of more than several thousands) was observed at the hyperactive state and that an insignificant amount of CO adsorption was demonstrated by in situ IRAS, they concluded that the active surface is a chemisorbed oxygen-rich surface for the hyperactive state. All together, the chemisorbed oxygen-rich surface is an active surface corresponding to the hyperactivity. The in situ IRAS results demonstrate that no palladium oxide was formed on the Pd(100) and polycrystalline Pd during CO oxidation at 500–525 K, even under oxygen-rich conditions or for the hyperactive state. These facts conclude that the chemisorbed oxygen-rich Pd surface is the active surface for the observed hyperactivity. The gas-phase CO is depleted at the hyperactive state and the observed hyperactive rate is limited by mass transfer of CO.

7.5.3 Oxidation Process of Pd(111) Probed by AP-XPS

Ketteler et al. reported photoemission spectroscopy (PES) measurements during the oxidation process of Pd(111), including subsurface incorporation and oxidation of the first few layers [78]. Figure 7.13 shows spectra corresponding to the three phases and metastable structures that were observed during exposure of Pd(111) to oxygen at pressures $>10^{-6}$ Torr. Each spectrum is characterized by peaks with unique binding energies and intensity ratios. Besides chemisorbed oxygen and surface oxide (spectrum (a)), a new structure ("subsurface oxide") can be seen (spectrum (b)) followed by a bulk oxide phase (spectrum (c)), each in specific pressure and temperature ranges. These structures were found to be stable over several minutes at a fixed temperature while increasing the oxygen pressure.

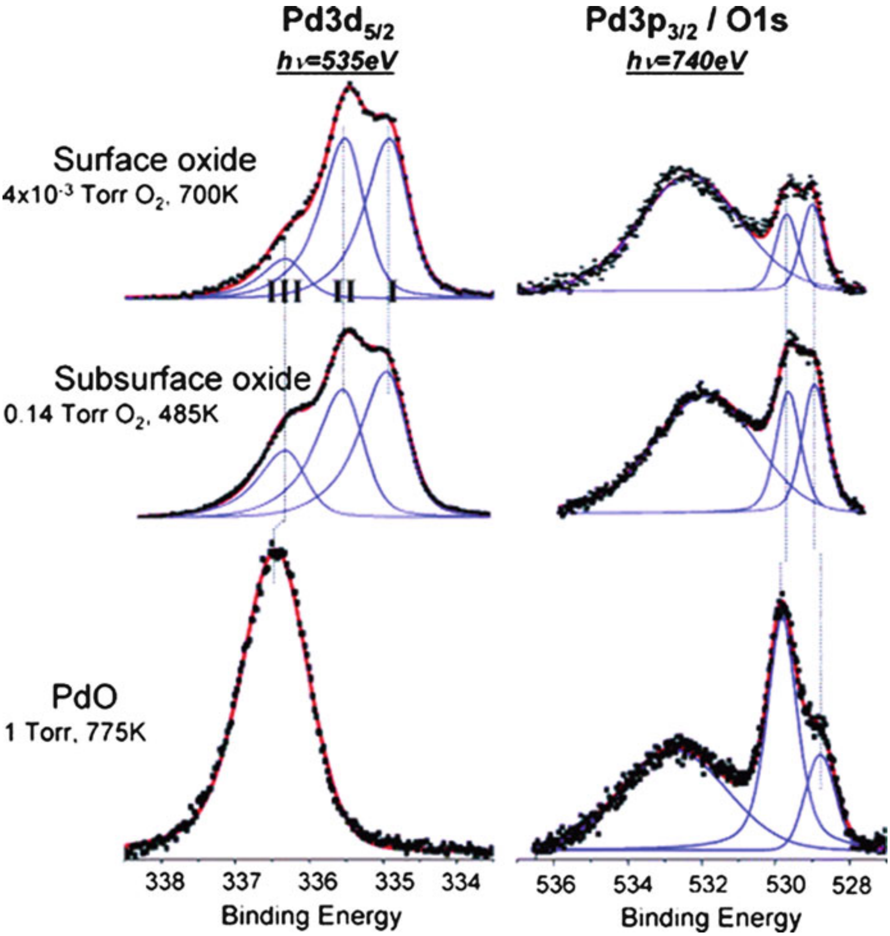

Fig. 7.13 Pd3$d_{5/2}$ (*left*) and O 1*s*/Pd3$p_{3/2}$ (*right*) XPS regions corresponding to different stages in the oxidation of Pd(111). (**a**) Surface oxide, (**b**) subsurface oxide, and (**c**) bulk PdO. Peaks are normalized to the total Pd3$d_{5/2}$ and Pd3$p_{3/2}$ area, respectively

7.5.4 Pd Oxide on Nanoparticles

Zorn et al. prepared well-defined high–surface–area palladium catalysts and prepared alumina-supported palladium nanoparticles in three different oxidation states: Pd^0 (reduction in 1 bar H_2 flow at 573 K for 1 h), $PdO_x<1$ (oxidation in 1 bar O_2 flow at 673 K for 1 h), and PdO (oxidation in 1 bar O_2 flow at 1,073–1,273 K for 1 h) [76].

The CO oxidation activities of the three different pretreated supported catalysts and commercial PdO were compared using a mixture of 50 mbar CO, 50 mbar O_2, and balance He to 1,000 mbar. Commercial unsupported PdO was basically unreactive with the reaction rate at least 4 orders of magnitude smaller than that of

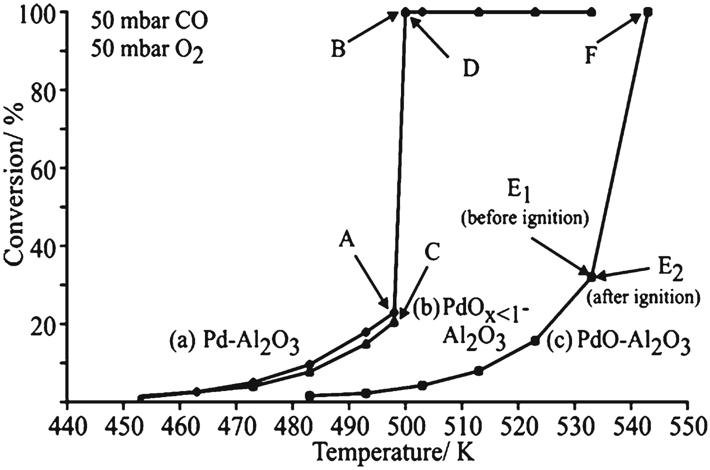

Fig. 7.14 CO oxidation (conversion) at different temperatures. Comparison of (**a**) reduced $Pd\text{-}Al_2O_3$, (**b**) substoichiometric $PdO_x < 1\text{-}Al_2O_3$, and (**c**) fully oxidized $PdO\text{-}Al_2O_3$

$PdO_x\text{-}Al_2O_3$ (x: 0–1). $Pd\text{-}Al_2O_3$, $PdO_x < 1\text{-}Al_2O_3$, and $PdO\text{-}Al_2O_3$ exhibited typical light-off (ignition) profiles (Fig. 7.14), with light-off temperatures of 498 and 535 K (for 50 % CO conversion). Below 535 K, the alumina-supported reduced Pd^0 particles and the $PdO_x < 1$ particles exhibited higher CO conversion than the fully oxidized supported PdO particles (Fig. 7.14). HRTEM images revealed comparable sizes for the Pd, PdO, and $PdO_x < 1$ nanoparticles. Thus, sintering cannot explain the lower catalytic activity of PdO. Based on in situ Fourier transform infrared (FTIR) spectra, they concluded that, under technically relevant conditions, metallic palladium will always dominate, whereas $PdO_x < 1$ phases are unstable due to their facile reducibility. Based on these and previous molecular beam results, the highest catalytic activity is assigned to oxygen-covered metallic palladium.

Kibis et al. reported another study in which oxidized palladium nanoparticles were prepared using RF-discharge under an oxygen atmosphere [79]. Pd^{2+} states were formed together with highly oxidized palladium species where the Pd^{2+} states acted as a stabilization matrix for the Pd^{4+} species. The highly oxidized palladium species were observed to have a relatively high thermal stability and a high reaction probability towards CO. The interaction of the oxidized palladium species with CO was studied by exposing oxidized palladium particles, step by step, to CO. Figure 7.15 shows the Pd3*d* spectra as a function of CO exposure at room temperature. The reduction of the Pd^{4+} species to Pd^{2+} and the metallic state can be clearly observed, even at room temperature. The overall intensity of the Pd3*d* spectrum remains practically unchanged. Note that the E_b ($Pd3d_{5/2}$) of metallic palladium was 335.6 eV. The formation of small metallic Pd^0 clusters may be responsible for this chemical shift of the Pd3*d* spectra to a higher E_b. XPS data were used to estimate the reaction probability (χ) of the oxidized palladium nanoparticles comprising the Pd^{2+}

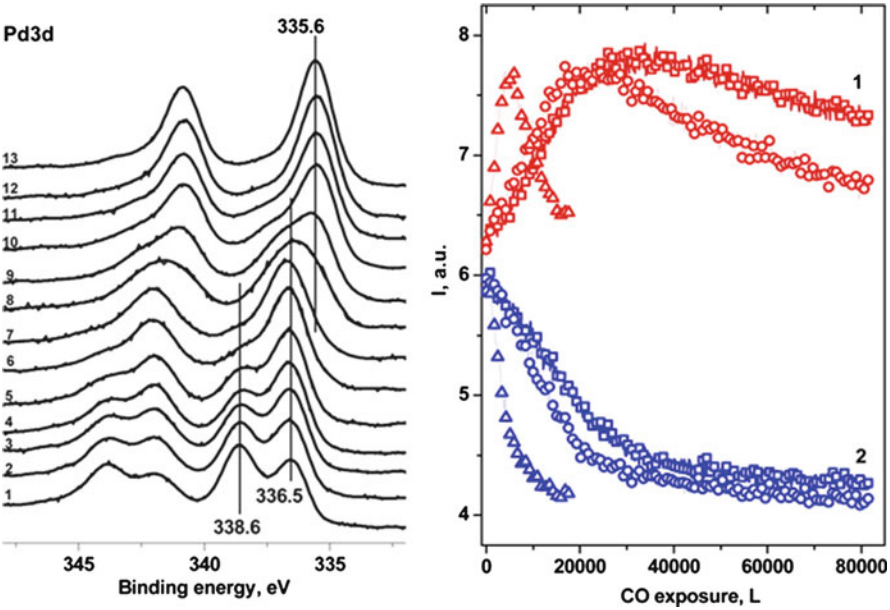

Fig. 7.15 (**a**) The Pd3*d* spectra of the oxidized palladium species after CO exposure at room temperature. (1) 0 L, (2) 3×10^3 L, (3) 6×10^3 L, (4) 9×10^3 L, (5) 1×10^4 L, (6) 2×10^4 L, (7) 4×10^4 L, (8) 2×10^7 L, (9) 5×10^7 L, (10) 2×10^8 L, (11) 9×10^8 L, (12) 3×10^9 L, and (13) 1×10^{10} L. (**b**) The intensity of peaks with E_b (Pd3$d_{5/2}$) is (1) 336.5 eV and (2) 338.6 eV at (*squares*) 300 K, (*circles*) 325 K, and (*triangles*) 350 K, depending on CO exposure

and Pd^{4+} species. The highly oxidized palladium species were observed to have a relatively high thermal stability and a high reaction probability towards CO.

Schalow et al. studied the formation of different oxygen species on a Pd/Fe_3O_4 model catalyst over a broad range of temperatures [80]. They found that, for oxidation temperatures up to 450 K, oxygen primarily chemisorbs dissociatively on the metallic Pd surface areas; however, at temperatures of 500 K and above, Pd oxide species also form. Oxide formation occurs initially at the particle–support interface and, at a later stage, on the outer particle surface as well. They found that the activity of the model catalyst for CO oxidation decreases drastically with increasing coverage of the Pd surface by oxides. For reaction temperatures below 450 K, partial oxidation of the Pd surface, obtained by oxygen exposure at higher temperatures, results in long-term deactivation of the catalyst because the decomposition of these surface oxides is kinetically hindered. However, at temperatures above 450 K, Pd oxide species can be formed under O-rich conditions and decompose under CO-rich conditions. As a result, the average oxidation state and the activity of the catalyst change dynamically, depending on the composition of the reactant environment. Nonetheless, the CO_2 formation rate of partially oxidized Pd particles is generally reduced significantly, compared to metallic Pd particles.

7.6 Concluding Remarks on the Role of Surface Oxide

In this chapter, we reviewed the role of surface oxide on Pt, Rh, Ru, and Pd nanoparticles, and showed that surface oxide plays an important role in the catalytic activity of CO oxidation. Increasing evidence shows that Pt oxide and Rh oxide are reactive species, while Ru bulk oxide is not reactive. Catalytic activity increases as the size of the Ru nanoparticles increases and as the size of the Rh nanoparticles decreases. AP-XPS studies indicate that the change in catalytic activity is correlated with the formation of surface oxide. Surface treatments, such as UV-ozone treatment, facilitate oxide layer engineering, which changes the catalytic activity. The active surface oxide on Rh NPs, formed after UV-ozone treatment, leads to increased catalytic activity. On the other hand, the inactive surface oxide on Ru NPs, formed by UV-ozone treatment, caused the catalytic activity to decrease. These results suggest an intriguing way to tune the catalytic activity of metal catalysts by engineering the surface oxide layer.

Acknowledgments This work was supported by the WCU (World Class University) program (31-2008-000-10055-0 and 2012R1A2A1A01009249) through the National Research Foundation, the Research Center Program (CA1201) of IBS (Institute for Basic Science), and from the Fundamental R&D Program for Core Technology of Materials funded by the Ministry of Knowledge Economy, Republic of Korea.

References

1. Ertl G, Norton PR, Rustig J (1982) Kinetic oscillations in the platinum-catalyzed oxidation of Co. Phys Rev Lett 49:177–180
2. Imbihl R, Cox MP, Ertl G (1986) Kinetic oscillations in the catalytic cooxidation on Pt(100)—experiments. J Chem Phys 84:3519–3534
3. Hendriksen BLM, Frenken JWM (2002) CO oxidation on Pt(110): scanning tunneling microscopy inside a high-pressure flow reactor. Phys Rev Lett 89:046101
4. Ackermann MD, Pedersen TM, Hendriksen BLM, Robach O, Bobaru SC, Popa I, Quiros C, Kim H, Hammer B, Ferrer S, Frenken JWM (2005) Structure and reactivity of surface oxides on Pt(110) during catalytic CO oxidation. Phys Rev Lett 95:255505
5. Butcher DR, Grass ME, Zeng ZH, Aksoy F, Bluhm H, Li WX, Mun BS, Somorjai GA, Liu Z (2011) In situ oxidation study of Pt(110) and its interaction with CO. J Am Chem Soc 133: 20319–20325
6. Baetzold RC, Apai G, Shustorovich E, Jaeger R (1982) Surface core-level shifts for Pt single-crystal surfaces. Phys Rev B 26:4022–4027
7. Li W, Hammer B (2005) Reactivity of a gas/metal/metal-oxide three-phase boundary: CO oxidation at the Pt(111)-c(4×2)-2CO/alpha-PtO_2 phase boundary. Chem Phys Lett 409:1–7
8. Park JY, Aliaga C, Renzas JR, Lee H, Somorjai GA (2009) The role of organic capping layers of platinum nanoparticles in catalytic activity of CO oxidation. Catal Lett 129:1–6
9. Joo SH, Park JY, Tsung CK, Yamada Y, Yang PD, Somorjai GA (2009) Thermally stable Pt/mesoporous silica core-shell nanocatalysts for high-temperature reactions. Nat Mater 8: 126–131
10. Berlowitz PJ, Peden CHF, Goodman DW (1988) Kinetics of carbon monoxide oxidation on single-crystal palladium, platinum, and iridium. J Phys Chem 92:5213–5221

11. Peden CHF, Goodman DW, Blair DS, Berlowitz PJ, Fisher GB, Oh SH (1988) Kinetics of carbon monoxide oxidation by oxygen or nitric oxide on rhodium(111) and rhodium(100) single crystals. J Phys Chem 92:1563–1567
12. Gustafson J, Mikkelsen A, Borg M, Andersen JN, Lundgren E, Klein C, Hofer W, Schmid M, Varga P, Kohler L, Kresse G, Kasper N, Stierle A, Dosch H (2005) Structure of a thin oxide film on Rh(100). Phys Rev B 71:115442
13. Gustafson J, Westerstroem R, Mikkelsen A, Torrelles X, Balmes O, Bovet N, Andersen JN, Baddeley CJ, Lundgren E (2008) Sensitivity of catalysis to surface structure: the example of CO oxidation on Rh under realistic conditions. Phys Rev B 78:045423
14. Gustafson J, Westerstrom R, Balmes O, Resta A, van Rijn R, Torrelles X, Herbschleb CT, Frenken JWM, Lundgren E (2010) Catalytic activity of the Rh surface oxide: CO oxidation over Rh(111) under realistic conditions. J Phys Chem C 114:4580–4583
15. Ligthart DAJM, van Santen RA, Hensen EJM (2011) Supported rhodium oxide nanoparticles as highly active Co oxidation catalysts. Angew Chem Int Ed 50:5306–5310
16. Lundgren E, Gustafson J, Resta A, Weissenrieder J, Mikkelsen A, Andersen JN, Kohler L, Kresse G, Klikovits J, Biederman A, Schmid M, Varga P (2005) The surface oxide as a source of oxygen on Rh(111). J Electron Spectrosc Relat Phen 144:367–372
17. Shaikhutdinov S, Freund HJ (2012) Ultrathin oxide films on metal supports: structure-reactivity relations. Annu Rev Phys Chem 63:619–633
18. Gustafson J, Westerstrom R, Resta A, Mikkelsen A, Andersen JN, Balmes O, Torrelles X, Schmid M, Varga P, Hammer B, Kresse G, Baddeley CJ, Lundgren E (2009) Structure and catalytic reactivity of Rh oxides. Catal Today 145:227–235
19. Grass ME, Zhang Y, Butcher DR, Park JY, Li Y, Bluhm H, Bratlie KM, Zhang T, Somorjai GA (2008) A reactive oxide overlayer on rhodium nanoparticles during co oxidation and its size dependence studied by in situ ambient-pressure X-ray photoelectron spectroscopy. Angew Chem Int Ed 47:8893–8896
20. Nehasil V, Stará I, Matolín V (1995) Study of CO desorption and dissociation on Rh surfaces. Surf Sci 331–333(pt A):105–109
21. Nehasil V, Stará I, Matolín V (1996) Size effect study of carbon monoxide oxidation by Rh surfaces. Surf Sci 352–354:305–309
22. Aliaga C, Park JY, Yamada Y, Lee HS, Tsung CK, Yang PD, Somorjai GA (2009) Sum frequency generation and catalytic reaction studies of the removal of organic capping agents from Pt nanoparticles by UV-ozone treatment. J Phys Chem C 113:6150–6155
23. Gong XQ, Liu ZP, Raval R, Hu P (2004) A systematic study of CO oxidation on metals and metal oxides: density functional theory calculations. J Am Chem Soc 126:8–9
24. Engel T, Ertl G (1979) Elementary steps in the catalytic oxidation of carbon monoxide on platinum metals. Adv Catal 28:1–78
25. Chen MS, Cai Y, Yan Z, Gath KK, Axnanda S, Goodman DW (2007) Highly active surfaces for CO oxidation on Rh, Pd, and Pt. Surf Sci 601:5326–5331
26. McClure SM, Goodman DW (2009) New insights into catalytic CO oxidation on Pt-group metals at elevated pressures. Chem Phys Lett 469:1–13
27. Lee H-I, White JM (1980) Carbon monoxide oxidation over Ru(001). J Catal 63:261–264
28. Peden CHF, Goodman DW (1986) Kinetics of carbon monoxide oxidation over ruthenium(0001). J Phys Chem 90:1360–1365
29. Over H, Kim YD, Seitsonen AP, Wendt S, Lundgren E, Schmid M, Varga P, Morgante A, Ertl G (2000) Atomic-scale structure and catalytic reactivity of the RuO_2(110) surface. Science 287:1474–1476
30. Kim YD, Over H, Krabbes G, Ertl G (2000) Identification of RuO_2 as the active phase in CO oxidation on oxygen-rich ruthenium surfaces. Top Catal 14:95–100
31. Over H, Muhler M (2003) Catalytic CO oxidation over ruthenium—bridging the pressure gap. Prog Surf Sci 72:3–17
32. Gao F, Wang Y, Cai Y, Goodman DW (2009) CO oxidation over Ru(0001) at near-atmospheric pressures: from chemisorbed oxygen to RuO_2. Surf Sci 603:1126–1134

33. Cant NW, Hicks PC, Lennon BS (1978) Steady-state oxidation of carbon monoxide over supported noble metals with particular reference to platinum. J Catal 54:372–383
34. Kiss JT, Gonzalez RD (1984) Catalytic oxidation of carbon monoxide over ruthenium/silicon dioxide. An in situ infrared and kinetic study. J Phys Chem 88:892–897
35. Assmann J, Narkhede V, Khodeir L, Löffler E, Hinrichsen O, Birkner A, Over H, Muhler M (2004) On the nature of the active state of supported ruthenium catalysts used for the oxidation of carbon monoxide: steady-state and transient kinetics combined with in situ infrared spectroscopy. J Phys Chem B 108:14634–14642
36. Aßmann J, Crihan D, Knapp M, Lundgren E, Löffler E, Muhler M, Narkhede V, Over H, Schmid M, Seitsonen AP, Varga P (2005) Understanding the structural deactivation of ruthenium catalysts on an atomic scale under both oxidizing and reducing conditions. Angew Chem Int Ed 44:917–920
37. Over H, Seitsonen AP (2002) Oxidation of metal surfaces. Science 297:2003–2005
38. Over H, Knapp M, Lundgren E, Seitsonen AP, Schmid M, Varga P (2004) Visualization of atomic processes on ruthenium dioxide using scanning tunneling microscopy. Chemphyschem 5:167–174
39. Boudart M (1969) Catalysis by supported metals. Adv Catal 20:153–166
40. Che M, Bennett CO (1989) The influence of particle size on the catalytic properties of supported metals. Adv Catal 36:55–172
41. Bond GC (1991) Supported metal catalysts: some unsolved problems. Chem Soc Rev 20: 441–475
42. Van Santen RA (2008) Complementary structure sensitive and insensitive catalytic relationships. Acc Chem Res 42:57–66
43. Somorjai GA, Frei H, Park JY (2009) Advancing the frontiers in nanocatalysis, biointerfaces, and renewable energy conversion by innovations of surface techniques. J Am Chem Soc 131:16589–16605
44. Narayanan R, El-Sayed M (2008) Some aspects of colloidal nanoparticle stability, catalytic activity, and recycling potential. Top Catal 47:15–21
45. Tao AR, Habas S, Yang P (2008) Shape control of colloidal metal nanocrystals. Small 4:310–325
46. Somorjai G, Park J (2008) Colloid science of metal nanoparticle catalysts in 2D and 3D structures. Challenges of nucleation, growth, composition, particle shape, size control and their influence on activity and selectivity. Top Catal 49:126–135
47. Chen J, Lim B, Lee EP, Xia Y (2009) Shape-controlled synthesis of platinum nanocrystals for catalytic and electrocatalytic applications. Nano Today 4:81–95
48. Qadir K, Joo SH, Mun BS, Butcher DR, Renzas JR, Aksoy F, Liu Z, Somorjai GA, Park JY (2012) Intrinsic relation between catalytic activity of CO oxidation on Ru nanoparticles and Ru oxides uncovered with ambient pressure XPS. Nano Lett 12:5761–5768
49. Singh J, Alayon EMC, Tromp M, Safonova OV, Glatzel P, Nachtegaal M, Frahm R, van Bokhoven JA (2008) Generating highly active partially oxidized platinum during oxidation of carbon monoxide over Pt/Al_2O_3: in situ, time-resolved, and high-energy-resolution X-ray absorption spectroscopy. Angew Chem Int Ed 47:9260–9264
50. Joo SH, Park JY, Renzas JR, Butcher DR, Huang W, Somorjai GA (2010) Size effect of ruthenium nanoparticles in catalytic carbon monoxide oxidation. Nano Lett 10:2709–2713
51. Kim S, Qadir K, Jin S, Satyanarayana Reddy A, Seo B, Mun BS, Joo SH, Park JY (2012) Trend of catalytic activity of CO oxidation on Rh and Ru nanoparticles: role of surface oxide. Catal Today 185:131–137
52. Böttcher A, Starke U, Conrad H, Blume R, Niehus H, Gregoratti L, Kaulich B, Barinov A, Kiskinova M (2002) Spectral and spatial anisotropy of the oxide growth on Ru(0001). J Chem Phys 117:8104–8109
53. Knop-Gericke A, Kleimenov E, Hävecker M, Blume R, Teschner D, Zafeiratos S, Schlögl R, Bukhtiyarov VI, Kaichev VV, Prosvirin IP, Nizovskii AI, Bluhm H, Barinov A, Dudin P, Kiskinova M (2009) X-Ray photoelectron spectroscopy for investigation of heterogeneous catalytic processes. Adv Catal 52:213–272

54. Moulder JF et al (1992) Handbook of X-ray photoelectron spectroscopy. Perkin-Elmer Corporation, Eden Prairie, MN
55. Blume R, Havecker M, Zafeiratos S, Teschner D, Vass E, Schnorch P, Knop-Gericke A, Schlogl R, Lizzit S, Dudin P, Barinov A, Kiskinova M (2007) Monitoring in situ catalytically active states of Ru catalysts for different methanol oxidation pathways. Phys Chem Chem Phys 9:3648–3657
56. Park J-N, McFarland EW (2009) A highly dispersed Pd–Mg/SiO_2 catalyst active for methanation of CO_2. J Catal 266:92–97
57. Obuya EA, Harrigan W, Andala DM, Lippens J, Keane TC, Jones WE Jr (2011) Photodeposited Pd nanoparticle catalysts supported on photoactivated TiO_2 nanofibers. J Mol Catal A: Chem 340:89–98
58. Castellazzi P, Groppi G, Forzatti P, Finocchio E, Busca G (2010) Activation process of Pd/Al_2O_3 catalysts for CH_4 combustion by reduction/oxidation cycles in CH_4-containing atmosphere. J Catal 275:218–227
59. Ntainjua EN, Piccinini M, Pritchard JC, Edwards JK, Carley AF, Kiely CJ, Hutchings GJ (2011) Direct synthesis of hydrogen peroxide using ceria-supported gold and palladium catalysts. Catal Today 178:47–50
60. Zheng G, Altman EI (2002) The oxidation mechanism of Pd(100). Surf Sci 504:253–270
61. Schalow T, Brandt B, Starr DE, Laurin M, Shaikhutdinov SK, Schauermann S, Libuda J, Freund HJ (2007) Particle size dependent adsorption and reaction kinetics on reduced and partially oxidized Pd nanoparticles. Phys Chem Chem Phys 9:1347–1361
62. van Rijn R, Balmes O, Resta A, Wermeille D, Westerstrom R, Gustafson J, Felici R, Lundgren E, Frenken JWM (2011) Surface structure and reactivity of Pd(100) during CO oxidation near ambient pressures. Phys Chem Chem Phys 13:13167–13171
63. Ludwig W, Savara A, Dostert K-H, Schauermann S (2011) Olefin hydrogenation on Pd model supported catalysts: new mechanistic insights. J Catal 284:148–156
64. Weaver JF, Hinojosa JA Jr, Hakanoglu C, Antony A, Hawkins JM, Asthagiri A (2011) Precursor-mediated dissociation of n-butane on a PdO(101) thin film. Catal Today 160:213–227
65. Gao F, Wang Y, Cai Y, Goodman DW (2008) CO oxidation on Pt-group metals from ultrahigh vacuum to near atmospheric pressures. 2. Palladium and platinum. J Phys Chem C 113: 174–181
66. Zheng G, Altman EI (2002) The reactivity of surface oxygen phases on Pd(100) toward reduction by CO. J Phys Chem B 106:1048–1057
67. Rupprechter G (2007) A surface science approach to ambient pressure catalytic reactions. Catal Today 126:3–17
68. Hendriksen BLM, Bobaru SC, Frenken JWM (2004) Oscillatory CO oxidation on Pd(100) studied with in situ scanning tunneling microscopy. Surf Sci 552:229–242
69. Lichtenberger J, Lee D, Iglesia E (2007) Catalytic oxidation of methanol on Pd metal and oxide clusters at near-ambient temperatures. Phys Chem Chem Phys 9:4902–4906
70. Gabasch H, Hayek K, Klötzer B, Unterberger W, Kleimenov E, Teschner D, Zafeiratos S, Hävecker M, Knop-Gericke A, Schlögl R, Aszalos-Kiss B, Zemlyanov D (2007) Methane oxidation on Pd(111): in situ XPS identification of active phase. J Phys Chem C 111:7957–7962
71. Campbell CT (2006) Transition metal oxides: extra thermodynamic stability as thin films. Phys Rev Lett 96:066106
72. Leisenberger FP, Koller G, Sock M, Surnev S, Ramsey MG, Netzer FP, Klötzer B, Hayek K (2000) Surface and subsurface oxygen on Pd(111). Surf Sci 445:380–393
73. Gabasch H, Unterberger W, Hayek K, Klötzer B, Kresse G, Klein C, Schmid M, Varga P (2006) Growth and decay of the Pd(111)–Pd_5O_4 surface oxide: pressure-dependent kinetics and structural aspects. Surf Sci 600:205–218
74. Kan HH, Shumbera RB, Weaver JF (2008) Adsorption and abstraction of oxygen atoms on Pd(111): characterization of the precursor to PdO formation. Surf Sci 602:1337–1346

75. Chen M, Wang XV, Zhang L, Tang Z, Wan H (2010) Active surfaces for CO oxidation on palladium in the hyperactive state. Langmuir 26:18113–18118
76. Zorn K, Giorgio S, Halwax E, Henry CR, Grönbeck H, Rupprechter G (2010) CO oxidation on technological Pd–Al_2O_3 catalysts: oxidation state and activity. J Phys Chem C 115: 1103–1111
77. Sheppard N, De La Cruz C (1998) In: Haag WO, Gates B, Eley DD, Helmut K (eds) Advances in catalysis, vol 42. Academic, pp 181–313
78. Ketteler G, Ogletree DF, Bluhm H, Liu H, Hebenstreit ELD, Salmeron M (2005) In situ spectroscopic study of the oxidation and reduction of Pd(111). J Am Chem Soc 127: 18269–18273
79. Kibis LS, Stadnichenko AI, Koscheev SV, Zaikovskii VI, Boronin AI (2012) Highly oxidized palladium nanoparticles comprising Pd4+ species: spectroscopic and structural aspects, thermal stability, and reactivity. J Phys Chem C 116:19342–19348
80. Schalow T, Brandt B, Laurin M, Schauermann S, Libuda J, Freund HJ (2006) CO oxidation on partially oxidized Pd nanoparticles. J Catal 242:58–70

Chapter 8
Influence of Atomic Structure, Steps, and Kinks on the Catalytic Activity: In Situ Surface Studies

Bas Hendriksen

8.1 Single-Crystal Studies of Heterogeneous Catalysis

The surface science approach to catalysis started with the emergence of surface-sensitive techniques that can probe the structure and composition of surfaces. These techniques were made possible by the development of modern vacuum technology [1]. The investigation of surface properties contributed significantly to the development of thin-film technologies for electronics and coatings and, at the same time, provided a basic understanding of surface chemistry and reactions related to catalysis. A substantial number of review articles and books treat the surface science of catalysis until the turn of the millennium. A particularly successful approach was, and still is, to use single crystals to study the surface chemistry of catalysts. The advantage of using single crystals is significant control over the structural features of the surface where the reaction takes place. The crystal face, step orientation, step density, and density of the kinks can be controlled by accurately cutting along specific directions of the bulk crystal. Although the single-crystal surface science approach was successful in providing knowledge of the elementary surface processes of catalysis, it also led to the so-called materials gap (i.e., the difference between the structure and catalytic properties of single crystals and those of complex, real catalysts consisting of nanoparticles on porous oxide supports with the addition of promoters). To bridge this materials gap, surface science studies have shifted towards more complex systems, such as nanoparticles on well-defined oxide surfaces (see Part II). This chapter discusses several examples of recent single-crystal studies. This is not intended to provide a comprehensive, complete overview of recent literature on the subject; instead, it is limited to studies that highlight recent insights on the influence of the atomic structure, steps, and kinks on the

---

B. Hendriksen (✉)
Institute for Molecules and Materials, Radboud University Nijmegen,
Nijmegen, The Netherlands
e-mail: B.Hendriksen@science.ru.nl

J.Y. Park (ed.), *Current Trends of Surface Science and Catalysis*,
DOI 10.1007/978-1-4614-8742-5_8,

catalytic activity of single-crystal surfaces. This chapter is organized as follows: First, the elementary steps of a catalytic reaction and the role of the atomic-scale structure, from the perspective of theoretical calculations, are discussed. Second, the importance of the formation of new structures under realistic reaction conditions for the case of surface oxides is discussed. The third part treats experiments that demonstrate the role of steps in catalytic systems.

8.2 Concepts and Theory: The Importance of Atomic-Scale Structure

8.2.1 Active Sites: Electronic and Geometric Effects

Chemical reactions are the breaking and forming of bonds between atoms in molecules. Catalysts enable, or speed up, reactions by reducing the activation energy of the reaction (i.e., the highest energy barrier), which needs to be overcome to get to the reaction products (see Fig. 8.1a). A catalytic reaction takes place in several steps. Typically, one of the steps in the sequence of events of the catalytic reaction (e.g., adsorption, dissociation, diffusion, bond formation, product desorption) limits the overall rate of formation of the final reaction product. But what makes a good catalyst? According to the Sabatier principle, the interaction of a molecule with a surface site should be sufficiently strong to be able to break the bond between the atoms in a molecule (activation), but not too strong to prevent further steps in the reaction with the dissociated molecule (i.e., diffusion, bond formation with other reactant species, desorption of the final product). If the dissociation of a reactant molecule is the rate-limiting step, then the catalytic activity (i.e., the number of reaction product molecules produced per second) is given by the so-called volcano curve. The turnover rate of the initial reactants to the final reaction product exhibits a maximum as a function of the dissociation energy (activation energy). Understanding and predicting the energies involved in the dissociation step of a catalytic reaction and their relationship with the atomic-scale structure of the catalyst is key to the rational design of new catalysts. Recent developments in theory, in particular, density functional theory (DFT), have provided an enormous step forward in our conceptual understanding and predicting power of catalytic reactions on crystal surfaces and the influence of the atomic structure.

In the 1990s, Hammer and Nørskov developed a model based on DFT, which relates the chemisorption energy of an adsorbate to the center of the electronic d-band of the metal catalyst surface before adsorption [2]. The center of the d-band determines both the energy shifts of the bonding and anti-bonding states of the adsorbate molecule and the degree of filling of the anti-bonding states. The higher the energy of the d-states relative to the Fermi level, the less filled the anti-bonding states are, which results in stronger adsorption. The position of the d-band center depends on the metal element, the surface atomic structure (i.e., the surface

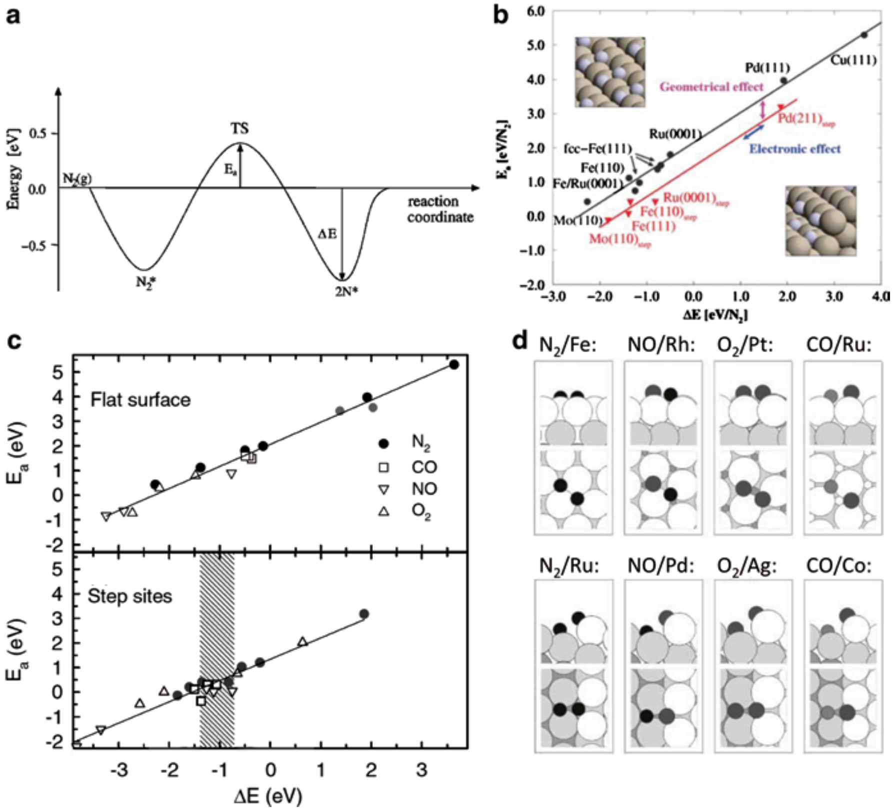

Fig. 8.1 Density functional theory calculations of electronic versus geometric effects. (**a**) Energy "landscape": successive steps of the dissociation of N_2. The activation energy for the dissociation, E_a, corresponds to the energy of the transition state (TS). The atoms of the dissociated molecule, 2N*, have a chemisorption energy, ΔE. (**b**) Density functional theory (DFT) calculations show that there is a linear BEP relation between E_a and ΔE because of the similarity between the TS and the final 2N* state. (**c**) This even holds for different molecules when the TS is similar. When the TS is different for a different surface structure or at a step (**d**), the whole BEP line shifts (**b**, **c**). Reproduced from Ref. [3] with permission from The Royal Society of Chemistry, and Ref. [4], © 2002, with permission from Elsevier

orientation), reconstruction, and steps and defects. The d-band model successfully explains the dependence of the chemisorption energy on the surface structure in terms of the electronic structure. The next step is to understand the energy barrier for the reaction: activation energy.

According to the empiric Brønsted–Evans–Polanyi (BEP) relation, the activation energy for dissociation of a molecule is a linear function of the chemisorption energy of the atoms of the dissociated molecule:

$$E_a = \alpha \Delta E + \beta \tag{8.1}$$

where E_a is the activation energy for dissociation and ΔE is the chemisorption potential energy of the dissociated products, and α and β are constants. Figure 8.1 shows the calculated BEP relationship for N_2 dissociation on various metal surfaces as a linear relation between the activation energy (barrier) and the chemisorption energy of the dissociation products. This is explained as follows: The activation energy, E_a, corresponds to the energy of the transition state E_{TS}. DFT calculations demonstrate that the transition state energy is directly related to the adsorption energy because the atomic geometry of the transition state is very similar to the final state geometry [3]. Thus, a lower energy of the final dissociated state associated with a stronger bond corresponds to a lower activation energy. The results of the calculations in Fig. 8.1b, c show that the BEP relationship is independent of the metal and that, for various diatomic molecules, it is even independent of the molecule [4]. The reason for this is that the transition states of these molecules on various close-packed surfaces are nearly identical, as shown in Fig. 8.1d. For a different transition state geometry, such as at the steps in Fig. 8.1d, the values fall on a different, shifted BEP line. In other words, moving along a BEP line, the geometry of the transition states remains the same and the linear variation of $E_a(\Delta E)$ is an electronic effect, explained by the d-band center model. Shifting a whole BEP line is a geometric effect. For example, the N_2 transition state is quite extended; for the close-packed surface, four surface atoms stabilize the transition state. On the other hand, at a step, five surface atoms are involved in the transition state, lowering the activation energy, and thereby shifting down the BEP line.

For catalytic reactions, the BEP relation is an essential element. A low activation energy benefits the efficiency of the reaction; however, the accompanying high stability of the dissociated reaction prevents subsequent steps of the reaction (i.e., surface diffusion, bond formation, and desorption). In other words, a good catalyst has a low activation energy and weak bonding of the dissociated intermediates.

The Sabatier principle implies that a good catalyst has a small activation energy for dissociation and a low chemisorption energy of the atoms of the dissociated molecule; the BEP relationship connects these two energies. An optimum combination may exist, providing a maximum reaction rate, depending on the metal. For example, Ru and Os are near the optimum for ammonia synthesis, corresponding to the maximum in the volcano curve (i.e., the reaction rate versus the chemisorption energy). These two metals are expensive and are therefore less interesting for large industrial processes. Jacobsen et al. found an alternative optimum by combining two metals as an alloy: one with a chemisorption energy that is too high and one with a chemisorption energy that is too low [5]. Calculations suggested an optimum combination of Co and Mo, and a CoMo-based catalyst was indeed found to be close to the maximum of the volcano curve.

In the steam-reforming process, hydrocarbons are converted to CO and H_2. A problem with nickel is that it also catalyzes graphite formation from hydrocarbons. By a combination of scanning tunneling microscopy (STM), molecular beam experiments, DFT calculations, and X-ray absorption spectroscopy, a NiAu surface alloy was characterized [6]. Nickel atoms near a Au atom experience a higher electron density. With increasing Au coverage, the dissociation probability for CH_4 decreases.

The more important effect of the Au is that the stability of C atoms on the Ni atoms near a Au atom is substantially destabilized compared with the pure Ni(111) surface. These less-stably adsorbed C atoms are more reactive to form CO than to form graphite. This concept was tested by adding 0.3 % weight of Au to a $MgAl_2O_4$-supported Ni catalyst, which demonstrated superior stability against graphite formation during steam reforming of butane.

The combination of single-crystal experiments and DFT calculations provides insight into the structure dependence of the catalytic activity of the metal surface. The chemisorption energy is determined by the electronic structure (the d-band center), which depends on the surface structure. The activation energy of dissociation is proportional to the chemisorption energy and depends on the geometric structure of the transition state.

8.2.2 The Importance of the Gas Phase

The previous section illustrated how DFT contributed to the current insight into how electronic and geometric structures influence the elementary steps of a catalytic reaction. Other recent DFT calculations, in particular, by Reuter and Scheffler, elucidate the nature of the pressure gap (i.e., the difference in catalytic behavior at ultra low gas pressures in surface science studies and near atmospheric pressure) where most real catalysts work occurs (see Part I). The new approach taken in these ab initio calculations is to include the influence of the pressure of the gas phase of the reactants on the structure and composition of the surface of a catalyst. When including the gas phase, one should consider situations where the gas constituents can either be part of the surface structure or remain in the gas phase. This can be evaluated by considering the surface free energy, $\gamma(T, p)$, which is the Gibbs free energy, G, of the structure per area, A, minus the energy gained by removal of the constituent from the gas phase (i.e., the chemical potential, μ).

$$\gamma(T,p) = \frac{1}{A}\left[G(T,,p,,N_i) - \sum_i N_i \mu_i(T,p)\right] \tag{8.2}$$

In these calculations, the surface free energy of the total system should be minimized to get the stable equilibrium structure. This was first shown for the surface termination of Al_2O_3 [7] and later for the more catalytically relevant RuO_2 [8]. The energy of an oxygen atom in the gas phase is given by the chemical potential, which is a function of the O_2 pressure, p, with respect to the standard pressure, p^o:

$$\mu_O(T,p) = \mu_O(T,p^o) + \frac{1}{2}kT\ln\left(\frac{p}{p^o}\right) \tag{8.3}$$

Here, k is the Boltzmann constant and T is the temperature. How much the chemical potential is reduced by insertion of the gas-phase species in the surface structure

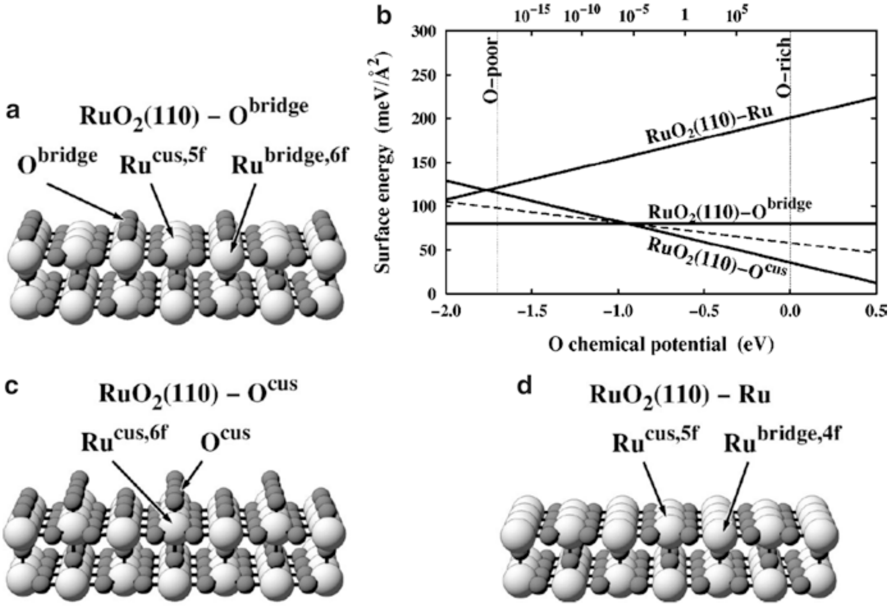

Fig. 8.2 Calculated effect of oxygen gas pressure on the surface structure/composition of RuO_2. The surface energy of the three compositions was calculated as a function of the oxygen pressure. (**c**) For the $RuO_2(110)$–Ru structure, neither the coordinationally unsaturated (cus) $Ru^{cus,5f}$ nor the $Ru^{bridge,4f}$ atoms are covered by O. (**a**) For the $RuO_2(110)–O^{bridge}$ structure, only the $Ru^{bridge,4f}$ are covered by an oxygen atom (O^{bridge}) and (**b**) for the $RuO_2(110)–O^{cus}$ structure, both the $Ru^{cus,5f}$ and the $Ru^{bridge,4f}$ are covered by oxygen. (**b**) The calculated surface energies show that, at low oxygen pressure, the $RuO_2(110)–O^{bridge}$ is lowest in energy; at higher oxygen pressures, the $RuO_2(110)–O^{cus}$ is lowest in energy and therefore the stable structure. The absolute value of the calculated transition pressure depends exponentially on the chemical potential and it is therefore highly sensitive to small variations and errors in the energy. Adapted from Ref. [8], © (2002), by The American Physical Society

depends on the gas pressure, p, and uptake (insertion), N, of the species, i, in the structure. Figure 8.2b shows the free energy as a function of the oxygen chemical potential of the gas phase (N.B. for O atoms). Figure 8.2 shows three calculated surface structures. The $RuO_2(110)$–Ru structure does not accommodate oxygen atoms from the gas phase and the oxygen atoms thus remain in the gas phase; with increasing oxygen pressure, the free energy increases. The $RuO_2(110)–O^{bridge}$ structure, on the other hand, takes up one oxygen atom; because this oxygen atom is no longer in the gas phase, the pressure-dependent part of the free energy is absent. The $RuO_2(110)–O^{cus}$ accommodates two oxygen atoms and, with respect to the chemical potential for one oxygen atom, the free energy decreases with the oxygen (atom) gas pressure. The lowest free energy line now represents the stable structure as a function of pressure, and the slopes of the curves are simply determined by the oxygen uptake for each structure. At low chemical potential, the $RuO_2(110)–O^{bridge}$ structure is lowest in energy, and with increasing oxygen pressure, the $RuO_2(110)–O^{cus}$ becomes the lowest in energy.

For reactant mixtures with more than a single gas component, the structure and composition of the surface depends on the partial pressures of the gas components [9]. For example, in a mixture of CO and O_2 with varying partial pressures, the Pd(100) surface shows a variety of CO and O chemisorbed structures on the metallic Pd: a surface oxide with or without CO adsorbed, and a PdO bulk oxide [10]. At present, it is common practice to include the chemical potential of the gas phase in structure calculations. Other examples include the S and H_2 pressure-dependent edge structure of MoS_2 particles, NO reduction under excess oxygen on Ir(111) and Ir(211), oxidation of Ag(111), and a range of transition metal oxides under oxidizing conditions [11–14].

8.3 Atomic Structure and the Active Phase

8.3.1 Structure-Sensitive Reactions

The direct comparison of the catalytic activity and selectivity of surfaces with different orientations provides information about the influence of the atomic structure. This has been well described (for example, see [15]). It is well established that catalytic reactions may depend on the atomic structure of the surface (i.e., they are structure sensitive). A classic example of a catalytic reaction that is sensitive to the atomic structure of the catalyst's surface is ammonia synthesis on iron surfaces [15]. The (111) and (211) surfaces of iron exhibit a significantly higher reaction rate than the (100), (210), and (110) faces. This structural effect has been ascribed to C7 sites (i.e., Fe atoms with a coordination number of 7, or number of nearest neighbors), which exist only on the (111) and (211) surfaces. Now, what if the structure of the catalytic surface during the reaction differs substantially from the initially pure, well-defined crystalline metal surface? For example, depending on the gas pressure (i.e., the chemical potential) new structures may become stable (see Sect. 8.2.2). Or what if only a small percentage of uncontrolled or varying defects and steps completely dominate the activity? In the remainder of this chapter, these questions will be addressed.

8.3.2 Oxides as the Active Phase

8.3.2.1 The Pressure-Gap Effect for Ruthenium

An example of a pressure-gap system is CO oxidation on ruthenium. Ruthenium does not exhibit any activity for CO oxidation at low pressures; however, at pressures in the several Torr regime, Ru has the highest activity of all relevant transition metals (i.e., Pt, Pd, Or, Rh, Ru) [16]. In 2000, a surface science study by Over et al. revealed that the active phase at high pressures is not the metal Ru(0001) surface, instead the catalytically highly active phase for CO oxidation is a RuO_2 film,

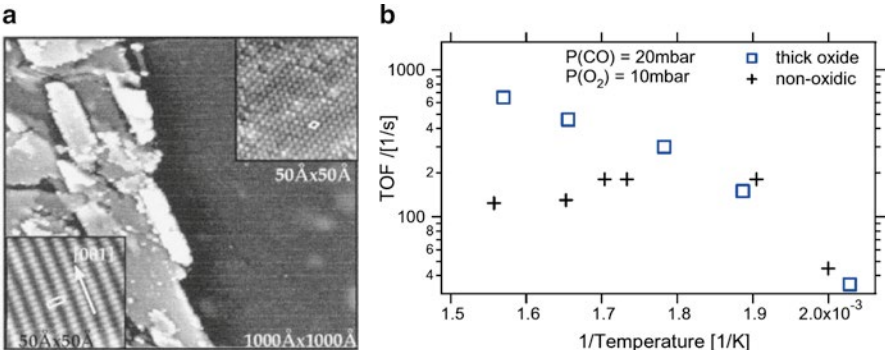

Fig. 8.3 (**a**) STM image of $RuO_2(110)$ patches (*left side* of the STM image) on Ru(0001) which have formed during exposure to oxygen gas at 10^{-2} mbar and 700 K. The *left* and *right insets* show the atomic structure of the oxide and the metal. (**b**) Turn over frequency (TOF) for CO oxidation on Ru(0001) as a function of temperature. *Open square* and *cross symbols* correspond to the oxidized Ru surface and to the metallic surface, respectively, as was determined by surface X-ray diffraction (SXRD) during the reaction. From Ref. [17], reprinted with permission from AAAS and Ref. [19] © (2009), with permission from Elsevier

see Fig. 8.3 [17]. This film forms on the Ru(0001) surface under reaction conditions at high pressures, but not at the low pressures typically used in ultrahigh vacuum (UHV) experiments. Calculations show that the high activity of the RuO_2 originates from differentiation of the Ru surface sites: the $RuO_2(110)$ surface has onefold, under-coordinated Ru sites ($Ru^{cus,5f}$) and Ru atoms at sites which bridge O atoms in the layer below ($Ru^{bridge,4f}$) [18]. On the pristine metal surface, the CO and O_2 reactant species compete for the same adsorption sites. However, on the $RuO_2(110)$ surface, CO adsorbs on the $Ru^{cus,5f}$ sites (CO^{cus}) and O adsorbs on the $Ru^{bridge,4f}$ sites (O^{bridge}), which is mediated by initial adsorption of O on the $Ru^{cus,5f}$ sites (O^{ontop}) followed by diffusion to the $Ru^{bridge,4f}$ sites. The occupation of these two nonequivalent sites depends on the CO and O_2 pressures, as was discussed in Sect. 8.2.2, and CO_2 forms by reaction of the CO molecules on $Ru^{cus,5f}$ with the O atoms on the $Ru^{bridge,4f}$ sites. Thus, the CO reacts with O atoms that are part of the RuO_2 oxide lattice structure. The removed lattice oxygen atoms are replenished by oxygen from the gas phase, which is the so-called Mars–Van Krevelen reaction mechanism.

Over et al. performed in situ surface X-ray diffraction experiments (SXRD, see Box 8.1) [19, 20]. The combination of online reaction product analysis with SXRD allowed them to correlate the turn over frequency (TOF—number of reaction products per site per second) for CO oxidation with the structure of the catalytic surface. Figure 8.3b shows that, in the mbar regime, two distinct phases can be present; the RuO_2 phase and a non-oxidic phase. At temperatures below 550 K, both phases have a nearly identical activity; for temperatures above 550 K, the oxide phase has the higher activity, showing that the oxide is indeed the active phase under these conditions.

Box 8.1 High-Pressure STM and in Situ SXRD

During the last few decades, in situ and *operando* surface-sensitive techniques have been developed that provide information about the structure or composition of a catalytic surface at (nearly) realistic conditions for heterogeneous catalysis. Thereby, they bridge the pressure gap between the traditional surface science studies performed under UHV conditions ($<10^{-6}$ mbar) and the conditions at which real technical/industrial catalysts operate (>1 mbar). One of these in situ/operando methods, ambient pressure XPS, is discussed in Chap. 9 of this book. In several of the single-crystal studies described in this chapter, the use of in situ/operando high-pressure scanning tunneling microscopy (HP-STM) and surface X-ray diffraction (SXRD) is essential. HP-STM was pioneered in the early 1990s by Salmeron and Somorjai [21]. By backfilling a small UHV chamber containing a special-purpose STM with hydrogen, carbon monoxide, or oxygen gas, the structural changes of a Pt(110) surface induced by these gases could be visualized at atmospheric pressure. Although, in absolute terms, atmospheric gas pressure or a pressure of several bar may not be particularly high, relative to UHV experiments, it can be considered as being *high pressure*. The backfilling HP-STM approach was used to study the structure of adsorption layers of reactants that form only at high pressure, and structural changes of the metal surface induced by the gas phase at high pressure (see Figs. 8.4 and 8.7). The integration of a STM in a gas microflow reactor allowed a direct correlation between the structure and structural changes of a catalyst surface with its catalytic activity by means of reaction product analysis of the gas flow leaving the reactor (see Fig. 8.8) [22, 23]. Where HP-STM provides the local structure and morphology information of a surface under high gas pressure in real space, in situ SXRD provides the reciprocal space structure of a relatively large surface area [24]. From the intensities of a synchrotron-generated X-ray beam, which diffracts from a single crystal, the atomic structure of the surface can be accurately determined. The formation of new gas-phase or reaction-induced structures at a surface, such as oxides or surface roughness (Figs. 8.3b, 8.5, and 8.9), can be detected by the occurrence of new diffraction peaks at characteristic positions in reciprocal space or by detailed analysis of the so-called crystal truncation rod. Because the X-rays are not strongly attenuated by the gas phase in the reaction chamber, which contains the crystal sample, the diffraction experiments can be performed ranging from UHV up to gas pressures of several bar. Again, changes in the surface structure and the catalytic activity can be directly correlated by reaction product detection via gas sampling from the batch reactor or flow reactor [25, 26].

(continued)

Box 8.1 (continued)

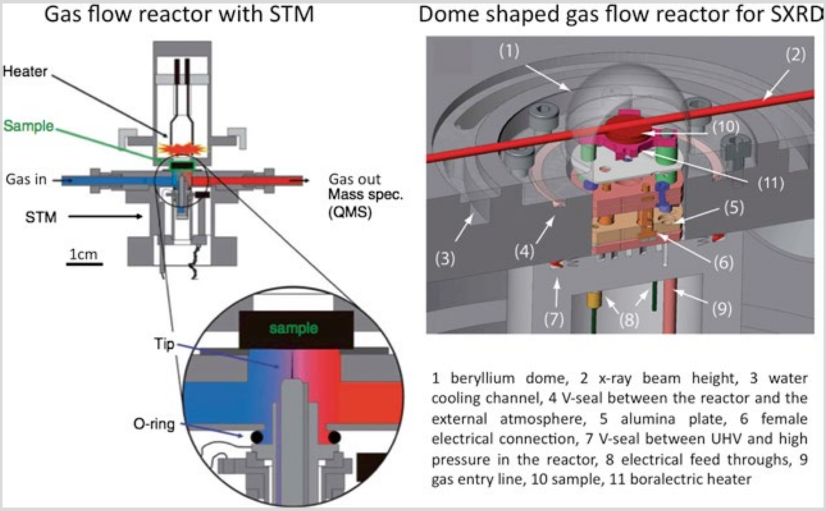

Schematics of a high-pressure scanning tunneling microscope integrated in a microflow reactor and a flow reactor for in situ SXRD. From Ref. [23], © 2007, Cambridge University Press and Ref. [26], reproduced with permission, © 2010, American Institute of Physics.

8.3.2.2 The Role of Oxides in CO Oxidation

The formation of a highly active oxide phase during CO oxidation was also found for the Pt(110) surface by in situ STM (see Box 8.1) [27]. The catalytic oxidation of CO by platinum can be considered as the model system for heterogeneous catalysis, and experimental studies date back to the work of Langmuir in the 1920s. Surface science studies on single crystals showed that the reaction follows Langmuir–Hinshelwood kinetics, which means that the reaction kinetics are determined by the surface coverage of O and CO adsorbates. In particular, the work by Ertl and coworkers showed that, for the Pt(110) and Pt(100) metallic surfaces, there is a coupling between the reaction kinetics and surface restructuring due to the CO and O adsorbates, which leads to beautiful spatio-temporal oscillations in the CO_2 production rate [28]. In low-pressure experiments with platinum single crystals, Pt oxides do not usually form, and at near atmospheric pressures of oxygen, where they do form, they are generally considered to deactivate the platinum catalysts [29]. The in situ STM experiments showed the opposite: under conditions where the oxide forms, the catalytic activity of the oxide is higher than that of the metallic phase, similar to the Ru(0001)/RuO_2(110) case.

Figure 8.4 shows a series of STM images, selected from a movie, together with the simultaneously recorded partial pressures of the reactants, CO and O_2, and the reaction product, CO_2. Figure 8.4a, b shows the stepped topography of the

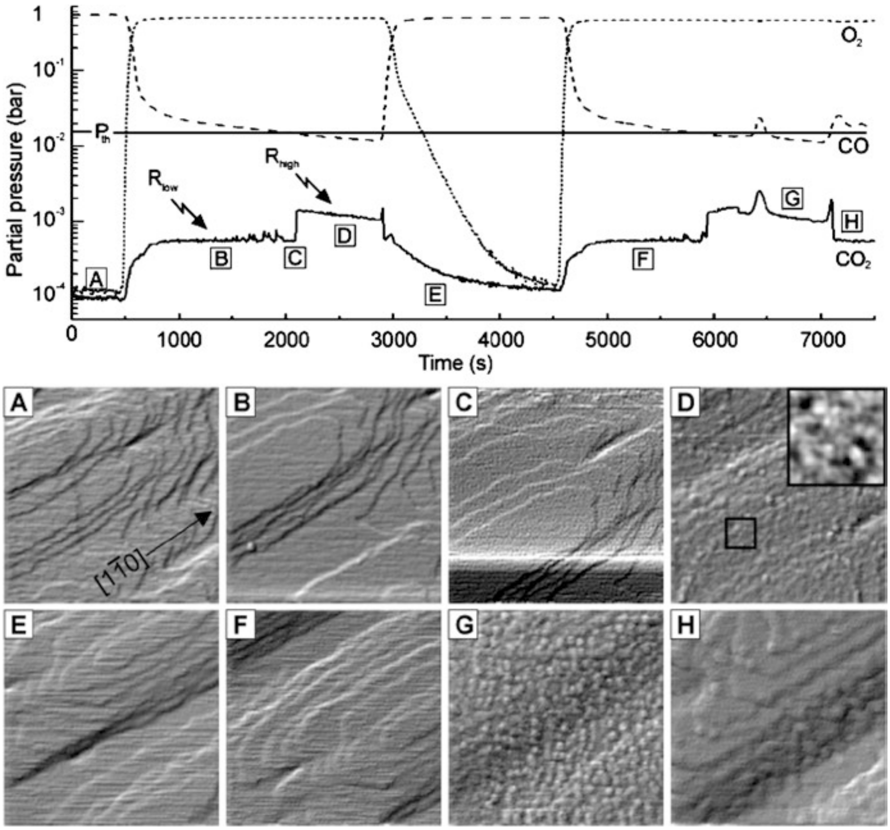

Fig. 8.4 STM during CO oxidation on Pt(110) (*Upper panel*) Mass spectrometer signals of O_2, CO, and CO_2, measured directly from the reactor cell. Labels (**a**–**h**) correspond to the STM images in the lower panel. R_{low} and R_{high} denote the low and high CO_2 production rate branches of the metallic surface and the oxidized surface, respectively. P_{th} indicates the threshold value of the CO pressure at which the rate switched from R_{low} to R_{high} and the surface changed from metallic to oxide. (*Lower panel*) STM images of 210×210 nm² from an STM movie of a Pt(110) surface at 425 K in a 3.0 ml/min flow of mixtures of CO and/or O_2 at 0.5 bar (65 s/image). The images were differentiated to enhance the contrast. From Ref. [27] © (2002), by The American Physical Society

unreconstructed Pt(110)–1×1 surface in a pure CO flow. At this length scale, it is not possible to see the adsorbate species, but the Langmuir–Hinshelwood reaction kinetics imply that the surface was completely covered by CO. Under UHV conditions, the Pt(110) surface is reconstructed to the 1×2 missing structure, and when CO is adsorbed on the surface, the reconstruction is lifted (removed), restoring the 1×1 bulk-terminated structure (see Sect. 8.4.2). This already starts at low pressures (i.e., 10^{-6} mbar), and for CO coverage of $\theta_{CO} = 1$, the transition to a smooth 1×1 surface is complete. At $t = 502$ s, the oxygen content of the flow was increased and the CO content was reduced. While the CO pressure gradually decreased, structural changes occurred on the surface at $t = 2{,}109$ s: during the scanning of image (C) from bottom to top, the topographic character changed from one scan line to the next. Coinciding with this structural change, there was a step up in the CO_2 concentration by a factor of 3, indicating a higher catalytic activity of the surface.

The change in the surface structure observed in STM before and immediately after the switch to the high-activity phase was subtle and was only seen during the following minutes: 2,109 s$<t<$2,913 s. The surface developed roughness at nanometer scale. This roughness did not correspond to multiple integers of the Pt(110) step height. When the flow was changed back to pure CO, the roughness left behind Pt adatom islands and vacancy islands, which slowly decayed to restore the initial, smooth 1 × 1 surface. Without oxygen present in the flow, no CO_2 was produced. Several observations suggested that the high-activity structure during the time interval 2,109 s$<t<$2,913 s was indeed a surface oxide: (1) The height variations of the STM topography for $t<$2,109 s and $t>$2,913 s corresponded exclusively to multiples of the Pt(110) step height, as expected for the metallic surface. By contrast, the high-activity structure had intermediate and convoluted height values, which indicate a composition different than pure Pt. (2) After switching to a pure CO flow, the roughness left Pt adatom islands behind, showing that the rough layer contained Pt atoms. Because the "PtX" structure formed only at high oxygen partial pressures, it was concluded that the high-activity structure was a thin platinum oxide film. Because the roughness of the oxide film scaled with the total amount of CO produced, the roughness was considered a by-product of the reaction.

The formation of platinum oxide and its high catalytic activity was later confirmed by SXRD on a Pt(110) surface in a batch reactor at 0.5 bar and 530 K [30]. In this experiment, the reactor was first filled with pure oxygen and then CO was added (N.B. not operated as a flow reactor). The O_2 and CO were slowly converted to CO_2, reducing both their partial pressures. Since the reaction consumes more CO than O_2 the CO/O_2 ratio decreased with time. Figure 8.5 shows a series of scans of the diffraction peaks of PtO-1 × 2 and α-PtO_2 oxides. The PtO-1 × 2 surface oxide was present during the CO oxidation reaction, and the accompanying increase in the partial pressure of CO_2 shows that this oxide had a higher activity than the metal phase. With decreasing CO pressure, a hexagonal, bulk-like PtO_2 layer formed, which remained stable after all the CO had been converted. The SXRD study confirmed earlier STM observations, but with more structural detail and over a wider range of temperatures and pressures.

More recently, in situ X-ray photoelectron spectroscopy (XPS) showed that bulk-like PtO_2 nanoislands, two monolayers thick, formed at oxygen pressures >0.5 mTorr and that chemisorbed O was also present [31]. Both the surface oxide and the chemisorbed O could be easily removed by CO exposure. The surface oxide had similar spectroscopic features as oxides on Pt nanoparticles. More structural information of the platinum oxide for high coverage of oxygen on Pt(110)–1 × 2 came from STM in UHV by atomic oxygen or at high oxygen pressure in a reactor. A high O coverage (12 × 2) chemisorption or surface oxide structure and a surface oxide, which is consistent with α- or β-PtO_2, have been observed [32]. Pedersen et al. reported low, calculated barriers for CO oxidation on Pt(110)–(12 × 2)–22O and (10–$\bar{1}$0) facets of α-PtO_2, which are in agreement with the high activity in the experiments [33].

Observation of the high activity of the surface oxide phases of Ru(0001) and Pt(110) was followed by a number of in situ and ex situ studies focusing on the

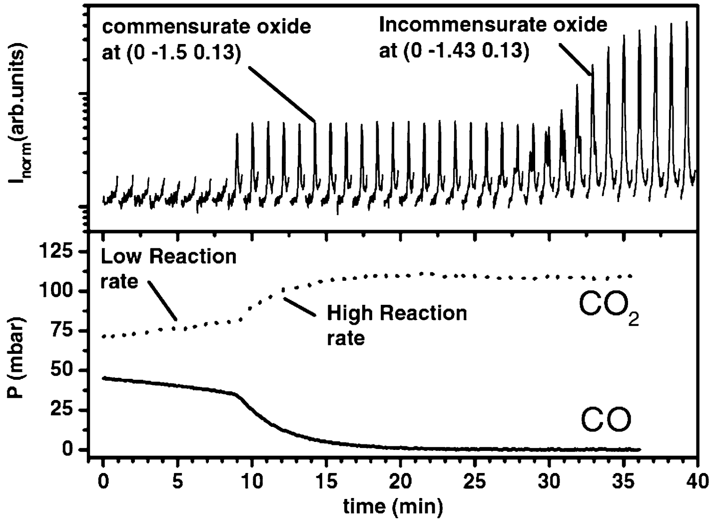

Fig. 8.5 SXRD during CO oxidation on Pt(110). (*Top*) Series of 38 scans of SXRD intensities ($H=0$, $K=-1.30$ to -1.65, $L=0.13$). (*Bottom*) Partial pressures of CO and CO_2, measured simultaneously at $P_{O_2}=500$ mbar and $T=625$ K. From $t=0$ to 9 min, the diffraction intensities at oxide positions (H, K, L) are absent and the Pt(110) surface is metallic. Together with the increase in the reaction rate, at $t=9$ min, a half-order diffraction peak appeared at $K=1.50$, corresponding to a commensurate (1×2) single layer oxide. When nearly all the CO had been consumed, at $t=30$ min, this diffraction peak decreased to 0 while the peak of α-PtO_2, at $K=1.43$, appeared. From Ref. [30] © (2005) by The American Physical Society

formation and structure of surface oxides on Pt group metals. For rhodium surfaces, similar O–Rh–O trilayer surface oxides form on Rh(111), Rh(100), Rh(110), and $Pt_{0.25}Rh_{0.75}(100)$ and on the facets of Rh nanoparticles on MgO(001) [34–39]. The identical catalytic behavior for CO oxidation on Rh(111) and Rh(100) suggests that, because the same surface oxide is formed on all surface orientations, the reaction is structure insensitive [40, 41]. Similar trilayer O–Ir–O oxides were found for Ir(111) [42]. On various Pd surfaces and nanoparticles, surface oxides or bulk-like oxides also form with a high activity for CO oxidation [43–51]. The formation of oxides was also found to cause size effects on the activity of Rh and Ru nanoparticles in CO oxidation [52, 53].

Although the formation of new surface structures and composition has been discussed for surface oxides, similar phases may form in other material and reaction systems (e.g., in carbon-based and sulfur-based reactions as carbides and sulfites) [54, 55].

8.4 Steps and Kinks

The local geometry and electronic structure of under-coordinated sites at steps, kinks, and defects often lead to a different activity and reactivity of these sites compared with terrace atoms. This can be desired when it increases the overall catalytic activity or undesired when it promotes unwanted side reactions, which may lead to catalyst deactivation. Furthermore, a large fraction of the surface of catalytic nanoparticles consists of steps and kinks, and their contribution to the catalyst's performance may be dominant. For these reasons, there is an on-going interest in understanding the role of step-edges, kinks, and defects in catalytic reactions through theory, as described in Sect. 8.2.1, and by single-crystal surface science experiments. A recent review of the role of defects is given by Vattuone et al. [56]. Here, we limit ourselves to a few examples demonstrating the catalytic activity of steps, the formation of steps induced by a reactant, and the influence of steps on surface oxidation.

8.4.1 Step Decoration Experiments

The dominant role steps may have in catalytic reactions was demonstrated by a study by Dahl et al. [57]. In ammonia synthesis, the rate-limiting step of the reaction is the dissociation of N_2. The dissociation rate of N_2 was measured by XPS and temperature-programmed desorption (TPD) for a Ru(0001) single-crystal surface that contained an average step density of 1 %. By evaporating 1 % of a monolayer of Au, the steps were passivated because Au preferentially decorates the Ru steps. As a result, the rate for N_2 dissociation was reduced by seven orders of magnitude relative to a surface with undecorated steps, showing that the 1 % step density completely dominated the dissociation reaction. The N_2 dissociation rate at the step sites was nine orders of magnitude higher than at terrace sites. Accompanying DFT calculations show a lowering of the activation barrier by the transition state configurations at the steps. Furthermore, they showed that the difference in the binding energy of atomic nitrogen between step and terrace sites is small. Therefore, after dissociation, the N atoms at the steps can easily diffuse away and do not block the step sites. In other words, the steps promote dissociation without being blocked by the reaction products. In a similar fashion, using sulfur as a step decoration, Engbaek et al. showed that CO dissociation on Ni(14 13 13) predominantly takes place at the steps [58].

Steps may also have a different selectivity. Using the method of step decoration again, Vang et al. demonstrated that steps on Ni(111) are more selective to C–C than C–H bond breaking [59, 60]. Figure 8.6 shows two STM images of a Ni(111) surface after exposure to ethylene. In Fig. 8.6a, the steps were initially clean and undecorated, and in Fig. 8.6b, the steps were intentionally decorated by silver atoms. At the upper side of the undecorated steps, a brim of decomposed ethylene can be observed, demonstrating that the Ni steps break the C–C bond. By covering the steps with Ag atoms, the dissociation was blocked and no decomposed ethylene was present after exposure. Comparison of the DFT-calculated transition states and their corresponding energies on the (111) terraces and at the steps (Fig. 8.6c) showed that indeed the steps have a lower activation energy for C–C bond breaking, whereas for the C–H bond breaking, there was no significant difference in activation energy. Based on this knowledge, Ag was added to a high-surface-area, oxide-supported nickel catalyst.

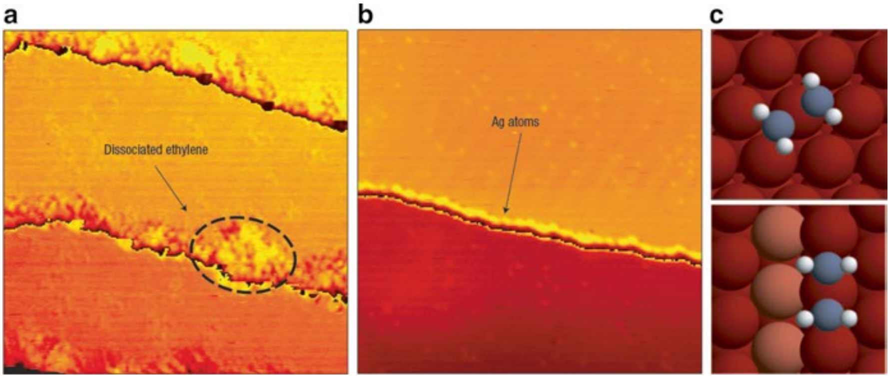

Fig. 8.6 STM images of a Ni(111) surface after exposure to ethylene. (**a**) The steps are covered by a brim of dissociated ethylene (image size 20 × 20 nm^2). (**b**) The steps decorated by Ag atoms remained clean (40 × 40 nm^2). (**c**) DFT-calculated transition state for C–C bond breaking of ethylene on a terrace (*top*) and at a step (*bottom*). From Ref. [59] © (2005), by The Nature Publishing Group

This catalyst was then used for ethane hydrolysis, which involves C–C dissociation. Compared to a catalyst without added Ag, the reaction rate constant was lower by about one order of magnitude, whereas the apparent activation energy was the same. This proved that indeed the steps are highly selective to C–C bond breaking.

8.4.2 CO-Induced Step Formation from UHV to Atmospheric Pressure

From the preceding discussion, the importance of naturally occurring steps in catalytic reactions is evident. Based on this knowledge, catalysts can be designed to have an intentionally high or low step density. However, there is a complication: steps can be created "spontaneously" during the reaction by interactions of the catalyst's surface with the adsorbates, as we will illustrate next by examples of CO adsorption on platinum single crystals.

In a vacuum, the Pt(110) surface reconstructs into the well-known 1 × 2 missing row structure. When the Pt(110)–1 × 2 surface is exposed to a low pressure of carbon monoxide, the reconstruction is lifted. This was already known from early surface science studies [63]. The CO adsorption moves Pt atoms from the close-packed rows (i.e., the "ridges") to 1 × 1 sites in the "troughs," leaving vacancies behind in the "ridges." This reduces the coordination of the involved Pt atoms, which is the driving force for removal of the 1 × 2 reconstruction. This can be understood as follows: According to the d-band model, CO binds more strongly to a low-coordinated metal atom (see Fig. 8.7d). The gain in the adsorption energy at a lower-coordinated atom outweighs the energy required to break the Pt–Pt bond to create the

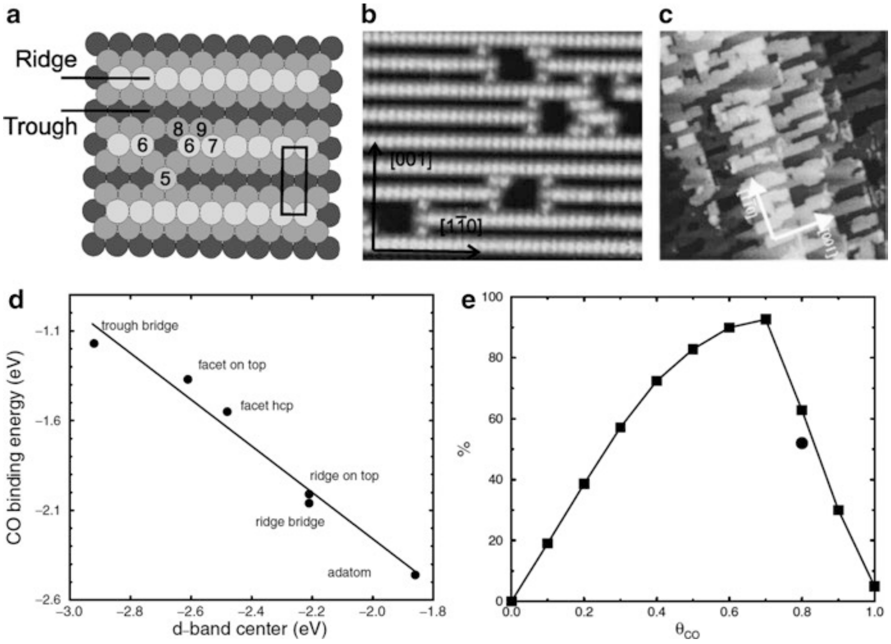

Fig. 8.7 CO-induced step formation. (**a**) Model of the Pt(110)–1 × 2 structure consisting of ridges and troughs. (**b**) STM image of CO adsorbates moving Pt atoms from the rows to the troughs. (**c**) STM image showing that this process creates 1 × 1 patches with a high density of steps (image size 30 × 30 nm^2) (**d**) Calculated binding energy for various adsorption sites showing that the d-band center shifts down for lower coordination, which leads to stronger binding. (**e**) Calculated step density as a function of the CO coverage. Reproduced from Ref. [61, 62], © (2001) by The American Physical Society reproduced with permission from [62], © 2003 AIP Publishing LLC

low-coordinated Pt site. CO molecules can thus create their own low-coordinated adsorption sites and this leads to an increasing step density with increasing CO coverage [61]. When more Pt row atoms are moved to a 1 × 1 site, more and more of the second layer of Pt atoms is exposed and becomes available for CO adsorption. With increasing CO coverage, the higher-coordinated sites also become populated with CO; next to CO adsorbed at the step-up site, CO adsorbs at the less-favorable step-down site as well. This undoes the energy gain from step formation and the step density decreases for the highest coverage (Fig. 8.7e). A smooth 1 × 1 surface is created with CO adsorbed in the (2 × 1)–*p2mg*–2CO structure. The increase and decrease of the step density with CO coverage is completely reversible.

The Pt(110)–1 × 1 surface can accommodate the high coverage of one CO molecule per Pt atom in the zigzagged (2 × 1)–*p2mg*–2CO adsorption structure. For more closely packed surface structures, the Van der Waals diameter of CO (0.32 nm), in combination with the smaller Pt lattice spacing (Pt atom diameter 0.278 nm), leads to steric hindrance by CO–CO repulsion; a high-coverage adsorption structure where CO only occupies on-top Pt positions is no longer possible. For Pt(111), CO now forms hexagonal and quasi-hexagonal commensurate and incommensurate adsorption structures with CO molecules shifted from their on-top position.

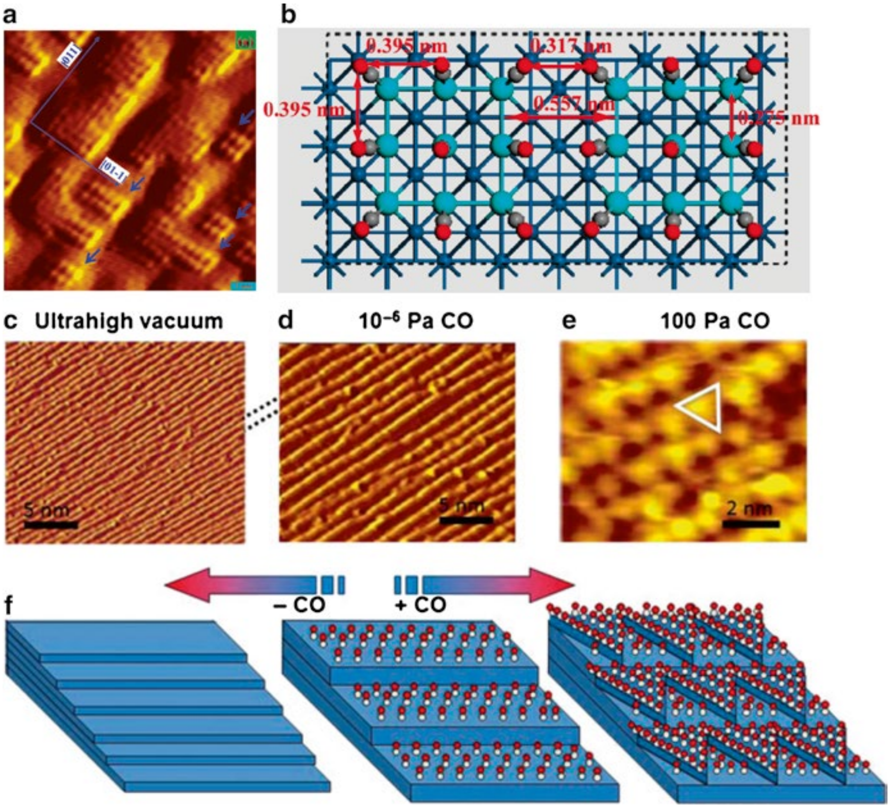

Fig. 8.8 STM observations of CO-induced restructuring of Pt(100) and Pt(553). The driving force of the restructuring is the strong CO–CO repulsion. By restructuring the Pt surface, space is created so that CO molecules can tilt and reduce their repulsive interaction. (**a**) Islands on Pt(100) under 10^{-6} Torr CO (image size 10×10 nm^2). (**b**) Model based on DFT calculations. Pt atoms form small islands with CO adsorbed to them. CO molecules at the edges can tilt away to reduce CO–CO interactions. (**c**) STM image of Pt(557) in ultrahigh vacuum (1×10^{-9} Pa) showing the monoatomic steps and terraces running diagonally. (**d**) Under $<10^{-6}$ Pa CO, the steps double in height and the terraces double in width. (**e**) Under 100 Pa CO, the surface breaks up into triangular clusters (one is marked by a *triangle*) that provide a high density of low-coordinated Pt atoms. (**f**) Schematic illustration of these three situations. The C and O atoms of the CO molecules are represented by white and red balls, respectively. From Ref. [65], reprinted with permission from AAAS Ref. [66], © (2009) by The American Chemical Society, and Ref. [67], © 2012, Cambridge University Press

The adsorption structures vary with CO pressure [64], and the Pt(111) surface itself remains unaffected. To accommodate a high coverage of CO, Pt(100) follows a different route. The Pt(100) breaks up to create space for exclusive on-top adsorption of CO [65]. Pt(100) exhibits a quasi-hexagonal surface reconstruction with an atom density at only 20 % of the bulk-terminated Pt(100)–1 × 1 surface. It is well known from various studies that CO adsorption lifts this surface reconstruction and restores the 1 × 1 surface structure. Tao et al. followed this lifting using STM. In the range of 10^{-6} mbar to several mbar of CO, they observed that the quasi-hexagonal structure broke up and the atoms segregated into islands (Fig. 8.8a). However, rather than the expected island coverage of 20 % due to density mismatch of the reconstructed and the unreconstructed surfaces, they observed a coverage of 45 %. Furthermore, there existed an atomic-scale corrugation on these islands with a spacing of 0.37–0.40 nm, which is 1.34–1.44 times the bulk-Pt lattice spacing. It was suggested that the corrugation was due to the CO molecules and that the large spacing was the result of steric hindrance from the repulsion of the CO molecules, which prevents them from getting closer than the Van der Waals diameter. The authors proposed two models: one in which Pt with adsorbed CO takes a large lattice spacing determined by the CO diameter and a second in which a few Pt atoms form small clusters from which the CO molecules at the edges can tilt away to the outside. DFT calculations supported the second model where platinum atoms in small clusters occupy the regular bulk positions and the large spacing of the corrugation was due to the tilted CO molecules (see Fig. 8.8b).

A similar phenomenon was found for stepped Pt surfaces, Pt(553) and Pt(332), which consist of six-atom-wide (111) terraces, but with the different step geometries of (100) and (111), respectively [65]. When exposed to a CO pressure of 0.1 Torr and higher, the (111) terraces of the Pt(553) surface broke up into nearly triangular nanoclusters with a size of 2.2 nm by 2.1 nm. The (111) terraces of the Pt(332) surface broke up into rectangular- and parallelogram-shaped nanoclusters. XPS of Pt(553) during CO exposure at pressures from 5×10^{-9} to 0.5 Torr showed that, in the low pressure regime, CO binds to top and bridge sites. As the pressure increased to 0.5 Torr, a new XPS peak developed, which was attributed to CO adsorbed to low-coordinated Pt atoms, in full agreement with the breakup of the terraces into the nanoclusters seen with STM. The appearance of this XPS peak was reversible with CO pressure variation. Quantitative analysis of the XPS intensities showed that the coverage varied from $\theta=0.5$ in the c(2×4) adsorption structure at 5×10^{-9} Torr to $\theta=0.97$ at 0.5 Torr. For unity coverage, each platinum atom has a CO molecule adsorbed to it and the strong repulsive CO–CO interactions dominate. CO molecules adsorbed to low-coordinated Pt atoms can tilt away from their neighbors and thereby reduce their interactions. This relaxation effect turns out to be strong enough to favor the formation of low-coordinated step Pt atoms and create nanoclusters. DFT calculations confirmed the stabilization of the nanoclusters at high CO coverage. In contrast to the Pt(553) and Pt(332) surface, the Pt(111) surface remained stable upon CO adsorption, showing that the preexisting step density is important for the breakup of the surface into clusters. If and how the CO-induced step formation affects the catalytic activity has not been studied experimentally.

8.4.3 Steps and the Catalytically Active Oxide Phase

As discussed in Sect. 8.4.1 steps may directly influence the catalytic activity of a surface. Here, we discuss how the presence of steps may affect the activity in an indirect way by playing a role in the formation and stability of catalytically active surface oxides.

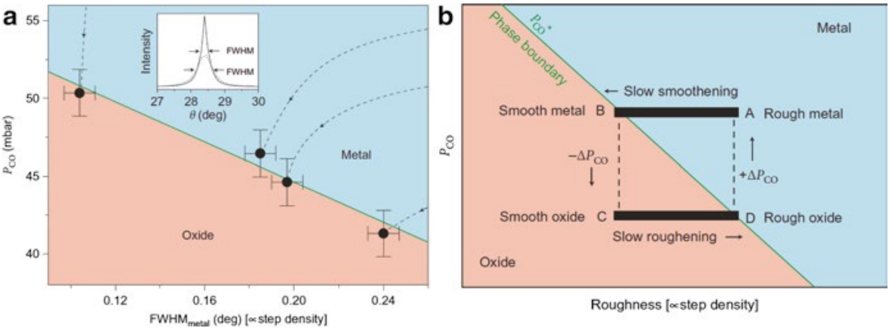

Fig. 8.9 (**a**) Stability diagram of metallic Pd(001) and PdO(001) during CO oxidation as a function of the CO partial pressure, P_{CO}, and the Pd(001) surface roughness, measured as the FWHM of the $(h,k,l) = (1,0,0.2)$ X-ray diffraction peak. The surface roughness (i.e., step density) shifts the metal–oxide phase transition to lower CO pressures. (**b**) Calculated cycle of a reaction rate oscillation. From Ref. [72] © (2010) by the Nature Publishing Group

Wang et al. showed via core level spectroscopy that a one-dimensional PtO_2 structure formed at steps on Pt(332) under conditions where bulk oxides are not yet favored [68]. The O atoms of the PtO_2 at the step were bonded more strongly than O chemisorbed at terrace sites; the O atoms of the 1D oxide still reacted more easily with CO. In this case, the preexisting steps of the Pt(332) surface promote the formation of the active PtO_2 phase. For two-dimensional oxide films on stepped metal surfaces, the formation and the structures are more complex. For example, on Rh(553), steps bunch and form (111) facets covered with a (2 × 1) O structure and (331) facets covered with a one-dimensional (10 × 1) oxide [69]. At higher oxygen pressures, the Rh(553) surface facets into (111) and (11–$\bar{1}$) both covered by a (9 × 9) two-dimensional surface oxide. A Rh(223) surface facets into (335) and (557) when exposed to oxygen and forms a (9 × 1) one-dimensional (1D) oxide with the same atomic spacing as the (9 × 9) two-dimensional (2D) oxide [70]. The oxide formation may also depend on the step orientation and structure, as was shown for the steps of Rh(111) vacancy islands. Whereas at the {111} steps, the same (10 × 1) 1D oxide forms as on Rh(553); the {100} steps are covered by a (9 × 1) 1D oxide. At higher oxygen pressure, the 2D (9 × 9) oxide forms from the defective {111} steps, but not from the smooth {100} steps. Only at higher temperatures (>250 °C), the 2D oxide also starts growing from the {100} steps, indicating a kinetic barrier for oxide formation at the {100} step. Finally, Pd(553) also facets, during exposure to oxygen, to {332} and a PdO(101)-like oxide forms. On larger {111} facets, a $\sqrt{6}$ surface oxide forms, and above 1 mbar of oxygen, a rough PdO(021) bulk oxide forms [71].

These examples illustrate that the structure of surface oxides depends on the presence of steps on the metal surface. The relative stability of these oxides may depend on the step density, as will be shown in this final example. Figure 8.9 shows data points of the roughness of a Pd(100) surface, as measured by the full width half maximum (FWHM) of the SXRD peak; the wider the peak, the rougher the surface.

Roughness on this single-crystal surface is equivalent to the average step density. The data points correspond to the FWHM of the metallic Pd(100) surface in a CO/O_2 mixture during CO oxidation at which the metal–oxide phase transition occurs. Figure 8.9a shows that, at a constant oxygen pressure and temperature, the critical CO pressure, P_{CO}, is a decreasing function of the step density. In other words, a Pd(100) surface with a higher step density requires a more oxidizing gas mixture to oxidize the surface (i.e., a lower CO/O_2 ratio). From the oxidation kinetics point of view, this is surprising because steps are usually considered nuclei for oxide growth (e.g., see above for 1D PtO_2). Structurally, however, a rough metal may be a bad template for the formation of a smooth oxide. With the naïve assumption that a smooth metal leads to a smooth oxide and a rough metal leads to a rough oxide, the stability of metal and oxide now depends on the respective free energies, which include the step free energies. On metal surfaces, CO adsorbs preferentially at the steps (e.g., see Fig. 8.7), but for CO adsorption on oxides, there is no indication that this is the case. For a rough/stepped metal surface, the CO adsorption at the steps may lower the free energy relative to the free energy of a stepped oxide. This stabilizes the rough metallic phase to more oxidizing conditions, as shown in Fig. 8.9a. The step density and changes therein control the catalytic activity, which can even lead to the reaction rate oscillations shown in Fig. 8.9b. In situ STM and SXRD in flow reactors showed that, during CO oxidation, the oxide phase roughened as a by-product of the reaction (see Sect. 8.3.2.2). On the other hand, the rough Pd metal surface became smoother with time, reducing the step density. Starting with a rough metal surface at fixed CO and O_2 partial pressures, the step density slowly reduces by becoming smoother (see Fig. 8.9b). On the metallic surface, the Pd atoms are mobile and the roughness, in the form of steps and vacancy islands, gradually decreases with time until the critical point B ($P_{CO,B}$, step density$_B$) is reached. The relatively smooth metal makes the transition to a smooth oxide. Similar to RuO_2 and PtO, the oxidized palladium surface, PdO, has a higher activity for CO oxidation, and more CO_2 is produced than for the metal surface. The increased CO conversion lowers the partial pressure of CO close to the surface (by $-\Delta P_{CO}$), pushing the system to more oxidizing conditions (i.e., a lower CO/O_2 ratio). The oxide slowly roughens until point D ($P_{CO,D}$, step density$_D$) is reached and the oxide to metal transition occurs. With the lower activity of the metal surface, the CO conversion is lower and the CO partial pressure is increased, pushing the system to more reducing conditions (higher CO/O_2 ratio). Now the system is at the starting situation again with the rough metal surface. These anti-clockwise circles around the metal–oxide transition (P_{CO}, step density) lead to the commonly observed self-sustained oscillations in CO_2 production at atmospheric pressures. The explanation for the step density dependence of the metal–oxide phase transition does not take into account any of the details of the structural changes required for formation of oxides on stepped metal surfaces. Still, it provides a simple relation between the critical CO pressure and the critical roughness. A kinetic model based on the CO- and roughness-dependent phase transition captures all the characteristics of self-sustained reaction rate oscillations.

8.5 Summary

The combination of DFT and single-crystal experiments carried out over the last decade has provided insight into the fundamental relationship between the atomic-scale structure of catalytic surfaces and their catalytic activity and selectivity. The geometry of the transition state and the electronic structure of the metal are key elements for understanding the structure dependence of the activation energy, and, for example, explain why steps have a high activity or selectivity in catalytic reactions. The structure of catalytic metal surfaces may change dramatically under the influence of reactant species. An example is the formation of steps and islands induced by CO adsorption. At sufficiently high pressures of the reactant gases, new surface structures may develop that act as the new active phase of the catalyst. For the catalytic oxidation of CO, oxides form on the commonly used Pt group metals. These metal oxides have a higher activity than the metal surface. Structure sensitivity of these metal oxides may still exist, as the conditions for formation of the oxides depend on the structure of the metal surface.

Acknowledgments I want to thank V. Navarro of Leiden University and J. A. A. W. Elemans of Radboud University Nijmegen for their useful comments and discussion.

References

1. Sinfelt JH (2002) Role of surface science in catalysis. Surf Sci 500(1–3):923–946. doi:10.1016/s0039-6028(01)01532-1
2. Hammer B, Norskov JK (1995) Electronic factors determining the reactivity of metal surfaces. Surf Sci 343(3):211–220. doi:10.1016/0039-6028(96)80007-0
3. Norskov JK, Bligaard T, Hvolbaek B, Abild-Pedersen F, Chorkendorff I, Christensen CH (2008) The nature of the active site in heterogeneous metal catalysis. Chem Soc Rev 37(10):2163–2171. doi:10.1039/b800260f
4. Norskov JK, Bligaard T, Logadottir A, Bahn S, Hansen LB, Bollinger M, Bengaard H, Hammer B, Sljivancanin Z, Mavrikakis M, Xu Y, Dahl S, Jacobsen CJH (2002) Universality in heterogeneous catalysis. J Catal 209(2):275–278. doi:10.1006/jcat.2002.3615
5. Jacobsen CJH, Dahl S, Clausen BS, Bahn S, Logadottir A, Norskov JK (2001) Catalyst design by interpolation in the periodic table: bimetallic ammonia synthesis catalysts. J Am Chem Soc 123(34):8404–8405. doi:10.1021/ja010963d
6. Besenbacher F, Chorkendorff I, Clausen BS, Hammer B, Molenbroek AM, Norskov JK, Stensgaard I (1998) Design of a surface alloy catalyst for steam reforming. Science 279(5358):1913–1915. doi:10.1126/science.279.5358.1913
7. Wang XG, Chaka A, Scheffler M (2000) Effect of the environment on alpha-Al_2O_3 (0001) surface structures. Phys Rev Lett 84(16):3650–3653. doi:10.1103/PhysRevLett.84.3650
8. Reuter K, Scheffler M (2002) Composition, structure, and stability of RuO_2(110) as a function of oxygen pressure. Phys Rev B 65(3):035406. doi:10.1103/PhysRevB.65.035406
9. Reuter K, Scheffler M (2003) Composition and structure of the RuO_2(110) surface in an O-2 and CO environment: implications for the catalytic formation of CO_2. Phys Rev B 68(4):045407. doi:10.1103/PhysRevB.68.045407
10. Rogal J, Reuter K, Scheffler M (2007) CO oxidation at Pd(100): a first-principles constrained thermodynamics study. Phys Rev B 75(20):205433. doi:10.1103/PhysRevB.75.205433

11. Bollinger MV, Jacobsen KW, Norskov JK (2003) Atomic and electronic structure of MoS2 nanoparticles. Phys Rev B 67(8):085410. doi:10.1103/PhysRevB.67.085410
12. Liu ZP, Jenkins SJ, King DA (2004) Car exhaust catalysis from first principles: selective NO reduction under excess O_2 conditions on Ir. J Am Chem Soc 126(34):10746–10756. doi:10.1021/ja0481833
13. Michaelides A, Bocquet ML, Sautet P, Alavi A, King DA (2003) Structures and thermodynamic phase transitions for oxygen and silver oxide phases on Ag{111}. Chem Phys Lett 367(3–4):344–350. doi:10.1016/s0009-2614(02)01699-8
14. Seriani N, Mittendorfer F (2008) Platinum-group and noble metals under oxidizing conditions. J Phys Condens Matter 20(18):184023. doi:10.1088/0953-8984/20/18/184023
15. Somorjai GA (1993) Introduction to surface chemistry and catalysis. Wiley, New York
16. Peden CHF, Goodman DW (1986) Kinetics of CO oxidation over Ru(0001). J Phys Chem 90(7):1360–1365. doi:10.1021/j100398a031
17. Over H, Kim YD, Seitsonen AP, Wendt S, Lundgren E, Schmid M, Varga P, Morgante A, Ertl G (2000) Atomic-scale structure and catalytic reactivity of the $RuO_2(110)$ surface. Science 287(5457):1474–1476. doi:10.1126/science.287.5457.1474
18. Over H, Muhler M (2003) Catalytic CO oxidation over ruthenium—bridging the pressure gap. Prog Surf Sci 72(1–4):3–17. doi:10.1016/s0079-6816(03)00011-x
19. Over H, Balmes O, Lundgren E (2009) Direct comparison of the reactivity of the non-oxidic phase of Ru(0001) and the RuO_2 phase in the Co oxidation reaction. Surf Sci 603(2):298–303. doi:10.1016/j.susc.2008.11.012
20. Over H, Balmes O, Lundgren E (2009) In situ structure-activity correlation experiments of the ruthenium catalyzed CO oxidation reaction. Catal Today 145(3–4):236–242. doi:10.1016/j.cattod.2008.10.048
21. McIntyre BJ, Salmeron M, Somorjai GA (1993) In situ scanning tunneling microscopy study of platinum (110) in a reactor cell at high-pressures and temperatures. J Vac Sci Technol A Vac Surf Films 11(4):1964–1968. doi:10.1116/1.578531
22. Rasmussen PB, Hendriksen BLM, Zeijlemaker H, Ficke HG, Frenken JWM (1998) The "reactor STM": a scanning tunneling microscope for investigation of catalytic surfaces at semi-industrial reaction conditions. Rev Sci Instrum 69(11):3879–3884. doi:10.1063/1.1149193
23. Frenken J, Hendriksen B (2007) The reactor-STM: a real-space probe for operando nanocatalysis. MRS Bull 32(12):1015–1021. doi:10.1557/mrs2007.210
24. Ferrer S, Ackermann MD, Lundgren E (2007) In situ investigations of chemical reactions on surfaces by X-ray diffraction at atmospheric pressures. MRS Bull 32(12):1010–1014. doi:10.1557/mrs2007.209
25. Bernard P, Peters K, Alvarez J, Ferrer S (1999) Ultrahigh vacuum high pressure chamber for surface x-ray diffraction experiments. Rev Sci Instrum 70(2):1478–1480. doi:10.1063/1.1149609
26. van Rijn R, Ackermann MD, Balmes O, Dufrane T, Geluk A, Gonzalez H, Isern H, de Kuyper E, Petit L, Sole VA, Wermeille D, Felici R, Frenken JWM (2010) Ultrahigh vacuum/high-pressure flow reactor for surface x-ray diffraction and grazing incidence small angle x-ray scattering studies close to conditions for industrial catalysis. Rev Sci Instrum 81(1):014101. doi:10.1063/1.3290420
27. Hendriksen BLM, Frenken JWM (2002) CO oxidation on Pt(110): scanning tunneling microscopy inside a high-pressure flow reactor. Phys Rev Lett 89(4):046101. doi:10.1103/PhysRevLett.89.046101
28. Imbihl R, Ertl G (1995) Oscillatory kinetics in heterogeneous catalysis. Chem Rev 95(3):697–733. doi:10.1021/cr00035a012
29. Sales BC, Turner JE, Maple MB (1982) Oscillatory oxidation of CO over Pt, Pd and Ir catalysts—theory. Surf Sci 114(2–3):381–394. doi:10.1016/0039-6028(82)90692-6
30. Ackermann MD, Pedersen TM, Hendriksen BLM, Robach O, Bobaru SC, Popa I, Quiros C, Kim H, Hammer B, Ferrer S, Frenken JWM (2005) Structure and reactivity of surface oxides on Pt(110) during catalytic CO oxidation. Phys Rev Lett 95(25):255505. doi:10.1103/PhysRevLett.95.255505

31. Butcher DR, Grass ME, Zeng ZH, Aksoy F, Bluhm H, Li WX, Mun BS, Somorjai GA, Liu Z (2011) In situ oxidation study of Pt(110) and its interaction with CO. J Am Chem Soc 133(50):20319–20325. doi:10.1021/ja207261s
32. Li WX, Osterlund L, Vestergaard EK, Vang RT, Matthiesen J, Pedersen TM, Laegsgaard E, Hammer B, Besenbacher F (2004) Oxidation of Pt(110). Phys Rev Lett 93(14):146104. doi:10.1103/PhysRevLett.93.146104
33. Pedersen TM, Li WX, Hammer B (2006) Structure and activity of oxidized Pt(110) and alpha-PtO2. Phys Chem Chem Phys 8(13):1566–1574. doi:10.1039/b515166j
34. Gustafson J, Mikkelsen A, Borg M, Lundgren E, Kohler L, Kresse G, Schmid M, Varga P, Yuhara J, Torrelles X, Quiros C, Andersen JN (2004) Self-limited growth of a thin oxide layer on Rh(111). Phys Rev Lett 92(12):126102. doi:10.1103/PhysRevLett.92.126102
35. Gustafson J, Mikkelsen A, Borg M, Andersen JN, Lundgren E, Klein C, Hofer W, Schmid M, Varga P, Kohler L, Kresse G, Kasper N, Stierle A, Dosch H (2005) Structure of a thin oxide film on Rh(100). Phys Rev B 71(11):115442. doi:10.1103/PhysRevB.71.115442
36. Dri C, Africh C, Esch F, Comelli G, Dubay O, Kohler L, Mittendorfer F, Kresse G, Dudin P, Kiskinova M (2006) Initial oxidation of the Rh(110) surface: ordered adsorption and surface oxide structures. J Chem Phys 125(9):094701. doi:10.1063/1.2345058
37. Westerstrom R, Wang JG, Ackermann MD, Gustafson J, Resta A, Mikkelsen A, Andersen JN, Lundgren E, Balmes O, Torrelles X, Frenken JWM, Hammer B (2008) Structure and reactivity of a model catalyst alloy under realistic conditions. J Phys Condens Matter 20(18):184018. doi:10.1088/0953-8984/20/18/184018
38. Mittendorfer F, Seriani N, Dubay O, Kresse G (2007) Morphology of mesoscopic Rh and Pd nanoparticles under oxidizing conditions. Phys Rev B 76(23):233413. doi:10.1103/PhysRevB.76.233413
39. Nolte P, Stierle A, Jin-Phillipp NY, Kasper N, Schulli TU, Dosch H (2008) Shape changes of supported Rh nanoparticles during oxidation and reduction cycles. Science 321(5896):1654–1658. doi:10.1126/science.1160845
40. Gustafson J, Westerstroem R, Mikkelsen A, Torrelles X, Balmes O, Bovet N, Andersen JN, Baddeley CJ, Lundgren E (2008) Sensitivity of catalysis to surface structure: the example of CO oxidation on Rh under realistic conditions. Phys Rev B 78(4):045423. doi:10.1103/PhysRevB.78.045423
41. Gustafson J, Westerstrom R, Resta A, Mikkelsen A, Andersen JN, Balmes O, Torrelles X, Schmid M, Varga P, Hammer B, Kresse G, Baddeley CJ, Lundgren E (2009) Structure and catalytic reactivity of Rh oxides. Catal Today 145(3–4):227–235. doi:10.1016/j.cattod.2008.11.011
42. He YB, Stierle A, Li WX, Farkas A, Kasper N, Over H (2008) Oxidation of Ir(111): from O-Ir-O trilayer to bulk oxide formation. J Phys Chem C 112(31):11946–11953. doi:10.1021/jp803607y
43. Lundgren E, Gustafson J, Mikkelsen A, Andersen JN, Stierle A, Dosch H, Todorova M, Rogal J, Reuter K, Scheffler M (2004) Kinetic hindrance during the initial oxidation of Pd(100) at ambient pressures. Phys Rev Lett 92(4):046101. doi:10.1103/PhysRevLett.92.046101
44. Hendriksen BLM, Bobaru SC, Frenken JWM (2004) Oscillatory CO oxidation on Pd(100) studied with in situ scanning tunneling microscopy. Surf Sci 552(1–3):229–242. doi:10.1016/j.susc.2004.01.025
45. Lundgren E, Mikkelsen A, Andersen JN, Kresse G, Schmid M, Varga P (2006) Surface oxides on close-packed surfaces of late transition metals. J Phys Condens Matter 18(30):R481–R499. doi:10.1088/0953-8984/18/30/r01
46. Westerstrom R, Weststrate CJ, Gustafson J, Mikkelsen A, Schnadt J, Andersen JN, Lundgren E, Seriani N, Mittendorfer F, Kresse G, Stierle A (2009) Lack of surface oxide layers and facile bulk oxide formation on Pd(110). Phys Rev B 80(12):125431. doi:10.1103/PhysRevB.80.125431
47. Nolte P, Stierle A, Kasper N, Jin-Phillipp NY, Reichert H, Ruhm A, Okasinski J, Dosch H, Schoder S (2008) Combinatorial high-energy x-ray microbeam study of the size-dependent oxidation of Pd nanoparticles on MgO(100). Phys Rev B 77(11):115444. doi:10.1103/PhysRevB.77.115444

48. Kasper N, Stierle A, Nolte P, Jin-Phillipp Y, Wagner T, de Oteyza DG, Dosch H (2006) In situ oxidation study of MgO(100) supported Pd nanoparticles. Surf Sci 600(14):2860–2867. doi:10.1016/j.susc.2006.05.030
49. van Rijn R, Balmes O, Resta A, Wermeille D, Westerstrom R, Gustafson J, Felici R, Lundgren E, Frenken JWM (2011) Surface structure and reactivity of Pd(100) during CO oxidation near ambient pressures. Phys Chem Chem Phys 13(29):13167–13171. doi:10.1039/c1cp20989b
50. Stierle A, Kasper N, Dosch H, Lundgren E, Gustafson J, Mikkelsen A, Andersen JN (2005) Surface x-ray study of the structure and morphology of the oxidized Pd(001) surface. J Chem Phys 122(4):044706. doi:10.1063/1.1834491
51. Ketteler G, Ogletree DF, Bluhm H, Liu HJ, Hebenstreit ELD, Salmeron M (2005) In situ spectroscopic study of the oxidation and reduction of Pd(111). J Am Chem Soc 127(51):18269–18273. doi:10.1021/ja055754y
52. Grass ME, Zhang YW, Butcher DR, Park JY, Li YM, Bluhm H, Bratlie KM, Zhang TF, Somorjai GA (2008) A reactive oxide overlayer on rhodium nanoparticles during CO oxidation and its size dependence studied by in situ ambient-pressure X-ray photoelectron spectroscopy. Angew Chem Int Ed 47(46):8893–8896. doi:10.1002/anie.200803574
53. Joo SH, Park JY, Renzas JR, Butcher DR, Huang WY, Somorjai GA (2010) Size effect of ruthenium nanoparticles in catalytic carbon monoxide oxidation. Nano Lett 10(7):2709–2713. doi:10.1021/nl101700j
54. Ackermann M, Robach O, Walker C, Quiros C, Isern H, Ferrer S (2004) Hydrogenation of carbon monoxide on Ni(111) investigated with surface X-ray diffraction at atmospheric pressure. Surf Sci 557(1–3):21–30. doi:10.1016/j.susc.2004.03.061
55. Lauritsen JV, Helveg S, Laegsgaard E, Stensgaard I, Clausen BS, Topsoe H, Besenbacher E (2001) Atomic-scale structure of Co-Mo-S nanoclusters in hydrotreating catalysts. J Catal 197(1):1–5. doi:10.1006/jcat.2000.3088
56. Vattuone L, Savio L, Rocca M (2008) Bridging the structure gap: chemistry of nanostructured surfaces at well-defined defects. Surf Sci Rep 63(3):101–168. doi:10.1016/j.surfrep.2007.11.001
57. Dahl S, Logadottir A, Egeberg RC, Larsen JH, Chorkendorff I, Tornqvist E, Norskov JK (1999) Role of steps in N-2 activation on Ru(0001). Phys Rev Lett 83(9):1814–1817. doi:10.1103/PhysRevLett.83.1814
58. Engbaek J, Lytken O, Nielsen JH, Chorkendorff L (2008) CO dissociation on Ni: the effect of steps and of nickel carbonyl. Surf Sci 602(3):733–743. doi:10.1016/j.susc.2007.12.008
59. Vang RT, Honkala K, Dahl S, Vestergaard EK, Schnadt J, Laegsgaard E, Clausen BS, Norskov JK, Besenbacher F (2005) Controlling the catalytic bond-breaking selectivity of Ni surfaces by step blocking. Nat Mater 4(2):160–162. doi:10.1038/nmat1311
60. Vang RT, Honkala K, Dahl S, Vestergaard EK, Schnadt J, Laegsgaard E, Clausen BS, Norskov JK, Besenbacher F (2006) Ethylene dissociation on flat and stepped Ni(111): a combined STM and DFT study. Surf Sci 600(1):66–77. doi:10.1016/j.susc.2005.10.006
61. Thostrup P, Christoffersen E, Lorensen HT, Jacobsen KW, Besenbacher F, Norskov JK (2001) Adsorption-induced step formation. Phys Rev Lett 87(12):126102. doi:10.1103/PhysRevLett.87.126102
62. Thostrup P, Vestergaard EK, An T, Laegsgaard E, Besenbacher F (2003) CO-induced restructuring of Pt(110)-(1×2): Bridging the pressure gap with high-pressure scanning tunneling microscopy. J Chem Phys 118(8):3724–3730. doi:10.1063/1.1540611
63. Gritsch T, Coulman D, Behm RJ, Ertl G (1989) Mechanism of the CO-induced 1×2→1×1 structural transformation of PT(110). Phys Rev Lett 63(10):1086–1089. doi:10.1103/PhysRevLett.63.1086
64. Longwitz SR, Schnadt J, Vestergaard EK, Vang RT, Laegsgaard E, Stensgaard I, Brune H, Besenbacher F (2004) High coverage structures of carbon monoxide adsorbed on Pt(111) studied by high pressure scanning tunneling microscopy. J Phys Chem B 108(38):14497–14502. doi:10.1021/jp0492218
65. Tao F, Dag S, Wang LW, Liu Z, Butcher DR, Bluhm H, Salmeron M, Somorjai GA (2010) Break up of stepped platinum catalyst surfaces by high CO coverage. Science 327(5967):850–853. doi:10.1126/science.1182122

66. Tao F, Dag S, Wang LW, Liu Z, Butcher DR, Salmeron M, Somorjai GA (2009) Restructuring of hex-Pt(100) under CO gas environments: formation of 2-D nanoclusters. Nano Lett 9(5):2167–2171. doi:10.1021/nl900809u
67. Besenbacher F, Thostrup P, Salmeron M (2012) The structure and reactivity of surfaces revealed by scanning tunneling microscopy. MRS Bull 37(7):677–681. doi:10.1557/mrs.2012.142
68. Wang JG, Li WX, Borg M, Gustafson J, Mikkelsen A, Pedersen TM, Lundgren E, Weissenrieder J, Klikovits J, Schmid M, Hammer B, Andersen JN (2005) One-dimensional PtO_2 at Pt steps: formation and reaction with CO. Phys Rev Lett 95(25):256102. doi:10.1103/PhysRevLett.95.256102
69. Gustafson J, Resta A, Mikkelsen A, Westerstrom R, Andersen JN, Lundgren E, Weissenrieder J, Schmid M, Varga P, Kasper N, Torrelles X, Ferrer S, Mittendorfer F, Kresse G (2006) Oxygen-induced step bunching and faceting of Rh(553): experiment and ab initio calculations. Phys Rev B 74(3):035401. doi:10.1103/PhysRevB.74.035401
70. Klikovits J, Schmid M, Merte LR, Varga P, Westerstrom R, Resta A, Andersen JN, Gustafson J, Mikkelsen A, Lundgren E, Mittendorfer F, Kresse G (2008) Step-orientation-dependent oxidation: from 1D to 2D oxides. Phys Rev Lett 101(26):266104. doi:10.1103/PhysRevLett.101.266104
71. Westerstrom R, Gustafson J, Resta A, Mikkelsen A, Andersen JN, Lundgren E, Seriani N, Mittendorfer F, Schmid M, Klikovits J, Varga P, Ackermann MD, Frenken JWM, Kasper N, Stierle A (2007) Oxidation of Pd(553): from ultrahigh vacuum to atmospheric pressure. Phys Rev B 76(15):155410. doi:10.1103/PhysRevB.76.155410
72. Hendriksen BLM, Ackermann MD, van Rijn R, Stoltz D, Popa I, Balmes O, Resta A, Wermeille D, Felici R, Ferrer S, Frenken JWM (2010) The role of steps in surface catalysis and reaction oscillations. Nat Chem 2(9):730–734. doi:10.1038/nchem.728

Chapter 9
The Development of Ambient Pressure X-Ray Photoelectron Spectroscopy and Its Application to Surface Science

Bongjin Simon Mun, Hiroshi Kondoh, Zhi Liu,
Phil N. Ross Jr., and Zahid Hussain

9.1 The Brief History of Ambient Pressure X-Ray Photoelectron Spectroscopy

In the community of nano-science, the so-called material gap has been one of the most important issues. The physical/chemical properties of nanoscale materials can be very different from those of bulk, even micron-scale materials, and it is crucial to understand how the characteristics of nano-materials can be related to those of bigger sized materials. In doing so, the unique functionalities of nano-materials can be fully utilized and the larger scale applications of these materials can be realized [1–3]. This effort, "bridging the material gap," has been constantly pushed forward and the community of nano-science research has made the significant progress with numerous advanced experimental tools and innovating ideas. Yet, there are still many challenges to be addressed in understanding how to build the bridge over this material gap.

On the other hand, in the community of surface science, another very well-known gap has existed for a long period of time, i.e., "pressure gap." Since the early days of surface science, the importance of surface characterization under elevated pressure has been realized. Traditionally, the most experimental researches in surface

---

B.S. Mun (✉)
Department of Physics and Photon Science, School of Physics and Chemistry,
Gwangju Institute of Science and Technology, Gwangju 500-712, South Korea
e-mail: bsmun@gist.ac.kr

H. Kondoh
Department of Chemistry, Keio University, Yokohama, Japan

Z. Liu • Z. Hussain
Advanced Light Source, Lawrence Berkeley National Laboratory, Berkeley, CA, USA

P.N. Ross Jr.
Material Science Division, Lawrence Berkeley National Laboratory, Berkeley, CA, USA

J.Y. Park (ed.), *Current Trends of Surface Science and Catalysis*,
DOI 10.1007/978-1-4614-8742-5_9, © Springer Science+Business Media New York 2014

science have been based on UHV model systems that enable one to look at the controlled surface under clean environment. Upon obtaining the precise physical and chemical properties under in situ model system, the results of model system are extrapolated and compared to the results of ex situ studies carried under elevated pressure condition. However, there have been many arguments and discussions over the interpretation of UHV results to those of high-pressure condition. The main focus of its argument is that what is happening in real world at atmospheric or higher pressure condition can be very different from those of model system. In 1978, in the early days of surface science, G. Somorjai mentioned, “New surface tools that can be operated under elevated pressure will disclose the underlying mechanism of surface catalysis” [4, 5]. Unfortunately, if one would like to look at the liquid–solid or liquid–gas interface, there are only few experimental tools available in surface science. As a typical example, in the community of electrochemistry, the information of liquid–solid interfacial layer under reaction conditions is very important, yet the direct observation of interfacial properties under electrochemical reaction condition has not been made. Similar to the case of bridging the material gap, there are also many challenges and difficulties in bridging pressure gap largely due to the limitations of current experimental techniques and theoretical understanding.

Among many important surface science tools, a soft X-ray photoelectron spectroscopy (XPS) has been one of the most popular choices in studying physical and chemical properties of surface, providing the element-specific, nondestructive, and quantitative information. As well known, the fundamental principle of XPS is based on Einstein’s photoelectric effect, i.e., photon-in and electron-out.

$$E_{Kineticenergy} = E_{Photonenergy} - E_{Bindingenergy} - Work\,function$$

When the photo-excited electrons from surface are collected as a function of its kinetic energy with specified photon energy, the binding energy of the electrons can be easily calculated, generating the information of chemical elements on the surface. In 1969, K. Sighbahn developed first XPS and reported the discovery of chemical shifts of elements on surface [6]. Later, in 1984, Nobel Prize was awarded to K. Sighbahn for the pioneering research on the development of XPS. The invention of XPS was an immediate success. The community of physics and chemistry, especially in the field of surface science, realized its potential use and continued its development for advanced uses in many basic sciences and practical applications. There are many good review papers and books available for XPS and its applications [7–11].

In general, XPS is known as a spectroscopic tool for providing precise chemical environment near surface layers. With the proper selections of photon energy, the polarization of photon, and the detection angles of electron, XPS can easily provide the complete “surface-sensitive” physical and chemical properties of surface, including electronic band structures and magnetic properties. In addition, XPS is one of a few tools that can directly map out both the localized (core-level) and delocalized (valence band level) atomic orbital in a *nondestructive* manner. Recently, the performance of the electron spectrometer has been significantly improved, which includes the energy resolution, the angle-resolving power, and time-resolved capability. For example, the spectral energy resolution of below meV can be routinely achieved, i.e., <0.001 eV [12].

One of the important characteristics of XPS is the extreme surface sensitivity. Intrinsically, electron has very short inelastic mean free path (IMFP) and only electrons near surface can be come off [13, 14]. Also, in most cases, the photon energy used in XPS is in the range of soft X-ray, i.e., below ~2.0 keV, and the inelastic mean free path below this energy is less than ~20 A. That is, a major contributing factor of XPS information is originating from a few top surface layers, suggesting XPS as an ideal spectroscopic tool for the investigation of surface properties [13, 14]. On the other hand, this short IMFP of electron creates a critical limitation over practical applications of XPS, generating the significant *pressure gap* in its application. Under the elevated pressure of gas environment, these photo-excited electrons from surface undergo many elastic and inelastic scattering with gas-phase molecules before reaching to the electron analyzer, which makes the use of XPS difficult under the high-pressure condition. In practical sense, it becomes very difficult to run XPS under the pressure 10^{-6} Torr or higher without any special equipment. Additionally, all of the electron energy analyzer uses the carbon-based electron amplification devices, e.g., channeltron or channelplate, which can only be functioning under UHV condition. For these two critical reasons, the operation of XPS always requires the UHV condition. Consequently, the in situ study of any system involves liquid or high pressure of gas phase cannot be adapted to XPS.

That is, the properties of liquid/solid or gas/liquid interfaces cannot be investigated properly with XPS. On the other hand, in case of using “photon-in and photon-out” techniques, e.g., sum frequency generation (SFG) spectroscopy [15] or polarization modulation infrared reflection-absorption spectroscopy (PM-IRAS) [16, 17], it is possible to look into various surfaces and interfaces under elevated pressure condition or even reaction conditions, including liquid/solid interface. However, the interpretation of its result is often not straightforward, and it often requires the advanced understanding to extract information, e.g., the difficulty in quantitative analysis.

Since the early days of XPS development, the effort of running XPS under elevated pressure condition had been continuously made. The Siegbahn group in Sweden, the same group invented XPS for the first time, adapted the concept of differential pumping scheme to the operation of XPS and obtained XP spectra of gas phase or liquid on solid system under the pressures of few mTorr [18–20]. The schematic of their first ambient pressure X-ray photoelectron spectroscopy (AP-XPS) is shown in Fig. 9.1. Later, the similar concept of the design in Fig. 9.1 was implemented by several other groups to build the similar electron spectrometers that can be run at elevated pressure environment [21–25]. However, these early AP-XP spectrometers were never fully utilized or adopted by the photoemission community mainly due to the low count rate of detected electrons with poor signal-to-noise ratio.

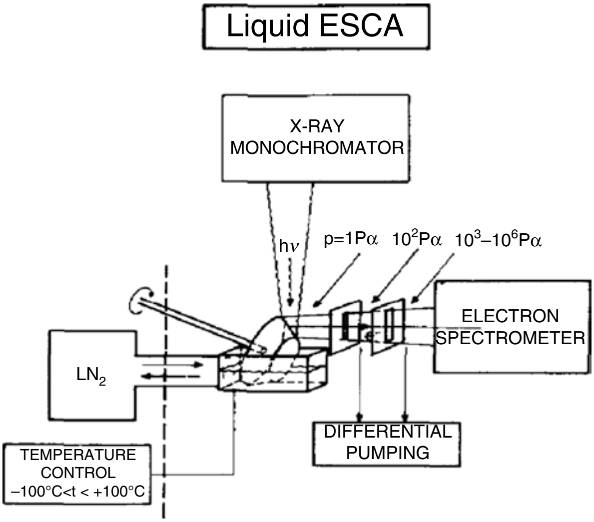

Fig. 9.1 The schematic of first liquid electron spectroscopy of chemical analysis (ESCA) designed by the Siegbahn group. Reproduced from refs. [18–20]

9.2 The First Development of Synchrotron-Based AP-XPS at ALS

In early 2002, the group in Lawrence Berkeley National Laboratory initiated the project of developing AP-XPS with new concepts of design [26]. The Berkeley group utilized the high-flux synchrotron radiation as excitation photon source and implemented the so-called differential-pumped electrostatic lens system for delivering electrons to analyzer under elevated pressure conditions. As shown in Fig. 9.2, the chamber is composed of three units, the high-pressure sample cell, the electrostatic lens system with differential pumping system, and the electron analyzer. The X-ray is delivered to the sample via beam transport line attached to the high-pressure cell. At the end of this transport line, a thin SiN or Al window (thickness 0.1 μm) is attached so that the high pressure of gas can be maintained inside of cell while the beamline remaining under UHV condition. The photoelectrons generated under the elevated pressure are collected through the electrostatic lens system which also works as the differential pumping stage.

The idea of using this *differential-pumped electrostatic lens system* is (a) to capture the electrons as soon as possible while pumping out the gas of the cell, i.e., minimizing the collisions of electrons with gas molecules, and (b) to increase the detection efficiency of analyzer, i.e., focusing the electrons to the center optical axis of electron analyzer. When the gas is being pumped out in a small diameter of front nozzle, a supersonic jet can be created along the line of electron trajectory, which can deteriorate the performance of AP-XPS. In order to avoid this unwanted jet flows of the gas, the proper lens tables need to be calculated with adequate electrostatic lens design. Also, it was necessary to have ample space of the first pumping

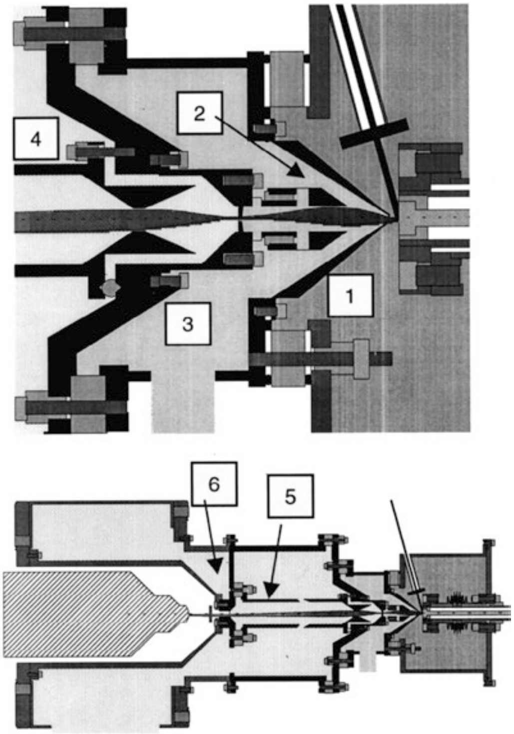

Fig. 9.2 The schematics of AP-XPS developed at Lawrence Berkeley National Laboratory. Lens elements: (*1*) nozzle, (*2*) control, (*3*) skimmer, (*4*) condenser, (*5*) quadrupole, (*6*) exit aperture. Reproduced from ref. [26]

stage, located at immediately after the front nozzle, for efficient pumping performance. The design of effective electrostatic lens system with the efficient differential pumping system is the most critical part of AP-XPS design. The maximum operating pressure can be also increased by adjusting the size of nozzle in the front nozzle and reducing the distance between the sample and the first lens. However, this requires precise beam alignment between analyzer and synchrotron radiation source. The performance of first AP-XPS at Berkeley Lab was so successful that the community of XPS started to respond with great interests. Immediately after success of the first AP-XPS at Berkeley Lab, the developments of the next AP-XPS have followed not only to enhance its functionality but also to make more user-friendly system [27]. In 2005, the second generation of AP-XPS was fabricated with help of *Specs* Inc., and two endstations were commissioned in separate synchrotron radiation facilities, ALS in Berkeley and BESSY in Berlin. The details of the design parameters and their functionality of this analyzer can be found in following review papers [28]. Now, by early year 2013, most of major synchrotron light sources have installed the AP-XPS endstations, e.g., SOLEIL in France, ALBA in Spain, and Photon Factory in Japan. In this chapter, two recent AP-XPS systems will be discussed, one installed at ALS in Berkeley and the other installed at KEK-Photon Factory in Japan.

9.3 AP-XPS at ALS

In 2010, a new AP-XPS system was developed at ALS in Berkeley, named as HiPP (*Hi*gh-*P*ressure *P*hotoemission Analyzer) in VG-Scienta Inc. The basic working principle of the HiPP system is similar as the first AP-XPS system in Berkeley, and the design and its construction of this new system are carried out as the collaboration efforts between VG-Scienta and ALS [29, 30]. The HiPP analyzer system is equipped with many additional features including one-dimension imaging mode, angle resolved detection mode, and highly efficient data acquisition process, shown in Fig. 9.3. Compared to previous system, the HiPP is equipped with many additional features including one-dimension imaging mode, angle resolved detection mode, and highly efficient data acquisition process. Also, collecting low kinetic energy electrons, e.g., as low as 50 eV, under elevated pressure condition was possible in this system.

In the development of R4000 HiPP system, a special care was given to the design of pre-lens system with differential pumping chamber. First, to maximize the efficiency of count rate under elevated pressure condition, gas dynamics near pre-lens system is calculated with Monte Carlo methods, which helped to improve the performance of differential pumping system without high-voltage breakdown under elevated gas pressure. In Fig. 9.4, the gas dynamic simulation shows that the pressure distribution near sample surface regions and the areas of pre-lens components

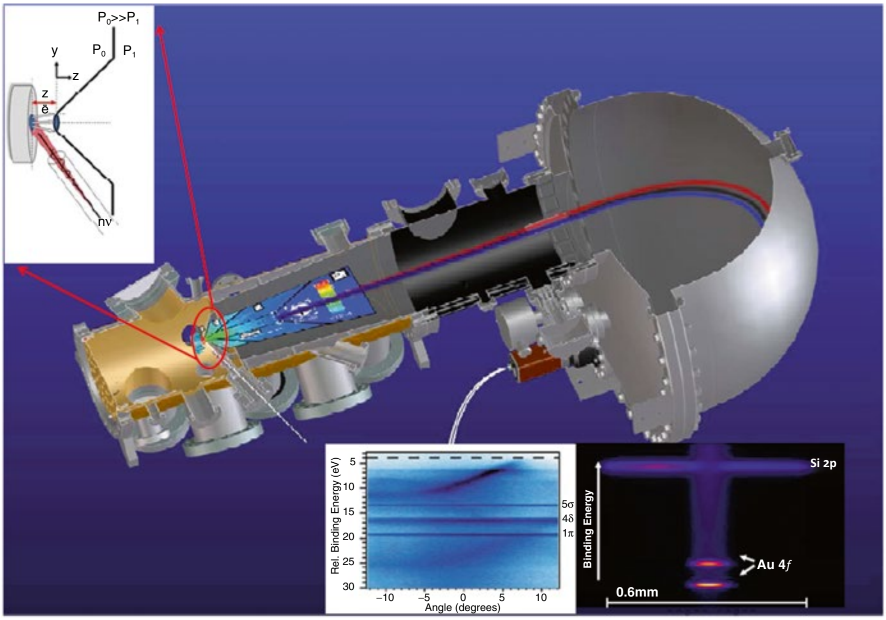

Fig. 9.3 The sectional view of HiPP with two-dimensional detector system of HiPP. The *bottom left insert* shows the angle resolved mode while the *bottom right inset* shows one-dimensional spatially resolved mode. (*Inset*: The geometric configuration near sample surface and first nozzle.) Reproduced from ref. [30]

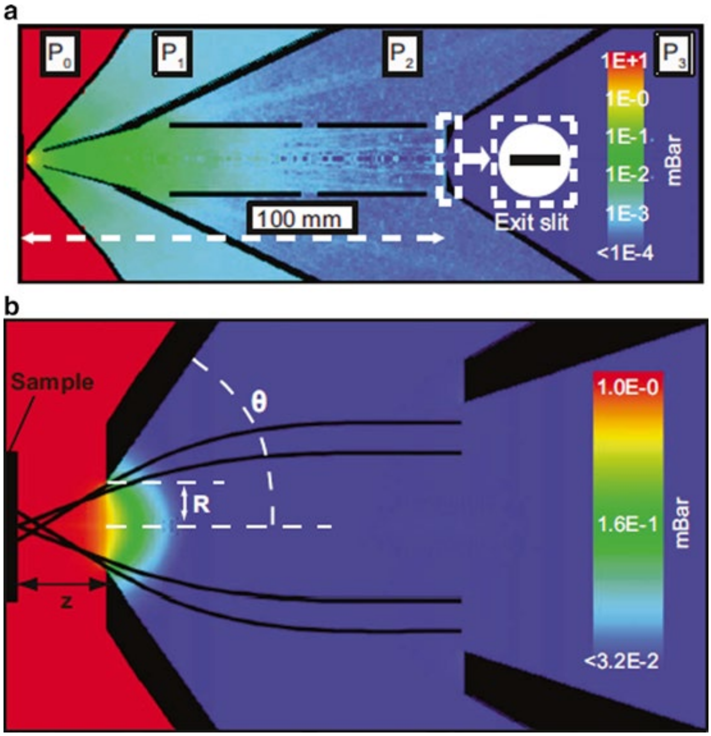

Fig. 9.4 Gas dynamic simulation based on Monte Carlo methods displays the efficient performance of differential pumping near pre-lens elements. (**a**) Calculated pressure distribution across the pre-lens system. (P_0 = pressure region in sample, $P_{1,2,3}$ = pressure region in each differential pumping regions.) (**b**) Calculated pressure distribution near sample surface and first pre-lens system. Reproduced from ref. [29]

exhibit efficient pumping performance; the pressure difference between the sample surface area and the first lens component is ~2 orders of magnitude.

As mentioned above, the effective differential pumping capability near first lens system plays important role in improving the detection efficiency of electrons, which in turn enhance the transmission of analyzer. Next, with improved electron lens table of analyzer and pre-lens, it was possible to achieve both spatially resolved XPS as well as angle resolved photoemission spectra without moving sample position. Under the improved electron lens system with μ-metal shielded chamber, it was possible to measure both one dimensional chemical imaging similar to PEEM and band dispersion from angle resolved mode, was possible without moving a sample. In R4000 electron analyzer, it is possible to capture two-dimensional information, one axis for electron energy and the other for take-off angle of electron from surface (i.e., angle resolved mode or ARPES) or spatial distribution of outgoing electron (i.e., spatially resolved mode), displayed in inset of Fig. 9.3. In either case, the operating principle is similar; the focal point of electron analyzer on sample surface and lens voltage tables are adjusted so that either angular or spatial information from surface is delivered to the electron detector. In HiPP, it was possible to record spatially

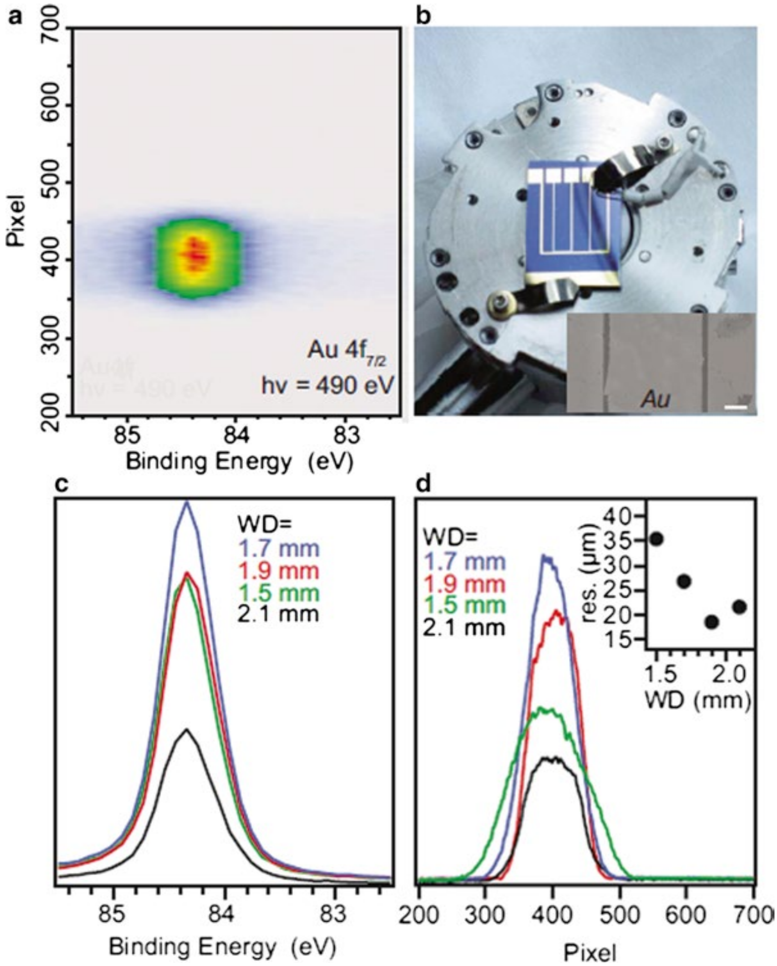

Fig. 9.5 (**a**) CCD image of Au $4f_{7/2}$ region of a 100 μm Au bar on SiO_2 using spatial resolved mode, (**b**) a picture image of sample tested, and (**c**, **d**) PE spectra and spatial uniformity across space direction, respectively, as a function of working distance. The *inset* of (**d**) shows the spatial resolution (20 μm) as a working distance. Reproduced from ref. [29]

resolved XPS in single-dimension with resolution down to 20 μm with the fine adjustment of lens table and the distance between sample and first pre-lens. Figure 9.5 shows the CCD images on the detector and its XPS spectra from a 100 μm Au bar on SiO_2. Figure 9.5c, d shows the degrees of uniformity and spatial resolution as a function of working distance, i.e., the distance from sample surface to pre-lens cone.

The magnification factor was recalibrated with sample images from microscope. This spatially resolving capability can be extremely useful when the in situ characterization of surface chemical distribution is required. In the case of ARPES mode, the dimension of previous spatial distribution information is now replaced with the

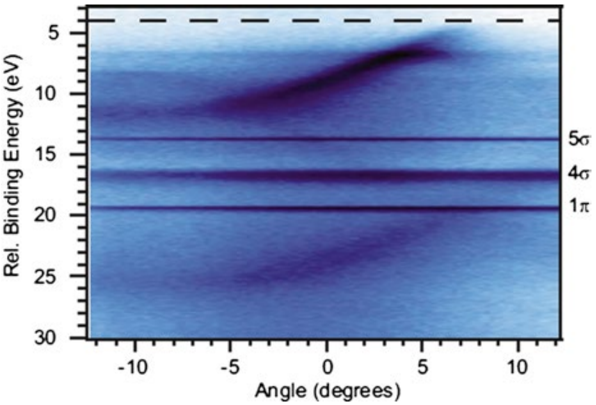

Fig. 9.6 Angle resolved AP-XPS spectra of HOPG under 0.25 mbar CO gas. Reproduced from ref. [29]

take-off angle information. Again, with careful tuning of electron lens table and optimizing sample working distance, ARPES was possible, shown in Fig. 9.6. The ARPES images of Fig. 9.6 were taken at 0.25 mbar CO gas with photon energy of 120 eV. So, the previous spatial information axis is now replaced with take-off angle information, i.e., in-plane momentum *k*. While three non-dispersive features can be clearly seen from gas phase of CO, the dispersion of HOPG graphite can be well resolved. Those non-dispersive features at 9.5, 12.5, and 15.3 eV (referenced to the Fermi level) are due to 5σ, 1π, and 4σ orbitals photoemission from gas phase, which is expected in the case of gas phase. The capability of ARPES adds a significant advancement in the development of AP-XPS and opens up a new window of opportunity for studying surface electronic structures under reaction conditions.

9.4 AP-XPS at Photon Factory

At the Photon Factory, several soft X-ray beamlines are available for ambient pressure XPS experiments via a free port. Taking advantage of this merit, the AP-XPS system was designed as a compact and transportable apparatus as shown in Fig. 9.7. The AP-XPS system consists of three vacuum chambers (analysis chamber, preparation chamber, and exchange chamber) which are all fixed on a single base frame. At the base frame three precise screw jacks are also fixed to adjust the height and the tilt angle of the apparatus. The bottoms of the three jacks are mounted on a sliding base in such a way that the horizontal position and the rotation of the apparatus can be adjusted.

With these features the alignment of the apparatus relative to the X-ray beam can be achieved within 30 min after transfer from one beamline to another one. At the moment three soft X-ray beamlines with different specifications are available for AP-XPS experiments at the Photon Factory: BL-7A (bending-magnet beamline with a VLSG monochromator covering photon energies of 100–1,500 eV), BL-13A (undulator beamline, VLSG, 30–1,200 eV), and BL-16A (variable-polarization undulator beamline with a fast polarization switching ability, VLSG, 100–1,500 eV).

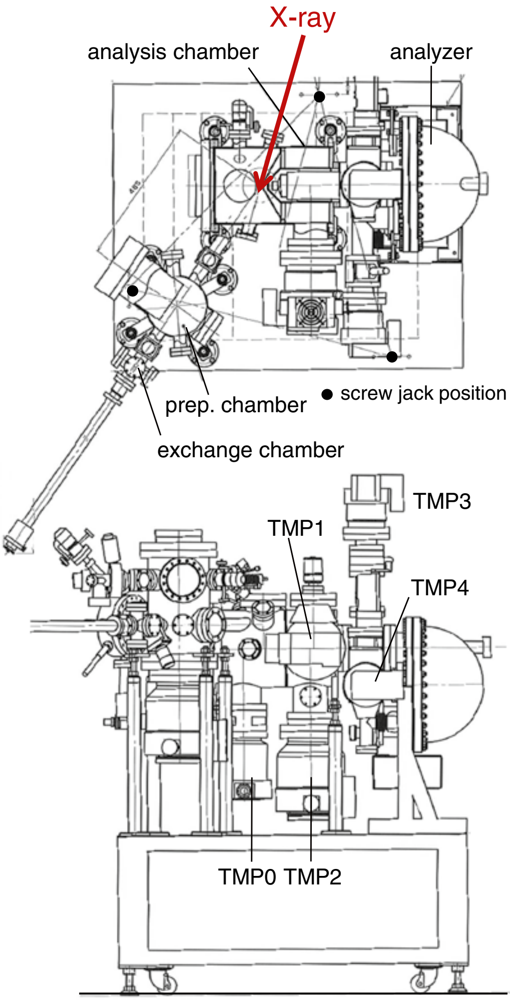

Fig. 9.7 Drawing of the transportable ambient pressure XPS apparatus consisting of three vacuum chambers

Figure 9.8 shows a schematic drawing of the analysis chamber which is evacuated by a differential pumping system. This is consisting of two separated stages pumped with turbo molecular pumps with pumping speeds of 500 L/s for the first stage and 700 L/s for the second stage. A hemispherical electron energy analyzer modified for high-pressure experiments (OMICRON, EA125HP) is mounted to the second differential pumping stage. A quadrupole mass spectrometer (HIDEN, HAL201) is also mounted to the second differential pumping stage to monitor the partial pressures of the reactant and product gases. Just as all other modern AP-XPS, the analyzer has the differential pumping electron lens system, which is separated into two stages via an aperture with 4 mm in diameter. The downstream stage of the electron lens system and the hemispherical chamber are pumped with two turbo molecular pumps with pumping speeds of 210 L/s. The detector of the analyzer is a seven-channeltron array and modified for the externally gated pulse counting which

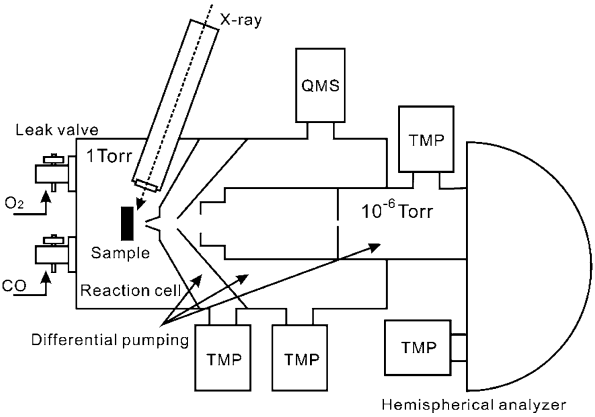

Fig. 9.8 Schematic drawing of the analysis chamber of the AP-XPS system

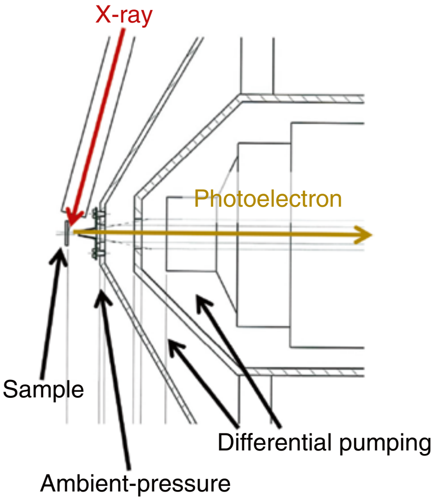

Fig. 9.9 Schematic drawing of the configuration of a sample, the X-ray introduction pipe, the aperture of the differential pumping system, and the entrance of the analyzer lens

enables to switch the TTL output signal from an optical receiver on and off in response to an external gate signal (up to 5 MHz). This will allow us to conduct *pump and probe* experiments with a time resolution of 30 ps when synchronizing with the RF signal of the synchrotron ring under the single-bunch operation mode at the Photon Factory.

The reaction cell is evacuated by a 300 L/s turbo molecular pump and equipped with a sample manipulator with a cryostat, variable leak valves for gas introduction, and a vacuum gauge. The incident X-ray beam is introduced through a 100 nm thick silicon nitride film which separates the beam line and the reaction cell. The sample is irradiated by the X-ray beam with a grazing incidence angle of 15° and emitted photoelectrons travel approximately 1 mm to the entrance of an aperture under near ambient pressure gas and enter the first stage of the differential pumping system via a hole of 1 mm in diameter as illustrated in Fig. 9.9. The electrons further travel

Fig. 9.10 Typical XP spectra measured with the AP-XPS system at the Photon Factory. The data except for the bottom spectrum were recorded for a Pd(100) surface under 0.2 Torr of O_2 at different temperatures. The bottom spectrum was taken for a clean surface under UHV at room temperature

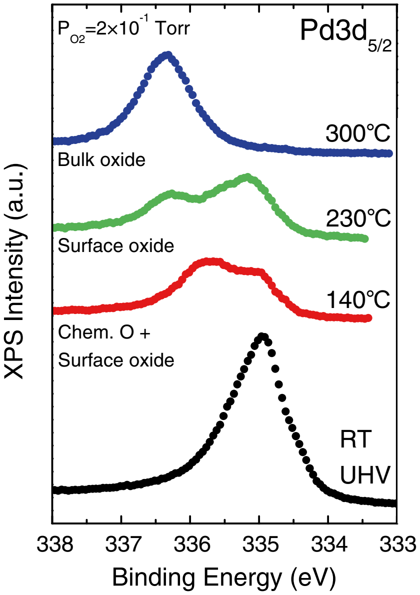

through the differential pumping system and reach the entrance of the analyzer. The distance between the sample surface and the analyzer entrance is 40 mm, which is in accordance with the focusing length of the first electron lens. With this system photoelectrons can be detected under a reaction cell pressure of up to 1 Torr with a collection angle of ±7°. Normally, the sample is spot-welded to a transferable sample holder. The sample holder is heated with a ceramics heater from the backside up to 600 °C under ambient pressure conditions. The temperature is measured using a thermocouple attached to the holder. The distance between the sample and thermocouple is about 4 mm or less. The sample can be cleaned in a preparation chamber under UHV conditions which is connected to the analysis chamber. The gases are introduced to the reaction cell using the variable leak valves with monitoring the partial pressures with the mass spectrometer.

Typical AP-XP spectra taken with this system are shown in Fig. 9.10. These were recorded for a Pd(100) surface under O_2 gas pressure of 0.2 Torr at elevated temperatures. The photon energy used here was 435 eV for Pd $3d_{5/2}$ and hence the kinetic energies of detected photoelectrons were approximately 100 eV. The exposure of the Pd(100) surface to O_2 gas at a near ambient pressure and elevated temperatures induces oxidation of the Pd surface. The oxidation process of Pd(100) surfaces under near ambient pressure conditions has been studied previously using AP-XPS, which reported several high pressure-induced O-containing phases [31]. With current AP-XPS, it was possible to obtain almost the same spectra as those previously reported and confirmed the in situ formation of surface and bulk oxides on the Pd surface under the elevated pressure and temperatures in the analysis chamber.

9.5 Oxidation Study of Transition Metal Single Crystals

9.5.1 CO Oxidation on Pt(110)

Pt has been one of the most well characterized materials due to its distinguished chemical properties and outstanding performance in catalytic reactions [32, 33]. Also, CO oxidation is one of the most standard surface chemical reactions. As a standard model to explain the adsorption and dissociation processes of molecules on Pt surface, Langmuir–Hinselwood (L–H) mechanism has been widely accepted [34]. In L–H mechanism, chemical reactions take place in most efficient manner when the surface remains as clean metallic state. That is, the most reactive surface is metallic surface. For example, in the case of CO oxidation, oxygen molecules make contact to metal surface and get dissociated into surface atomic oxygen. Then, this surface oxygen reacts to CO molecule to form CO_2. During this process, surface remains clean and there is no residue remains on the surface. In the past, many studies of model system under low-pressure experiments have demonstrated the validity of L–H model.

In 2002, the Frenken group from Netherlands has published the study of surface oxides on Pt(110) [35], which has received much attentions due to its unique oscillatory behavior of surface morphology under CO oxidation reaction conditions. With a combined high-pressure scanning tunneling microscope (HP-STM) and mass spectrometer, the group demonstrated the existence of roughening of the Pt(110) surface during CO oxidation at 425 K, pressures near 0.5 bar, and an O_2/CO ratio >45. Under the enhanced CO oxidation condition, the formation of surface roughening is observed, which was interpreted as Pt oxide. Later, the same group confirmed the existence of surface oxide with high-pressure X-ray diffraction and density functional theory (DFT) calculation and claimed that this surface oxide formed during reactive condition was mainly responsible for active catalytic reaction [36]. That is, the CO oxidation under high pressure (~1 bar) and at a high O_2/CO ratio may follow the Mars–van Krevelen (M–vK) mechanism [37] rather than the previously mentioned L–H mechanism [34]. Under M–vK mechanism, the most reactive surface state is a metallic oxide, not a metallic state.

Furthermore, the characteristics of Pt oxide were investigated with DFT calculations under elevated pressure. Li et al. [38] reported the importance of a phase boundary between metal and gas during CO oxidation. It was determined that the surface oxides provided lower activation barriers for the CO redox process, which favors the M–vK mechanism under highly reactive conditions. The explanation of CO oxidation on Pt(110) surface with the M–vK mechanism has stirred up a big discussion among the community of surface science because the L–H mechanism had been widely accepted as a standard model in understanding CO redox mechanism in Pt surface. Immediately after the report of Hendriksen and Frenken [35], many surface science groups around the world started their investigation on this intriguing issue [39, 40]. Notably, the Goodman group in Texas A&M University

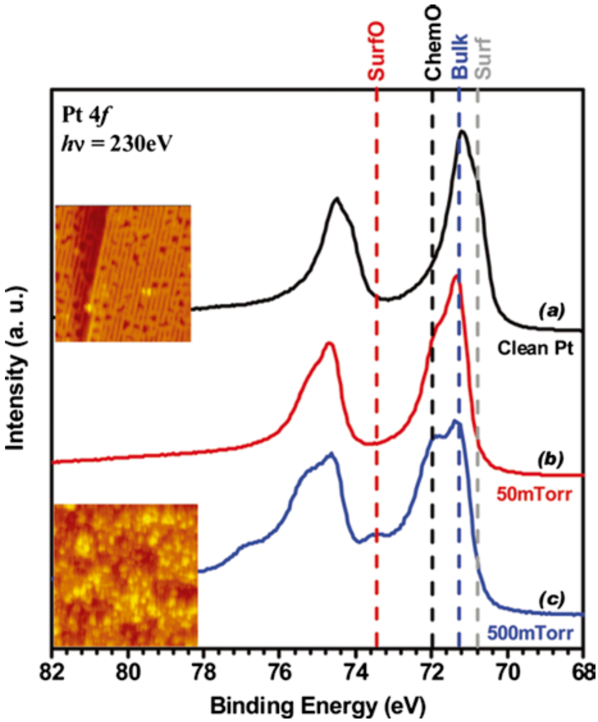

Fig. 9.11 Pt 4*f* spectra taken under various oxygen pressure conditions. The inset shows the images of STM taken under similar pressure conditions of oxygen gas. Reproduced from ref. [41]

approached to this system with application of PM-IRAS and suggested that Pt metallic surface was still active phase under high temperature, in which the CO_2 formation rate was limited either by mass-transfer mechanism on a metallic surface or by the reduced reactivity of the oxidized surface, which was exactly opposite to what the Frenken group reported previously [39].

The group in Berkeley started their own investigation on this issue with applications of AP-XPS, AP-STM, and DFT calculation [41]. Especially, the application of AP-XPS was the ideal choice for resolving this issue since it could provide elemental-specific chemical information of surface under reaction condition. That is, the chemical species from oxide can be directly monitored if there is any presence of oxide under reaction conditions.

In Fig. 9.11, Pt 4*f* XP spectra are shown under various atmospheric conditions, (a) UHV, (b) 50 mTorr of oxygen, and (c) 500 mTorr of oxygen, using R4000 HiPP endstation at ALS. Figure 9.11 shows that surface oxide is not being formed until the pressure of oxygen gas reaches up to 500 mTorr. Under 500 mTorr of oxygen pressure, the surface oxide peak at 73.4 eV started to appear in Pt 4*f* spectra, and STM images also exhibit the roughened surface with nanometer islands under similar conditions, shown together with spectra. In order to identify the surface oxide structures, the depth profile information is achieved by varying the photon excitation energy, i.e., varying the kinetic energy of electrons.

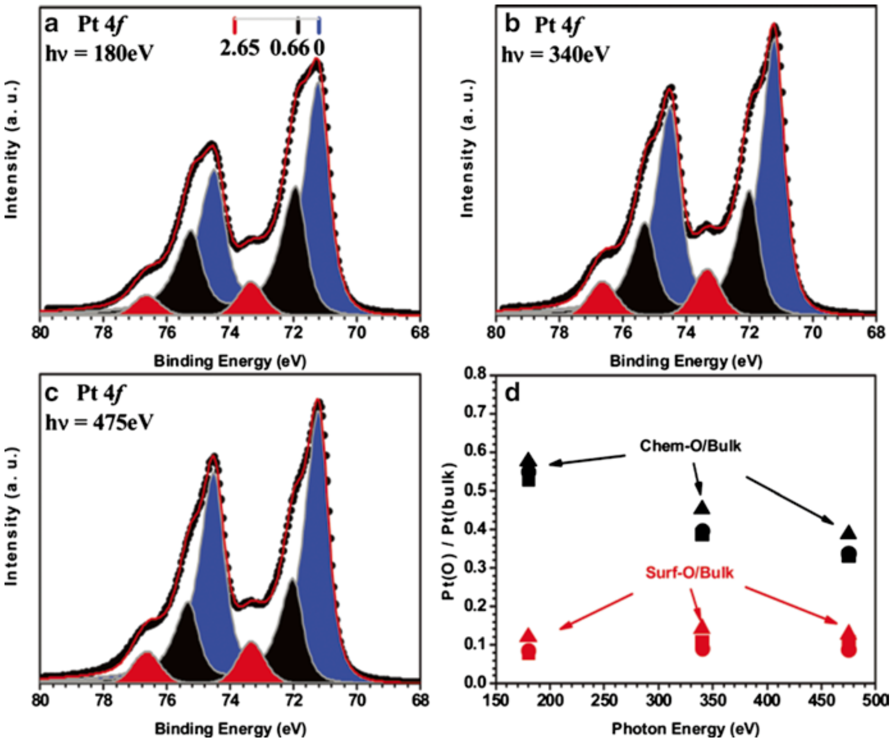

Fig. 9.12 (**a**–**c**) Pt 4*f* spectra taken at various photon energies under 500 mTorr of oxygen. While the bulk component is fitted with *blue*, the chemisorbed and surface oxide is fitted with *black* and *red*, respectively. (**d**) As the photon energy is increased, the ratio of bulk and chemisorbed component drops fast while the surface/bulk component shows little change. Reproduced from ref. [41]

Figure 9.12 shows the Pt 4*f* spectra obtained at 180, 340, and 475 eV under 0.5 Torr of O_2 at 473 K which are shown in (a), (b), and (c), respectively. The fitted curves under the measured spectra of Fig. 9.12a–c represent the bulk Pt component (blue) at 71.2 eV, the chemisorbed oxygen (black) at 71.9 eV, and surface oxide component (red) at 73.4 eV. Also, in Fig. 9.12d, the intensity ratios of Pt(Chem-O)/Pt(bulk) and Pt(Surf-Ox)/Pt(bulk) are plotted as a function of photon energy.

As the photon energy increases, the intensity ratio of Pt(Surf-Ox)/Pt(bulk) remains constant while the one of Pt(Chem-O)/Pt(bulk) shows decrease, which indicates the oxide being formed stays under subsurface layer.

In order to investigate further on the structures and reactivity of surface oxide, DFT model calculations are carried out and their results are compared to the experimental results. Figure 9.13 shows the various surface oxide structures of test models and Table 9.1 displays their comparison to experimental results with the degrees of surface core-level shifts. From this comparison, the measured surface oxide in both AP-XPS and STM matches fairly well with α-PtO_2-like nanoscale surface oxide. Finally, in order to find out the surface reactivity of surface oxide, CO titration

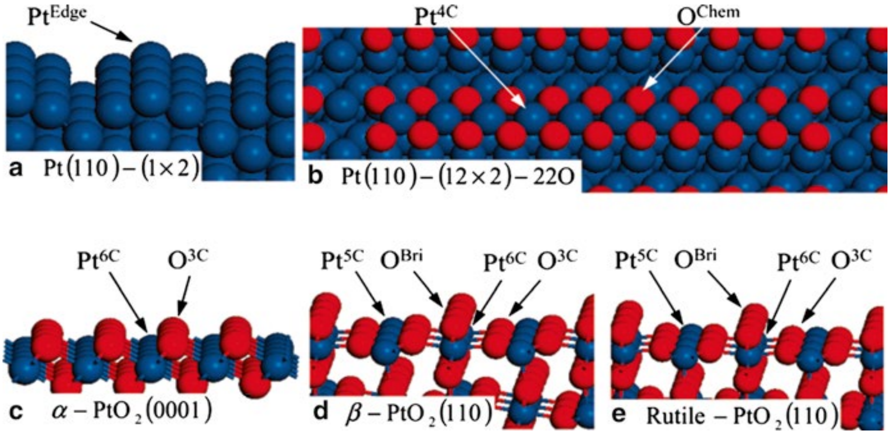

Fig. 9.13 Suggested structures of Pt metal and Pt oxide used for DFT calculations. (**a**) Metal Pt(110)-(1×2) missing row, (**b**) Pt(110)-(12×2)-22O chemisorption, (**c**) **α**-PtO_2(0001), (**d**) β-PtO_2(110), and (**e**) rutile-PtO_2(110) surfaces. Reproduced from ref. [41]

Table 9.1 Calculated Pt 4*f* and O 1*s* CLS (eV) on various clean, reconstructed chemisorption and oxide surfaces

	Pt 4*f* (eV)	O 1*s* (eV)
Pt(110)−(1×2)	−0.42 (Pt^{Edge})	–
Pt(110)−(12×2)−22O	0.66 (Pt^{4C})	−2.40 to −2.60 (O^{Chem})
α−PtO_2(0001)−(2×2)	2.65 (Pt^{6C})	−1.80 (O^{3C})
β−PtO_2(110)−(2×1)	2.25 (Pt^{6C})	−3.98 (O^{Bri})
	1.20 (Pt^{5C})	−2.32 (O^{3C})
rutile PtO_2(110)−(2×1)	2.15 (Pt^{6C})	−4.02 (O^{Bri})
	1.15 (Pt^{5C})	−2.39 (O^{3C})

The energy reference is metallic bulk Pt and O 1*s* of on-top CO on Pt(110)−(1×2) surface. Reproduced from ref. [41]

experiments are carried out, shown in Fig. 9.14. Interestingly, both surface oxide and chemisorbed oxygen show almost similar surface reactivity during the titration test. However, it is not still clear whether O atoms in the α-PtO_2 react directly with CO or if α-PtO_2 destabilized at interfaces with CO-covered Pt and O from this phase decomposes into chemisorbed O on neighboring Pt sites. Further atomic scale analysis in ultrafast time domain will help to resolve this issue.

9.5.2 NO Dissociation on Pt(111) [42]

The adsorption of NO molecules on metal surfaces has attracted attention because it is a simple model system for the catalytic conversion of NO_x species to N_2 by the three-way catalyst for automotive exhaust gases. Three-way catalysts utilize

Fig. 9.14 O and CO coverage of a Pt(110) surface exposed to 500 mTorr O_2, then exposed to 10^{-6} Torr CO at 270 K. Reproduced from ref. [41]

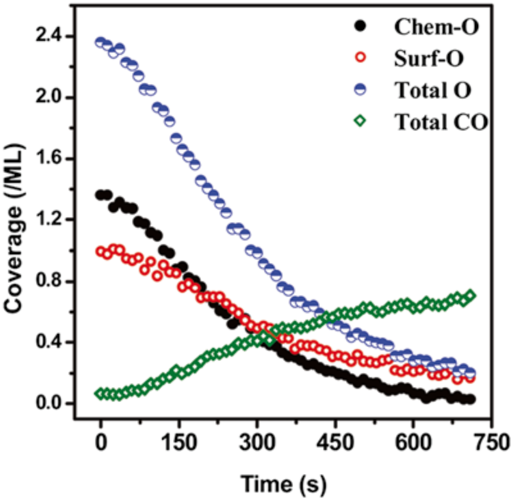

platinum, rhodium, and/or palladium as active metals. It is widely known that NO molecularly adsorbs on Pt(111) without dissociation under UHV conditions, though it readily dissociates on the practical Pt catalyst surfaces. The adsorption structures of NO on Pt(111) have been extensively studied under UHV conditions by STM [43, 44], high-resolution electron energy loss spectroscopy [44], IRAS and low-energy electron diffraction (LEED)-IV analysis [45], DFT calculations [46], XPS [47], and near-edge X-ray absorption fine structure (NEXAFS) [48]. According to these studies, NO molecules sequentially occupy three different sites as increasing coverage. However, the adsorption behavior on such model systems under UHV conditions can often differ from that on practical catalysts under ambient pressure conditions.

To bridge the gap between model surfaces and the practical surfaces, the AP-XPS technique can provide a good opportunity. In this section, the adsorption behavior of NO on Pt(111) from UHV to elevated NO pressure (up to 1 Torr) observed with AP-XPS is presented. It will be evidenced that NO adsorbs at atop sites reversibly at 10^{-7} Torr and irreversible dissociation of NO and formation of NO + O domains occur exclusively at NO pressures higher than 10^{-6} Torr [42].

AP-XPS experiments were performed at the soft X-ray beamline 9.3.2 of the Advanced Light Source, Lawrence Berkeley National Laboratory [49]. AP-XPS measurements were performed at RT and recorded with photon energies of 620 and 635 eV for N 1*s* and O 1*s*, respectively. After cleaning, a Pt(111) sample was transferred to a high-pressure cell for the AP-XPS measurements. Figures 9.15 and 9.16 show N 1*s* and O 1*s* XP spectra of the Pt(111) surface taken under various NO pressures. All the spectra were normalized using the baseline intensity and background subtraction and fitted with asymmetric Gaussian functions. Both of the bottom spectra in Figs. 9.15 and 9.16 were measured under UHV condition at RT after NO exposure of 18 Langmuir (1 Langmuir = 1×10^{-6} Torr s), which is enough to saturate the surface with adsorbed NO. A single asymmetric peak is observed in the N 1*s*

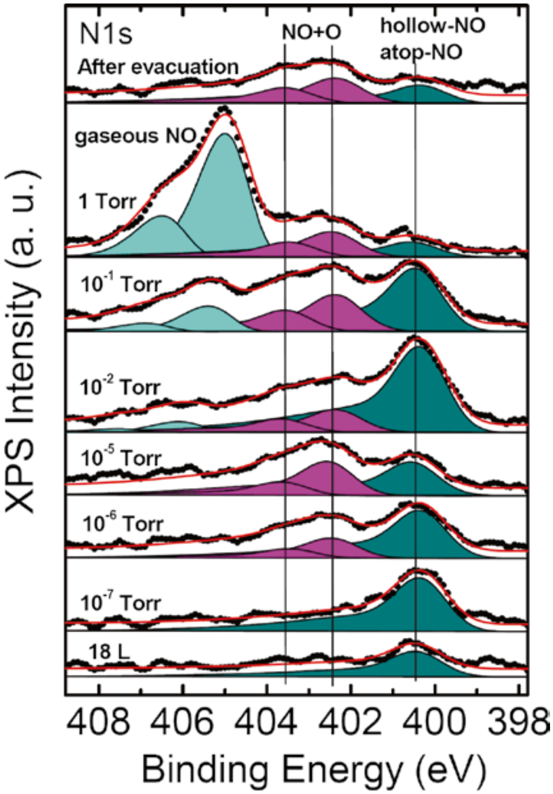

Fig. 9.15 N 1*s* X-ray photoelectron spectra for NO on Pt(111) under different conditions. From *bottom* to *top*: After dose of 18 L NO taken under UHV; 1×10^{-7} Torr NO; 1×10^{-6} Torr NO; 1×10^{-5} Torr NO; 1×10^{-2} Torr NO; 1×10^{-1} Torr NO; 1 Torr NO; after NO evacuation. All the spectra were recorded at RT. Reproduced from ref. [42] with modification

spectrum at a binding energy of 400.4 eV and assigned to NO molecules occupying fcc-hollow sites [13]. The asymmetric shape is due to the presence of a shake-up satellite at a higher binding energy. While in the corresponding O 1*s* spectrum, two peaks are observed at 530.7 and 533.0 eV; the lower binding-energy peak at 530.7 eV is attributed to NO at the fcc-hollow sites [50] and the higher binding-energy peak at 533.0 eV is ascribed to CO molecules inevitably adsorbed from the residual gas. The CO molecules seem to give no significant effects on the fcc-hollow NO, since CO molecules adsorb at atop sites at RT.

Under 10^{-7} Torr NO, N 1*s* and O 1*s* XP spectra appear at the same binding energies as those taken after 18 L dose, though the peak intensity is increased, which indicates that the NO population at the hollow sites increases under the presence of gas-phase NO. Under higher NO pressures, however, the XP spectra exhibit drastic changes. At 10^{-6} Torr, another broad component appears in the N 1*s* spectrum at 402–404 eV in addition to NO adsorbed at the hollow sites (400.4 eV). Since the N 1*s* binding energy of NO adsorbed on Pt(111) is almost independent of adsorption sites [47, 48], such a high binding energy suggests that NO does not occupy the ordinary sites and may be in a highly oxidized form. Similarly a higher biding-energy peak also appears at 531.4 eV in the O 1*s* spectrum at 10^{-6} Torr. It should be

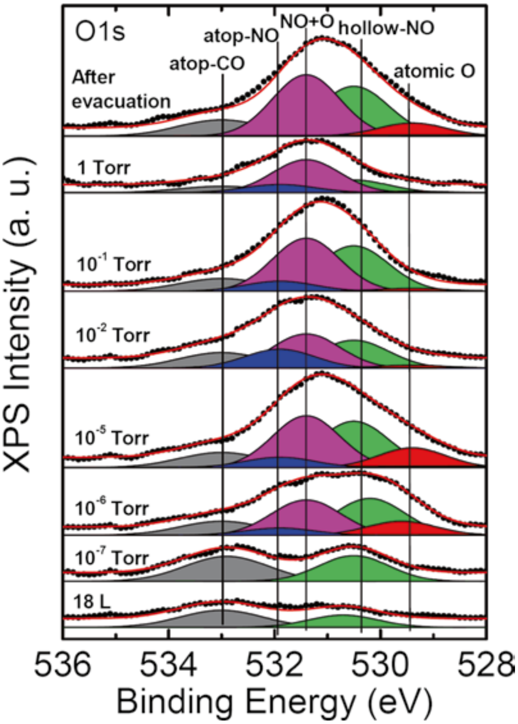

Fig. 9.16 N 1*s* X-ray photoelectron spectra for NO on Pt(111) under different conditions. From *bottom* to *top*: After dose of 18 L NO taken under UHV; 1×10^{-7} Torr NO; 1×10^{-6} Torr NO; 1×10^{-5} Torr NO; 1×10^{-2} Torr NO; 1×10^{-1} Torr NO; 1 Torr NO; after NO evacuation. All the spectra were recorded at RT. Reproduced from ref. [42] with modification

noted here that atomic oxygen is clearly observed at 529.5 eV at the same pressure. This means that dissociation of NO readily takes place at this pressure, though it has been reported that NO molecularly adsorbs on Pt(111) under UHV conditions. Since NO-adsorbed Pt(110) surfaces exhibit partial dissociation above 350 K, low-coordination Pt atoms at irregular sites like steps and defects may play a crucial role for the dissociation. It is also possible that the high-pressure NO induces dissociation on the terraces of Pt(111) even at RT.

Interestingly no atomic nitrogen is observed in the corresponding N 1*s* spectrum. Since the associative desorption of N_2 from atomic nitrogen usually does not occur at RT, one possible explanation for the absence of atomic nitrogen is that nitrogen atoms are removed from the surface by the following reaction: $N(a) + NO(a) \rightarrow N_2O(g)$ [50, 51]. Another explanation is formation and decomposition of NO dimers on the surface as shown in the following scheme: $2NO(g) \rightarrow (NO)_2(a) \rightarrow N_2O(a) + O(a)$ [52, 53]. $N_2O(a)$ is spontaneously decomposed into $N_2(g)$ and O(a) at RT. Although this pathway was initially found at low temperature, evidence for formation of NO dimers even at RT has recently been observed on NO-covered Rh(111) [51]. Since the NO dimer is in equilibrium with gas-phase NO, high-pressure conditions could increase the contribution of this pathway.

At 10^{-2} Torr, the hollow-NO peak at 400.4 eV in the N 1*s* XP spectrum significantly increases in intensity. This can be interpreted as an increase in NO population. The corresponding O 1*s* spectrum exhibits a growth of a peak at 531.9 eV,

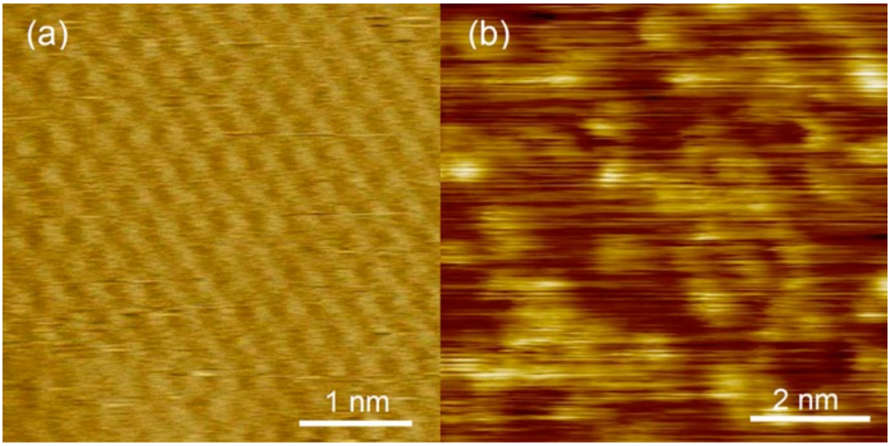

Fig. 9.17 STM images of (**a**) clean Pt(111) ($I = 0.2$ nA, $V = -0.15$ V, 4×4 nm^2) and (**b**) after 1 Torr NO exposure ($I = 0.1$ nA, $V = -1.2$ V, 10×10 nm^2). Both images were taken under UHV at RT. Reproduced from ref. [42] with modification

which can be attributed to an atop-NO species [47]. This species appears at 10^{-6} Torr and disappears at 1 Torr and after evacuation. These spectral changes indicate that the presence of gaseous NO induces a high-density phase under a pressure range from 10^{-6} to 10^{-1} Torr where NO molecules occupy atop sites in addition to the hollow sites on Pt(111).

The new feature observed at 402–404 eV in the N 1*s* spectra and that at 531.4 eV in the O 1*s* spectra are maintained at all pressures above 10^{-6} Torr and remain observable even after NO gas evacuation. The atomic oxygen exhibits the same trend. This suggests that the higher binding-energy component is irreversibly formed concomitantly with formation of atomic oxygen. Since the AP-XPS results clearly show the higher binding-energy peaks remain even after NO evacuation, we observed the surface structure with UHV-STM after 1 Torr NO exposure at RT and evacuation. Figure 9.17 shows STM images of a clean Pt(111) surface (a) and a NO(1 Torr)-dosed Pt(111) surface (b). The clean surface exhibits a (1 × 1) atomic arrangement, while after the NO dose any periodicity is not observed at all and small domains with a typical size of 1 nm in diameter and 0.08 nm in apparent height are randomly distributed over the surface. The small domains are associated with the higher binding-energy species, while the rest of the surface should be occupied by the hollow-NO species. Taking account of the presence of atomic oxygen, the higher binding-energy species in the domains is attributed to a NO + O coadsorption phase. It has been reported that NO_2 molecules dissociatively adsorb into NO + O at RT on Pt(110)-(1 × 2) and this NO species coadsorbed with atomic oxygen gives a broad N 1*s* peak at around 402.8 eV and an O 1*s* peak at 531.2 eV [54] which are in good agreement with those in the present study (402–404 eV for N 1*s* and 531.4 eV for O 1*s*). The high-binding-energy shift for this NO species is primarily ascribed to the electropositive property of the NO due to coadsorption with

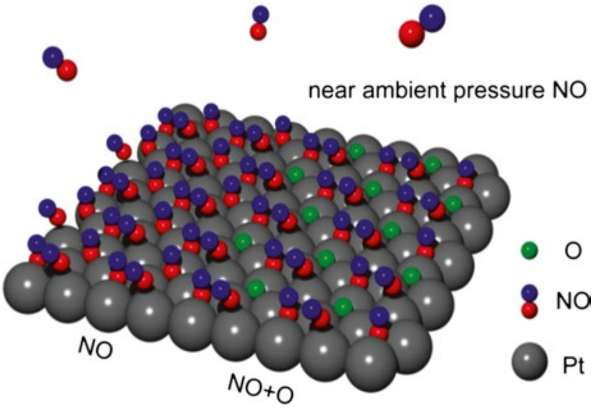

Fig. 9.18 Structure model for NO adsorption on Pt(111) under near ambient pressure conditions of NO. Reproduced from ref. [42]

atomic oxygen. It is noted that from 10^{-2} to 1 Torr, the atomic oxygen peak (529.5 eV) is almost absent as shown in Fig. 9.16. In such a high-pressure range, the NO + O domains would be able to accommodate more NO molecules, leading to increase in local NO coverage and strengthening of NO–O interactions. For NO + O/Ag(111), for instance, only one O 1*s* peak is observed at 531.0 eV without any contribution from isolated atomic oxygen. This was interpreted as a result of a strong NO–O interaction [55]. Therefore, one possible explanation for the absence of the atomic oxygen peak at the high pressures is that the increased NO coverage causes isolated atomic oxygen to disappear.

From the AP-XPS and STM data, we propose an adsorption model at elevated NO pressures above 10^{-6} Torr as shown in Fig. 9.18. There are two types of domains; the NO + O domain and the pure NO domain. In the NO + O domain NO molecules strongly interact with atomic oxygen, while the pure NO domain includes both hollow-NO and atop-NO species. The NO + O domain is formed via generation of atomic oxygen from NO under the high-pressure conditions. The counterpart N atoms are absent from the surface via reaction with NO and/or formation of NO dimers and decomposition into N_2O and O. After NO evacuation, the atop NO in the pure NO domain disappears, while the NO + O domains remain on the surface. Under the high-pressure conditions of NO several new pathways for adsorption can be opened, i.e., reversible formation of a high-density phase, high-pressure-induced dissociation, and irreversible formation of a novel adsorption phase that is different from that formed under UHV. The high-pressure dose induces rich surface chemistry.

9.5.3 CO Oxidation on Pd(111) [56]

Pd is the most used material for the three-way catalyst for automotive exhaust gases. The interactions of O_2 and CO with Pd surfaces and the catalytic reaction between them on the Pd surfaces have been extensively studied with various surface science

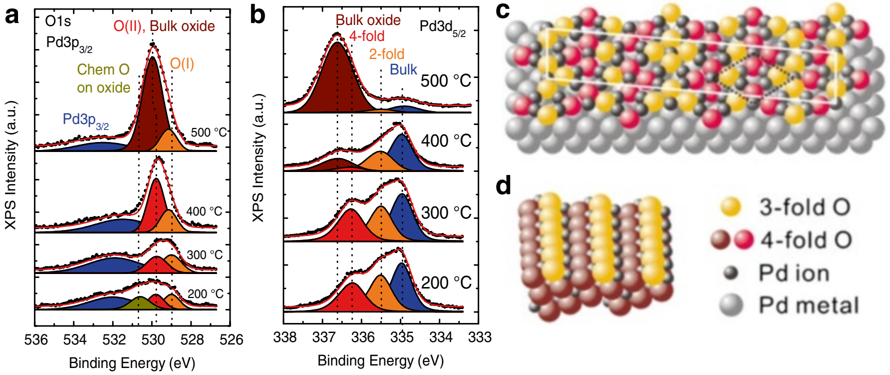

Fig. 9.19 XP spectra of O 1*s*/Pd 3$p_{3/2}$ (**a**) and Pd 3$d_{5/2}$ (**b**) regions for a Pd(111) surface taken at various temperatures under the presence of O_2 gas at 200 mTorr. The XP spectra are deconvoluted into several components as indicated by different colors. Structure models of the Pd_5O_4 surface oxide (**c**) and the PdO bulk oxide with the (101) surface orientation (**d**). Reproduced from ref. [56] with modification

techniques under UHV conditions [57–63]. In the past, a consensus has emerged for the CO oxidation reaction on the Pd surfaces; the reaction obeys the Langmuir–Hinshelwood (L–H) mechanism on the metallic surfaces under UHV conditions. However, under realistic conditions where practical catalysts operate, the Pd catalysts can be oxidized more or less which may lead to a different reaction mechanism. A high-pressure scanning tunneling microscopy (HP-STM) study on the CO oxidation on Pd(100) [64] suggested that formation of a surface oxide accompanies an enhancement of reaction activity. On one hand, it is reported from reaction kinetics measurements and PM-IRAS that the CO-free (metallic) surface, which is transiently formed during phase transition from a CO-poisoned metallic surface to an oxide surface, exhibits the highest catalytic activity [39, 65–67]. It needs in situ direct observations of the Pd surfaces under reaction conditions to understand the surface chemical state when the reaction activity is maximized.

First, the oxidation of Pd(111) surfaces was investigated by means of the AP-XPS technique. A Pd(111) surface was exposed to gaseous oxygen with a pressure of 2×10^{-1} Torr at different temperatures. Figure 9.19 shows temperature dependence of O 1*s*/Pd 3$p_{3/2}$ (a) and Pd 3$d_{5/2}$ (b) XP spectra taken for a Pd(111) surface under 2×10^{-1} Torr O_2. At 200 and 300 °C, the O 1*s* XP spectra exhibit two components at O(I) and O(II) with an intensity ratio of 1:1, which can be attributed to three- and fourfold coordinated oxygen species, respectively, of a Pd_5O_4 surface oxide [68] as illustrated in Fig. 9.19c. A higher binding-energy (530.6 eV) peak observed at 200 °C is assigned as a high-coverage chemisorbed O adlayer [69, 70] and completely disappears at 300 °C. The Pd 3$d_{5/2}$ XP spectra show existence of two- and fourfold coordinated surface Pd atoms and support the formation of the surface oxide. Further heating above 400 °C gives rise to formation of PdO bulk oxide [69–71], which is evidenced by appearance of a prominent high-binding-energy

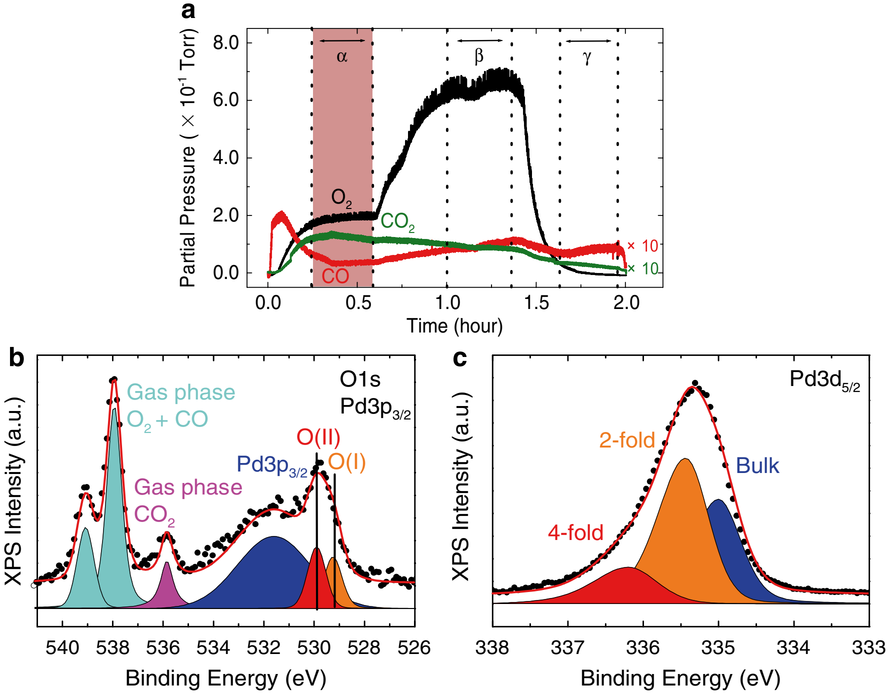

Fig. 9.20 CO oxidation reaction on Pd(111) at 300 °C. (**a**) Partial pressures of O_2, CO, and CO_2 monitored by mass spectroscopy, and (**b**) O 1*s*/Pd 3$p_{3/2}$ and (**c**) Pd 3$d_{5/2}$ AP-XP spectra of a Pd(111) surface taken at region a in (**a**) where the CO_2 formation rate is maximized under exposure to 2×10^{-1} Torr O_2 and 2×10^{-2} Torr CO gases. Reproduced from ref. [56] with modification

peak at 336.6 eV in the Pd 3$d_{5/2}$ region (Fig. 9.19b). According to a previous study on the growth of the bulk oxide [72], the PdO(101) surface is preferential formed, of which structure model is illustrated in Fig. 9.19d. Note that the bulk oxide is covered by the threefold O species as evidenced by the presence of O(I) species at 500 °C.

Next, the CO oxidation on Pd(111) under near ambient pressure conditions was studied by the combination of the AP-XPS technique and the differential pumping mass spectroscopy. In Fig. 9.20 is depicted a monitoring result of the progress of the CO oxidation reaction at 300 °C. Figure 9.20a shows partial pressure changes of O_2, CO, and CO_2. When the Pd(111) surface was exposed to 2×10^{-1} Torr O_2 and 2×10^{-2} Torr CO at 300 °C, the CO_2 formation rate was maximized, which results in that most of the CO gas was converted to CO_2 (Region α in Fig. 9.20a). At this moment, the O 1*s* XP spectrum exhibits a photoelectron peak from gaseous CO_2 at 536 eV as well as those from O_2 and CO gases. The Pd(111) surface under this condition gives two components for O 1*s* region and three components for Pd 3$d_{5/2}$ region as shown in Fig. 9.20b, c, which are almost the same as those of the Pd_5O_4 surface oxide and thus it is most likely that the surface oxide is formed under the highly active condition. The Pd_5O_4 surface oxide contains the three- and fourfold coordinated O atoms with 1:1 atomic ratio and the two- and fourfold coordinated Pd atoms with 4:1 atomic ratio as shown in Fig. 9.19c. Actual peak area ratios seen in Fig. 9.20b, c are in good agreement with these atomic ratios, which suggests that the surface is almost covered by the surface oxide phase. However, note that coexistence of chemisorbed O species cannot be completely excluded because its binding energy is the same as that of O(I).

At a higher temperature of 400 °C, the Pd_5O_4 surface oxide phase still contributes to the reaction as shown in Fig. 9.21. When the Pd(111) surface was exposed to 2×10^{-1} Torr O_2 and 2×10^{-2} Torr CO at 400 °C, initially most of the introduced CO gas was consumed (Region α) and the O 1*s* and Pd $3d_{5/2}$ spectra taken at Region α indicate formation of the surface oxide. The observation of the surface oxide under the highly active conditions (Region α at 300 and 400 °C) suggests that the surface oxide contributes to the highly active state [56]. This active phase cannot survive for a long time and changes to a less active state (Region β) as seen in Fig. 9.21a. At this moment, a new O 1*s* component appears at 530.5 eV (denoted by O(III)) and a bulk oxide component at 336.6 eV slightly contributes to the Pd $3d_{5/2}$ spectrum. Note that the appearance of O(III) species is accompanied by a relative growth of the twofold Pd component. This suggests that the O(III) species is bound to the twofold (low-coordination) Pd atoms, which in turn means the O(III) species is highly coordinated by the surrounding Pd atoms. Furthermore, since the binding energy of O(III) (530.5 eV) is the highest among oxygen species observed under the reaction condition, the O 1*s* core-level excitation of the O(III) species may be poorly screened in the final state by a lack of free electrons of the Pd conduction band. All these facts suggest that the O(III) species is included in oxygen-deficient Pd cluster oxides. Because the O(III) species is strongly bound to the Pd cluster due to the oxygen deficiency, the availability of the O(III) species for CO oxidation is low. The appearance of O(III) is also accompanied by a significant increase of O(II) species. This is not simply due to a population increase of the fourfold O species in the surface oxide, but due to an increase of subsurface O, which appears at the same binding energy as that of O(II) and is considered as a precursor to bulk oxide [71]. However, the formation of the bulk-like oxide causes a drastic decrease in reactivity as seen in Region β; the bulk oxide is not active either. At the final stage of this monitoring, we stopped only O_2 dose with keeping CO dose constant and the Pd oxide surface is reduced by CO as shown in Region γ of Fig. 9.21. Interestingly only the O(I) species is consumed, which means that the threefold coordinated O species of the surface oxide is reactive while the other O species, O(II) and O(III), are nonreactive. Since both of the O(II) and O(III) species can be assumed as highly coordinated O species as mentioned above, the low Pd coordination is important for the reactivity. Under the CO reduction condition (Region γ), the coverage of O(III) species is increased. This suggests that the O(III) species is formed via reduction of the surface oxide. Finally it should be noted that the bulk oxide does not induce a high reactivity though its surface is covered by the threefold O species. The reactivity of threefold O species alters depending on chemical environment. The configuration of the surface oxide sitting on the metallic substrate may give a crucial effect on the reactivity of the threefold O species.

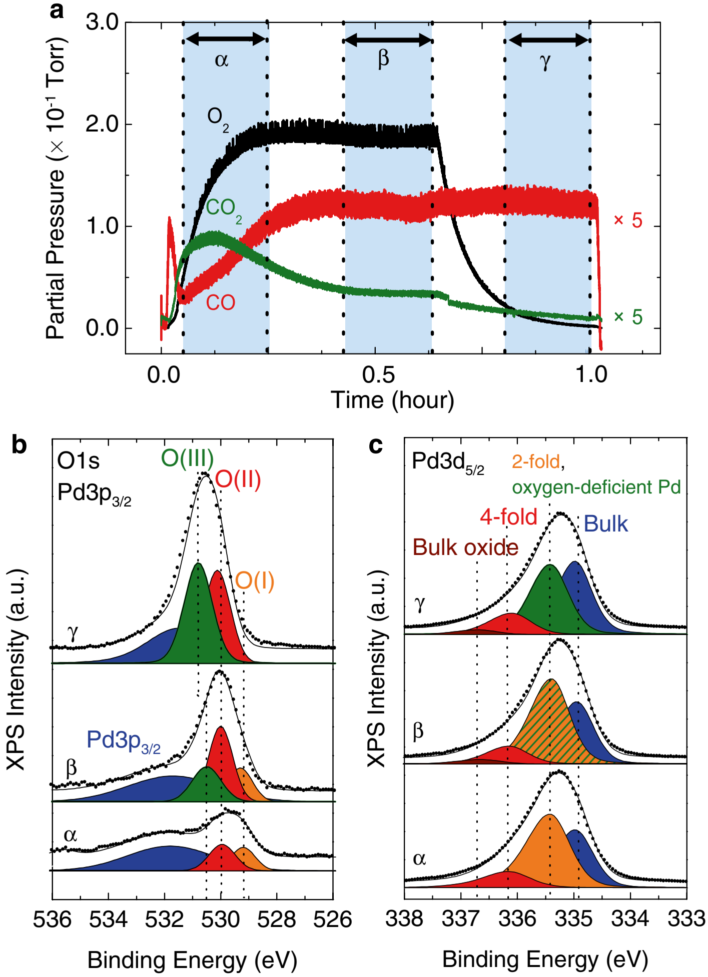

Fig. 9.21 CO oxidation reaction at 400 °C. (**a**) Partial pressures of O_2, CO, and CO_2 monitored by mass spectroscopy, and (**b**) O 1*s*/Pd 3$p_{3/2}$ and (**c**) Pd 3$d_{5/2}$ AP-XP spectra of a Pd(111) surface under exposure to O_2 and CO gases, up to 200 and 20 mTorr, respectively. Reproduced from ref. [56]

9.6 Application to Real System: Solid Oxide Fuel Cell

In electrochemistry, the lack of in situ characterization tools for studying electrochemical interfaces has been a chief obstacle, which puts a delay in the development of the next generation electrochemical devices, such as batteries, fuel cells, and supercapacitor [73]. In fact, several in situ diagnostic tools are employed for the particular use of electrochemical studies, i.e., in situ X-ray emission/absorption spectroscopy, scanning tunneling microscope, and X-ray Raman spectroscopy.

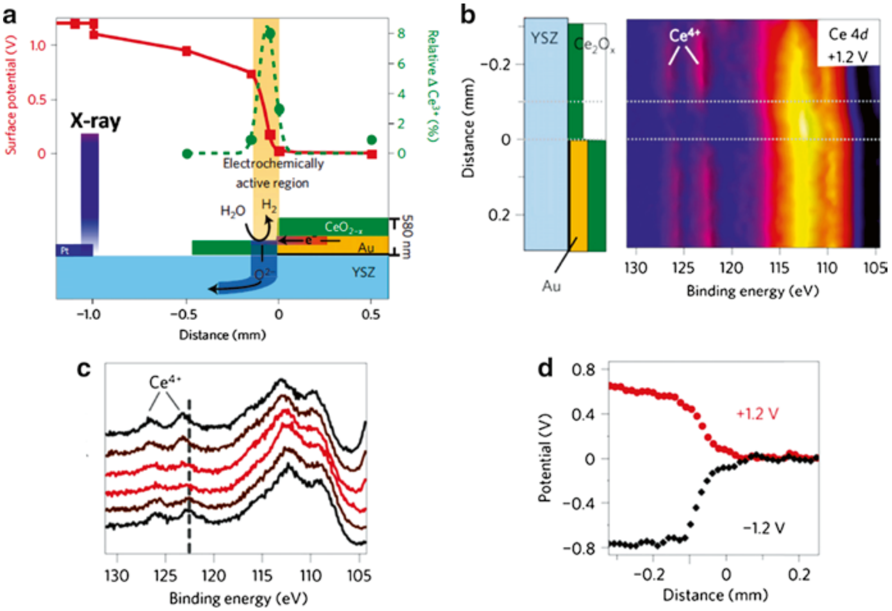

Fig. 9.22 (**a**) Simple experimental layout for SOC using AP-XPS. AP-XPS reveals local surface potentials (*red squares*) and the relative shift of Ce oxidation state out of equilibrium (*green circles*) in this region. (**b**) Using spatial resolved mode of electron analyzer, distance-resolved XPS spectra of the Ce 4*d* region at +1.2 V applied potential recorded with 490 eV photon energy. The *dotted lines* denote the electrochemically active regions corresponding to the schematic cell drawing on the left side. (**c**) Integrated spectra taken from 50 μm slices corresponding to distance coordinates of –0.15 to 0.1 mm in the schematic cell drawing; spectra from the active region are shown in *red*. The peaks labeled as Ce^{4+} are associated only with Ce^{4+} species. (**d**) The potentials across the ceria surface calculated from +1.2 V bias as in (**b**) and −1.2 V are shown. Reproduced from ref. [80] with modification

However, in electron detection tools, only ex situ characterization technique was possible, i.e., Auger electron spectroscopy (AES) or EELS in electrochemistry [74]. Now, with the emergence of AP-XPS, another opportunity is opened up in the fields of electrochemistry, providing in situ quantitative information on chemical and electronic states of surface/interface under operating condition, i.e., *operando analysis* [75, 76].

As one of the first applications in electrochemistry toward AP-XPS, solid oxide fuel cells (SOCs) have been chosen and tested successfully [77–80]. SOCs, as one of the solid state electrochemical devices for electrochemical power, operate under gaseous fuel condition to generate the electrical power at relatively high temperature condition (>700 °C). And, these operating conditions of SOCs, e.g., high temperature and elevated pressure, have been the hurdle for the in situ characterization of surface/interface properties of SOCs.

At ALS, a special sample holder and electrodes are developed and adapted to AP-XPS system to run the high temperature AP-XPS experiment. With use of angular mode, local surface potential, electrochemically active regions, and dynamics of surface oxidation states under operation conditions are disclosed. The result of measurement is shown in Fig. 9.22. In Fig. 9.22a, cross section of the model device, including its dimensions, is shown at the bottom. The incident X-ray spot was much smaller (diameter ~0.1 mm) than the elements of the model fuel cell device so that it was possible to collect data from selected regions of interest or across the whole device. A bias of +1.2 V was applied to the Pt counter electrode while the Au current collector was grounded. This leads to electrolysis of water on ceria, with oxygen ions moving from the ceria electrode through the YSZ to the Pt electrode where they react with H_2. A gradual decrease of the potential is observed across the YSZ and parts of the ceria surface, up to the area where ceria meets the Au current collector and the potential drops sharply to 0 V. Figure 9.22b shows the spectral images of the Ce 4*d* core-level across a 50 nm thick ceria electrode. With the imaging capability, one can clearly visualize the marked chemical change and potential drop across the ceria film in the active region of the electrode. By monitoring the intensity of the Ce 4*d* peaks at 126.1 and 122.8 eV (Fig. 9.22c), the authors of ref. [80] observed changes in the Ce^{3+}/Ce^{4+} ratios through reduction and oxidation, respectively, of ceria in the active region at different applied potentials. The ceria surface potential at different applied potential is plotted in Fig. 9.22. This demonstrated that the active electrochemical region on ceria extends 100–150 μm away from the current collector and that significant shifts from the equilibrium surface concentrations of Ce^{3+}/Ce^{4+} are needed to drive the electro-oxidation of H_2 and the electrolysis of H_2O. The correlations between local potential losses and local chemical state changes were obtained directly from working SOC devices. From the measurement of such a model cell, the origins of changes in the individual overpotentials with applied bias can be interpreted using the different electro-catalytic activities of Ni and Pt for the H_2O splitting and H_2 oxidation reactions.

9.7 Concluding Remarks: Futures on AP-XPS

Clearly, the emergence of AP-XPS has made a significant impact and opened up many windows of opportunities to the community of surface science and its related fields. Since its first appearance, AP-XPS has generated many important and exciting results from the experiments that are not feasible in previous time. In recent years, the demand of using AP-XPS has exceeded the available supply and the commissioning of AP-XPS user-endstation has been sharply increased at major synchrotron radiation facilities.

In this section, we consider how AP-XPS can be developed further to meet the demand of future scientific agenda and provide several options for future progresses in several directions.

1. Extension to AP XAS measurements

X-ray absorption spectra (XAS) have been already measured under AP conditions with the Auger electron yield method. If circularly polarized lights are used for XAS measurements, surface magnetic information will be obtained via XMCD under realistic conditions. At the moment, the photon energy is scanned with a

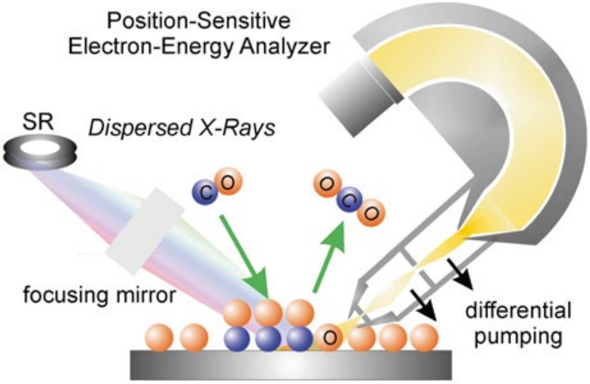

Fig. 9.23 Simple illustration for energy dispersive X-ray absorption technique using AP-XPS

monochromator for AP XAS measurements. It takes typically several minutes to record a spectrum, which prevents application to dynamic processes. When wavelength-dispersed X-rays are used under a combination with a position-sensitive analyzer [72] for AP XAS measurements as illustrated in Fig. 9.23, the data acquisition time will be reduced by a factor of 100, which allows us to apply this technique to moderately fast surface processes.

2. Time-resolved experiments under AP conditions

In order to monitor the real-time dynamics of gas molecules interacting with surface, time-resolved study is required. It is generally known that the time domains for the gas adsorption/desorption on surface are within pico-second regime while the molecular vibration on surface is within femto-second regime. To accommodate this time-requirement as well as chemical analysis on surface, a type of "pump and probe" experiment is required, which makes use of synchronization between a laser pulse and a synchrotron radiation pulse of AP-XPS endstation. For example, the carrier dynamics and reaction mechanism of photocatalysts under AP conditions can be an ideal system to look at with this time-resolved experimental set-up. At present, the synchronization technique has been well developed as shown in a block diagram (Fig. 9.24). This time-resolved set-up can be further refined and adapted into advanced system when the free electron X-ray source is available.

3. Extension to hard-X-ray PES (HAXPES) under AP conditions

HAXPES is a promising choice because high kinetic energies of photoelectron can (a) increase the maximum operating pressure and (b) provide information from deeper surface layers. When the kinetic energy of electron is increased from 500 to 5,000 eV, the inelastic mean free paths of electrons increase about five times more [81, 82]. This allows us to apply AP-XPS to detect photoelectrons from higher pressure solid–gas interfaces and even solid–liquid interfaces and expand the research target areas. The field of electrochemistry in which the liquid–solid interface plays a critical role could receive the significant benefits when this HAXPES becomes available to the community. Currently, the Berkeley group has been developing this high energy AP-XPS system and made a significant progress.

Fig. 9.24 Block diagram for time-resolved experiments using XPS

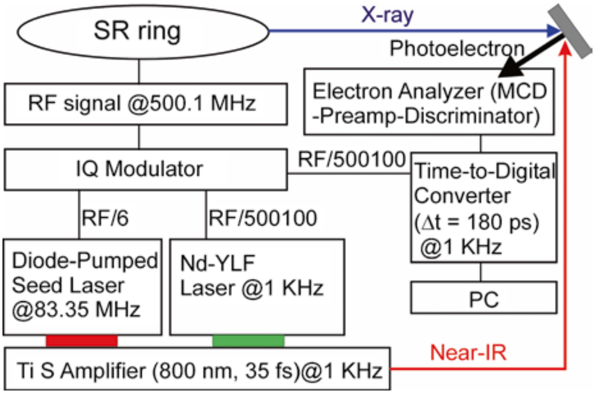

Acknowledgments The Advanced Light Source is supported by the Director, Office of Science, Office of Basic Energy Sciences, of the U.S. Department of Energy under Contract No. DE-AC02-05CH11231. We acknowledge the Grants-in-Aid for scientific research (No. 20245004) and the MEXT-Supported Program for the Strategic Research Foundation at Private Universities, 2009–2013 for financial supports. The experiments have been performed under the approval of the Advanced Light Source (ALS-02305) and the Photon Factory Program Advisory Committee (PF PAC Nos. 2008G192 and 2010G151). B.S.M. would like to thank the support by Basic Science Research Program through the NRF by the MEST (2012R1A1A2001745) and by GIST College's 2013 GUP Research Fund.

References

1. Freund H-J, Kuhlenbeck H, Bäumer M (2000) Catalysis and surface science: what do we learn from studies of oxide-supported cluster model systems? Adv Catal 45:333–384
2. Bäumer M, Freund H-J (1999) Metal deposits on well-ordered oxide films. Prog Surf Sci 61:127–198
3. Freund H-J, Kuhlenbeck H, Libuda J, Rupprechter G, Bäumer M, Hamann H (2001) Bridging the pressure and materials gaps between catalysis and surface science: clean and modified oxide surfaces. Top Catal 15:201–209
4. Somorjai GA (1994) Introduction to surface chemistry and catalysis. Wiley, New York
5. Somorjai GA (1978) Surface science. Science 201:489–497
6. Siegbahn K, Nordling C, Fahlman A, Hamrin K, Hedman J, Nordberg R, Johansson C, Bergmark T, Karlsson S-E, Lindgren I, Lindberg B (1967) ESCA: atomic, molecular and solid state structure studied by means of electron spectroscopy. Almqvist and Wiksell, Uppsala
7. Fadley CS, Brundle CR, Baker AD (1978) Electron spectroscopy: theory, techniques, and applications, vol 2. Academic, London
8. Hüfner S (2003) Photoelectron spectroscopy: principles and applications, 3rd edn. Springer-Verlag Berlin Heidelberg New York
9. Siegbahn K, Nordling C, Johansson G, Hedman J, Heden P-F, Hamrin K, Gelius U, Bergmark T, Werme LO, Manne R, Baer Y (1970) ESCA applied to free molecules. North-Holland, Amsterdam
10. Fadley CS (1974) The International Journal on Theoretical and Experimental Aspects of Electron Spectroscopy Instrumentation for surface studies: XPS angular distributions. J Electron Spectrosc Rel Phen 5:725–754

11. Fadley CS (1984) Progress in surface science. In Davison S (ed). Pergamon Press, New York, vol 16, p 275
12. Wannberg B (2009) Electron optics development for photo-electron spectrometers. Nucl Instrum Methods Phys Res, Sect A 601:182–194
13. Powell CJ, Jablonski A, Tilinin IS, Tanuma S, Penn DR (1999) Surface sensitivity of Auger-electron spectroscopy and X-ray photoelectron spectroscopy. J Electron Spectrosc Rel Phen 98–99:1–15
14. Tanuma S, Powell CJ, Penn DR (2005) Calculations of electron inelastic mean free paths, VIII. Data for 15 elemental solids over the 50–2000 eV range. Surf Interface Anal 37:1–14
15. Su X, Cremer PS, Shen YR, Somorjai GA (1996) Pressure dependence (10^{-10}–700 Torr) of the vibrational spectra of adsorbed CO on Pt(111) studied by sum frequency generation. Phys Rev Lett 77:3858–3860
16. Rupprechter G (2004) 8 Surface vibrational spectroscopy on noble metal catalysts from ultra-high vacuum to atmospheric pressure. Annu Rep Prog Chem Sect C Phys Chem 100: 237–311
17. Rupprechter G, Weilach C (2008) Spectroscopic studies of surface–gas interactions and catalyst restructuring at ambient pressure: mind the gap! J Phys Condens Mater 20:184019
18. Siegbahn H, Siegbahn K (1973) ESCA applied to liquids. J Electron Spectrosc Rel Phen 2:319–325
19. Fellner-Feldegg H, Siegbahn H, Asplund L, Kelfve P, Siegbahn K (1975) ESCA applied to liquids IV. A wire system for ESCA measurements on liquids. J Electron Spectrosc Rel Phen 7:421–428
20. Siegbahn H, Svensson S, Lundholm M (1981) A new method for ESCA studies of liquid-phase samples. J Electron Spectrosc Rel Phen 24:205–213
21. Joyner RW, Roberts MW, Yates K (1979) A "high-pressure" electron spectrometer for surface studies. Surf Sci 87:501–509
22. Ruppender HJ, Grunze M, Kong CW, Wilmers M (1990) *In situ* X-ray photoelectron spectroscopy of surfaces at pressures up to 1 mbar. Surf Interface Anal 15:245–253
23. Kaichev VV, Sorokin AM, Timoshin AI, Vovk EI (2002) An information measuring system for thermodesorption studies. Instrum Exp Tech 45:50–54
24. Joyner RW, Roberts MW (1979) A study of the adsorption of oxygen on silver at high pressure by electron spectroscopy. Chem Phys Lett 60:459–462
25. Kaichev VV, Prosvirin IP, Bukhtiyarov VI, Unterhalt H, Rupprechter G, Freund H-J (2003) High-pressure studies of CO adsorption on Pd(111) by X-ray photoelectron spectroscopy and sum-frequency generation. J Phys Chem B 107:3522–3527
26. Ogletree DF, Bluhm H, Lebedev G, Hussain Z, Fadley C, Salmeron M (2002) A differentially pumped electrostatic lens system for photoemission studies in the millibar range. Rev Sci Instrum 73:3872–3877
27. Ogletree DF, Bluhm H, Hebenstreit ED, Salmeron M (2009) Photoelectron spectroscopy under ambient pressure and temperature conditions. Nucl Instrum Methods Phys Res A 601: 151–160
28. Salmeron M, Schlögl R (2008) Ambient pressure photoelectron spectroscopy: a new tool for surface science and nanotechnology. Surf Sci Rep 63:169–199
29. Grass ME, Karlsson PG, Aksoy F, Lundqvist M, Wannberg B, Mun BS, Hussain Z, Liu Z (2010) New ambient pressure photoemission endstation at Advanced Light Source beamline 9.3.2. Rev Sci Instrum 81:053106
30. Aksoy F, Grass ME, Joo SH, Jabeen N, Hong YP, Hussain Z, Mun BS, Liu Z (2011) Study of electro-chemical properties of metal–oxide interfaces using a newly constructed ambient pressure X-ray photoelectron spectroscopy endstation. Nucl Instrum Methods Phys Res, Sect A 645:260–265
31. Westerström R, Messing ME, Blomberg S, Hellman A, Grönbeck H, Gustafson J, Martin NM, Balmes O, van Rijn R, Andersen JN, Deppert K, Bluhm H, Liu Z, Grass ME, Hävecker M, Lundgren E (2011) Oxidation and reduction of Pd(100) and aerosol-deposited Pd nanoparticles. Phys Rev B 83:115440

32. Imbihl R, Ertl G (1995) Oscillatory kinetics in heterogeneous catalysis. Chem Rev 95:697–733
33. Oertzen AV, Mikhailov AS, Rotermund HH, Ertl G (1998) Subsurface oxygen in the CO oxidation reaction on Pt(110): experiments and modeling of pattern formation. J Phys Chem B 102:4966–4981
34. Campbell CT, Ertl G, Kuipers H, Segner J (1980) A molecular beam study of the catalytic oxidation of CO on a Pt(111) surface. J Chem Phys 73:5862–5873
35. Hendriksen BLM, Frenken JWM (2002) CO oxidation on Pt(110): scanning tunneling microscopy inside a high-pressure flow reactor. Phys Rev Lett 89:046101
36. Ackermann MD, Pedersen TM, Hendriksen BLM, Robach O, Bobaru SC, Popa I, Quiros C, Kim H, Hammer B, Ferrer S, Frenken JWM (2005) Structure and reactivity of surface oxides on Pt(110) during catalytic CO oxidation. Phys Rev Lett 95:255505
37. Mars P, van Krevelen DW (1954) Oxidations carried out by means of vanadium oxide catalysts. Spec Suppl Chem Eng Sci 3:41–59
38. Li WX, Osterlund L, Vestergaard EK, Van RT, Matthiesen J, Pedersen TM, Laegsgaard E, Hammer B, Besenbacher F (2004) Oxidation of Pt(110). Phys Rev Lett 93:146104–146107
39. Gao F, Wang Y, Cai Y, Goodman DW (2009) CO oxidation on Pt-group metals from ultrahigh vacuum to near atmospheric pressures. 2. Palladium and platinum. J Phys Chem C 113:174–181
40. Chung J, Aksoy F, Grass ME, Kondoh H, Ross P Jr, Liu Z, Mun BS (2009) *In-situ* study of the catalytic oxidation of CO on a Pt(110) surface using ambient pressure X-ray photoelectron spectroscopy. Surf Sci 603:L35–L38
41. Butcher DR, Grass ME, Zeng Z, Aksoy F, Bluhm H, Li W-X, Mun BS, Somorjai GA, Liu Z (2011) In situ oxidation study of Pt(110) and its interaction with CO. J Am Chem Soc 133:20319–20325
42. Shimada T, Mun BS, Nakai I, Banno A, Abe H, Iwasawa Y, Ohta T, Kondoh H (2010) Irreversible change in the NO adsorption state on Pt(111) under high pressure studied by AP-XPS, NEXAFS, and STM. J Phys Chem C 114:17030–17035
43. Matsumoto M, Tatsumi N, Fukutani K, Okano T, Yamada T, Miyake K, Hate K, Shigekawa H (1999) Adsorption structures of NO/Pt(111) investigated by scanning tunneling microscopy. J Vac Sci Technol A 17:1577–1580
44. Matsumoto M, Fukutani K, Okano T, Miyake K, Shigekawa H, Kato H, Okuyama H, Kawai M (2000) Study of the adsorption structure of NO on Pt(111) by scanning tunneling microscopy and high-resolution electron energy-loss spectroscopy. Surf Sci 454–456:101–105
45. Matsumoto M, Tatsumi N, Fukutani K, Okano T (2002) Dynamical low-energy electron diffraction analysis of the structure of nitric oxide on Pt(111). Surf Sci 513:485–500
46. Aizawa H, Morikawa Y, Tsuneyuki S, Fukutani K, Ohno T (2002) A density-functional study of the atomic structures and vibrational spectra of NO/Pt(111). Surf Sci 514:394–403
47. Zhu JF, Kinne M, Fuhrmann T, Denecke R, Steinrück H-P (2003) In situ high-resolution XPS studies on adsorption of NO on Pt(111). Surf Sci 529:384–396
48. Zhu P, Shimada T, Kondoh H, Nakai I, Nagasaka M, Ohta T (2004) Adsorption structures of NO on Pt(111) studied by the near edge X-ray absorption fine structure spectroscopy. Surf Sci 565:232–242
49. Hussain Z, Huff WRA, Kellar SA, Moler EJ, Heimann PA, McKinney W, Padmore HA, Fadley CS, Shirley DA (1996) High resolution soft X-ray bending magnet beamline 9.3.2 with circularly polarized radiation capability at the Advanced Light Source. J Electron Spectroc Relat Phenom 80:401–404
50. Zaera F, Gopinath CS (2000) Evidence for an N_2O intermediate in the catalytic reduction of NO to N_2 on rhodium surfaces. Chem Phys Lett 332:209–214
51. Nakai I, Kondoh H, Shimada T, Nagasaka M, Yokota R, Katayama T, Amemiya K, Orita H, Ohta T (2009) Mechanism of N + NO reaction on Rh(111) surfaces: a precursor-mediated reaction. J Phys Chem C 113:13257–13265
52. Brown WA, Gardner P, King DA (1995) Very low temperature surface reaction: N_2O formation from NO dimers at 70 to 90 K on Ag{111}. J Phys Chem 99:7065–7074

53. Carlisle CI, King DA (2001) Direct molecular imaging of NO monomers and dimers and a surface reaction on Ag{111}. J Phys Chem B 105:3886–3893
54. Jiang Z, Huang W, Tan D, Zhai R, Bao X (2006) Surface chemistry of NO and NO_2 on the Pt(110)-(1 × 2) surface: a comparative study. Surf Sci 600:4860–4869
55. Polzonetti G, Alnot P, Brundle CR (1990) The adsorption and reactions of NO_2 on the Ag(111) surface: I. XPS/UPS and annealing studies between 90 and 300 K. Surf Sci 238:226–236
56. Toyoshima R, Yoshida M, Monya Y, Kousa Y, Suzuki K, Abe H, Mun BS, Mase K, Amemiya K, Kondoh H (2012) In situ ambient pressure XPS study of CO oxidation reaction on Pd(111) surfaces. J Phys Chem C 116:18691–18697
57. Campbell CT, Ertl G, Kuipers H, Segner J (1981) A molecular beam study of the adsorption and desorption of oxygen from a Pt(111) surface. Surf Sci 107:220–236
58. Nakai I, Kondoh H, Amemiya K, Nagasaka M, Shimada T, Yokota R, Nambu A, Ohta T (2005) Mechanism of the CO oxidation reaction on O-precovered Pt(111) surfaces studied with near-edge x-ray absorption fine structure spectroscopy. J Chem Phys 122:134709
59. Nakai I, Kondoh H, Shimada T, Resta A, Andersen JN, Ohta T (2006) Mechanism of CO oxidation reaction on O-covered Pd(111) surfaces studied with fast x-ray photoelectron spectroscopy: change of reaction path accompanying phase transition of O domains. J Chem Phys 124:224712
60. Witterlin J, Völkening S, Janssens TVW, Zambelli T, Ertl G (1997) Atomic and macroscopic reaction rates of a surface-catalyzed reaction. Science 278:1931–1934
61. Méndez J, Kim SH, Cerdá J, Wintterlin J, Ertl G (2005) Coadsorption phases of CO and oxygen on Pd(111) studied by scanning tunneling microscopy. Phys Rev B 71:085409
62. Kim SH, Méndez J, Wintterlin J, Ertl G (2005) Enhanced reactivity of adsorbed oxygen on Pd(111) induced by compression of the oxygen layer. Phys Rev B 72:155414
63. Nakao K, Watanabe O, Sasaki T, Ito S, Tomishige K, Kunimori K (2007) CO oxidation on Pd(111), Pt(111), and Rh(111) surfaces studied by infrared chemiluminescence spectroscopy. Surf Sci 601:3796–3800
64. Hendriksen BLM, Bobaru SC, Frenken JWM (2004) Oscillatory CO oxidation on Pd(100) studied with in situ scanning tunneling microscopy. Surf Sci 552:229–242
65. Chen MS, Cai Y, Gath KK, Axnanda S, Goodman DW (2007) Highly active surfaces for CO oxidation on Rh, Pd, and Pt. Surf Sci 601:5326–5331
66. Gao F, McClure SM, Cai Y, Gath KK, Wang Y, Chen MS, Guo QL, Goodman DW (2009) CO oxidation trends on Pt-group metals from ultrahigh vacuum to near atmospheric pressures: a combined *in situ* PM-IRAS and reaction kinetics study. Surf Sci 603:65–70
67. Chen M, Wang XV, Zhang L, Tang Z, Wan H (2010) Active surfaces for CO oxidation on palladium in the hyperactive state. Langmuir 26:18113–18118
68. Lundgren E, Kresse G, Klein C, Borg M, Andersen JN, De Stantis M, Gauthier Y, Konvicka C, Schmid M, Varga P (2002) Two-dimensional oxide on Pd(111). Phys Rev Lett 88:246103
69. Zemlynov D, Aszalos-Kiss B, Kleimenov E, Teschner D, Zafeiratos S, Hävecker M, Knop-Gericke A, Schlögl R, Gsbasch H, Unterberger W, Hayek K, Klötzer B (2006) *In situ* XPS study of Pd(111) oxidation. Part 1: 2D oxide formation in 10^{-3} mbar O_2. Surf Sci 600:983–994
70. Gabasch H, Unterberger W, Hayek K, Klötzer B, Klemenov E, Teschner D, Zafeiratos S, Hävecker M, Knop-Gericke A, Schlögl R, Han J, Ribeiro FH, Aszalos-Kiss B, Curtin T, Zemlyanov D (2006) *In situ* XPS study of Pd(111) oxidation at elevated pressure, Part 2: palladium oxidation in the 10^{-1} mbar range. Surf Sci 600:2980–2989
71. Ketteler G, Ogletree DF, Bluhm H, Liu H, Hebenstreit ELD, Salmeron M (2005) In situ spectroscopic study of the oxidation and reduction of Pd(111). J Am Chem Soc 127: 18269–18273
72. Amemiya K, Kousa Y, Nakamoto S, Harada T, Kozai S, Yoshida M, Abe H, Sumii R, Sakamaki M, Kondoh H (2011) Real-time observation of CO oxidation reaction on Ir(111) surface at 33 ms resolution by means of wavelength-dispersive near-edge x-ray absorption fine structure spectroscopy. Appl Phys Lett 99:074104
73. Faulkner LR (1988) In situ characterization of electrochemical processes. J Electrochem Soc 135:245C–246C

74. Ross PN (1979) Structure sensitivity in the electrocatalytic properties of Pt. I. Hydrogen adsorption on low index single crystals and the role of steps. J Electrochem Soc 126:67–77
75. Bard AJ, Faulkner LR (1980) Electrochemical methods: fundamentals and applications. Wiley, New York
76. Adler SB (2004) Factors governing oxygen reduction in solid oxide fuel cell cathodes. Chem Rev 104:4791–4843
77. DeCaluwe SC, Grass ME, Zhang CJ, El Gabaly F, Bluhm H, Liu Z, Jackson GS, McDaniel AH, McCarty KF, Farrow RL, Linne MA, Hussain Z, Eichhorn BW (2010) In situ characterization of ceria oxidation states in high-temperature electrochemical cells with ambient pressure XPS. J Phys Chem C 114:19853–19861
78. El Gabaly F, Grass M, McDaniel AH, Farrow RL, Linne MA, Hussain Z, Bluhm H, Liu Z, McCarty KF (2010) Measuring individual overpotentials in an operating solid-oxide electrochemical cell. Phys Chem Chem Phys 12:12138–12145
79. Whaley JA, McDaniel AH, El Gabaly F, Farrow RL, Grass ME, Hussain Z, Liu Z, Linne MA, Bluhm H, McCarty KF (2010) Note: fixture for characterizing electrochemical devices in-operando in traditional vacuum systems. Rev Sci Instrum 81:086104
80. Zhang CJ, Grass ME, McDaniel AH, DeCaluwe SC, El Gabaly F, Liu Z, McCarty KF, Farrow RL, Linne MA, Hussain Z, Jackson GS, Bluhm H, Eichhorn BW (2010) Measuring fundamental properties in operating solid oxide electrochemical cells by using in situ X-ray photoelectron spectroscopy. Nat Mater 9:944–949
81. Gray AX, Papp C, Ueda S, Balke B, Yamashita Y, Plucinski L, Minár J, Braun J, Ylvisaker ER, Schneider CM, Pickett WE, Ebert H, Kobayashi K, Fadley CS (2011) Probing bulk electronic structure with hard X-ray angle-resolved photoemission. Nat Mater 10:759–764
82. Woicik JC, Fischer DA, Vescovo E, Arena DA, Starr DE, Wells BO, Fadley CS (2010) International workshop for new opportunities in hard x-ray photoelectron spectroscopy: HAXPES 2009. Synchron Radiat News 23:19–21

Chapter 10
Electronic Excitation on Surfaces During Chemical and Photon Processes

Jeong Young Park

10.1 Introduction

Energy dissipation at surfaces and interfaces is mediated by excitation of elementary processes, including phonons and electronic excitation, once external energy is deposited to the surface during exothermic chemical processes [1–4]. Electron excitation in exothermic catalytic reactions or the incidence of photons on metal surfaces results in the flow of high-energy electrons with an energy of 1–3 eV, assuming that most of the chemical or photon energy is converted to electron flow on a short (femtosecond) time scale before atomic vibration adiabatically dissipates the energy (in picoseconds). These energetic electrons that are not in thermal equilibrium with the metal atoms are called "hot electrons" [5–8]. There have been a number of studies demonstrating the influence of hot electrons on atomic and molecular processes. The detection of hot electron flow under atomic or molecular processes and understanding its role in chemical reactions have been major topics in surface chemistry. Recent experimental and theoretical studies have demonstrated electronic excitation production during atomic or molecular processes on surfaces [9, 10]. In this chapter, I will outline recent research developing energy conversion devices based on hot electrons. The chemicurrent, or hot electron flow, is well correlated with the turnover rate of CO oxidation or hydrogen oxidation measured separately by gas chromatography, suggesting an intrinsic relation between the catalytic reactions and hot electron generation. We found that photon energy can be directly converted to hot electron flow through the metal–semiconductor interface of catalytic nanodiodes. We showed that hot electron flow generated on a gold thin

---

J.Y. Park (✉)
Graduate School of EEWS (WCU) and NanoCentury KI, Korea Advanced Institute of Science and Technology (KAIST), Daejeon 305-701, South Korea

Center for Nanomaterials and Chemical Reactions, Institute for Basic Science, Daejeon 305-701, South Korea
e-mail: jeongypark@kaist.ac.kr

J.Y. Park (ed.), *Current Trends of Surface Science and Catalysis*,
DOI 10.1007/978-1-4614-8742-5_10,

film by photon absorption (or internal photoemission) is amplified by localized surface plasmon resonance. The influence of the flow of hot charge carriers on the chemistry at the oxide–metal interface and the turnover rate for the chemical reaction, for the cases of Pt–CaSe–Pt nanodumbbells and Pt/GaN substrates, are discussed.

10.2 Theoretical Background of Energy Dissipation on Surfaces

The basic mechanism for energy dissipation involves phonons, nonadiabatic electron–hole excitation processes, plasmons, exoemission, and chemiluminescence, as described below.

Phonon or quantized lattice vibration: The energy of phonons is in tens of meV, which is two orders of magnitude smaller than chemical energies. The direct transfer of energy into the phonon system of the metal requires multiple excitations of phonons during chemical processes.

Excitation of electron–hole pairs: The excitation of an electron–hole pair leads to a hot electron with energy above the Fermi level and to a hot hole with energy below the Fermi level. The excitation of an electron–hole pair takes place via a nonadiabatic process.

Emission of charged particles (*exoelectron*) [11, 12] and light (*chemiluminescence*) [13–15] during gas adsorption or reaction is generally attributed to a nonadiabatic charge transfer process.

The phenomena of chemical dynamics often rely on the Born–Oppenheimer approximation (BOA). The approximation relies on the fact that electrons move on a much shorter time scale than nuclei because of the considerable difference in mass [16]. As the nuclei positions change, electrons have ample time to sample the space available to them and find the energy minimum, preventing nuclear motion from causing electronic excitation. This makes it considerably easier to describe the potential energy landscape of polyatomic systems: each electronic level has its own distinct potential surface, with the nuclear coordinates as the only variables. A system that behaves this way is described as adiabatic. Several theoretical models have been developed to explain these phenomena that involve an electronic friction approach or a weak coupling approximation [17–19]. For many gas-phase reactions, the BOA, particularly at low total energies, gives rise to an excellent agreement between experimental and theoretical results, confirming that the BOA is valid for many systems [20–22].

For certain reactions on metal surfaces, however, different nonadiabatic coupling plays a crucial role in energy transfer between the adsorbate and the substrate, and the BOA breaks down [23–26]. Along a given reaction coordinate, two potential energy surfaces, corresponding to two different electronic states, may cross. At the crossing point, an electronic transition requires no change in energy.

Another view to justify the generation of hot electrons is related to the difference in the heat capacity of electrons and phonons. The hot electrons thermalize within

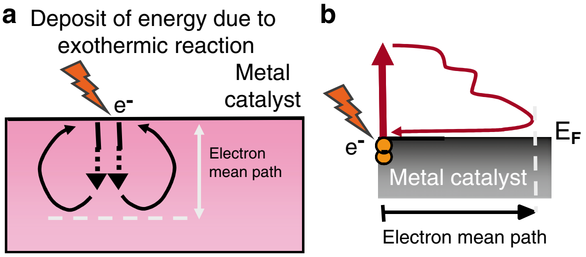

Fig. 10.1 (**a**) Schematic and (**b**) energy diagrams of nonadiabatic electronic excitation during an exothermic reaction on a metallic surface. Hot electrons are generated on the surface, dissipate energy, and turn into low-energy electrons within the length scale of the electron mean free path

picoseconds by electron–phonon interactions. The phenomenon of hot electron creation can be rationalized as follows: The electronic heat capacity (C_{electron}) of most metals in thermal equilibrium is about 100 times smaller than the lattice heat capacity (C_{lattice}) at 300 K. For example, for copper,

$$\frac{C_{electron}}{C_{lattice}} \approx \frac{\gamma \cdot T}{3R} = \frac{0.70\times10^{-3}\times300}{3\times8.3} = 0.008 \tag{10.1}$$

where R is the gas constant and γ is the Sommerfeld constant [0.70 mJ/ (mol K^2) for Cu]. When heat is deposited as a result of exothermic surface reactions or photon flux, the electrons heat up much faster (femtoseconds) than the lattice (picoseconds) because their heat capacity is much lower.

Electronic excitation in exothermic catalytic reactions involves the flow of hot electrons with an energy of 1–3 eV, assuming that most of the chemical energy is converted into electron flow. Thermalization of hot electrons in metals and at metal surfaces occurs on femtosecond time scales due to efficient electron–electron (e–e) scattering with the conduction-band electrons. The electron gas equilibrates with the lattice by electron–phonon (e–p) scattering on a longer, but still subpicosecond time scale. Once the electrons on the metal surface become energetic (or hot) through nonadiabatic electronic excitation, these hot electrons move into the bulk of the metal catalyst, as shown in Fig. 10.1a, and eventually dissipate energy and turn into low-energy electrons through lattice atom relaxation within the length scale of the electron mean free path, which is in the 3–7 nm range. These low-energy electrons can move back to the surface to fill vacancies left by the departed hot electrons. The flow of electrons is analogous to circulation of hot water upon heating, as shown in Fig. 10.1a. This flow of hot electrons takes place only at the near-surface region and is spatially limited by the electron mean free path. Figure 10.1b shows the energy diagram of the flow of hot electrons in the metal catalyst. The role of hot electrons in the metal catalyst is therefore limited, since hot electrons are localized at the near-surface region, and have short lifetimes (10 fs). However, since most metal catalysts are nanoparticles in the 1–10 nm range, hot electrons can reach the oxide–metal interface and overcome the potential barrier to be transported into the oxide.

10.3 Detection of Hot Electrons

A pulse of electrons of high kinetic energy (1–3 eV) in metals can be generated in atomic/molecular processes. Detection of this electron flow has become one of the frontier areas of research in the surface physics and chemistry communities. Showing that nuclear motion couples to electronic excitation is more difficult if the excitation is too small to cause emission. Relaxation of these hot electrons happens on the femtosecond to picosecond timescale, and their mean free path is on the order of 10 nm. This implies two detection strategies: the first is to obtain sufficient time resolution to observe these excitations. The second is to employ an energy barrier at nanometer scale for the irreversible transport of hot electron flows.

10.3.1 Hot Electron Generation by Photons

Two-photon time-resolved photoemission (TPTRP) spectroscopy has been developed to directly study the dynamics of optically excited electrons at metal and semiconductor surfaces. This technique has been applied to direct measurement of hot electron relaxation in noble and transition metals [27, 28], surface-state dynamics on clean and adsorbate-covered metal surfaces [29, 30], as well as charge carrier dynamics in semiconductors, where much work has been performed.

Two-photon photoemission (2PPE) is a variation of photoelectron spectroscopy that allows the investigation of occupied and unoccupied electronic states in a metal or semiconductor [31, 32]. The investigated states are located below the vacuum level in an interval defined by the pump photon energy. To study electron dynamics, we employ femtosecond laser pulses to perform pump–probe experiments. As shown in Fig. 10.2, an initial laser pulse (pump) perturbs the equilibrium population and a second laser pulse (probe), irradiated after time t, probes that transient electron distribution by photoemitting electrons. Measurement of the electrons' kinetic energy provides a straightforward means to determine the binding energy of the perturbed state with respect to the vacuum level. The user-controlled optical path difference between the pump and the probe laser pulses gives temporal resolution in the investigated electronic states.

10.3.2 Hot Electron Generation by Transfer of Energetic Molecules

Hot electrons were also detected in the presence of molecular interactions or exothermic surface reactions at metal surfaces. Huang et al. [23, 33] studied the energy transfer of highly vibrationally excited molecules at surfaces and found efficient (>50 %) excitation of electrons in gold on the subpicosecond timescale by

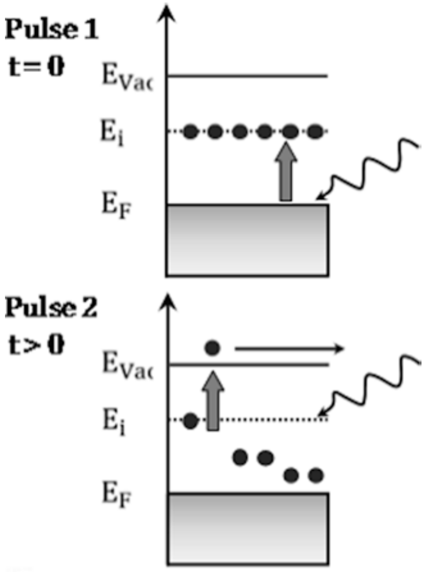

Fig. 10.2 Scheme of two-photon photoemission. Hot electron dynamics are measured by inducing photoemission of hot electrons with a time-delayed probe pulse

NO molecules prepared in high vibrational states ($n=15$) impinging on the metal surface. They found that vibrational energy losses to metals and insulators are quite different. As shown in Fig. 10.3, on a metal, NO ($v=15$) loses on average about half of its vibrational energy in a direct scattering collision (subpicosecond time scale); while on an insulator, NO ($v=12$) loses only a small amount of vibrational energy even when trapping/desorption dominates (piconanosecond time scale). They showed that, compared with the short timescale of molecular-vibration–metal–electron energy transfer (10 fs), other forms of molecular energy transfer processes (vibration–rotation and vibration–translation) have a very low probability and become important only on picosecond timescales. A similar result of multiquantum relaxation was also observed for NO scattering from Cu(111) and O/Cu(111) [34, 35].

10.3.3 Hot Electron Generation by Electron Beams

The detection of photon- or chemically induced electronic excitation became possible with metal–insulator–metal (MIM) tunnel junctions as well as with Schottky devices. In this case, excited carriers are detected that have enough energy to overcome either a tunnel or a Schottky barrier. Therefore, the metal film acts as a substrate for the reaction, as a photon-adsorbing layer, and as an emitter of hot carriers. There have been many experimental attempts to elucidate the nature of hot carriers using the MIM junction structure [1, 36–46]. It was found that hot electrons injected in MIM structures influence the surface reactivity [47–49].

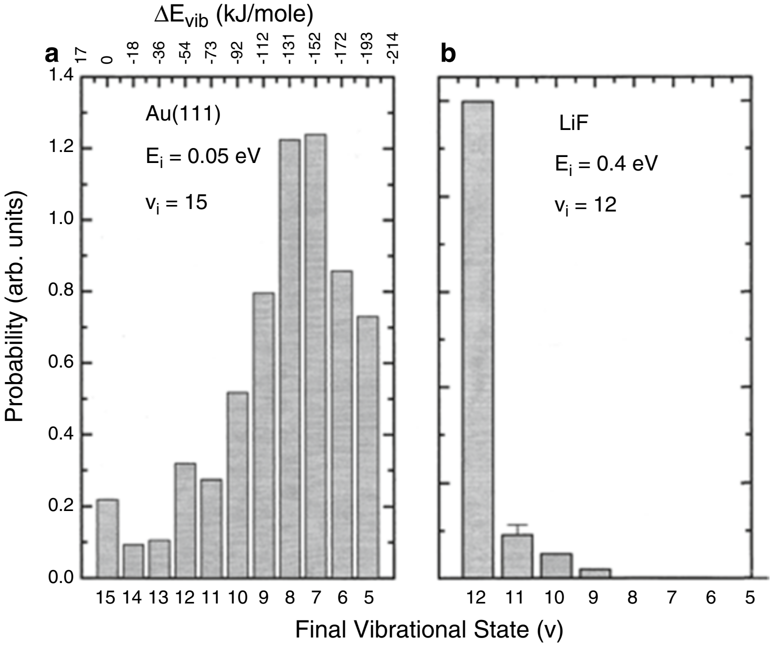

Fig. 10.3 The experimental results of NO vibration on metal or Li are shown. Loss of ~1.5 eV within 100 fs on Au implies an electron-mediated process and almost no vibrational relaxation on the LiF insulating surface [23]. (**a**) Plot of vibrational energy loss to an insulator and (**b**) metal surface for collisions of highly vibrationally excited NO. When NO is prepared in $v=12$, energy transfer to LiF is approximately vibrationally elastic; however, when NO is prepared in $v=15$, collisions with Au(111) transfer an average of 1.3 eV to the surface (Reprinted with permission from ref. [23]. © 2000 AAAS.)

This electronic excitation induces an Auger process leading to hot electron production in the metal that can be emitted into a vacuum or collected using a Schottky diode configuration. Such a process is sensitive to the chemical nature of the reacting molecules, such as O_2 or H_2. A Schottky diode is a type of metal–semiconductor contact. The energy diagram and scheme of Schottky diodes for chemicurrent measurement are shown in Fig. 10.4a, b, respectively. When two different solids are brought into contact, electrons in the higher chemical potential solid tend to flow into the solid with the lower chemical potential until the potentials equilibrate. A negative charge forms where the electrons migrated, and a positive charge forms where the nuclei were left behind. This gives rise to an electric field in the semiconductor that can be represented by bending the energy bands. If electrons are the majority carrier in the semiconductor (an n-type semiconductor), the bands bend downward, leaving no barrier to electron flow. This is referred to as an Ohmic contact, since current through this interface is proportional to voltage.

Nienhaus et al. were the first to successfully measure chemicurrent on a nanodiode [3, 50]. Their devices consisted of Ag and Cu thin films deposited onto n- and p-doped Si wafers, with ohmic contacts on both sides of the wafer. When these diodes were exposed to a beam of H atoms, a current on the order of 0.01–1 nA was

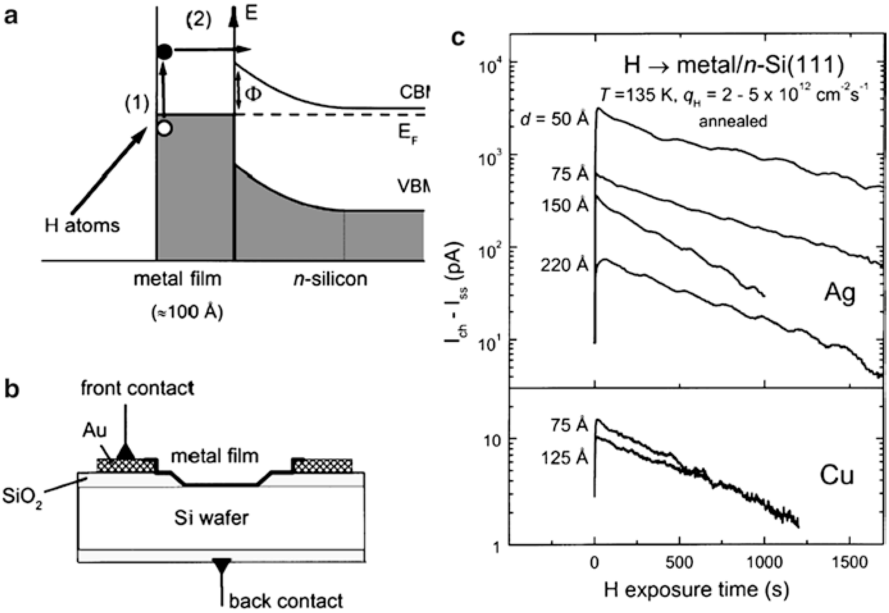

Fig. 10.4 (**a**) Energy and (**b**) schematic diagrams of Schottky diodes for chemicurrent measurement. (a) Hydrogen atoms react with the metal surface, (1) creating electron–hole pairs, followed by (2) the ballistic transport of hot carriers through the metal film. Hot carriers go over the Schottky barrier and move into the semiconductor where the chemicurrent is measured. (**c**) Plot of chemicurrent on Ag and Cu surfaces as a function of hydrogen exposure time [3]. (Reprinted with permission from ref. [50]. © 1999 American Physical Society.)

observed. This chemicurrent decayed exponentially to a steady-state value that agreed with the kinetics of the impinging particles competing for surface sites [3, 50, 51]. Figure 10.4c shows a plot of the chemicurrent on Ag and Cu surfaces as a function of hydrogen exposure time. Nienhaus et al. found that the number of electrons detected per adsorption event (or chemicurrent yield) is 4.5×10^{-3} for Ag and 1.5×10^{-4} for Cu. This sensitivity difference can be attributed to the shorter mean free path of electrons in Cu films, compared with that of Ag films [52]. Also, the difference in sensitivity was attributed to the possible formation of silicide between the copper and silicon, giving rise to higher roughness and thus, more scattering centers in the Cu/Si.

10.4 Detection of Hot Electrons from Exothermic Catalytic Reactions

One of the key issues in heterogeneous catalysis is the role of metal–oxide interfaces in altering catalytic activity. The smart design of nanocatalysts can improve the catalytic activity of transition metals on reducible oxide supports, such as Pt nanoparticles or nanowires on a titania substrate, via strong metal–support interactions (SMSI). The SMSI effect refers to changes in the catalytic activity when group VIII metals (i.e., Fe, Ni, Rh, Pt, Pd, and Ir) are supported on certain oxides (e.g., TiO_2, TaO_5, CeO_2, NbO), where, for example, methane formation from CO or CO_2 and H_2 is enhanced by 3 orders of magnitude [53–56].

The role of the metal–oxide interface in enhancing catalytic activity was first suggested by Schwab and others, who performed oxidation of carbon monoxide on Ag/NiO [57, 58]. As reported by Hayek and others, the reaction rate in the oxide–metal model system depends on the oxidation state of the supporting oxide, the free metal surface area, and the number of sites at the interface between the metal and the support [59–61]. The origin of such metal–oxide interactions is attributed to either geometric or electronic effects. The geometric effect assumes that the active surface area of the noble metal changes during the reduction process.

The electronic effect involves charge transfer between the metal and the oxide support. Elucidation of the origin of the metal–support interaction requires measurement of the charge transfer through the oxide–metal interface. To detect this charge transfer (or flow of hot electrons) under catalytic reaction conditions, metal–semiconductor Schottky diodes have been developed [3, 62]. In this section, we will outline recent research on catalytic nanodiodes. The detection of hot electrons under various catalytic reactions and the influence of hot electrons in catalytic reactivity will also be discussed in this section.

10.4.1 Concept of Catalytic Nanodiodes

If the metal particle or film is the diameter or thickness of the electron mean free path (~10 nm), hot electrons can be collected as they are transported across the metal without collision, as shown in Fig. 10.5a. For an n-type Schottky diode, hot electrons are detected as a chemicurrent if their excess energy, E_{ex}, is larger than the effective Schottky barrier, $E_{ex} = |E - E_F|$, which is the difference between the conduction band minimum and the Fermi energy, E_F, at the interface. Once hot electrons arrive at the oxide, they dissipate energy and thus cannot go back to the metal. Therefore, the Schottky energy barrier leads to irreversible, one-way charge transfer of hot electrons from the metal to the semiconductor, as shown in Fig. 10.5b. After hot electrons move from the metal to the semiconductor, they are replaced by low-energy electrons supplied by the external leads connected to the Pt and the semiconductor, resulting in the continuous flow of hot electrons generated by the catalytic reaction. The hot electron flows also correlate with the turnover rate of CO oxidation, as measured separately by gas chromatography [63]. Photon energy has been observed being converted into hot electron flows with metal–semiconductor diodes [64, 65]. The detection of hot electrons may lead to a fundamental understanding of energy dissipation and conversion processes, which would introduce new opportunities for energy conversion.

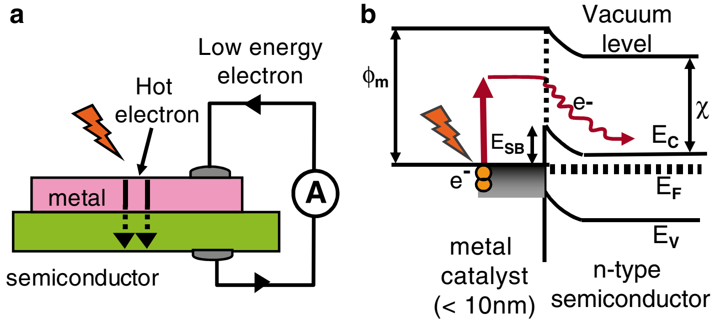

Fig. 10.5 (**a**) Scheme and (**b**) energy diagram of catalytic nanodiodes. Hot electrons can be generated by exothermic catalytic reactions

10.4.2 *Fabrication and Characterization of Metal–Semiconductor Nanodiodes*

Vertically oriented metal/TiO_2 Schottky diodes were fabricated on an insulating Si(100) wafer covered by 100 nm SiO_2. The back electrode was formed by an electron beam evaporating a 100 nm Au contact pad on top of a 30 nm titanium adhesion layer, as shown in Fig. 10.6. A portion of the Au contact pad was then covered with 30 nm of titanium, forming an ohmic contact between the Au pad and the titanium oxide semiconductor, due to the low work function of titanium. Reactive direct current (dc) magnetron sputtering was used to deposit approximately 150 nm of titanium oxide. During sputtering, the bias voltage was 430 V, O_2 pressure was 11–12 sccm, and Ar pressure was 37 sccm. The resistivity of titanium oxide is 0.3–0.4 Ω cm, as measured using a four-point probe. A portion of the titanium oxide layer was covered by 200 nm of silicon nitride deposited by plasma-enhanced chemical vapor deposition to prevent electrical shorting between the titanium oxide and the top contact layer. The Schottky contact was then formed by electron-beam evaporation of 5 nm of metal in a 3 mm diameter circle, one-third of which contacted the titanium oxide and two-thirds of which contacted the silicon nitride insulating layer. The top electrical contact was then formed on top of the Pt or Pd on the silicon nitride by an electron beam again depositing a 100 nm Au contact pad.

The Pt/GaN diode was fabricated on n-type GaN/sapphire substrates. The GaN crystal has the wurtzite structure and the orientation of (0001) c-axis Ga face within 0.5°. The thickness of the GaN epitaxial layer is 5 μm, and the resistivity is 1–5 Ω cm. The wafers were sonicated successively in trichloroethylene, acetone, and methanol to remove contaminants and boiled in 1.0 N KOH for 10 min to modify the surface topography. A 200 nm SiO_2 insulating layer was formed on the GaN surface via electron-beam evaporation, as shown in Fig. 10.6. This layer prevents the low-work-function contact pads from short circuiting the devices. Five nanometers of Pt were then deposited via electron-beam evaporation to form the Schottky contact. The Pt/GaN contact area is approximately 1 mm^2. Finally, the Ti/Al ohmic contacts were deposited to complete the devices.

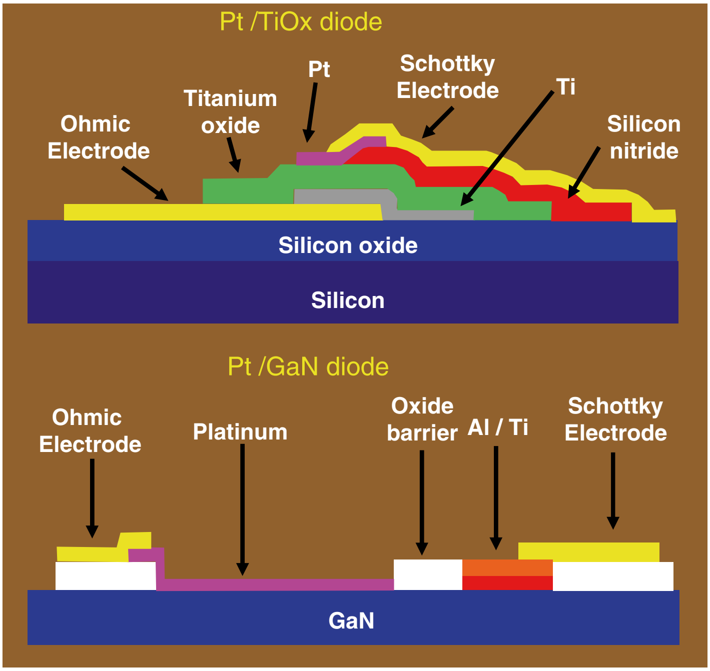

Fig. 10.6 Scheme of Pt/TiO_2 and Pt/GaN nanodiodes. (Reprinted with permission from ref. [70]. © 2007 American Chemical Society.)

The formation of a Schottky barrier between Pt and TiO_2 or GaN has been reported previously. Ali et al. fabricated Pt/GaN gas sensors and measured a Schottky barrier height of 0.92 eV based on thermionic emission theory [66]. Wang et al. reported barrier heights of 1.1 and 0.96 eV based on current–voltage measurements on Pt/GaN and Pd/GaN diodes, respectively [67]. Dittrich et al. reported Schottky barrier heights of 1.2–1.3 eV on Pt/TiO_2 diodes [68]. This energy barrier is high enough to suppress the contribution of the thermal excitation of electrons to electron flow.

To determine barrier heights and ideality factors for the nanodiodes, we fit the current–voltage curves of our devices to the thermionic emission equation. For thermionic emission over the barrier, the current density of Schottky contacts as a function of applied voltage is given by [69].

$$I = FA^{*}T^{2}\exp\left(-\frac{\phi_n}{k_B T}\right)\cdot\left[\exp\left(\frac{e_0\left(V_a - R_S I\right)}{\eta k_B T}\right) - 1\right] \tag{10.2}$$

where F is the area, A^* is the effective Richardson constant, Φ_n is the Schottky barrier height, η is the ideality factor, and R_S is the series resistance. The effective mass of the conduction electrons in GaN, $m^* = 0.22m_0$, gives an effective Richardson constant: 2.64×10^4 A/cm^2 K. The effective Richardson constant for TiO_2 is 24 A/cm^2 K.

10.5 Hot Electron Flows Detected on Catalytic Nanodiodes Under Exothermic Catalytic Reaction

A batch reaction system, combined with electrical measurement, was built to carry out the gas-phase reaction [71]. The reaction cell was evacuated down to 5×10^{-8} Torr by a turbomolecular pump. A ceramic heater was used to change the temperature of the sample. Since the thermocouple was fixed between the backside of the sample and the ceramic heater, the temperature difference between the thermocouple and the sample surface can be ignored. The temperature controller provided feedback to the current applied to the heater that kept the fluctuations of the temperature below 0.5 K. A sampling loop, including a gas chromatograph and a circulation pump, continuously measured reaction rates from the reactant and product concentrations. The hot electron current between the two gold electrodes was measured during the chemical reaction using a current preamplifier. For electrical characterization of the diodes, current–voltage measurements were performed by sweeping the voltage between the two electrodes and measuring the resulting current. For the case of measuring the chemicurrent under a chemical reaction, the current signal between the two electrodes was measured with an applied voltage of 0 V.

It was found that a continuous flow of ballistic charge carriers was generated by an exothermic catalytic reaction and detected using various catalytic metal–semiconductor Schottky diodes. Ji et al. found that hot electron currents were generated at steady state for several hours using two types of catalytic nanodiodes, Pt/TiO_2 and Pt/GaN Schottky nanodiodes, under carbon monoxide oxidation catalyzed by the platinum [72, 73]. This experiment clearly verified that the proposed method converts chemical reaction energy directly into hot electrons. This contrasted sharply with prior work, which generated transient currents utilizing adsorption reactions in ultrahigh vacuum at 130 K.

The current signal was measured between two gold contacts of Pt/TiO_2 diodes under reaction conditions and under pure He. Zero bias was applied between two Au contacts during the current measurement. When the diode was under 1 atm He, the thermoelectric current due to the elevated temperature was observed. The thermoelectric current is caused by the difference in electrical potential between the two electrodes because of the Seebeck effect. We found that the thermoelectric current was mainly influenced by the Seebeck coefficient of each layer of diodes. In the case of the Pt/TiO_2 and Pd/TiO_2 diodes, the thermoelectric current moved in the opposite direction as the chemicurrent. In case of the Pt/GaN diode, while the thermoelectric current was smaller than that of Pt/TiO_2, the chemicurrent increased at a lower temperature than Pt/TiOx. Interestingly, the thermoelectric current in the Pt/GaN diode was in the same direction as the chemicurrent and the current value was much smaller than that of the Pt/TiO_2 and Pd/TiO_2 diodes. This suggests that the thermoelectric current is crucially influenced by the thermoelectrical properties of the semiconductor layer. The higher thermoelectric current of the TiOx-based diode could be associated with the extraordinarily high Seebeck coefficient of TiO_2 (the Seebeck coefficient of TiO_2 is 0.4 mV/K at 573 K). The smaller value and different

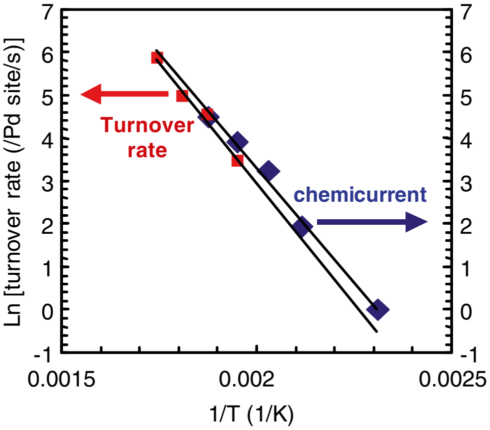

Fig. 10.7 Arrhenius plots of chemicurrent and turnover rate measured on the Pd/TiO_2 diode under CO oxidation. (Reprinted with permission from ref. [70]. © 2007 American Chemical Society.)

polarity of the Seebeck coefficient for GaN (–0.05 mV/K at 300 K) is consistent with the variation of thermoelectric currents measured on the Pt/GaN.

Heat transfer from the exothermic chemical reaction to the Pt surface could also increase the local sample temperature independent of the heater. We found the increase in temperature caused by the exothermic reaction in our experimental range (up to a turnover rate of 10^3 molecules per Pt site per second) based on the thermal transport equation can be ignored (less than 10^{-3} K) [6]. The small increase in local temperature is due to the structure of the diode (nanometer-scale layer thickness and millimeter-scale spatial size of layers).

Figure 10.7 shows the chemicurrent and turnover rate under 100 Torr O_2 and 40 Torr CO as a function of the temperature measured on the Pd/TiO_2 diode. The chemicurrent suddenly starts at 413 K. While the detection of current flow between 413 and 473 K is clear, the accumulation of CO_2 in that temperature range was too low to be detected by gas chromatography. This suggests that the hot electron current is a more sensitive probe than gas chromatography to measure and monitor the catalytic chemical reaction. This increased sensitivity for hot electron detection may have potential applications for chemical sensors. The number of electrons per the number of CO_2 molecules produced is estimated to be $1–2 \times 10^{-4}$, from the measurement of chemicurrent and turnover rates. We note that this value depends on surface cleanness, Pt thickness, and the conductivity of the TiO_2 layer. From the slope of the Arrhenius plot of chemicurrent and turnover rate in the temperature range of 413–573 K, the activation energy of the carbon monoxide reaction on the Pt/TiO_2 nanodiode was determined. The activation energy obtained from the current measurement was 21 kcal/mol, and a similar value was derived from gas chromatography (~22 kcal/mol) [63, 70]. Likewise, the Pd/TiO_2 diode exhibits an E_a of 20.4 kcal/mol (chemicurrent measurement) and 21.1 kcal/mol (turnover measurement) [70]. This excellent correlation between hot electron flux and turnover rate observed both on the Pt/TiO_2 and Pd/TiO_2 diodes suggests that current measurement can indeed be used for monitoring the chemical reaction in a quantitative manner.

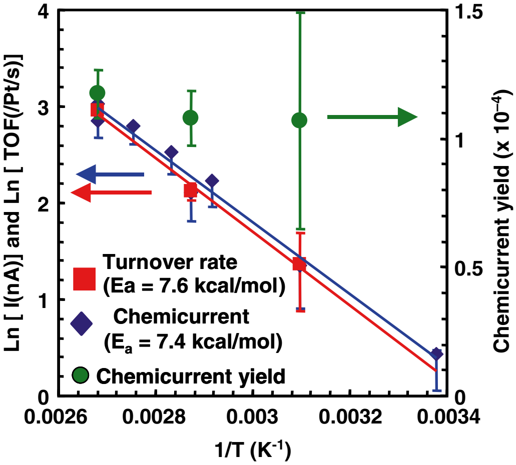

Fig. 10.8 Arrhenius plots obtained from chemicurrent and turnover measurements on a Pt/TiO_2 diode with a pressure of 6 Torr H_2 and 760 Torr O_2. Both give similar activation energies, which implies that hot electron generation under hydrogen oxidation is proportional to the catalytic turnover rate. The error is associated with multiple measurements of the chemicurrent and turnover rates. (Reprinted with permission from ref. [62]. © 2009 American Chemical Society.)

Continuous flux of energetic (hot) electrons during catalytic hydrogen oxidation was detected using Pt/TiO_2 catalytic nanodiodes at atmospheric pressures. Chemicurrent was measured at different temperatures on a Pt/TiO_2 diode in 6 Torr H_2 and 760 Torr O_2, as shown in Fig. 10.8a. Since TiO_2 is quickly (within seconds) reduced by atomic hydrogen, which diffuses through the platinum film [74], and since the hydrogen/oxygen mixture is explosive in certain conditions, oxygen is used in large excess (>99 %). The reaction is conducted in a ~1 L batch reactor and pumped down to 10^{-6} Torr between runs. Under these hydrogen oxidation conditions, where we have a large excess of oxygen, the diodes sustain their rectifying behavior [62]. This suggests that the oxygen keeps the semiconductor portion of the diode oxidized, or prevents the hydrogen from diffusing through the platinum. With spillover largely absent, the Schottky barrier remains constant on the time scale of these experiments.

Figure 10.8 shows the number of water molecules per platinum site produced on the Pt/TiO_2 diode under 6 Torr H_2 and 760 Torr O_2, as a function of time; it is assumed that the surface Pt site density is equivalent to that of Pt(111). The turnover frequency at different temperatures, obtained by taking the slope of the plots, increases with temperature. The thermoelectric current was measured separately under 760 Torr He and was found to be lower than 0.3 nA at 373 K. Because the current detected under hydrogen oxidation at 373 K (17 ± 1 nA) is much higher than the thermoelectric current, most of the current signal can be attributed to the chemicurrent. The reaction is concurrently monitored using a gas chromatograph to determine the chemicurrent yield (number of electrons detected per reaction event).

The activation energy is determined using the turnover rate and chemicurrent measured as a function of temperature.

The resulting Arrhenius plots are shown on the same graph. The error bars in the plot correspond to the standard deviations of the measurements. The two resulting activation energies match (7.4 ± 0.3 kcal/mol for chemicurrent and 7.6 ± 0.6 kcal/mol for turnover rate), which implies that the chemicurrent originates from the catalytic reaction. Again, the thermoelectric current is negligible (<0.3 nA) in the temperature range (298–373 K) used here. Previously, the effect of an increase in the sample temperature due to the heat of reaction has been shown to be negligible [63]. The activation energy for hydrogen oxidation under identical conditions (6 Torr H_2 and 760 Torr O_2) measured separately on a Pt foil is 8.3 (± 0.6) kcal/mol, which is comparable, within the experimental error, to that on Pt/TiO_2 nanodiodes. The dependence of chemicurrent and turnover rate on the partial pressure of H_2 was also investigated. The partial pressure dependence shows a linear relationship between water formation and H_2 partial pressure, consistent with the Langmuir–Hinshelwood mechanism.

The apparent chemicurrent yield can be obtained by dividing the chemicurrent (number of electrons per second) by the turnover rate (number of product molecules per platinum site per second). Therefore, the chemicurrent yield represents the hot electrons collected per product molecule formed on a single metal site. Its value in hydrogen oxidation, based on measurements at several different temperatures, is $(1.1 \pm 0.1) \times 10^{-4}$. The apparent yield in CO oxidation on the same 5 nm Pt/TiO_2 diode [70] is $2.3 \pm 0.5 \times 10^{-4}$. The lower chemicurrent yield of H_2 oxidation compared with CO oxidation may be associated with the lower reaction heat of H_2 oxidation (2.5 eV per product molecule, H_2O [75, 76]) versus that of CO oxidation (2.9 eV per product molecule, CO_2 [77]).

10.6 Hot Electron Flows Detected Upon Photon Absorption

The concept of photon energy conversion to hot electron flow was suggested by McFarland and Tang [78]. In this scheme, photons are harvested by dye molecules adsorbed on a Schottky diode composed of a thin gold layer on TiO_2. When light falls on the dye layer, electrons are released from the dye molecules and injected into the conduction band of the metal layer. The disadvantage of this scheme is the ineffectiveness of the adsorbed dye molecules in producing photocurrents. One reason for this is that electrons injected by the dye layer into the metal can be immediately recaptured through reverse charge transfer from the filled electronic states of the metal into the dye, resulting in no net current flow.

Use of a metal–semiconductor Schottky diode allowed for the measurement of the steady-state current from the continuous flow of ballistic charge carriers generated by the absorption of photons. Schemes of the photovoltaic device are also described in Fig. 10.9a. To generate electric current through the device, these electrons need enough energy to travel over the Schottky barrier and into the TiO_2 conduction band.

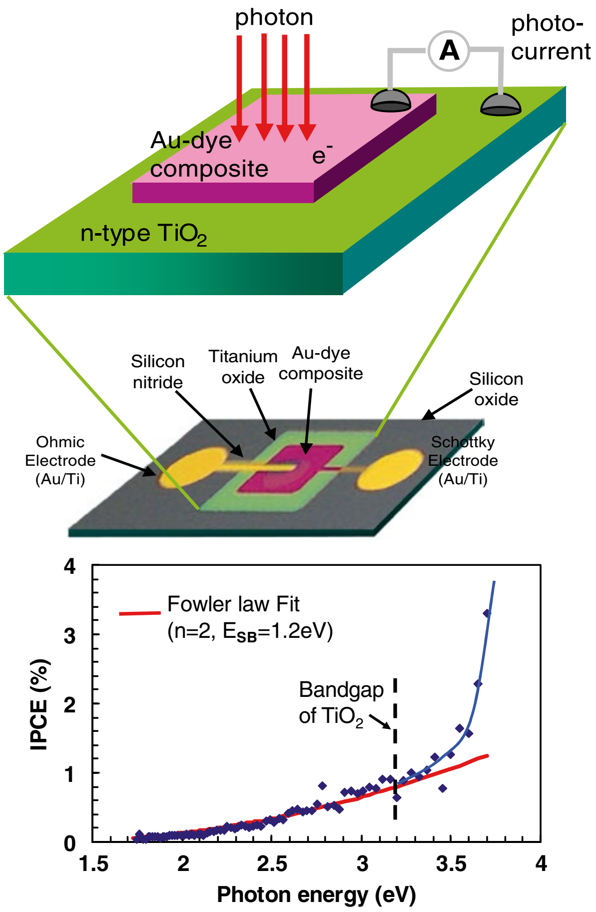

Fig. 10.9 (**a**) Schemes for hot electron flow detection from photon absorption and surface plasmon-driven hot electrons on the modified metal–semiconductor diode. (**b**) Photocurrent measured as a function of photon energy on a Pt/TiO_2 diode with a metal film thickness of 5 nm. The *red line* represents the Fowler's law fit with fitting parameters of $n = 2$ and $E_{SB} = 1.2$ eV

The short-circuit photocurrent was measured as a function of the wavelength of light on the metal–semiconductor Schottky diodes. Figure 10.9b shows the plot of the short-circuit photocurrent as a function of photon energy measured on a Pt/TiO_2 diode with a metal film thickness of 5 nm. The photocurrent increases with increasing photon energy. In order to verify the relation between the hot electron flux and the photon energy, we fit the photocurrent to Fowler's law [79, 80]. According to Fowler's law, the photoelectric current, I, is

$$I = c\left(h\nu - \phi\right)^n$$

where c is a constant, ϕ is the work function of the sample, and $h\nu$ is the photon energy. For most metals, $n = 2$; other exponents apply to semiconductors. Figure 10.9b also shows the fit of photocurrent to Fowler's law with the fitting parameter of $n = 2$ and ϕ (in our case, E_{SB}, the Schottky barrier height) of 1.2 eV.

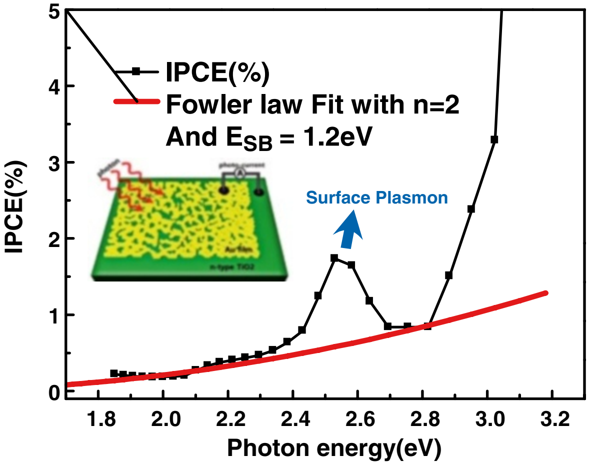

Fig. 10.10 Incident photon to current conversion efficiency (IPCE) measured as a function of photons on a Au/TiO$_2$ diode after heating at 433 K to obtain Au island structures. The inset depicts the formation of the metallic nanoscale domains. (Reprinted with permission from ref. [65]. © 2011 American Chemical Society.)

The fitting result shows that the measured photocurrent is in good agreement with Fowler's law. This result confirms that the measured photocurrent is mainly attributed to the hot electron flow, assuming that the contribution by defect states localized in the bandgap of TiO$_2$ can be ignored. At high photon energy (>3.2 eV), the photocurrent increases significantly, showing a departure from the Fowler's law fit, indicating an additional contribution of electron–hole pair excitation in the titanium oxide. This result indicates that the steady-state flow of hot electrons generated from photon absorption can be directly probed with metal–semiconductor Schottky diodes.

Recently, Lee et al. [65] proposed a scheme for enhanced light absorption with localized surface plasmon resonance and, therefore, for enhanced hot electron generation by utilizing Au/TiO$_2$ Schottky diodes with no dye layers, as illustrated in Fig. 10.10. The morphology of the metal thin film was modified to a connected gold island structure that exhibited surface plasmons. The nanometer-scale domains in the connected gold island structure were electrically connected to the ohmic pad, ensuring measurement of the flow of hot electrons. The photocurrent was measured to determine the correlation between surface plasmons and hot electron flows on the modified Au/TiO$_2$ Schottky diodes. An enhancement of the internal photoemission was observed by changing the surface morphology [65, 81] or adapting the dye molecules [82] or nanowires [83] in such a way that the surface exhibits nanoscale domains with a strong localized surface plasmon resonance.

10.7 Influence of Hot Electrons on Surface Chemistry

Understanding the mechanisms for electronic excitation in exothermic chemical processes on surfaces is a long-standing question of both fundamental and practical importance. Recent experimental and theoretical studies have demonstrated electronic excitation due to chemisorption and physisorption of gases at surfaces and by chemical reactions at surfaces. Electronic excitation in exothermic catalytic reactions involves the flow of hot electrons (1–3 eV), assuming that most of the chemical energy is converted to electron flow [3, 9, 84]. A catalytic nanodiode was reported that detected a steady-state flux of hot (>1 eV) conduction electrons generated during a gas-phase exothermic reaction on the surface of Pt metal [6, 62, 71, 85]. Earlier studies on Pt/TiO_2 catalytic nanodiodes show that the activation energy of chemicurrent and catalytic activity are quite similar (~21 kcal/mol for CO oxidation [63, 71]; 7.4–7.6 kcal/mol for H_2 oxidation [62]), which indicates a correlation between the hot electron flows and catalytic reaction. Furthermore, it has been demonstrated that hot electron flows can influence atomic or molecular processes, including desorption [86], diffusion [87], and isomerization of molecules [88, 89]. In this chapter, we outline recent results revealing the influence of hot electrons on surface chemistry and catalysis.

10.7.1 Influence of Hot Electrons on Atomic and Molecular Processes

It was found that incident hot electrons could induce atomic-scale hydrogen desorption through electronic and vibrational excitation mechanisms. Shen et al. [86] utilized hot electrons released from scanning tunneling microscopy (STM) to desorb hydrogen from hydrogen-terminated Si(100) surfaces. Two atomic-scale mechanisms were suggested in this study: direct electronic excitation of the Si–H bond by field-emitted hot electrons, and multiple-vibrational excitation by tunneling electrons at low tip voltage.

It was found that the hot electrons promote other molecule processes, such as diffusion and isomerization. Fomin et al. [87] investigated the diffusion of isolated H_2O and D_2O molecules on Pd(111) using STM at low temperature (~40 K). While at low tunneling voltage, the diffusion is thermally activated; the diffusion rate is enhanced by several orders of magnitude when the tunneling electron has enough energy to excite the vibrational “scissor” mode of the molecule. Choi et al. [88] and Henzl et al. [89] reported a *trans*-*cis* conformational change of isolated azobenzene (AB) molecules induced by the hot electrons from the STM tips. Based on spatially resolved STM or scanning tunneling spectroscopy, Choi et al. observed that a reversible, conformational change in AB can take place.

There are a growing number of experimental and theoretical evidences showing that surface reactivity can be affected by hot electrons. For example, theoretical work by Gadzuk et al. on hot electrons at the MIM electrode suggests the concept of “hot electron chemistry” [9, 90]. Diesing et al. found that the hydrogen evolution reaction is promoted under bias voltage to the junction [36]. Promotion of decomposition of chlorinated hydrocarbons by electron emission was observed by Sharpe et al. [47]. Bias-voltage-induced decomposition of 2-methyl-1,4-naphthoquinone was observed by Wadayama et al. on the MIM tunnel junction [48].

10.7.2 Hot Electron Effect on Metal–Oxide Hybrid Nanocatalysts

Hybrid nanostructures, such as metal–semiconductors [91–93] and semiconductor–semiconductors [94, 95], offer an interesting platform to investigate the effect of the metal–semiconductor junction on heterogeneous catalysis. The critical issue in synthesizing these nanostructures is controlling the interface between the metal–semiconductor, which plays an important role in determining the type of barrier and in generating hot electrons. Recently, Kim et al. studied the catalytic activity of the CO oxidation reaction on Pt–CdSe–Pt nanodumbbells and Pt nanoparticles on GaN substrates in the dark and with light irradiation to elucidate the role of hot electrons in the catalytic reaction [96].

Figure 10.11a shows schematic drawings (*left*) of the flow of hot electrons formed on a Pt–CdSe–Pt nanodumbbell under light irradiation, and how the hot electrons participate in the CO oxidation reaction. Electron–hole pairs can be generated on the semiconducting region upon absorption of photons, and the hot electrons can go over the barrier between the semiconductor and the metal and be injected onto the surface of the Pt nanoparticles, as illustrated in the energy band diagram (*right*). Figure 10.11b shows representative TEM images of the Pt–CdSe–Pt nanodumbbells, which reveal both-sided growth of Pt nanoparticles onto 15 × 4 nm (length × diameter) CdSe quantum rods. The average size of the Pt nanoparticle is 2.2 nm, and the length of the CdSe nanorod is 15 nm.

CO oxidation on Pt–CdSe–Pt nanodumbbells was carried out to identify the role of hot electrons in surface chemical reactions during light irradiation. It was shown that, during light irradiation, the nanodumbbells show a higher catalytic activity than when in the dark. This result implies that hot electrons created by light absorption influence the CO oxidation reaction on the Pt–CdSe–Pt nanodumbbells. CO oxidation carried out on bare Pt nanoparticles didn't show any change with light irradiation. The influence of photon energy on catalytic enhancement was studied by using both a short-wave pass filter (SWF) that passed light with a photon energy ($h\nu$) between 2.0 and 3.0 eV and a long-wave pass filter (LWF) that passed light with a photon energy ($h\nu$) between 1.0 and 2.0 eV. As shown in Fig. 10.11c, the Pt–CdSe–Pt nanodumbbells irradiated by light with a higher photon energy ($2.0\ \text{eV} < h\nu < 3.0\ \text{eV}$) were two times more active for CO oxidation, compared with irradiation by light with a lower photon energy ($1.0\ \text{eV} < h\nu < 2.0\ \text{eV}$). In the latter case, the catalytic activity was very similar to CO oxidation in the dark. Therefore, this additional experiment affirms that hot electrons are generated when irradiated with light having a photon energy above the bandgap energy (E_g) of the CdSe rods and that the hot electrons promote the CO oxidation reaction on the Pt metal.

In order to elucidate the effect of the type of hot carrier in a catalytic chemical reaction, the CO oxidation reaction was carried out on colloidal Pt nanoparticles on p- and n-type GaN under light irradiation. Schafer et al. observed that the type of gallium nitride (GaN) doping affected the reactivity of the Pt nanoparticles. They suggest that this is due to the strong electronic interaction between the nanoparticles

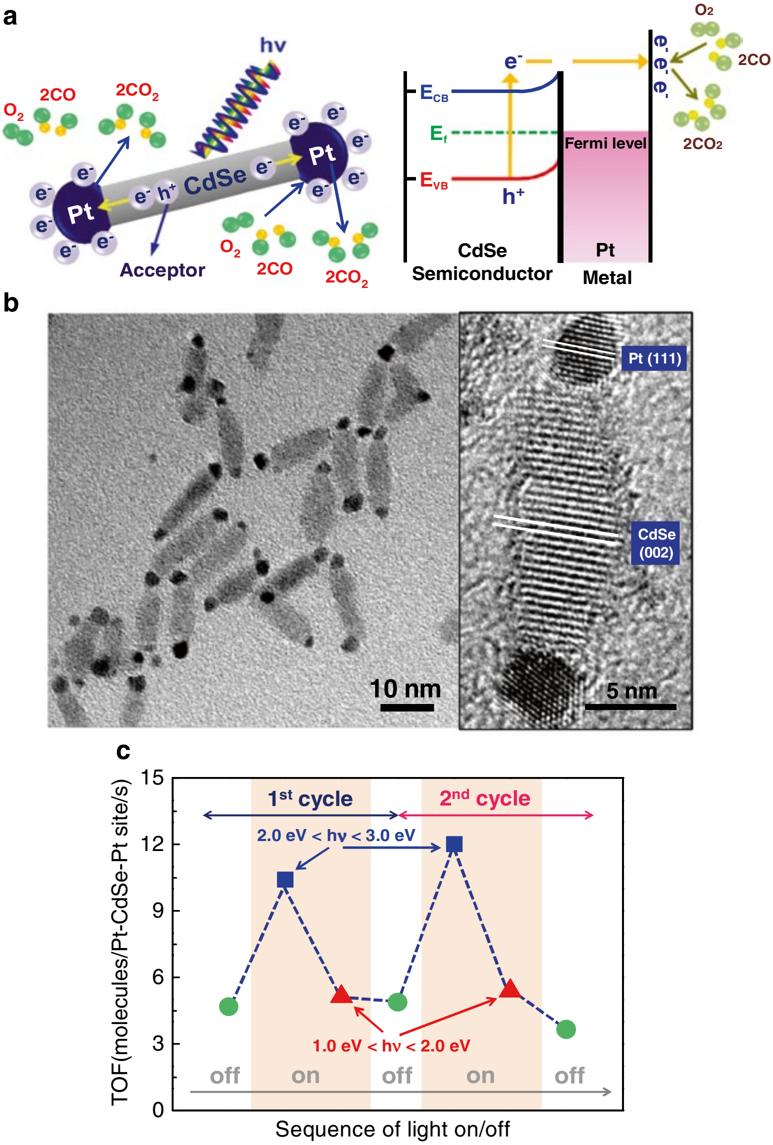

Fig. 10.11 (**a**) Schematic drawing representing the flow of hot electrons formed on a Pt–CdSe–Pt nanodumbbell under light irradiation, (*right*) the contribution of hot electrons in the CO oxidation reaction, and (*left*) the band alignment between the CdSe semiconductor and the Pt metal tips. (**b**) TEM images of Pt–CdSe–Pt nanodumbbells. The CdSe lattice for the rod in the center and Pt tips at the rod edges can be identified, as marked. (**c**) Catalytic activity of Pt–CdSe–Pt nanodumbbells without light, with light having high photon energy (2.0 eV < $h\nu$ < 3.0 eV), and with light having low photon energy (1.0 eV < $h\nu$ < 2.0 eV) measured under CO oxidation at 553 K. (Reprinted with permission from ref. [96]. © 2013 American Chemical Society.)

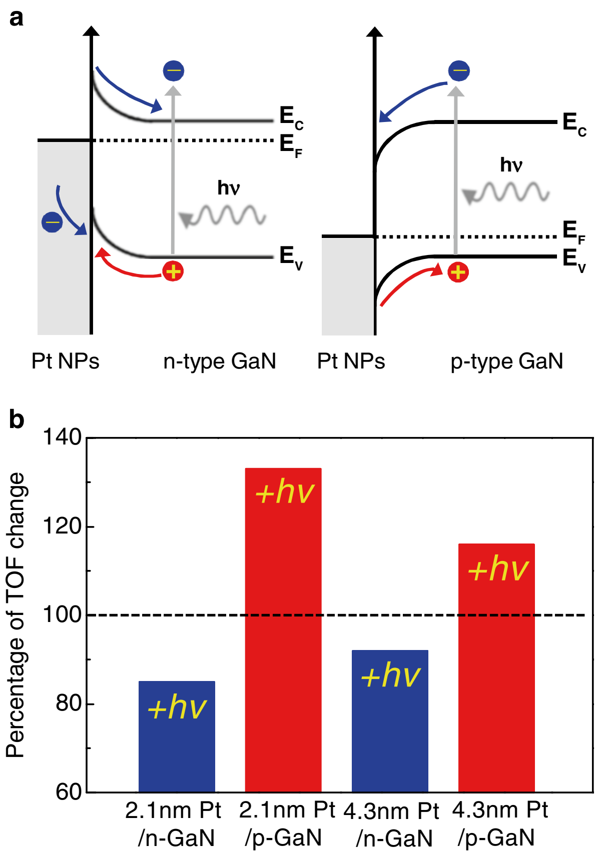

Fig. 10.12 (**a**) Band diagram of Pt/GaN substrates revealing the intrinsic relationship between hot electron flows and catalytic activity according to the type of doping of the semiconductor. (**b**) Plot of percentage change of turnover rate on Pt nanoparticle/n-type GaN and Pt/p-type GaN for two different nanoparticle sizes (2.1 and 4.3 nm). (Reprinted with permission from ref. [98]. © 2013 Royal Society of Chemistry.)

and the n- or p-type GaN substrates, showing a large influence on the chemical composition and oxygen affinity of the supported nanoparticles under X-ray irradiation [97].

Kim et al. carried out the CO oxidation reaction on Pt colloid nanoparticles on n- and p-doped GaN substrates with and without light to identify the role of hot carriers in the chemical reaction [98]. The capping layer-free Pt nanoparticles deposited with arc plasma deposition [99, 100] on the GaN substrate were also used as model catalysts to understand the role of capping layers. With the given energetic alignment, recombination of electrons from the nanoparticles with holes from the n-type semiconductor under illumination is expected. Likewise, electron transfer to the Pt nanoparticles is expected for the p-type supports, as illustrated in the energy band diagram (Fig. 10.12a). Such an interfacial charge transfer process would lead to a reduced net charge of the Pt nanoparticles on the n-type GaN and an increased net charge on the p-type GaN. This change in net charge according to the type of GaN doping will influence the difference in catalytic activity.

As shown in Fig. 10.12b, the catalytic activity of the Pt nanoparticles supported on GaN under light irradiation exhibited a distinct change, depending on the doping type. The catalytic activity of the Pt nanoparticles on the n-doped GaN wafer decreased by 8–28 % under light irradiation compared with no irradiation (i.e., in the dark), while the Pt nanoparticles on the p-doped GaN wafer increased by 11–33 % under light irradiation compared with no irradiation. The catalytic activity increased on the smaller Pt nanoparticles compared with the larger nanoparticles, presumably due to the mean free path of the hot carriers. Also, the capping layer-free Pt nanoparticles deposited via arc plasma deposition showed the same trend, with increased activity on the p-doped GaN wafer, suggesting that the observation is general.

The change in catalytic effect influenced by hot electron flow is due to the electron–hole pairs generated by the absorption of photons on CdSe, causing the ballistic transport of hot electrons to the Pt surface, which then affects the catalytic CO oxidation reaction. The negatively charged CO^{2-} or O^{2-} transition states, after accepting electrons from the CdSe, can be formed on the Pt surfaces. The hole generated in CdSe can move to the silicon substrate (in the case of Pt–CdSe–Pt nanodumbbells) or to the GaN bulk (in the case of Pt/GaN) to complete the closed cycle. Earlier theoretical density functional theory studies showed that hot electron generation is mediated via a negatively charged CO^{2-} transition state [5], implying the important role of negatively charged reaction intermediates and leading to a correlation between turnover rates and electron flow. Another plausible mechanism involves activation of Pt–O bonds by hot electrons, resulting in their reaction with coadsorbed CO [101]. Nevertheless, these results demonstrate the effect of hot electrons on catalytic reactions with metal–semiconductor hybrid nanocatalysts.

10.8 Concluding Remarks and Future Perspective

As to the future direction of hot electron studies, several topics, including development of hybrid nanoparticle–nanodiode systems, and in situ surface characterization, are illustrated in Fig. 10.13. A more fundamental understanding of hot electron phenomena would be required on both the theoretical and experimental sides. Hot electrons on a metallic surface can be created by external energy deposition in the form of photons, ions, electrons, and chemical reactions. Therefore, we can consider hot electrons to be a major mediator for general energy conversion. The scheme of energy conversion from chemical (catalytic reactions) and photon energy to electrical energy (hot electron current) may give insight into other types of energy sources, including solar cell and photocatalytic devices, as illustrated in Fig. 10.14.

In this chapter, we discussed recent studies of the role of hot electron flows in surface chemistry and heterogeneous catalysis. We reviewed various energy

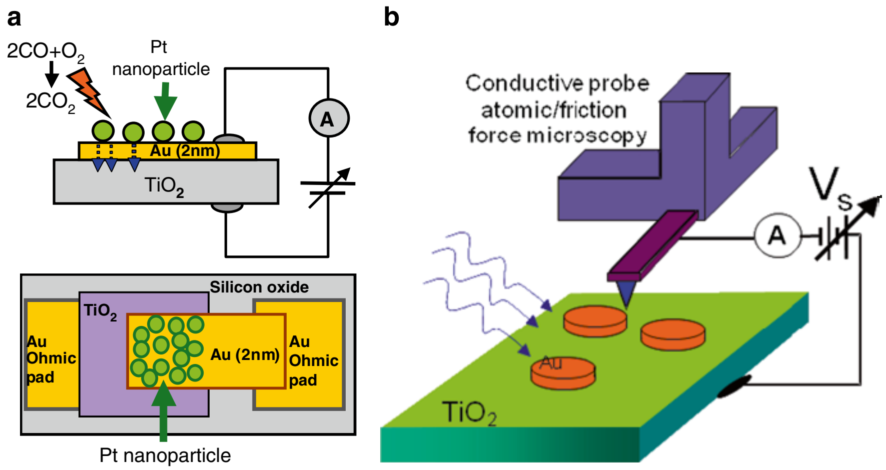

Fig. 10.13 Future directions of hot electron studies, including (**a**) development of hybrid nanoparticle–nanodiode systems, and (**b**) in situ surface characterization. The cartoon depicts the conductive atomic force microscopy experiments on Au/TiO_2 nanostructures under exothermic catalytic reactions or photon irradiation

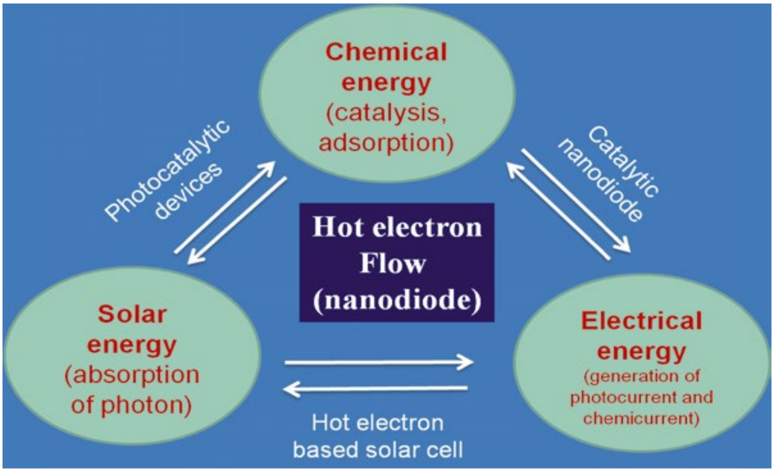

Fig. 10.14 Illustration showing energy conversion between chemical, photon, and electrical energies mediated by hot electrons

dissipation mechanisms and detection schemes for hot electrons. We discussed the SMSI effects for various catalytic systems to address the role of the metal–oxide interface in heterogeneous catalysis. Hot electron flow through a catalytic nanodiode provides insights into the role of electronic excitation leading to energy conversion processes using heterogeneous metal catalysis. We found that hot electron flux is well correlated with the turnover rates of catalyzed reactions, which suggests possible applications for chemical sensors and novel energy conversion. We showed that hot electrons could affect heterogeneous catalysis for various catalytic systems, ranging from catalytic nanodiodes to metal–semiconductor hybrid nanocatalysts. We showed that the hot electron is the main mediator of energy conversion between chemical, photon, and electrical energies, suggesting a new energy conversion mechanism based on hot electrons.

Acknowledgments The work was supported by the WCU (World Class University, R-31-2008-000-10055-0) program, and 2012R1A2A1A01009249 through the National Research Foundation (NRF) funded by the Ministry of Education, Science and Technology (MEST) and by the Research Center Program (CA1201) of IBS (Institute for Basic Science) of Republic of Korea.

References

1. Schindler B, Diesing D, Hasselbrink E (2011) Electronic excitations induced by hydrogen surface chemical reactions on gold. J Chem Phys 134:034705
2. Gergen B, Nienhaus H, Weinberg WH, McFarland EW (2001) Chemically induced electronic excitations at metal surfaces. Science 294:2521–2523
3. Nienhaus H (2002) Electronic excitations by chemical reactions on metal surfaces. Surf Sci Rep 45:3–78
4. Tully JC (2000) Chemical dynamics at metal surfaces. Annu Rev Phys Chem 51:153–178
5. Maximoff SN, Head-Gordon MP (2009) Chemistry of fast electrons. Proc Natl Acad Sci U S A 106:11460–11465
6. Park JY, Renzas JR, Contreras AM, Somorjai GA (2007) The genesis and importance of oxide-metal interface controlled heterogeneous catalysis; the catalytic nanodiode. Top Catal 46:217–222
7. Shenvi N, Cheng HZ, Tully JC (2006) Nonadiabatic dynamics near metal surfaces: decoupling quantum equations of motion in the wide-band limit. Phys Rev A 74:10
8. Somorjai GA, Park JY (2007) The impact of surface science on the commercialization of chemical processes. Catal Lett 115:87–98
9. Gadzuk JW (2002) On the detection of chemically-induced hot electrons in surface processes: from X-ray edges to schottky barriers. J Phys Chem B 106:8265–8270
10. Shenvi N, Roy S, Parandekar P, Tully J (2006) Vibrational relaxation of NO on Au(111) via electron–hole pair generation. J Chem Phys 125:9
11. Kasemo B, Tornqvist E, Norskov JK, Lundqvist BI (1979) Photon and electron-emission as indicators of intermediate states in surface-reactions. Surf Sci 89:554–565
12. Bottcher A, Imbeck R, Morgante A, Ertl G (1990) Nonadiabatic surface-reaction: mechanism of electron-emission in the Cs + O-2 system. Phys Rev Lett 65:2035–2037
13. Kasemo B (1974) Photon emission during chemisorption of oxygen on Al and Mg surfaces. Phys Rev Lett 32:1114–1117
14. Kasemo B, Wallden L (1975) Photon and electron-emission during halogen adsorption on sodium. Surf Sci 53:393–407
15. Norskov JK, Newns DM, Lundqvist BI (1979) Molecular-orbital description of surface chemi-luminescence. Surf Sci 80:179–188
16. Born M, Oppenheimer R (1927) Zur quantentheorie der molekeln. Ann Phys 389:457–484
17. Schaich WL (1974) Brownian-motion model of surface chemical-reactions: derivation in large mass limit. J Chem Phys 60:1087–1093
18. Schaich WL (1975) Model calculation of Brownian-motion parameters at a metal-surface. Surf Sci 49:221–235

19. Dagliano EG, Kumar P, Schaich W, Suhl H (1975) Brownian-motion model of interactions between chemical species and metallic electrons: bootstrap derivation and parameter evaluation. Phys Rev B 11:2122–2143
20. Head-Gordon M, Tully JC (1992) Vibrational-relaxation on metal-surfaces: molecular-orbital theory and application to CO/Cu(100). J Chem Phys 96:3939–3949
21. Persson BNJ, Persson M (1980) Vibrational lifetime for co adsorbed on Cu(100). Solid State Commun 36:175–179
22. Persson BNJ, Persson M (1980) Damping of vibrations in molecules adsorbed on a metal-surface. Surf Sci 97:609–624
23. Huang YH, Rettner CT, Auerbach DJ, Wodtke AM (2000) Vibrational promotion of electron transfer. Science 290:111–114
24. White JD, Chen J, Matsiev D, Auerbach DJ, Wodtke AM (2005) Vibrationally promoted emission of electrons from low work function surfaces: oxygen and Cs surface coverage dependence. J Vac Sci Technol A 23:1085–1089
25. White JD, Chen J, Matsiev D, Auerbach DJ, Wodtke AM (2005) Conversion of large-amplitude vibration to electron excitation at a metal surface. Nature 433:503–505
26. Wodtke AM, Tully JC, Auerbach DJ (2004) Electronically non-adiabatic interactions of molecules at metal surfaces: can we trust the born-oppenheimer approximation for surface chemistry? Int Rev Phys Chem 23:513–539
27. Ogawa S, Petek H (1996) Two-photon photoemission spectroscopy at clean and oxidized Cu(110) and Cu(100) surfaces. Surf Sci 363:313–320
28. Suarez C, Bron WE, Juhasz T (1995) Dynamics and transport of electronic carriers in thin gold-films. Phys Rev Lett 75:4536–4539
29. Hertel T, Knoesel E, Wolf M, Ertl G (1996) Ultrafast electron dynamics at Cu(111): response of an electron gas to optical excitation. Phys Rev Lett 76:535–538
30. Lingle RL, Ge NH, Jordan RE, McNeill JD, Harris CB (1996) Femtosecond studies of electron tunneling at metal-dielectric interfaces. Chem Phys 205:191–203
31. Ogawa S, Nagano H, Petek H (1997) Hot-electron dynamics at Cu(100), Cu(110), and Cu(111) surfaces: comparison of experiment with Fermi-liquid theory. Phys Rev B 55:10869–10877
32. Petek H, Ogawa S (1997) Femtosecond time-resolved two-photon photoemission studies of electron dynamics in metals. Prog Surf Sci 56:239–310
33. Huang Y, Wodtke AM, Hou H, Rettner CT, Auerbach DJ (2000) Observation of vibration excitation and deexcitation for NO($\nu = 2$) scattering from Au(111): evidence for electron–hole-pair mediated energy transfer. Phys Rev Lett 84:2985–2988
34. Hou H, Huang Y, Gulding SJ, Rettner CT, Auerbach DJ, Wodtke AM (1999) Direct multiquantum relaxation of highly vibrationally excited NO in collisions with O/Cu(111). J Chem Phys 110:10660–10663
35. Hou H, Rettner CT, Auerbach DJ, Huang Y, Gulding SJ, Wodtke AM (1999) The interaction of highly vibrationally excited molecules with surfaces: vibrational relaxation and reaction of NO(v) at Cu(111) and O/Cu(111). Faraday Discuss 113:181–200
36. Diesing D, Winkes H, Otto A (1997) Time resolved investigation of the hydrogen evolution reaction on Ag(111), Ag(100), smooth polycrystalline, and activated polycrystalline silver surfaces. Phys Status Solidi A 159:243–254
37. Diesing D, Merschdorf M, Thon A, Pfeiffer W (2004) Identification of multiphoton induced photocurrents in metal-insulator-metal junctions. Appl Phys B-Lasers O 78:443–446
38. Thon A, Merschdorf M, Pfeiffer W, Klamroth T, Saalfrank P, Diesing D (2004) Photon-assisted tunneling versus tunneling of excited electrons in metal-insulator-metal junctions. Appl Phys A-Mater 78:189–199
39. Kovacs DA, Babkina T, Gans T, Czarnetzki U, Diesing D (2006) Electronic excitation in metals through hyperthermal atoms. J Phys D: Appl Phys 39:5224–5229
40. Kovacs DA, Winter J, Meyer S, Wucher A, Diesing D (2007) Photo and particle induced transport of excited carriers in thin film tunnel junctions. Phys Rev B 76:235408
41. Mildner B, Hasselbrink E, Diesing D (2006) Electronic excitations induced by surface reactions of H and D on gold. Chem Phys Lett 432:133–138

42. Kovacs DA, Peters T, Haake C, Schleberger M, Wucher A, Golczewski A, Aumayr F, Diesing D (2008) Potential electron emission induced by multiply charged ions in thin film tunnel junctions. Phys Rev B 77:245432
43. Marpe M, Heuser C, Diesing D, Wucher A (2011) Internal electron emission in metal-insulator-metal thin film tunnel devices bombarded with keV argon and gold-cluster projectiles. Nucl Instrum Methods Phys Res, Sect B 269:972–976
44. Peters T, Haake C, Diesing D, Kovacs DA, Golczewski A, Kowarik G, Aumayr F, Wucher A, Schleberger M (2008) Hot electrons induced by slow multiply charged ions. New J Phys 10:073019
45. Stella K, Kovacs DA, Diesing D, Brezna W, Smoliner J (2011) Charge transport through thin amorphous titanium and tantalum oxide layers. J Electrochem Soc 158:P65–P74
46. Thissen P, Schindler B, Diesing D, Hasselbrink E (2010) Optical response of metal-insulator-metal heterostructures and their application for the detection of chemicurrents. New J Phys 12:113014
47. Sharpe RG, Dixonwarren S, Durston PJ, Palmer RE (1995) The electronic catalyst: dissociation of chlorinated hydrocarbons by metal-insulator-metal electron emitters. Chem Phys Lett 234:354–358
48. Wadayama T, Kojim A, Hatta A (2004) Bias-voltage-induced decomposition of 2-methyl-1,4-naphthoquinone on Ag/AlOx/Al tunnel junction. Appl Phys A-Mater 79:1891–1894
49. Wadayama T, Yokawa M (2006) Hot-electron assisted reaction of p-nitrobenzoic acid adsorbed on metal-insulator-metal tunnel junction's electrode surface. Chem Phys Lett 428:348–351
50. Nienhaus H, Bergh HS, Gergen B, Majumdar A, Weinberg WH, McFarland EW (1999) Electron–hole pair creation at Ag and Cu surfaces by adsorption of atomic hydrogen and deuterium. Phys Rev Lett 82:446–449
51. Nienhaus H, Bergh HS, Gergen B, Majumdar A, Weinberg WH, McFarland EW (2000) Direct detection of electron–hole pairs generated by chemical reactions on metal surfaces. Surf Sci 445:335–342
52. Resasco DE, Haller GL (1983) A model of metal-oxide support interaction for Rh on TiO_2. J Catal 82:279–288
53. Haller GL, Resasco DE (1989) Metal support interaction: group-VIII metals and reducible oxides. Adv Catal 36:173–235
54. Tauster SJ (1987) Strong metal-support interactions. Acc Chem Res 20:389–394
55. Tauster SJ, Fung SC, Baker RTK, Horsley JA (1981) Strong-interactions in supported-metal catalysts. Science 211:1121–1125
56. Goodman DW (2005) "Catalytically active Au on titania": yet another example of a strong metal support interaction (SMSI)? Catal Lett 99:1–4
57. Schwab GM (1967) Boundary-layer catalysis. Angew Chem Int Ed 6:375
58. Schwab GM, Siegert R (1966) Inverse Mischkatalysatoren. I. Kohlenmonoxid-Oxydation an Nickeloxid Auf Silber. Z Phys Chem (Frankfurt) 50:191
59. Hayek K, Fuchs M, Klotzer B, Reichl W, Rupprechter G (2000) Studies of metal-support interactions with "real" and "inverted" model systems: reactions of CO and small hydrocarbons with hydrogen on noble metals in contact with oxides. Top Catal 13:55–66
60. Penner S, Wang D, Podloucky R, Schlogl R, Hayek K (2004) Rh and Pt nanoparticles supported by CeO_2: metal-support interaction upon high-temperature reduction observed by electron microscopy. Phys Chem Chem Phys 6:5244–5249
61. Penner S, Wang D, Su DS, Rupprechter G, Podloucky R, Schlogl R, Hayek K (2003) Platinum nanocrystals supported by silica, alumina and ceria: metal-support interaction due to high-temperature reduction in hydrogen. Surf Sci 532:276–280
62. Hervier A, Renzas JR, Park JY, Somorjai GA (2009) Hydrogen oxidation-driven hot electron flow detected by catalytic nanodiodes. Nano Lett 9:3930–3933
63. Park JY, Somorjai GA (2006) The catalytic nanodiode: detecting continous electron flow at oxide-metal interfaces generated by a gas-phase exothermic reaction. Chemphyschem 7: 1409–1413

64. Somorjai GA, Frei H, Park JY (2009) Advancing the frontiers in nanocatalysis, biointerfaces, and renewable energy conversion by innovations of surface techniques. J Am Chem Soc 131:16589–16605
65. Lee YK, Jung CH, Park J, Seo H, Somorjai GA, Park JY (2011) Surface plasmon-driven hot electron flow probed with metal–semiconductor nanodiodes. Nano Lett 11:4251–4255
66. Ali M, Cimalla V, Lebedev V, Romanus H, Tilak V, Merfeld D, Sandvik P, Ambacher O (2006) Pt/GaN Schottky diodes for hydrogen gas sensors. Sensor Actuat B-Chem 113: 797–804
67. Wang L, Nathan MI, Lim TH, Khan MA, Chen Q (1996) High barrier height GaN Schottky diodes: Pt/GaN and Pd/GaN. Appl Phys Lett 68:1267–1269
68. Dittrich T, Zinchuk V, Skryshevskyy V, Urban I, Hilt O (2005) Electrical transport in passivated Pt/TiO_2/Ti Schottky diodes. J Appl Phys 98:104501
69. Schlatter JC, Boudart M (1972) Hydrogenation of ethylene on supported platinum. J Catal 24:482–492
70. Park JY, Renzas JR, Hsu BB, Somorjai GA (2007) Interfacial and chemical properties of Pt/TiO_2, Pd/TiO_2, and Pt/GaN catalytic nanodiodes influencing hot electron flow. J Phys Chem C 111:15331–15336
71. Park JY, Somorjai GA (2006) Energy conversion from catalyic reaction to hot electron current with metal–semiconductor Schottky nanodiodes. J Vac Sci Technol B 24:1967–1971
72. Ji XZ, Zuppero A, Gidwani JM, Somorjai GA (2005) Electron flow generated by gas phase exothermic catalytic reactions using a platinum-gallium nitride nanodiode. J Am Chem Soc 127:5792–5793
73. Ji XZ, Zuppero A, Gidwani JM, Somorjai GA (2005) The catalytic nanodiode: gas phase catalytic reaction generated electron flow using nanoscale platinum titanium oxide Schottky diodes. Nano Lett 5:753–756
74. Roland U, Braunschweig T, Roessner F (1997) On the nature of spilt-over hydrogen. J Mol Catal A 127:61–84
75. Hanson FV, Boudart M (1978) Reaction between H_2 and O_2 over supported platinum catalysts. J Catal 53:56–67
76. Hellsing B, Kasemo B, Zhdanov VP (1991) Kinetics of the hydrogen oxygen reaction on platinum. J Catal 132:210–228
77. Kwong DWJ, Deleon N, Haller GL (1988) Desorption of carbon-dioxide molecules from a Pt(111) surface: a stochastic classical trajectory approach. Chem Phys Lett 144:533–540
78. McFarland EW, Tang J (2003) A photovoltaic device structure based on internal electron emission. Nature 421:616–618
79. Fowler RH (1931) The analysis of photoelectric sensitivity curves for clean metals at various temperatures. Phys Rev 38:45–56
80. Stuckless JT, Moskovits M (1989) Enhanced 2-photon photoemission from coldly deposited silver films. Phys Rev B 40:9997–9998
81. Knight MW, Sobhani H, Nordlander P, Halas NJ (2011) Photodetection with active optical antennas. Science 332:702–704
82. Lee YK, Park J, Park JY (2012) The effect of dye molecules and surface plasmons in photon-induced hot electron flows detected on Au/TiO_2 nanodiodes. J Phys Chem C 116: 18591–18596
83. Lee YK, Lee J, Lee H, Lee JY, Park JY (2013) Probing polarization modes of Ag nanowires with hot electron detection on Au/TiO_2 nanodiodes. Appl Phys Lett 102:123112
84. Somorjai GA, Bratlie KM, Montano MO, Park JY (2006) Dynamics of surface catalyzed reactions; the roles of surface defects, surface diffusion, and hot electrons. J Phys Chem B 110:20014–20022
85. Ji XZ, Somorjai GA (2005) Continuous hot electron generation in Pt/TiO_2, Pd/TiO_2, and Pt/GaN catalytic nanodiodes from oxidation of carbon monoxide. J Phys Chem B 109:22530–22535
86. Shen TC, Wang C, Abeln GC, Tucker JR, Lyding JW, Avouris P, Walkup RE (1995) Atomic-scale desorption through electronic and vibrational-excitation mechanisms. Science 268: 1590–1592

87. Fomin E, Tatarkhanov M, Mitsui T, Rose M, Ogletree DF, Salmeron M (2006) Vibrationally assisted diffusion of H_2O and D_2O on Pd(111). Surf Sci 600:542–546
88. Choi BY, Kahng SJ, Kim S, Kim H, Kim HW, Song YJ, Ihm J, Kuk Y (2006) Conformational molecular switch of the azobenzene molecule: a scanning tunneling microscopy study. Phys Rev Lett 96:156106
89. Henzl J, Mehlhorn M, Gawronski H, Rieder KH, Morgenstern K (2006) Reversible cis-trans isomerization of a single azobenzene molecule. Angew Chem Int Ed 45:603–606
90. Gadzuk JW (1996) Resonance-assisted, hot electron femtochemistry at surfaces. Phys Rev Lett 76:4234–4237
91. Saunders AE, Popov I, Banin U (2006) Synthesis of hybrid CdS-Au colloidal nanostructures. J Phys Chem B 110:25421–25429
92. Mokari T, Sztrum CG, Salant A, Rabani E, Banin U (2005) Formation of asymmetric one-sided metal-tipped semiconductor nanocrystal dots and rods. Nat Mater 4:855–863
93. Mokari T, Rothenberg E, Popov I, Costi R, Banin U (2004) Selective growth of metal tips onto semiconductor quantum rods and tetrapods. Science 304:1787–1790
94. Milliron DJ, Hughes SM, Cui Y, Manna L, Li JB, Wang LW, Alivisatos AP (2004) Colloidal nanocrystal heterostructures with linear and branched topology. Nature 430:190–195
95. Kuo HS, Hwang IS, Fu TY, Wu JY, Chang CC, Tsong TT (2004) Preparation and characterization of single-atom tips. Nano Lett 4:2379–2382
96. Kim SM, Lee SJ, Kim SH, Kwon S, Yee KJ, Song H, Somorjai GA, Park JY (2013) Hot carrier-driven catalytic reactions on Pt-CdSe-Pt nanodumbbells and Pt/GaN under light irradiation. Nano Lett 13:1352–1358
97. Schafer S, Wyrzgol SA, Caterino R, Jentys A, Schoell SJ, Havecker M, Knop-Gericke A, Lercher JA, Sharp ID, Stutzmann M (2012) Platinum nanoparticles on gallium nitride surfaces: effect of semiconductor doping on nanoparticle reactivity. J Am Chem Soc 134:12528–12535
98. Kim SM, Park D, Yuk Y, Kim SH, Park JY (2013) Influence of hot carriers on catalytic reaction; Pt nanoparticles on GaN substrates under light irradiation. Faraday Discuss 162:355–364
99. Kim SH, Jung CH, Sahu N, Park D, Yun JY, Ha H, Park JY (2013) Catalytic activity of Au/TiO_2 and Pt/TiO_2 nanocatalysts prepared with arc plasma deposition under CO oxidation. Appl Catal A-Gen 454:53–58
100. Qadir K, Kim SH, Kim SM, Ha H, Park JY (2012) Support effect of Arc plasma deposited Pt nanoparticles/TiO_2 substrate on catalytic activity of CO oxidation. J Phys Chem C 116:24054–24059
101. Bonn M, Funk S, Hess C, Denzler DN, Stampfl C, Scheffler M, Wolf M, Ertl G (1999) Phonon- versus electron-mediated desorption and oxidation of CO on Ru(0001). Science 285:1042–1045

Index

A
Activation energy, 8, 9, 49, 50, 83, 110, 148–151, 158, 159, 172–175, 184, 185, 191, 242–244, 247
Activity, 3, 4, 6, 8–10, 12–14, 16, 21–40, 45, 53, 54, 56–59, 67, 69, 77–82, 85, 86, 93, 94, 96–106, 108–110, 113–115, 121–124, 134–139, 145–166, 171–191, 210–212, 218, 220, 223, 237, 238, 247–251
Aggregation, 6, 94, 96, 99, 106, 113, 125
Alloy, 25, 59, 94, 122–124, 128–133, 135–138, 174
Ambient pressure X-ray photoelectron spectroscopy (AP-XPS), 13, 146, 157–163, 166, 197–225
Ammonia decomposition, 98, 99
AP-XPS. *See* Ambient pressure X-ray photoelectron spectroscopy (AP-XPS)
Arc plasma deposition, 45–61, 250, 251
Atomic structure, 3, 171–191
Au catalysts, 38

B
Bandgap, 246, 248
Beamline, 200, 205, 213
Bimetallic nanocatalysts, 121–139
Bimetallic nanoparticle, 6–10, 58, 59
Bimetallic nanorods, 131
Bimetallic nanowires, 131
Born–Oppenheimer approximation (BOA), 232
Brønsted–Evans–Polanyi (BEP) relation, 173, 174

C
Capping agent, 6, 23–25, 27, 29, 33, 35–38, 45, 67, 68, 77, 79, 95, 96, 122, 126, 127, 129–133, 139, 148
Capping layers, 13, 14, 149, 150, 158, 250, 251
Catalytic activity, 3, 6, 8, 9, 12–14, 21–40, 45, 54–60, 66, 67, 69, 79, 80, 93, 94, 96, 99, 102–105, 109, 110, 113, 122, 123, 134–135, 137–139, 145–166, 171–191, 218, 223, 237, 238, 247–251
Catalytic nanodiodes, 6, 15, 231, 238–239, 241–244, 247, 252, 253
Cetyltetramethylammonium bromide (CTABr), 98, 100
Channelplate, 199
Chemical stability, 93, 110, 113
Chemicurrent, 15, 231, 236–238, 241–244, 247
Chemiluminescence, 232
Chemisorption(s), 153, 172–175, 182, 212, 247
Chemisorption energy, 153, 172–175
Chemoselectivity, 85–86, 102
Clusters, 5, 6, 76–77, 84, 86, 164, 187, 188, 220
CO adsorption, 78, 137, 154, 161, 162, 185–188, 190, 191
CO-induced restructuring, 187
Colloid chemistry, 9, 93, 145
Colloid nanoparticle, 3, 6–8, 13, 250
Composition, 3, 6–10, 13, 93–95, 98, 99, 101, 121, 122, 125, 126, 134, 137, 138, 145, 161, 171, 175–177, 179, 182, 183, 215, 217, 247, 250

J.Y. Park (ed.), *Current Trends of Surface Science and Catalysis*, DOI 10.1007/978-1-4614-8742-5, © Springer Science+Business Media New York 2014

CO oxidation, 8–10, 13, 16, 34, 49, 53, 57, 58, 61, 96–98, 100, 102, 108, 110, 145–166, 177–183, 189, 190, 209–212, 217–221, 231, 238, 241, 244, 247–251
CO poisoning, 31, 121
Core-shell catalysts, 94, 98–100
Core-shell nanoparticle, 40, 70, 71, 160
Core-shell structures, 94, 96, 98, 99, 101–105, 113, 123
CO stripping, 32
Crystallinity, 126
CTABr. *See* Cetyltetramethylammonium bromide (CTABr)
Cubes, 24, 25, 27, 31–35, 37, 40, 124, 125, 130, 131, 133
Cuboctahedron, 7, 23, 25, 26, 31, 33, 34

D
Dendrimer-encapsulated nanoparticles (DENs), 67–86
Dendrimer-templated synthesis, 68–70, 77
Density functional theory (DFT), 32, 137, 146, 172–175, 184, 185, 187, 188, 191, 209–213, 251
Diastereoselectivity, 85–86
Differential-pumped electrostatic lens system, 200
Direct methanol fuel cells (DMFCs), 121, 134
Dodecahedrons, 124, 129
Dry process, 45, 52, 61
Durability, 121, 123

E
Electrocatalytic reaction(s), 21, 32, 33, 77, 122, 139
Electrodeposition, 70
Electron analyzer, 199, 200, 203, 222
Electron beam lithography, 46
Electronic excitations, 231–253
Electronic heat capacity, 233
Electron spectroscopy of chemical analysis (ESCA), 200
Energy conversion, 3, 16, 231, 238, 244, 251–253
Energy engineering, 3
ESCA. *See* Electron spectroscopy of chemical analysis (ESCA)
Ethylene hydrogenation, 25, 78, 96
Exoelectron, 232
Exothermic catalytic reactions, 231, 233, 237–244, 247, 252

F
Fowler's law, 245, 246

G
Galvanic redox displacement, 69–71

H
Heat of mixing, 123
Heterogeneous catalysis, 1–16, 45, 66, 77, 78, 81, 85, 93, 115, 134, 145, 171–172, 179, 180, 237, 248, 251–253
Heterostructure, 122, 123
High pressure scanning tunneling microscopy (HP-STM), 146, 179, 180, 209, 218
Hot electron, 3, 15, 16, 231–239, 241–253
Hydrogen oxidation, 231, 243–244
Hydrolysis, 95, 98–100, 102, 185
Hyperbranched structure, 65

I
Icosahedrons, 124, 128, 129, 137
IMFP. *See* Inelastic mean free path (IMFP)
Impregnation, 5, 45, 53, 54, 58
Impregnation reduction, 121, 122
Imprint lithography, 46, 48
Inelastic mean free path (IMFP), 199, 224
Initial state, 153
In-situ spectroscopic technique, 3, 149
Intermetallic compound, 123
Internal photoemission, 232, 246
Isomerization, 33, 247

K
Kinks, 4, 125, 138, 171–191
Kirkendall effect, 126

L
Langmuir–Hinselwood (L–H) mechanism, 209, 219
Linked structure, 123

M
Mars–van Krevelen (M–vK) mechanism, 178, 209
Materials gap, 4, 171, 197, 198
Metal–insulator–metal (MIM) tunnel junctions, 235, 247

Metal-ligand bonds, 71, 72
Metal nanoparticle(s), 6, 45, 59, 65–86, 93, 110, 145
Metal-oxide interface, 237, 238, 252
Metal precursors, 23, 24, 26, 67, 69, 72, 122, 125–128, 133, 139
Methanation, 100
Methanol oxidation reaction (MOR), 121, 134, 135, 137
MIM tunnel junctions. *See* Metal–insulator–metal (MIM) tunnel junctions
Molecular interactions, 234
Monochromator, 205, 224
MOR. *See* Methanol oxidation reaction (MOR)
M–vK mechanism. *See* Mars–van Krevelen (M–vK) mechanism

N
Nanodendrites, 29–30, 129
Nanodiode, 3, 5, 6, 15, 231, 236, 238–244, 247, 251–253
Nanolithography, 6, 45–61
Nanoparticles, 3–10, 13–15, 21–40, 45, 46, 51–61, 65–86, 93, 98, 110, 113, 122, 145, 148–151, 153–161, 163–166, 171, 182–184, 233, 238, 248, 250–252
Nanoparticle size, 60, 79–81, 160, 250
Nanopillar, 47, 48
Nanoreactor, 94, 104, 113
Nanorods, 34, 131, 132, 248
Nanowire, 5, 14, 46–50, 129, 131, 132, 238, 246
Nonadiabatic charge transfer process, 232
Non-colloidal nanocatalysts, 45–61

O
Octahedron, 124, 125, 128–131, 133
Operando analysis, 222
Operando conditions, 86
Organometallic complexes, 65–67
ORR. *See* Oxygen reduction reaction (ORR)
Overpotential, 30, 121, 134, 223
Oxidation state, 3, 6, 14, 35, 53, 72–76, 78, 86, 95, 145, 148–150, 156, 158, 159, 161–163, 165, 222, 238
Oxide shell, 99–103
Oxygen reduction reaction (ORR), 28–31, 34, 36, 37, 121–124, 134–138

P
PAMAM dendrimer. *See* Polyamidoamine (PAMAM) dendrimer
Pd oxide, 58, 161–165, 220
PEMFCs. *See* Proton exchange membrane fuel cells (PEMFCs)
Phonons, 231–233
Platinum oxide, 182
Polyvinylpyrrolidone (PVP), 8, 13, 24, 25, 33, 35, 67, 79, 82, 85, 106, 107, 126, 127, 133, 150, 157
Polyamidoamine (PAMAM) dendrimer, 67–69, 71, 72, 74, 76–79, 82, 84–86
Polyol methods, 8, 126
2PPE. *See* Two-photon photoemission (2PPE)
Pressure gap(s), 3–16, 175, 177–180, 197–199
Proton exchange membrane fuel cells (PEMFCs), 121
Pt(100), 21, 22, 33, 180, 187
Pt(111), 12, 21, 22, 24, 28, 31, 33, 135, 137, 186–188, 212–217, 243
Pt–CdSe–Pt nanodumbbells, 232
Pt@mSiO_2 core-shell NPs, 95–98
Pt nanoparticle, 6, 8–10, 14, 15, 24–27, 29, 32, 33, 36–40, 52–58, 60, 74, 78–82, 98, 113, 148, 149, 182, 248, 250, 251
Pt oxide, 146–149, 166, 180, 209, 212
Pt/Rh bimetallic nanoparticles, 6–9
PVP. *See* Polyvinylpyrrolidone (PVP)
Pyrrole hydrogenation, 79, 80

R
Reductants, 106, 127, 129
Reduction rate, 26, 122, 126–129, 139
Renewable energy conversion, 3, 16
Resonance Raman spectroscopy, 71, 72
Rh oxide, 13, 149–153
Ru oxide, 153–161
Ruthenium, 156, 177–180

S
Scanning tunneling microscopy (STM), 4, 11, 12, 21, 22, 146, 147, 154, 155, 157, 162, 174, 178–182, 184–188, 190, 210, 211, 213, 216, 217, 221, 247
Schottky barrier, 15, 235, 237, 238, 240, 243–245
Schottky diode, 15, 236–239, 241, 244–246
Selectivity, 3–6, 8, 21–40, 66, 69, 77, 79, 80, 85, 86, 93, 94, 103, 110, 113, 115, 130, 177, 184, 191

SFG. *See* Sum frequency generation (SFG)
Shape, 3, 6–8, 21–40, 56, 60, 66, 68, 79, 93, 96, 121–139, 145, 214
Single crystal, 4–6, 9–11, 13, 30, 55, 93, 110, 121, 128, 145, 146, 149, 153–155, 157, 161–162, 171–172, 175, 179, 180, 184, 185, 190, 191, 209–221
Sintering, 58, 70, 78, 94, 96–98, 102, 108, 109, 113, 115, 164
Size, 3–10, 24, 25, 27, 29, 35, 37–40, 46, 47, 50, 52, 55–58, 60, 61, 66, 68, 70, 73, 77, 79–81, 86, 93, 98, 102, 104–111, 113, 114, 122, 126, 128, 134, 139, 145, 149, 150, 156–157, 160, 164, 166, 183, 185–188, 201, 216, 242, 248, 250
Size reduction lithography, 46, 47
Solid solution, 123
Solubility, 125
Step(s), 4, 7, 23, 25, 34, 38–39, 46, 47, 66–68, 71, 77, 84, 95, 100, 104, 107–109, 114, 123, 125, 126, 131, 133–135, 138, 139, 154, 164, 171–191
Step decoration, 184–185
STM. *See* Scanning tunneling microscopy (STM)
Strong metal-support interaction, 15, 53, 94, 238
Structure-sensitive reactions, 117
Sum frequency generation (SFG), 22
Sum frequency generation (SFG) spectroscopy, 4, 8, 10, 11, 199
Supersaturation, 125, 128
Surface free energy, 128, 175
Surface oxide, 148–166, 172, 177, 182, 183, 188, 189, 209–212, 218–220
Surface plasmon, 232, 245, 246
Surface science, 3–16, 171, 175, 177, 179, 180, 184, 185, 197–225
Surface structure, 4, 21, 22, 39, 139, 146, 147, 149, 156, 159, 173, 175, 176, 179, 182, 183, 186, 187, 191, 216
Surface X-ray diffraction (SXRD), 146, 178–180, 182, 183, 189, 190
Synchrotron radiation source, 200, 201

T
Temperature-programmed desorption (TPD), 162, 184
Tetradecyltrimethylammonium bromide (TTAB), 13, 29, 35–37, 40, 95–98, 148, 149
Tetra-ethyl-ortho-silicate (TEOS), 96, 98
Tetrahedron, 124, 128–130, 137
Thermal stability, 58, 96, 110, 112, 114, 164, 165
TPD. *See* Temperature-programmed desorption (TPD)
TTAB. *See* Tetradecyltrimethylammonium bromide (TTAB)
Turnover frequency, 9, 12, 25, 50, 53, 80, 104, 105, 150, 151, 243
Two-photon photoemission (2PPE), 234, 235

U
Underpotential deposition, 31, 122, 133
UV-ozone treatment, 36, 150–153, 157–159, 166

V
Vibrational energy, 235, 236

W
Wet-chemical process, 45, 52, 55

X
X-ray photoelectron spectroscopy (XPS), 4, 8–11, 13, 53–55, 58, 73–75, 78, 103, 146, 148–152, 158–161, 163, 164, 182, 184, 188, 197–225

Y
Yolk-shell catalysts, 94, 105